INTERACTION OF GERMANIUM WITH PLATINUM GROUP METALS IN LATERAL DIFFUSION COUPLES

A dissertation submitted to the University of Cape Town in fulfillment of the requirements for the degree of Doctor of Philosophy (Physics)

by

Adrian Habanyama

September 2004

Abstract

Existing materials and technologies in the semiconductor industry are approaching their physical limits as device sizes decrease significantly below 100 nm. The challenges of achieving the required lateral abruptness of semiconductor junctions and low junction leakage as well as low contact resistance require a careful rebuilding of the fundamental physics and materials platform on which to base a reliable manufacturing capability. As feature size continues to decrease, interconnects will also pose increasingly difficult challenges in terms of physics and materials.

The study of lateral diffusion couples is particularly well suited for dealing with the above concerns. This thesis looks at metal-germanium systems of the Platinum Group Metals (PGMs). It is of particular relevance to study possible applications of PGMs in South Africa, the country being one of the major producers of these metals in the world today.

The diffusion lengths in standard thin-film couples range from a few angstroms to several thousand angstroms. In lateral diffusion couples, phase formation could extend to lengths of around 100 μm. Solid-state interactions in both thin-film and bulk diffusion couples can therefore be investigated using lateral diffusion couples. In particular the transition between the two types of interactions can be studied.

Our approach to this investigation was essentially twofold. Firstly, conventional thin film couples were used to study the sequence of phase formation in germanide systems of the four Platinum Group Metals, Ir, Pt, Pd and Rh. Using conventional thin film couples we also monitored the direction of atomic mobility during the formation of the phases IrGe, Ir_4Ge_5 and Pt_2Ge by interposing a thin layer of Ti to act as an inert marker between the coupling layers. Secondly, we observed and analysed several aspects of the lateral diffusion reactions, including activation energies and diffusion mechanisms, in these four systems. Several germanide phases were seen to spread out from the source regions in each system exhibiting unique reproducible features. The results are largely discussions in the framework of the Effective Heat of Formation (EHF) model and the geometrically modified kinetic model of Gösele and Tu.

We will show that Particle Induced X-ray Emission (PIXE) on the Nuclear Microprobe (μPIXE) can be used to study systems like the Ni-Ge and Co-Ge where micro Rutherford Backscattering Spectroscopy (μRBS) can not be used due to excessive peak overlap.

To Kate

Acknowledgements

First and foremost, I am greatly indebted to my supervisor at the University of Cape Town, Prof. C.M. Comrie for guiding me into the world of lateral diffusion couples. His effort, patience and meticulous attention to detail regarding every aspect of this work is greatly appreciated.

I wish to acknowledge the support of my first local supervisor Prof. C.V. Sheth. Words alone do not begin to express my gratitude for the mentor he has been both professionally and personally, throughout my career.

I am also grateful to Dr. H. V. Mweene who took over as my University of Zambia supervisor upon the departure of Prof. Sheth. The good intentions behind his tough approach to seeing this work to completion did not pass without note on my part.

I owe much to many at the iThemba Labs (formally the National Accelerator Center) at Faure, but for sheer shortage of space will limit myself to expressing my gratitude to those whom I feel I bothered the most: Prof. R. Pretorius for his numerous words of encouragement during the earlier parts of this work, Mr. Karl Springhorn who taught me how to operate the Nuclear Microprobe and was always there to assist me, Dr. Chris Theron for his support and numerous useful discussions regarding the theoretical aspects of this work, Dr. Wojtek Przybylowicz for guiding me through the PIXE analysis. Johan Mars for his friendship and the endless nights we spent together in the control room. My friends Kevin Meyer and Jayne Paddaychee for sharing their IDL expertise with me. Dr. Cecil Churms for his Labview analysis programs. Messr. Hendrick de Waal, Thulani Kubeka and Stanley Hendricks for their friendship and encouragement.

During the course of this work some excellent technical support was also received from outside the iThemba Labs. In this regard I thank Ms Terry Davies of the X-ray unit in the Geological Sciences Department at UCT, Miranda Waldron in the Electron Microscope unit at UCT and the Atomic Force Microscopy team at the University of Stellenbosch.

I thank the entire Physics Departments at UCT for its support. At the University of Zambia I enjoyed the fruitful discussions on computing with Dr. Teddy Chibuye. I also thank Dr. Godfrey Chinyama, Dr. Geoffrey Munyeme, Dr. Kachiduli Nkunika and Mr. Evans Lampi for their friendship and encouragement.

I would finally like to take the opportunity to express my gratitude to the University Science, Humanities and Engineering Partnerships in Africa (USHEPIA) program for a research grant to complete this work.

Contents

CHAPTER 1

INTRODUCTION

1.1 Background

Due to the high electron mobility and very low carrier freeze-out temperature in germanium, there has been a renewed interest in the physical properties, stability and structure of metal germanides during the last couple of decades. They have a great potential in the development of new materials for integrated electronics technology, magnetic devices and detection systems. Most interest has been in metal reaction with silicon-germanium alloys and germanium is viewed as a possible replacement of silicon in the Information Technology (IT) industry. A thorough understanding of solid state interactions in metal-germanium systems is necessary for the achievement of improved reliability and reproducibility in devices.

The six metallic elements iridium, platinum, palladium, rhodium, ruthenium and osmium are chemically similar and are generally referred to as Platinum Group Metals (PGM). They have unique properties that make them important over a wide range of applications including, as catalysts, for chemical synthesis electrode coatings, for power generation (fuel cells) and for control of vehicle pollution (auto catalysts). They also have a wide range of medical applications notably in implants, in anti-cancer drugs and in alloys for dental restoration. Electronically, PGMs are used in the fabrication of multi-layer ceramic capacitors (palladium), computer hard disks (platinum) and crucibles for single crystal growth (iridium). Rhodium and platinum are also used in chemical and gas sensors.

Iridium, platinum and osmium are the densest known metals, platinum being about 10% denser than gold. Palladium, rhodium and ruthenium are lighter, with densities about the same as silver. Table 1.1 gives some general properties of the PGMs.

Metal	Iridium	Platinum	Palladium	Rhodium	Ruthenium	Osmium
Density (g/cm^3)	22.65	21.45	12.02	12.41	12.45	22.61
Melting point (°C)	2443	1769	1554	1960	2310	3050
Electrical resistivity ($\mu\Omega$/cm at 0°C)	4.71	9.85	9.93	4.33	6.8	8.12
Thermal conductivity (W/m/ °C)	148	73	76	150	105	87
Tensile strength (annealed condition) (kg/mm^2)	112	14	17	71	165	–

Table 1.1: General properties of the Platinum Group Metals.

Platinum and palladium are easy to work (for most fabrication processes), as they are soft, ductile and resistant to oxidation and high temperature corrosion. Iridium and rhodium are much more difficult to work, while ruthenium and osmium are almost unworkable in their pure metallic state. The latter two are hard, brittle, and with poor oxidation resistance; they are not investigated in the present work.

PGMs have been used in the micro-electronic industry. PtSi has been used in ohmic contacts, it was later replaced by $TiSi_2$ and more recently by $CoSi_2$. Incorporation of PGMs in the already expanding germanium technology opens up a wide range of new possibilities. It is the aim of this study to augment the knowledge base in this regard.

1.2 Bulk diffusion couples and thin film technology

For many years, conventional bulk diffusion has been studied to understand the problems that arise when two different materials are coupled. Bulk diffusion couples are prepared in a variety of ways including hot dipping, cold pressing and butt welding.[1-3] Samples are annealed in vacuum or in an inert atmosphere. Thickness of coupling phases in bulk couples may vary from several hundreds of micrometers to a few millimeters. Analytical techniques used to monitor phase formation are microprobe tracing of a section to obtain compositional information,[1] X-ray diffraction for phase identification[1,4] and light microscopy[2] of etched cross-sections of the sample for phase identification and growth characterization. Apart from a few exceptions, experiments with bulk diffusion couples result in the formation of all possible equilibrium phases in the binary system.

Development of the integrated circuit industry in the early 1960s caused massive interest in thin film technology. Thin film structures are the building blocks for integrated circuits and a host of other solid state devices (e.g., solid state lasers and photovoltaic cells). Thin film diffusion couples are normally prepared by various vapor deposition techniques; the full process is described in Chapter 2. During diffusion experiments, only one phase at a time is usually found to grow in thin film couples. A well defined sequence of phase formation is observed. A critical thickness is defined to explain the absence of multiple phases. This is the thickness at which a second phase can coexist with the first. Phases are said to coexist if they are both observed to grow simultaneously, normally one grows at the expense of the other i.e. the other gets consumed. The deposited metal layer serves as a supply of reactant at the reaction interface; this is usually very thin and is exhausted before the first phase grows to its critical thickness. The technique of Rutherford Backscattering Spectrometry (RBS) is generally favored for monitoring reaction kinetics in thin films. Resistivity measurements[5,6] and differential scanning calorimetry[7,8] have also been used successfully in this regard. X-ray diffraction methods or electron diffraction during transmission electron microscopy (TEM) are usually employed for phase identification.

Bulk and thin film diffusion couples can be viewed as two extreme regimes in which solid state interaction is investigated. Lateral diffusion couples, which are described later, are the bridge between the two.

1.3 Thermodynamics of phase formation

When the change in heat capacity at constant pressure (ΔC_p) of reactants and products is known during a chemical reaction, the heats of formation ($\Delta H°$) and the change in entropies ($\Delta S°$) can be calculated. These values are usually tabulated for a temperature of 298 K. The value of the heat of formation ΔH_T at a temperature T above 298 K can be calculated from that at 298 K by the equation

$$\Delta H_T = \Delta H_{298} + \int_{298}^{T} \Delta C_p dT \qquad (1.1)$$

For solid state chemical reactions, the heat capacity of the products is approximately equal to that of the reactants; therefore $\Delta C_p \cong 0$ (Neumann-Kopp rule). Therefore, at any temperature T of practical interest, $\Delta H_T \cong \Delta H_{298}$. This also applies to the entropy, i.e. $\Delta S_T \cong \Delta S_{298}$. The change in Gibbs-Helmholz free energy at temperature T, which is the driving force for a process to take place, can therefore be simplified by relating it to theoretical or experimentally determined values of $\Delta H°$ and $\Delta S°$ at 298 K by the equation

$$\Delta G_T^\circ = \Delta H_{298}^\circ - T\Delta S_{298}^\circ \tag{1.2}$$

For ordered alloys (compounds), $\left|\Delta H_{298}^\circ\right| >> \left|T\Delta S_{298}^\circ\right|$ and the Gibbs free energy can be approximated by the standard enthalpy alone, i.e.,

$$\Delta G_T^\circ = \Delta H_{298}^\circ \tag{1.3}$$

1.3.1 The semi-empirical Miedema model

A number of models have been developed to predict the formation enthalpy (or heat of formation) $\Delta H°$, of binary alloys. One of the most successful is the semi-empirical model of Miedema.[9] This model of alloy cohesion is essentially based on two parameters, which are the difference in electron density and work function between the elements in an alloy and in their pure elemental state. The model was developed for metallic alloys.

The Wigner-Seitz cells of the different metal atoms are regarded as macroscopic pieces of the two metals. Hence this model is referred to as a macroscopic atomic model.

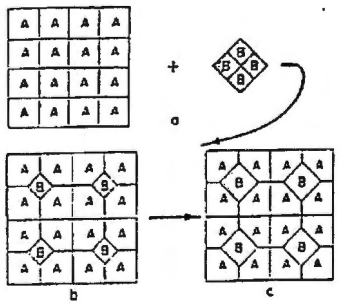

Figure 1.1: Change of Wigner-Seitz cells upon alloy formation between elements A and B [9].

If we consider the change in the Wigner-Seitz cells' during the formation of an alloy AB, as illustrated in Fig. 1.1, the electronic charge densities n_{ws} at the cell boundaries are discontinuous before contact interaction of the dissimilar atoms. When the Wigner-Seitz cells make contact, the condition for an equilibrium state is that the electron density at the boundary of the cells be continuous. The charge distribution therefore changes, creating a charge density gradient over the interface. This requires energy, giving an endothermic or positive contribution to $\Delta H°$ defined by an empirical factor Q such that

$$\Delta H_{BinA}^{pos} \propto Q(\Delta n_{ws}^{1/3})^2 \tag{1.4}$$

The more electronegative atoms in a binary alloy have a greater attraction for valence electrons. Change in charge distribution when cells are brought in contact may result in a transfer of charge due to the difference in electronegativity between the atoms. The work function ϕ, which is the energy needed above the Fermi level to remove an electron from a metal surface, is therefore different for the alloy from that of the pure metal. This transfer of charge gives a negative ionic contribution to $\Delta H°$,

$$\Delta H_{BinA}^{neg} \propto -P(\Delta\phi)^2 \tag{1.5}$$

The constant P, like Q, is determined by empirical fitting. The total value of $\Delta H°$ is then given by the expression

$$\Delta H^\circ = C_B f_A^B \left(\frac{-P(\Delta\phi)^2 + Q(\Delta n_{ws}^{1/3})^2}{n_{ws,A}^{-1/3} + n_{ws,B}^{-1/3}} \right) \tag{1.6}$$

where f_A^B accounts for the degree to which B atoms are surrounded by A atoms and C_B takes care of the units.

This treatment assumes that the atoms are in a metallic state. By means of an additional ΔH term, semiconducting elements such as Ge and Si can be converted to hypothetical metals. The heat of formation can then be predicted with respect to this metallic state. The values of the additional ΔH values for Ge and Si are 25 and 34 kJ(mol at.)$^{-1}$ respectively. Fig. 1.2 illustrates the curve of predicted heat of formation values as a function of composition, for the Ir–Ge system, as calculated on the basis of this model. Corresponding heats of formation values for some known phases are marked on the figure.

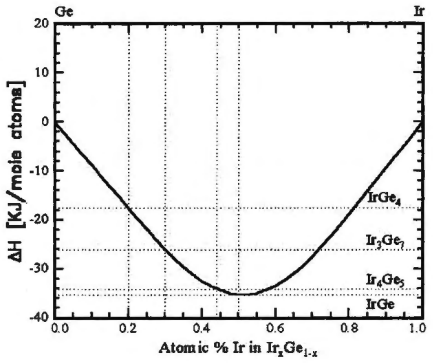

Figure 1.2: Predicted heat of formation values as a function of composition, in the Ir–Ge system, as calculated on the basis of Miedema's semiempirical model.

The Miedema model has been seen to predict the formation enthalpies of many alloys with reasonable accuracy. Meschel and Kleppa[10] have, using direct synthesis calorimetry and the so-called solute-solvent drop calorimetry, obtained the standard enthalpies of formation for a considerable number of metal germanides. Experimental values obtained by them that are of relevance to this work are presented in Table 1.2 along with predicted enthalpies calculated on the basis of Miedema's semiempirical model. The results show reasonable agreement in most cases, exceptions being in the Pd-Ge and Rh-Ge systems.

Compound	ΔH (Experimental) (kJ mol^{-1} atm^{-1})	Experimental method	ΔH (Miedema predicted) (kJ mol^{-1} atm^{-1})
IrGe	-33.1 ± 0.9 -32.5 ± 5.9	DSC SSD	-35
PtGe Pt_2Ge	-45.4 ± 1.2 -37.1 ± 1.6	DSC DSC	-43 -37
PdGe Pd_2Ge	-46.5 ± 0.8 -52.3 ± 0.9	DSC DSC	-51 -44
RhGe	-56.9 ± 1.1	DSC	-31

Table 1.2: Direct synthesis calorimetry (DSC) and solute-solvent drop calorimetry (SSD) results of Meschel and Kleppa [10]. Experimental values are presented along with enthalpies calculated on the basis of Miedema's semiempirical model.

1.3.2 Phase formation sequence and related models

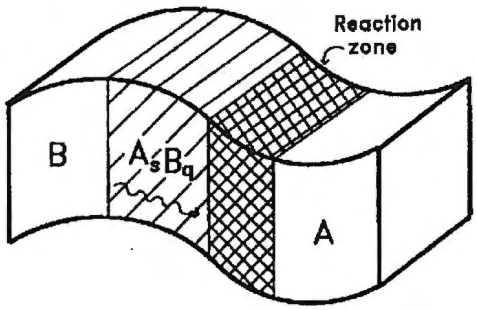

Figure 1.3: Schematic diagram of the formation of a compound A_sB_q at the reaction zone or growth interface.

Fig. 1.3 shows a diffusion couple of two pure elements A and B, phase A_sB_q being formed upon annealing. The figure shows the reaction zone assuming that B is the dominant moving species. In the study of thin film compound phase formation, there are two distinct concerns. The first is the prediction of the first phase A_sB_q to form and the phase formation sequence of following phases. The second is a kinetic description of the thin film reactions, which gives a relationship for the growth rate of the phases with time. The latter will be dealt with in the next section.

One of the first rules for predicting phase formation was that of Walser and Bené[11] which states: The first compound phase formed in planar binary reaction couples is the most stable congruently melting compound adjacent to the lowest temperature eutectic on the bulk equilibrium phase diagram.

The rule predicted first phase formation in metal-silicon systems with reasonable success and was later extended by Tsauer et al.[12] to subsequent phase formation sequence, as follows: The second phase formed is the compound with the smallest ΔT that exists in the phase diagram between the composition of the first phase and the unreacted element. ΔT is defined as the temperature difference between the liquidus curve and the peritectic (or peritectoid) point, which is the point where a solid breaks up into a liquid and a solid, both with new composition.

A more fundamental Effective Heat of Formation (EHF) model, proposed by Pretorius,[13] has been successfully applied to metal-metal, silicon-metal and germanium-metal systems. It was the first model based on fundamental thermodynamic principles. The background to this approach lies in the fact that the driving force for a chemical reaction is the change in Gibbs free energy which, as shown in a previous section, can be approximated by the standard enthalpy of reaction alone, for solid state reactions.

The following illustration of the concept of an effective heat of formation ($\Delta H'$) is adopted from an excellent review article by Pretorius, Marias and Theron.[14] In this illustration, they consider a solid state interaction between Cr and Si to form the compound phase CrSi. As shown in the schematic figure (Fig. 1.4), 10 atoms are assumed present initially in the reaction zone. When the effective concentration matches that of the compound to be formed, i.e., for CrSi (50 atomic % Cr and 50 atomic % Si), five atoms of Si and five of Cr. For this interaction, the amount of heat released or the effective heat of formation is equal to the standard heat of formation ($\Delta H' = \Delta H°$), which is 30.2 kJ $(mol.at)^{-1}$. In the second case, we have three atoms of Cr and seven of Si. The limiting

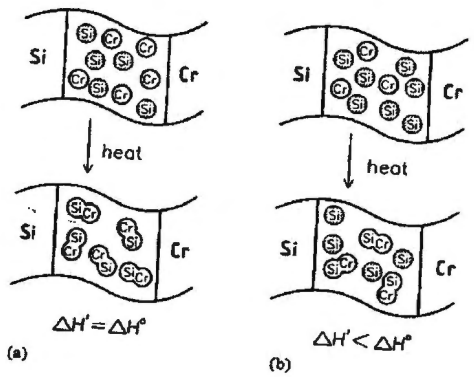

Figure 1.4: Schematic illustration of the concept of an effective heat of formation (ΔH') considering a solid state interaction between Cr and Si to form the compound phase CrSi [14].

element is Cr with an effective concentration of 30 atomic percent. The compound concentration of the limiting element (percentage of Cr in CrSi) is 50 percent. In this case, not all atoms take part in the reaction, and therefore the amount of heat released will be less than that in the previous case and is represented by an effective heat of formation $\Delta H'$, which is defined as,

$$\Delta H' = \Delta H^{\circ} \times \left(\frac{\textit{effective concentration of limiting element}}{\textit{compound concentration of limiting element}} \right) \qquad (1.7)$$

In this case $\Delta H'$ = -30.2 (0.30/0.50) = -18.1 kJ(mol at)$^{-1}$. For an arbitrary effective concentration x, of the limiting element in CrSi is $\Delta H' = 30.2\ (x/50)$. Fig. 1.5 shows a plot of $\Delta H'$ vs x. Such plots are generally referred to as EHF diagrams and they are made use of in this work.

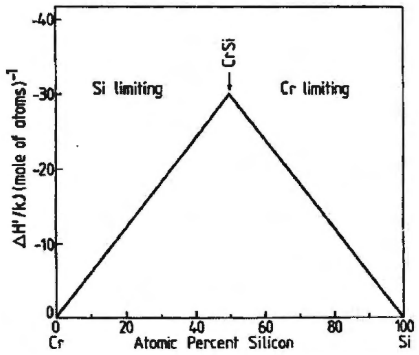

Figure 1.5: A plot of effective heat of formation, ΔH' versus atomic percent for the Cr-Si binary system constructed for the phase CrSi only [14].

It is not possible to calculate the actual effective concentrations of the reactants at the growth interface. It is therefore assumed as being equal to the concentration leading to the highest mobility and is thus given by the composition at the liquidus minimum of the binary system.

In metal-silicides, congruency plays a decisive role during phase formation. It was recognized that non-congruent phases did not easily form at the moving interface. To predict first phase formation, the following rule was formulated for metal-silicon systems: The first phase to form is the congruent phase with the most negative effective heat of formation ($\Delta H'$) at the concentration of the lowest eutectic temperature (minimum of the liquidus curve) of the binary system.

An example of a metal-silicide system is the Ni-Si system. In this system Ni_3Si_2 yields the largest effective heat of formation but it is non-congruent. The EHF model predicts both NiSi and Ni_2Si to form first since their $\Delta H'$ values are next in negativity and close to each other at the concentration of the lowest eutectic. This prediction agrees with experimental results.[15 - 20]

In metal-metal systems, congruency does not play a role during phase formation. In this case, the phase with the most negative $\Delta H'$ forms first, regardless of congruency. An example is the Au-Al system. At the concentration of the lowest eutectic, effective heats of formation of the phases Au_2Al and Au_5Al_2 have the most negative $\Delta H'$ values which are close to each other. These two phases are indeed found to form first experimentally.[21-23]

From a chemical point of view, germanium is more metallic in nature than Si and lies between silicon and the metals. Germanides therefore occupy a position between that of silicides where only congruent phases form first and metal-metal systems where phases form regardless of congruency. Some metal-germanium systems seem to behave like silicides, while others have a metal-metal behavior. An appropriate rule for first phase formation in metal-germanium systems according to the EHF model is: The first phase to form in metal-germanium systems is either the congruent phase (metal-silicon type) or the non-congruent phase (metal-metal type) with the most negative effective heat of formation at the concentration of the liquidus minimum of the binary system.

This rule is extended to incorporate the subsequent phase formation sequence as follows (for the metal-silicon case): After first phase formation, the next phase formed at the interface between the compound and remaining element is the next congruent phase richer in the unreacted element, which has the most negative effective heat of formation. If the compounds between a formed phase and the remaining element are all non-congruent, the next phase that will form is the non-congruent phase with the most negative effective heat of formation.

For the metal-metal case, the condition of congruency does not apply. It can therefore be seen that the EHF model links standard thermodynamic concepts (heats of formation) with kinetics (effective concentrations), presenting a unique thermodynamic-kinetic point of view.

1.4 Kinetics of phase formation

During solid state interaction, if the growing phase is sufficiently thick, the limiting factor to growth is the diffusion rate of material across the film to the reaction interface.

During the initial stages of reaction, the reacting species are in close proximity, and hence the diffusion rate can be considered as infinite. During this stage of the growth, the rate is not limited by diffusion but is reaction controlled or nucleation controlled. In describing the solid state kinetics of thin film growth, we therefore identify three different categories.

(i) Reaction-controlled kinetics

For reaction-controlled growth, the film thickness increases linearly with time. In this case, the activation energy is derived from the slopes of plots of phase thickness against time. The values are generally higher than those for diffusion-controlled growth (typically larger than 2.5 eV).

(ii) Diffusion-controlled kinetics

When growth is diffusion-controlled the growth rate decreases as the reaction proceeds because the diffusion path increases, it is found that the thickness of the film increases proportionally to the square root of the time of annealing. If for diffusion-controlled kinetics the square of the film thickness x_β^2 is plotted against time for different temperatures, a series of straight lines is obtained. The slopes of these lines give a quantity, K_β, called the diffusional growth constant or diffusivity, which is directly related to the diffusion coefficient D, as will be shown later. When diffusivities are displayed in an Arrhenius plot, which is a plot of lnK_β versus $1/k_bT$ (k_b being the Boltzman constant and T the absolute temperature), an activation energy, E_a (which generally has a value between 1-2 eV), is obtained from the slope of the straight line fit. This is not the activation energy for lattice diffusion processes (rotational, interstitial, crowdian and vacancy mechanisms) alone but has components from grain boundary diffusion and from mechanisms due to variations of the concentration gradient resulting from saturation and deficiencies of the diffusing species at the interface.

(iii) Nucleation-controlled kinetics

In this type of growth, compound phase formation starts at a specific nucleation site and rapidly proceeds towards the surface. In thin films, this is followed by lateral growth. The sample surface morphology makes the surface to appear somewhat wavy and dull.

According to classical nucleation theory, if the gain in the Gibbs free energy of the newly formed phase is ΔG_v and the increase in surface energy associated with the extra interface formed is $\Delta\sigma$, the activation energy barrier ΔG^* is proportional to $\Delta\sigma^3/\Delta G_v^2$ where ΔG_v is in units of free energy per unit volume of the newly formed phase. Nucleation is more prominent whenever the heat of reaction ΔH_R is small or nearly equal to zero.

1.4.1 The kinetic model of Gösele and Tu

The first model which attempted to explain the phenomenon of single phase growth in thin films was developed by Gösele and Tu.[24] This model centers around the observation that every growth phase has two growth regimes. Initially the growth rate of a phase is reaction controlled with an atomic flux that is assumed constant. As the thickness of the diffusion zone increases, the reaction controlled regime gives way to growth kinetics that are diffusion dominated, in which case the atomic flux is proportional to the reciprocal of the growth length.

(i) Single phase growth

Fick's first law of diffusion, $J = -D\frac{\partial C}{\partial x}$, states that the flow J of material across unit area in unit time is proportional to the concentration gradient. The proportionality factor D is the diffusion coefficient which for diffusion couples is more correctly referred to as the interdiffusion coefficient $\tilde{D}$. If the diffusion coefficients of the component elements are equal, then the interdiffusion coefficient also has this value; otherwise its value becomes a weighted average.

Fig. 1.6 shows two saturated phases $A_\alpha B$ and $A_\gamma B$ between which a compound layer $A_\beta B$ is growing ($\alpha>\beta>\gamma$). $A_\alpha B$ and $A_\gamma B$ will represent the pure phases A and B if α and γ are equal to ∞ and 0, respectively. The concentration profile of A in the absence of interfacial reaction barriers is as shown by the dashed line, with the concentrations at the

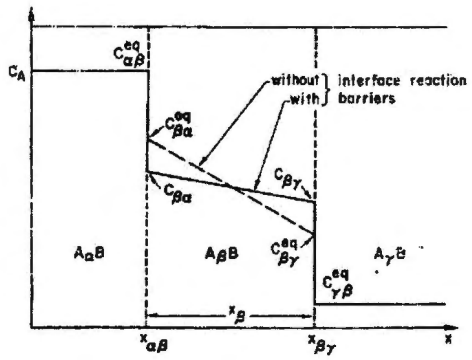

Figure 1.6: Concentration profile of A atoms across saturated phases $A_\alpha B$, $A_\beta B$ and $A_\gamma B$ of a model diffusion couple, with and without interface reaction barriers. ($\alpha > \beta > \gamma$) [24].

two interfaces equal to the equilibrium values $C^{eq}_{\beta C}$ and $C^{eq}_{\beta\gamma}$. In the presence of interfacial reaction barriers, $C_{\beta\alpha} < C^{eq}_{\beta C}$ and $C_{\beta\gamma} > C^{eq}_{\beta\gamma}$. Assuming that the $A_\alpha B$ layer may be characterized by a constant chemical interdiffusion constant $\tilde{D}_\beta$, and applying Fick's first law of diffusion it is found that the position change of the two interfaces with time is[24]

$$\left(C^{eq}_{\alpha\beta} - C_{\beta\alpha}\right)\frac{dx_{\alpha\beta}}{dt} = \tilde{D}_\beta\left(\frac{dC^A_\beta}{dx}\right)_{\beta\alpha} \tag{1.8}$$

at the $\alpha\beta$ interface and

$$\left(C_{\beta\gamma} - C^{eq}_{\gamma\beta}\right)\frac{dx_{\beta\gamma}}{dt} = -\tilde{D}_\beta\left(\frac{dC^A_\beta}{dx}\right)_{\beta\gamma} \tag{1.9}$$

at the $\beta\gamma$ interface. Here C^A_β is the concentration of A in $A_\beta B$. If steady state conditions apply for the diffusion fluxes and formation is only at the interfaces, the diffusion flux of A atoms in the $A_\beta B$ phase is

$$J^A_\beta = -\tilde{D}_\beta\left(\frac{dC^A_\beta}{dx}\right)_{\beta\alpha} = -\tilde{D}_\beta\left(\frac{dC^A_\beta}{dx}\right)_{\beta\gamma} \tag{1.10}$$

or

$$J_{\beta}^{A} = -\tilde{D}_{\beta}\left(\frac{C_{\beta\alpha} - C_{\beta\gamma}}{x_{\beta}}\right) \tag{1.11}$$

When the flux is considered from the reaction-limited viewpoint[24]

$$J_{\beta}^{A} = \kappa_{\beta\alpha}\left(C_{\beta\alpha}^{eq} - C_{\beta\alpha}\right) \tag{1.12}$$

or

$$J_{\beta}^{A} = \kappa_{\beta\gamma}\left(C_{\beta\gamma} - C_{\beta\gamma}^{eq}\right) \tag{1.13}$$

where $\kappa_{\beta\alpha}$ and $\kappa_{\beta\gamma}$ are interfacial reaction constants at the two interfaces. A time independent equilibrium value of the concentration difference $C_{\beta\alpha}$ - $C_{\beta\gamma}$ may be expressed in terms of the time independent equilibrium value:

$$\Delta C_{\beta}^{eq} = C_{\beta\alpha}^{eq} - C_{\beta\gamma}^{eq} \tag{1.14}$$

Combining equations 1.11 to 1.14 results in

$$J_{\beta}^{A} = \frac{\Delta C_{\beta}^{eq}\kappa_{\beta}^{eff}}{1 + \frac{x_{\beta}\kappa_{\beta}^{eff}}{\tilde{D}_{\beta}}} \tag{1.15}$$

where

$$\frac{1}{\kappa_{\beta}^{eff}} = \frac{1}{\kappa_{\beta\alpha}} + \frac{1}{\kappa_{\beta\gamma}} \tag{1.16}$$

The change in layer thickness $x_{\beta} = x_{\beta\gamma}$ - $x_{\alpha\beta}$ with time is given by

$$\frac{dx_{\beta}}{dt} = \left\{\frac{1}{C_{\alpha\beta}^{eq} - C_{\beta\alpha}} + \frac{1}{C_{\beta\gamma} - C_{\gamma\beta}^{eq}}\right\} J_{\beta}^{A} \tag{1.17}$$

A narrow range of homogeneity for the phase $A_{\beta}B$ is assumed for simplicity. In this case, $C_{\beta\alpha}$ and $C_{\beta\gamma}$ may be approximated by the same value

$$C_{\beta\alpha} = C_{\beta\gamma} = \frac{\beta}{[\Omega_0(1+\beta)]} \tag{1.18}$$

where β is the number of A atoms per B atoms in $A_{\beta}B$ and Ω_0 is the volume per A or B atom, assumed constant throughout the sample. Substituting equation 1.15 into 1.17 yields

$$\frac{dx_\beta}{dt} = \frac{G_\beta \Delta C_\beta^{eq} \kappa_\beta^{eff}}{1 + \frac{x_\beta \kappa^{eff}}{\tilde{D}_\beta}} \tag{1.19}$$

where

$$G_\beta = \Omega_0 (1+\beta)^2 \left(\frac{1}{\alpha - \beta} + \frac{1}{\beta - \gamma} \right) \tag{1.20}$$

while α and γ represent the number of A atoms per B atom in the $A_\alpha B$ or $A_\gamma B$ compound, respectively.

For the change from reaction controlled to diffusion controlled kinetics we can define a characteristic thickness x_β^* as

$$x_\beta^* = \frac{\tilde{D}_\beta}{\kappa_\beta^{eff}} \tag{1.21}$$

From equation 1.19, if $x_\beta << x_\beta^*$, then it is found that

$$\frac{dx_\beta}{dt} \sim G_\beta \Delta C_\beta^{eq} \kappa_\beta^{eff} \tag{1.22}$$

which when integrated gives

$$x_\beta \propto t \tag{1.23}$$

which is the result for reaction controlled kinetics.

When $x_\beta >> x_\beta^*$, equation 1.19 gives,

$$\frac{dx_\beta}{dt} \sim \frac{G_\beta \Delta C_\beta^{eq} \tilde{D}_\beta}{x_\beta} \tag{1.24}$$

which when integrated gives

$$x_\beta \propto t^{1/2} \tag{1.25}$$

This is the result for diffusion dominated kinetics.

As explained earlier, the diffusion growth constant or diffusivity is related to the film thickness and annealing time by the expression $x_\beta^2 = K_\beta t$. It was mentioned that K_β is

directly related to the interdiffusion constant $\tilde{D}_\beta$. By integrating equation (1.24) and assuming that $x_\beta = 0$ at t = 0, we get the expression

$$K_\beta = \frac{x_\beta^2}{t} = 2G_\beta \Delta C_\beta^{eq} \tilde{D}_\beta \tag{1.26}$$

which relates K_β and $\tilde{D}_\beta$ for diffusion limited growth.

(ii) Multiple phase growth

In investigating the influence of interfacial reaction barriers in a multiphase system, the Gösele and Tu model considers a system of two intermediate compound layers of composition $A_\beta B$ and $A_\gamma B$ between saturated phases $A_\alpha B$ and $A_\delta B$, where $\alpha > \beta > \gamma > \delta$. α, β, γ and δ stand for the number of atoms A per B atom in the phases α, β, γ and δ. As shown in Fig. 1.7, $A_\beta B$ and $A_\gamma B$ are assumed to be already present with thickness x_β and x_γ, respectively.

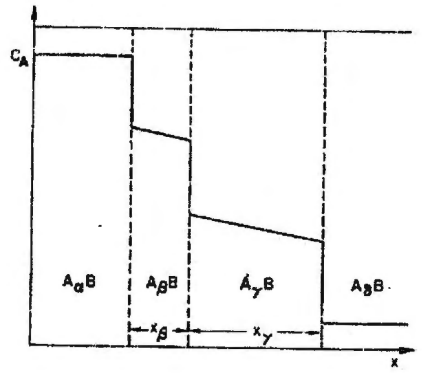

Figure 1.7: Concentration profile of A atoms across saturated phases $A_\alpha B$, $A_\beta B$, $A_\gamma B$ and $A_\delta B$ of a model diffusion couple ($\alpha > \beta > \gamma > \delta$) [24].

The layers $A_\beta B$ and $A_\gamma B$ are characterized by chemical interdiffusion coefficients $\tilde{D}_\beta$ and $\tilde{D}_\gamma$ respectively. In the simplest case, $\tilde{D}_\beta$ may be approximated in terms of component diffusion coefficients $\tilde{D}_\beta^A$ and $\tilde{D}_\beta^B$. Thus

$$\tilde{D}_\beta = \frac{D_\beta^A}{\beta + 1} + \frac{\beta D_\beta^B}{\beta + 1} \tag{1.27}$$

The time rates of change in x_β and x_γ are

$$\frac{dx_\beta}{dt} = G_\beta J_\beta^A - G_{\beta\gamma} J_\gamma^A \tag{1.28}$$

$$\frac{dx_\gamma}{dt} = G_\gamma J_\gamma^A - G_{\gamma\beta} J_\beta^A \tag{1.29}$$

The diffusion fluxes of A atoms in $A_\beta B$ and $A_\gamma B$ are

$$J_\beta^A = \frac{\Delta C_\beta^{eq} \kappa_\beta^{eff}}{1 + \frac{x_\beta \kappa_\beta^{eff}}{\tilde{D}_\beta}} \tag{1.30}$$

$$J_\gamma^A = \frac{\Delta C_\gamma^{eq} \kappa_\gamma^{eff}}{1 + \frac{x_\gamma \kappa_\gamma^{eff}}{\tilde{D}_\gamma}} \tag{1.31}$$

The quantities G_β, $G_{\beta\gamma}$, G_γ and $G_{\gamma\beta}$ are given by[24]

$$G_\beta = \Omega_0 (1+\beta)^2 \left(\frac{1}{\alpha - \beta} + \frac{1}{\beta - \gamma} \right) \tag{1.32}$$

$$G_\gamma = \Omega_0 (1+\gamma)^2 \left(\frac{1}{\beta - \gamma} + \frac{1}{\gamma - \delta} \right) \tag{1.33}$$

$$G_{\gamma\beta} = G_{\gamma\beta} = \Omega_0 (1+\beta) \frac{(1+\gamma)}{(\beta - \gamma)} \tag{1.34}$$

The volume Ω_0 per atom is assumed constant in all phases. For a fast reaction at the interface, κ_β^{eff} and $\kappa_\gamma^{eff} \rightarrow \infty$, in which case equations 1.28 to 1.31 simplify to describe purely diffusion limited growth.

(iii) Criteria for phase growth or shrinkage

For the phase $A_\beta B$ to grow, $\frac{dx_\beta}{dt} > 0$. From equation 1.28, the flux ratio then satisfies the relationship

$$r = \frac{J_\beta^A}{J_\gamma^A} > \frac{G_{\beta\gamma}}{G_\beta} = r_1 \tag{1.35}$$

Similarly the phase $A_\gamma B$ will grow if $\frac{dx_\gamma}{dt} > 0$, which, from equation 1.29 gives

$$r = \frac{J_\beta^A}{J_\gamma^A} < \frac{G_\gamma}{G_{\gamma\beta}} = r_2 \tag{1.36}$$

From equations 1.32 to 1.34 we get

$$r_1 = (1+\gamma)(\alpha-\beta)/(1+\beta)(\alpha-\gamma) \tag{1.37}$$

and

$$r_2 = (1+\gamma)(\beta-\delta)/(1+\beta)(\gamma-\delta) \tag{1.38}$$

which implies that

$$r_2 > r_1 \tag{1.39}$$

since $(\alpha\text{-}\beta)<(\alpha\text{-}\gamma)$ and $(\beta\text{-}\delta)>(\gamma\text{-}\delta)$.

From the equations above, it can be seen that r_1 and r_2 depend only on the composition of the compounds. From equations 1.15 and 1.16, the flux ratio r depends on x_β, x_γ, $\tilde{D}_\beta$, $\tilde{D}_\gamma$, κ_β^{eff} and κ_γ^{eff}. From the above equations, when $r > r_2$, the phase $A_\beta B$ grows while $A_\gamma B$ will not grow and hence shrinks. If $r_1 < r < r_2$, both $A_\beta B$ and $A_\gamma B$ grow simultaneously. When $r < r_1$, $A_\beta B$ shrinks while $A_\gamma B$ grows. The above explanation is shown diagrammatically in Fig. 1.8.

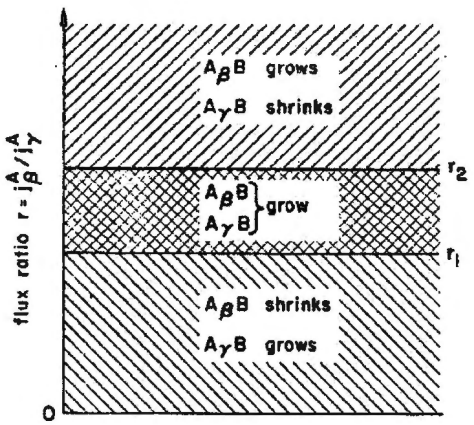

Figure 1.8: Illustration of various growth and shrinkage regimes for the model diffusion couple depicted in Fig. 1.7 in relation to the ratio r of the diffusion fluxes of A atoms across phases $A_\beta B$ and $A_\gamma B$ [24].

As mentioned earlier, r depends on x_β, x_γ, $\tilde{D}_\beta$, $\tilde{D}_\gamma$, κ_β^{eff} and κ_γ^{eff}. Its actual form depends on the transport-control mechanisms across the two layers. We get three cases:

(a) Diffusion-controlled across both layers

In this case the flux ratio r simplifies to (from equation 1.15)

$$r = \frac{(\Delta C_\beta^{eq} \tilde{D}_\beta)}{(\Delta C_\gamma^{eq} \tilde{D}_\gamma)} \frac{x_\gamma}{x_\beta} \tag{1.40}$$

Since $r \propto x_\gamma / x_\beta$, if an interdiffusion experiment starts with a thickness ratio such that $r > r_2$ (case a), the phase $A_\beta B$ grows while $A_\gamma B$ shrinks, hence reducing the value of r until $r_1 < r < r_2$, at which point the two phases start to grow simultaneously. The starting point of the ratio r could also be in the region $r_1 < r < r_2$ (case b) or the region $r < r_1$ (case c). For all three cases, the final state is one where both layers grow proportionally to $t^{1/2}$ (diffusion controlled). This means that in the ratio x_γ / x_β, the time dependence will cancel out, resulting in a time-independent value for r. The paths followed by these three cases are shown in Fig. 1.9. As can be seen in the figure, for all three cases, the diffusion system is self-regulating, always leading to the same ratio r^{eq}. This behavior reflects the predictions of all theories based on diffusion-controlled transport across multilayers.

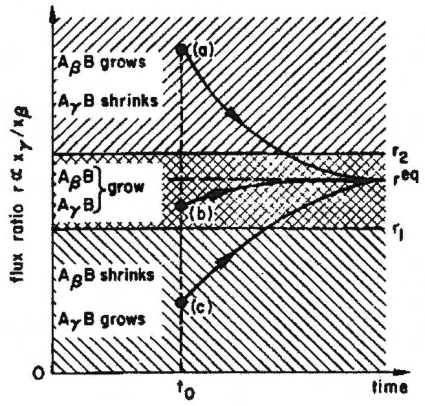

Figure 1.9: Growth/shrinkage behavior assuming transport across both layers $A_\beta B$ and $A_\gamma B$ is diffusion controlled [24].

(b) Interfacial reaction-controlled across both layers

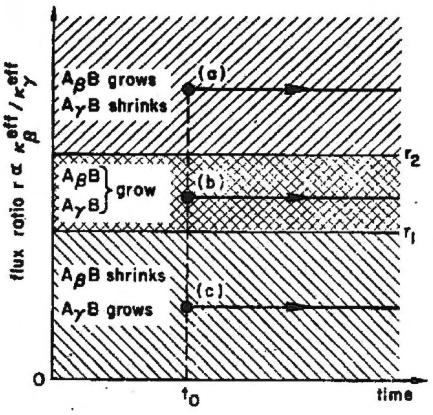

Figure 1.10: Growth/shrinkage behavior assuming transport across both layers $A_\beta B$ and $A_\gamma B$ is interface (reaction) controlled [24].

Assuming that the transport across each layer is controlled by interface reaction barriers, the flux ratio would be given by (from equation 1.15)

$$r = \frac{\Delta C_\beta^{eq} \kappa_\beta^{eff}}{\Delta C_\gamma^{eq} \kappa_\gamma^{eff}} \tag{1.41}$$

Here r is independent of x_β and x_γ and therefore remains constant with growth for all three possible starting points as shown in Fig. 1.10. Eventually however, one or both of the phase layers will exceed the change-over thickness at which diffusion-controlled growth sets in. At this point, r will depend on the thickness, as seen in the previous section.

(c) Different transport-control mechanisms across the two layers

Suppose the transport in $A_\gamma B$ is diffusion controlled while that in $A_\beta B$ is reaction controlled. Here $x_\gamma >> x_\gamma^*$ and $x_\beta << x_\beta^*$, where x_γ^* and x_β^* are the respective changeover thicknesses, as described earlier. From equation 1.15, the flux ratio r is then given by

$$r = \frac{(\Delta C_\beta^{eq} \kappa_\beta^{eff})}{(\Delta C_\gamma^{eq} \tilde{D}_\gamma)} x_\gamma \tag{1.42}$$

As shown in Fig. 1.11, in the case (a) where $r > r_2$, the phase $A_\beta B$ grows all the time

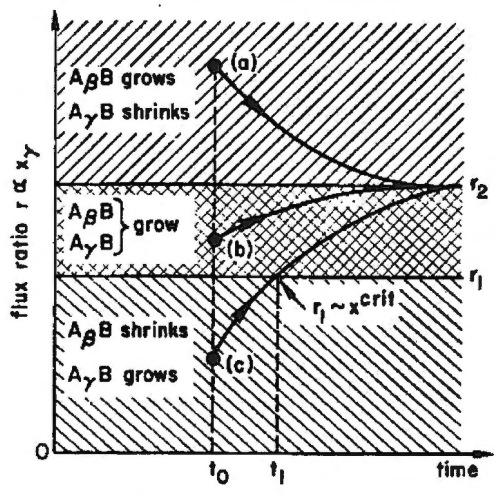

Figure 1.11: Growth/shrinkage behavior assuming transport across layers $A_\beta B$ reaction controlled while that across $A_\gamma B$ is diffusion controlled [24].

while the phase $A_\gamma B$ shrinks, thereby reducing the value of r. Once r goes below the value of r_2, $A_\gamma B$ will grow, thereby increasing r and pushing its value above r_2 where the phase will shrink again. The net result is that $A_\gamma B$ will keep a constant thickness at $r = r_2$. Although $A_\beta B$ keeps growing, r will remain constant as it only depends on the thickness of $A_\gamma B$ (x_γ). For the case (b) where $r_1 < r < r_2$, both phases will grow simultaneously. The growth of $A_\gamma B$ will increase the value of r until it becomes equal to r_2, a point above which this phase would start to shrink so that its thickness remains constant and the situation then proceeds much as in case (a). In case (c) the starting value of r is less than r_1. The layer $A_\gamma B$ grows, thereby increasing the value of r while $A_\beta B$ shrinks. In the usual interdiffusion experiment, where both phases are not initially present, the phase $A_\beta B$ cannot coexist with the phase $A_\gamma B$ in this region. $A_\gamma B$ will grow until it reaches a critical thickness x_γ^{crit}, where $r = r_1$; at this point $A_\beta B$ will start to grow simultaneously with $A_\gamma B$. The process then proceeds as described for case (b). The critical thickness x_γ^{crit} is given by

$$x_\gamma^{crit} = \frac{r_1 \Delta C_\gamma^{eq} \tilde{D}_\gamma}{\Delta C_\beta^{eq} \kappa_\beta^{eff}} \tag{1.43}$$

(iv) General behavior of thin-film diffusion couples

Considering an example related to this work, assume that A stands for germanium and B for a metal in a germanium-metal diffusion couple. Upon annealing, the germanide with the lowest effective interface reaction barrier, say $A_\gamma B$, will form first and initially grow linearly with time (reaction controlled) and then with a parabolic growth law (diffusion controlled). When the thickness x_γ of the phase $A_\gamma B$ exceeds the critical thickness x_γ^{crit} (as described in the last section), the second phase, say $A_\beta B$, will start to form and grow, first linearly (reaction controlled) and then proportionally to $t^{1/2}$ (diffusion controlled), this reduces the growth rate of $A_\gamma B$. At this point x_γ / x_β will be such that the flux ratio r reaches the time independent value r^{eq} described earlier. The process described above is shown in Fig. 1.12.

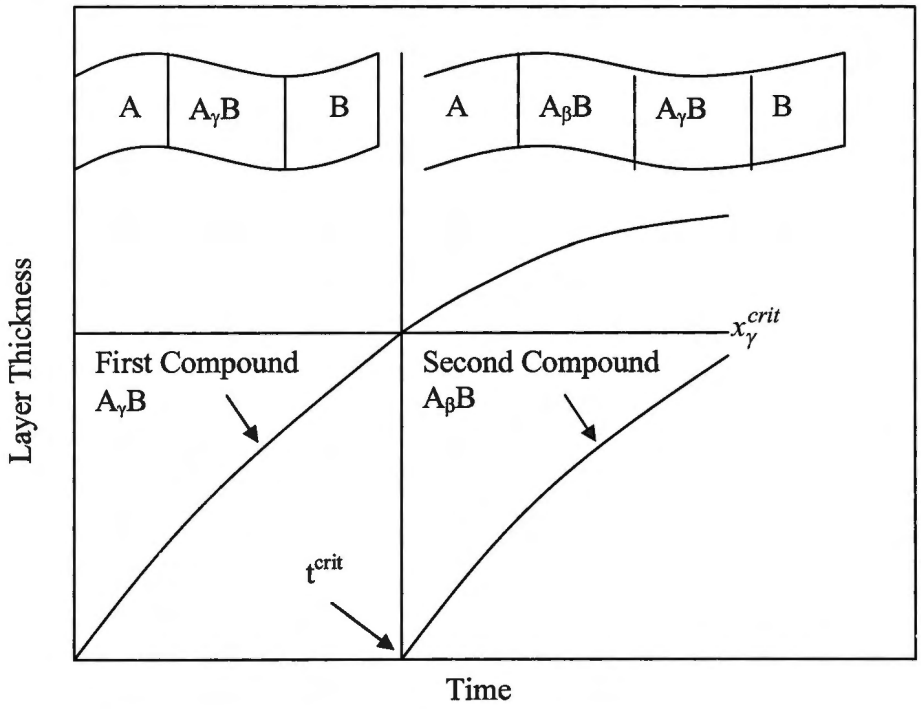

Figure 1.12: The first forming layer $A_\gamma B$, in an A-B diffusion couple, reaches its critical thickness x_γ^{crit} at time t^{crit} after which the second phase $A_\beta B$ starts to form [24].

1.5 Lateral diffusion reactions

The samples used for studying lateral diffusion reactions are composed of a thick island of one material on top of a much thinner film of another material. The island material is deposited through a mask (as explained in more detail in Chapter 2) and its thickness is chosen such that the atomic ratio of island material to thin film material is greater than that of the most island material rich phase on the equilibrium phase diagram, leaving excess island material to diffuse laterally outwards. It is possible to measure the extent, composition and structure of the compounds formed during lateral interaction using various experimental techniques.

Lateral diffusion couples have been used to study interaction between a metal and a semiconductor[25-31] or between two metals.[31-37] With respect to the former, the bulk of the work was done with silicon as will be seen later in Table 1.3. Both configurations of a silicon island on a thin metal film and a metal island on a thin silicon film were used as will also be seen in that table. Consider a silicon island on a metal M film as shown schematically in Fig. 1.13. Upon annealing the silicon would react with the underlying film, going through a sequence of phases until the most silicon rich phase is formed. Since no further reaction with the underlying film is possible, excess silicon diffuses laterally. The most silicon rich phase may then grow laterally until it attains a critical width after which other phases appear and grow as shown in Fig. 1.13. Conventional reasoning would lead us to expect that the phases formed would be less silicon rich as the reaction proceeds further away from the original island i.e. $w < x < y$ etc. This is a case of multiple phase formation as would be found in bulk diffusion couples. Lateral diffusion couples thus provide the transition between thin film and bulk behavior.

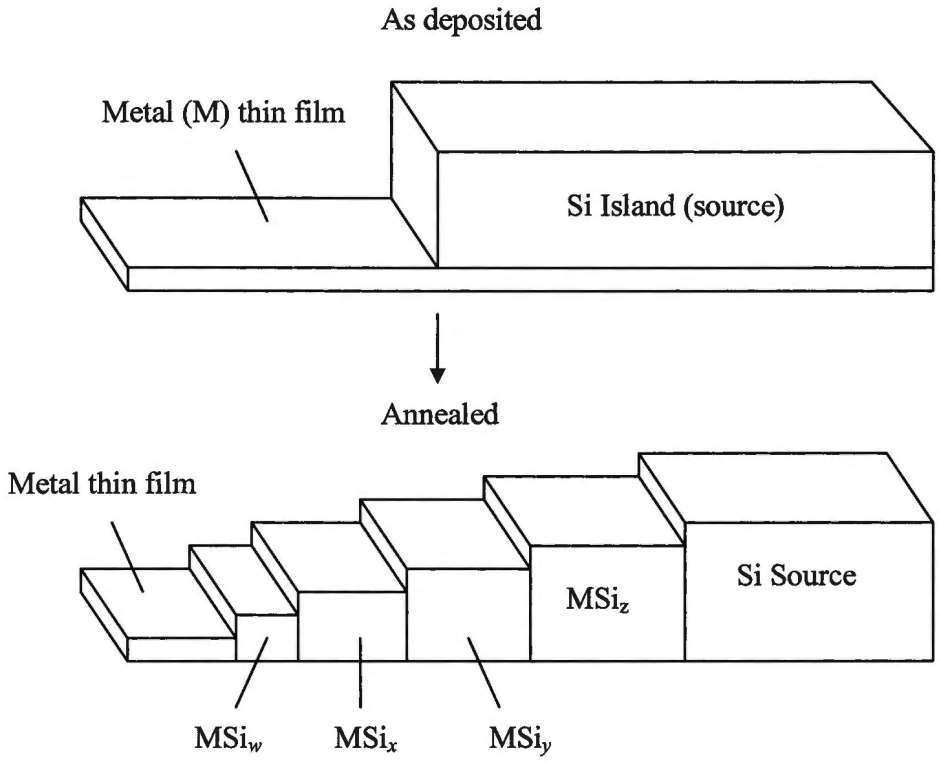

Figure 1.13: Representation of a lateral diffusion couple before and after annealing. The system is of a metal M and silicon. The numerical value of the subscripts will ascend in alphabetical order.

Various procedures have been developed to study lateral diffusion couples. Initially, sample structures were grown on Al_2O_3 substrates or oxide coated silicon wafers; the oxide (SiO_2) provided an insulating buffer layer to prevent reaction with the underlying silicon. For quantitative analysis, the diffusion length was measured with scanning electron microscopy (SEM)[25-27] and the composition by energy dispersive spectroscopy (EDS).[25-27]

To improve lateral resolution a procedure developed by Chen et al,[28] has been used by a number of workers.[28,32-37] This procedure involves the deposition of lateral diffusion sample structures on a single crystal sodium chloride substrate. The diffusion couples are then floated off on de-ionized water which dissolves the sodium chloride there-by leaving self-supporting sample structures which are then annealed. The reaction kinetics are analyzed using transmission electron microscopy (TEM), the reacted phases having been identified from their crystallographic structure by selected area diffraction (SAD).[28,32-37] Here too the chemical composition is determined by energy dispersive spectroscopy (EDS). More recently, Microbeam Rutherford Backscattering Spectroscopy (μRBS) has been used to

study lateral diffusion couples.[29-31] Table 1.3 gives a summary of previous lateral diffusion studies.

System	Island material	Diffusing species	Lateral phases formed	Techniques used and references
Pt-Ge	Pt Ge	No reaction Ge	- $PtGe_2$, Pt_2Ge_3 and $PtGe_2$	μRBS[30] and SEM[30]
Pt-Si	Pt Si	Pt Not reported	Pt_2Si -	SEM[27] and EDS[27]
Pt-Al	Pt Al	Islands peeled off Al	- $PtAl_2$, Pt_8Al_{21} and Pt_5Al_{21}	μRBS[31] and SEM[31]
Pd-Si	Pd Si	Pd Not reported	Pd_2Si	TEM[28] SAD[28] and EDS[28]
Pd-Al	Pd Al	Islands peeled off Al	- Pd_2Al_3 and $PdAl_3$	TEM,[32-34] SAD[32-34] and EDS[32-34]
Ni-Si	Ni Si	Ni Ni	NiSi, Ni_3Si_2 and Ni_2Si Ni_5Si_2, Ni_3Si and Ni_2Si	SEM,[25,26,29] EDS[25,26] and μRBS[29]
Ni-Al	Ni Al	Not reported Al below 500°C Ni above 500°C	- $NiAl_3$ and Ni_2Al_3	TEM[35-37] SAD[35-37] and EDS[35-37]
Cr-Si	Cr Si	Si Si	Voids formed around the island region $CrSi_2$	μRBS[31] and SEM[31]
Ru-Al	Ru Al	Al Al	Voids formed around the island region $RuAl_6$ and Ru_4Al_{13}	μRBS[31] and SEM[31]

Table 1.3: Summary of previous lateral diffusion studies.

1.5.1 Critical length phenomenon

The equations referred to below where derived in section 1.4.1 in relation to thin film couples but the concepts expressed are applicable to lateral diffusion couples.

Consider the competing growth of two phases $A_\beta B$ and $A_\gamma B$. According to the kinetic barrier model for phase growth, the rates of growth of the two phases are given by equations 1.28 and 1.29 respectively. The values of the effective interface barrier constants κ_β^{eff} and κ_β^{eff}, which appear in the expressions for the atomic flux of element A (expressions 1.30 and 1.31), could be such that they give a negative growth rate for the phase $A_\beta B$ in equation 1.28 and a positive growth rate for $A_\gamma B$ in equation 1.29. This implies that only the phase $A_\gamma B$ will grow. Looking at expression 1.31, as $A_\gamma B$ increases its growth length x_γ the atomic flux j_γ^A reduces. The second term in equation 1.28 will therefore become smaller as the phase $A_\gamma B$ grows. The moment the second term in equation 1.28 becomes smaller than the first term, the growth rate of the phase $A_\beta B$ becomes positive and this phase too will start to grow. The growth length of the first phase at which the second phase appears is referred to as the critical length x^{crt}.

The concept of a critical thickness can also be viewed in the light of the EHF model. During the growth of a phase, the effective concentration at the reaction interface falls as a result of the long diffusion path that the diffusing material has to cover. The effective concentration is then moved to a region in the EHF diagram where another phase becomes thermodynamically favored. The first phase does however continue to grow and hence we get simultaneous growth of the two phases. The critical length x_β^{crit} depends on the microstructure of the compound layer and also on temperature. This critical length phenomenon has been observed in several lateral diffusion couple studies; examples are given below.

In a lateral diffusion investigation by Zheng et al.[26] where Ni islands were deposited on Si films, Ni reacted with Si to form Ni_3Si in the Ni-rich island region. Subsequent annealing resulted in Ni diffusing laterally forming Ni_2Si as the first phase outside the island region. This phase grew until its length exceeded a critical length of about 25 μm (at 600°C), then the three other phases that where observed in bulk diffusion couple

studies of this system appeared and grew together with a shrinkage of the first phase Ni_2Si. Of these other phases Ni_5Si_2 appeared between Ni_2Si and the island region. Ni_3Si_2 and NiSi appeared between Ni_2Si and the unreacted Si film.

Liu and Mayer[37] formed diffusion couples of Al islands on films of Ni_2Si. This was achieved by depositing multiple layers of Ni and Si such that the Ni to Si atomic ratio was 2 to 1. Thick Al islands were deposited onto the Ni-Si multiple layers. A pre-anneal at about 300°C for 5 minutes resulted in the formation of Ni_2Si in the Ni-Si multiple layer area with limited lateral diffusion of Al atoms from the island. Upon annealing at higher temperatures the Al diffused laterally forming Al_3Ni as the first phase outside the island region. After the width of Al_3Ni exceeded a critical value (which was 0.8μm at 525°C), Al_3Ni_2 started to form at the Al_3Ni/Ni_2Si interface and grew simultaneously with Al_3Ni_2. When the width of the Al_3Ni and Al_3Ni_2 phases extended to 0.9 and 0.2μm (at 525°C) respectively, the phase Ni_3Si_2 began to nucleate at the Al_3Ni_2/Ni_2Si interface. The three phases then grew together.

Al islands were deposited on Pd films in an investigation by Blanpain et al.[32,33] Al_3Pd_2 was the first lateral phase to form upon annealing. Once this phase reached a critical length (which varied from 6.5 to 3.9 μm between 343 and 431°C) the phase Al_3Pd appeared between Al_3Pd_2 and the island region. The two phases grew simultaneously but the growth rate of the Al_3Pd_2 slowed down after the appearance of Al_3Pd. The growth rate of Al_3Pd was much lower than that of Al_3Pd_2.

The diagram presented earlier (Fig. 1.12) is that used by Gösele and Tu to discuss the work presented above.

1.5.2 Geometrical modification of the growth equations for lateral diffusion couples

In bulk and thin film diffusion couples uninhibited expansion is only one-dimensional and in the direction of phase growth. In lateral diffusion couples, the geometry only inhibits expansion in the plane of the film, parallel to the phase interface. Apart from elongation in the growth direction (perpendicular to the phase interface and in the plane of the film) we get thickening perpendicular to the plane of the film. The resulting difference in thickness

between various phase regions requires that some modifications should be included in equations of the kinetic model of Gösele and Tu. These modifications were presented by Blanpain.[32-34]

Considering the single phase growth regime shown in Fig. 1.14 (a), the growth rate of the phase $A_\gamma B$ is given by[32,33]

$$\frac{dx_\gamma}{dt} = \frac{d(x_{\gamma\beta} - x_{A\gamma})}{dt} \tag{1.44}$$

where $x_{A\gamma}$ is the interface between A and $A_\gamma B$ while $x_{\gamma B}$ is that between $A_\gamma B$ and B. In this description of the $x_{A\gamma}$ interface, it must be remembered that the pure element A overlays the phase $A_\gamma B$ in the source region. Therefore, from equation 1.19, we obtain

$$\frac{dx_\gamma}{dt} = G_\gamma j_\gamma^A \tag{1.45}$$

where

$$G_\gamma = \Omega_0 \frac{(1+\gamma)(1+B)}{\gamma - B} \tag{1.46}$$

The variation in thickness between different regions has no influence in this case.

Consider the two phase regime shown in Fig. 1.14 (b). In this case we have to include the thickness ratio z_γ / z_β of the phases $A_\gamma B$ and $A_\beta B$ in the kinetic equations and they now become

$$\frac{dx_\beta}{dt} = \frac{d(x_{\beta\gamma} - x_{A\beta})}{dt} = G_\beta j_\beta^A - \frac{z_\gamma}{z_\beta} G_\beta j_\gamma^A \tag{1.47}$$

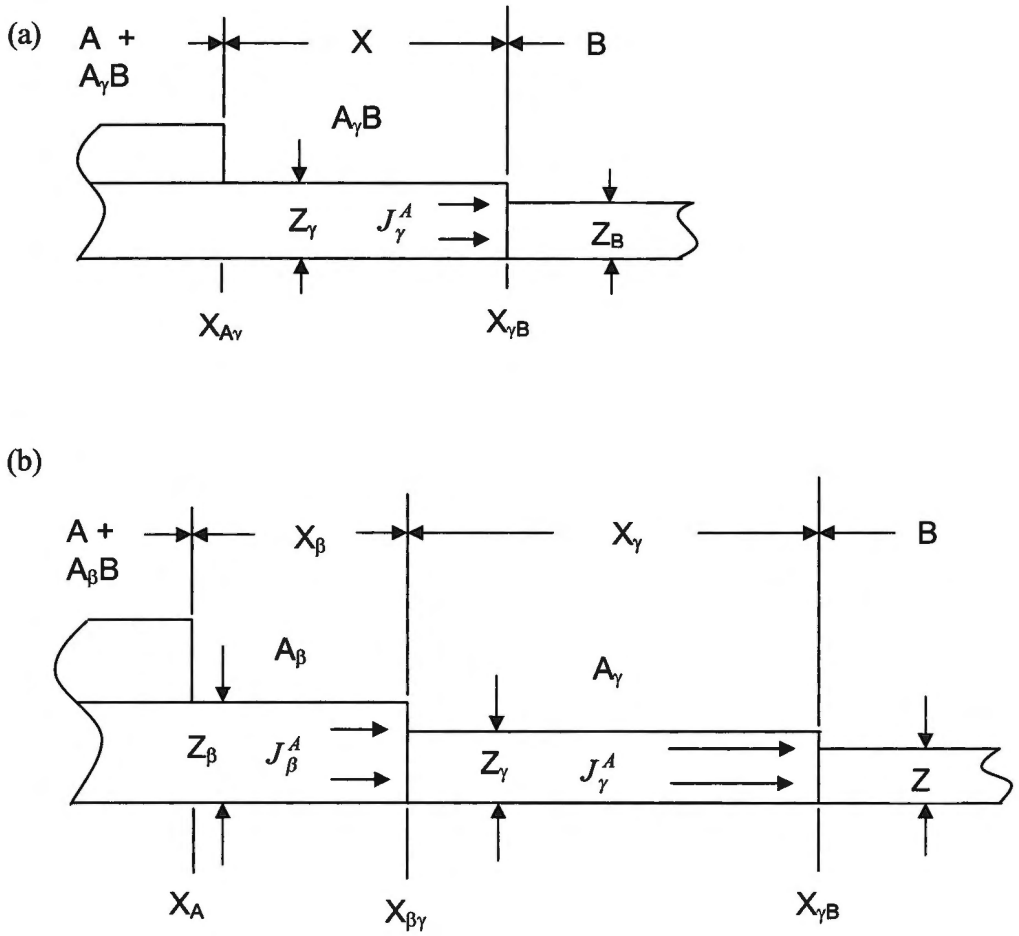

Figure 1.14: Schematic illustration of geometries, showing different phase regions and the various parameters used to characterize growth kinetics for lateral diffusion couples in the (a) single phase growth regime and (b) the two phase growth regime [32,33].

and

$$\frac{dx_\gamma}{dt} = \frac{d(x_{\gamma B} - x_{\beta\gamma})}{dt} = G_\gamma j_\gamma^A - G_\beta j_\beta^A \tag{1.48}$$

where

$$G_\beta = \Omega_0 \frac{(1+\beta)(1+\gamma)}{\beta - \gamma} \tag{1.49}$$

and

$$G_\gamma = \Omega_0 (1+\gamma)\left[\frac{1+B}{\gamma - B} + \frac{z_\gamma (1+\beta)}{z_\beta (\beta - B)}\right]. \tag{1.50}$$

1.6 Scope of the thesis research

The primary objective of this investigation was to develop an understanding of the interactions between germanium and Platinum Group Metals in lateral diffusion couples. In Chapter 2, we describe the sample preparation and characterization techniques. The film depositions were done using electron beam deposition and reaction in the samples was induced by annealing in a vacuum furnace. Rutherford Backscattering Spectrometry (RBS) was used to study the composition and depth profiles of the samples. The Nuclear Microprobe (NMP) was used in its μRBS scanning mode to obtain compositional and depth information as a function of lateral position. Particle Induced X-ray Emission (PIXE) was also used on the Nuclear Microprobe in the μPIXE scanning mode. The results were novel because there is no work reported in the literature on the use of PIXE in the study of lateral diffusion couples. It was hoped that PIXE would complement RBS in two ways:
(i) in studying systems where RBS peaks overlap making it difficult to resolve them, and
(ii) as a direct way of obtaining percentage concentration of the diffusing species as a function of lateral position, which can then be used to estimate the concentration drop across a phase region $\Delta C_{\beta}^{eq} = C_{\beta\alpha}^{eq} - C_{\beta\gamma}^{eq}$, described earlier in the framework of the kinetic model of Gösele and Tu. It is non-trivial to achieve this from raw RBS data.

Phases were identified crystallographically using X-ray Diffraction (XRD), while imaging of samples was done using Optical and Scanning Electron Microscopy (SEM). Atomic Force Microscopy (AFM) was used (in the Ir-Ge and Pd-Ge systems) to further study the surface morphology and complement RBS in thickness determination.

Using the above techniques, this study attempts to determine all basic parameters required in understanding the phase composition and formation temperature range, the sequence of phase formation, the dominant diffusing species, phase growth kinetics and activation energies of growing phases. This was carried out for the family M_xGe_y using the platinum group metals Ir, Pt, Pd and Rh. Both conventional thin film and lateral diffusion couples were studied for each system. For the Ir-Ge and Pt-Ge systems, the so called marker technique was employed in the investigation of the dominant diffusing species.

The results are detailed, discussed and elaborated upon in Chapters 3 to 6. The discussions are largely in terms of the effective heat of formation model and the modified kinetic model of Gösele and Tu.

To demonstrate how μPIXE can be used to study lateral diffusion systems that can not be studied using μRBS due to excessive peak overlap, lateral diffusion couples of the systems Co-Ge and Ni-Ge were also studied. Some representative results from this study are included in Chapter 6.

The summary of important results obtained is given in Chapter 7. Various conclusions and comparisons between the systems are made. A few aspects regarding possible future work on this project are also discussed in that chapter.

CHAPTER 2

EXPERIMENTAL METHODS

2.1 Sample Preparation and Processing

During the sample preparation, thermally oxidized single crystal silicon wafers were used as substrates. The relatively low molecular mass of silicon made it easy to resolve the deposited elements, which were generally much heavier, during Rutherford Backscattering Analysis. The amorphous SiO_2 on the surface rendered the wafers chemically inert to most metals within the temperature ranges of interest. They were cleaved to processable sizes, depending on the type of experiment and cleaned by ultrasonic washing in trichloroethylene, acetone and ethanol. They were then blown dry with nitrogen gas and loaded onto a rotating sample holder in the vacuum evaporation chamber. The deposition technique depended on the sample structures required.

2.1.1 Conventional thin film structures

Thin films were deposited sequentially by electron beam vacuum deposition. To achieve the high vacuum required, the double-chamber evaporation system was fitted with a rotary roughing pump and a turbo molecular pump that could pump down the upper chamber pressure to below 10^{-5} torr. A partitioning baffle valve was then opened, allowing a set of six titanium ionization pumps in the lower chamber to reduce the pressure to below 10^{-6} torr. The lower chamber was constantly maintained at high vacuum. In the ionization pumps, titanium atoms were used to getter the oxygen and nitrogen part of the gas. A liquid nitrogen filled cryopanel condenses out gases like water vapour and carbon dioxide, which are condensable under the conditions, while other gases could be trapped within the condensate.

During evaporation, a titanium sublimation pump was enabled and controlled manually to keep the vacuum in the low 10^{-7} torr range.

The samples of material to be evaporated were placed in a three-crucible copper hearth, which was water-cooled. Electron-beam heating was used to accomplish the evaporation. The deposition rate was kept typically around 0.3 nms^{-1} by controlling the current through the electron gun. A vibrating quartz crystal monitored the thickness.

2.1.2 Markers

The marker technique is used to determine the moving species during solid state reactions. During germanide formation the moving species could be germanium atoms, metal atoms or both. The term marker refers to a material deposited in the sample as a reference plane in monitoring the direction of flow of atoms. A schematic representation of the marker movement upon annealing is shown in Fig. 2.1.

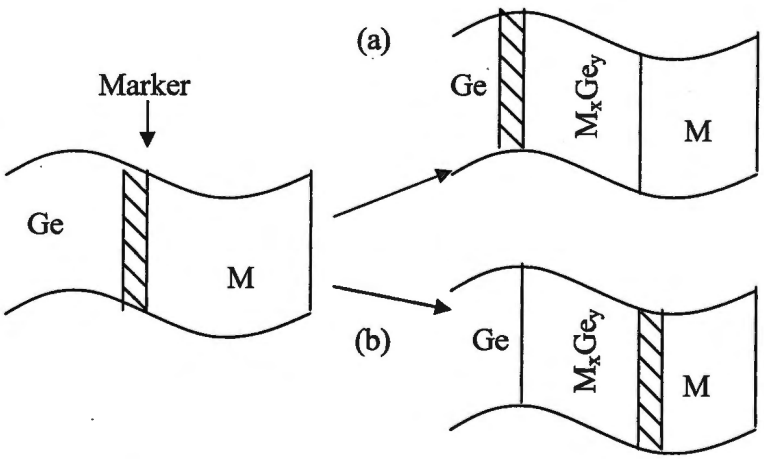

Figure 2.1: The relative shift in position of a marker schematically represented for; (a) germanium as the diffusing species, and (b) metal dominated interdiffsion.

If Ge is the moving species it can be shown[38] that during interdiffusion, the marker moves with a velocity

$$v = (D_{Ge} - D_M)\frac{\partial N_{Ge}}{\partial x} \qquad (2.1)$$

in a direction opposite to that of the flow of Ge atoms. D_{Ge} and D_M are the diffusion coefficients of pure Ge and metal M respectively while N_{Ge} is the mole fraction of Ge

atoms. This picture is reversed when M is the moving species. The technique of RBS is used to determine the relative shift in position of the marker. To get valid results, the marker must be:

(i) inert at the annealing temperature, which means that it should not take part in the diffusion,

(ii) thin enough not to act as a diffusion barrier for any component and must not introduce lattice or stress defects, and

(iii) should be of such material as to be readily identifiable both before and after annealing.

It is difficult to meet all these criteria but an attempt is made to meet them as far as possible. Marker samples of the conventional thin film structure were prepared as described in section 2.1.1. Titanium was used as an inert marker in this study.

2.1.3 Lateral diffusion couples

Lateral diffusion couples were prepared in much the same way as the conventional thin films. In this cases however, a silicon mask with an array of 390×780 μm^2 openings, made by photolithographic techniques and selective etching on a (110) wafer, was brought into good contact with the substrate. This was done after an underlying film had been deposited without breaking vacuum. Another material was then deposited through the mask forming structures consisting of islands of one material on a thin film of another. Two adjacent samples were made in each case with the silicon mask only having covered one of them, leaving the other with a conventional thin film geometry that could easily be analyzed for layer thickness by RBS. The sample holder was such that three sets of these sample pairs were prepared at the same time. Each of the samples with islands were then diced into nine or twelve identical samples, each with two or three islands, which were then annealed and analyzed in the same experiment.

Furnace annealing was used to activate solid state interaction for both the thin films described in the previous section and lateral diffusion couples. The samples were placed in eight quartz boats which were slid into the furnace individually from a rotating wheel. A pressure of 10^{-7} torr was maintained during annealing. The furnace was fitted with a feed back system comprising an external microprocessor unit controlling a power supply

to heating elements, in the middle of which was placed a thermocouple. A preset temperature could be maintained with good stability. Our range of interest was from 100°C to 800°C.

2.2 Sample characterization

The techniques used in this study were primarily employed to characterize the couples with respect to:

1. elemental redistribution;
2. phase formation and transformation;
3. layer thickness;
4. layer morphology;
5. and surface morphology.

Well established techniques that are extensively documented in the literature were used. These techniques are authoritatively dealt with in standard texts.[39-57] This section summarizes their main analytical features.

2.2.1 Essentials of Rutherford Backscattering Spectrometry (RBS)

RBS[39,40] is an excellent tool for the analysis of the first three primary quantities listed in the above section. The identity of elemental constituents, their concentrations and subsurface distribution can be determined. Elemental depth profiles are essential for a comprehensive study of lateral diffusion couples. RBS is also used to determine layer thickness; it is non-destructive and its spectral output can be interpreted with relative ease.

2 MeV alpha particles were used in this study, this is well below the energy required for any nuclear activation and only collisions that could be modeled as elastic occur. A solid state detector is used to record backscattered particles for eventual characterization. The energies and numbers of these particles are proportional to the atomic mass and the square of the atomic number of the atoms from which they are scattered. Depth information is derived from the energy loss of the particles resulting from attenuation by

the potential field in the solid. The analytical capabilities described above are related to three basic RBS concepts:

1. the kinematic factor K (mass analysis);
2. the differential scattering cross section $d\sigma/d\Omega$ (quantitative analysis); and
3. the energy loss ΔE (depth analysis).

Consider an elastic collision between two particles of masses m and M respectively (Fig. 2.2).

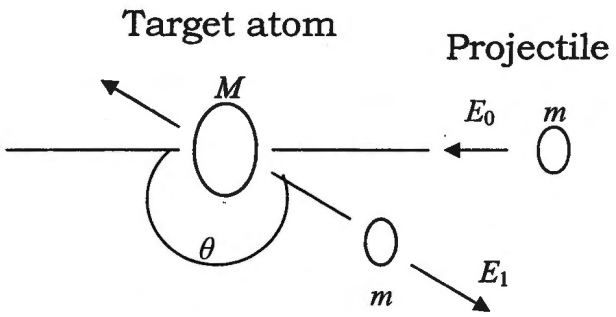

Figure 2.2: Illustration of elastic backscattering between a light projectile of mass m and heavier target atom of mass *M*, initially at rest.

The kinematic factor K is the ratio of the backscattered energy E_1 to the incident energy E_0. The mechanics of the system are solved by considering the conservation of energy and momentum. In the laboratory system[39]

$$K = \frac{E_1}{E_0} = \left[\frac{m\cos\theta + \left(M^2 - m^2 \sin\theta\right)^{\frac{1}{2}}}{M+m} \right]^2 \qquad (2.2)$$

The only unknown quantity in a standard RBS experiment is *M*, which can therefore be determined.

The likelihood of a scattering event taking place is given by the scattering cross-section σ. The probability that a scattered particle will be recorded by a detector subtending a solid angle $d\Omega$ at an angle θ with respect to the incident beam direction is determined using the differential scattering cross-section $d\sigma/d\Omega$. For elastic coulomb scattering in laboratory co-ordinates[39]

$$\frac{d\sigma}{d\Omega}=\left[\frac{zZe^2}{2E\sin^2\theta}\right]^2\frac{\left\{\cos\theta+\left[1-\left(\frac{m}{M}\sin\theta\right)^2\right]^{\frac{1}{2}}\right\}^2}{\left[1-\left(\frac{m}{M}\sin\theta\right)^2\right]^{\frac{1}{2}}} \qquad (2.3)$$

where z and Z are the atomic numbers of the projectile atom of mass m and the target of mass M respectively. Backscattering yields give quantitative analysis because the differential scattering cross-section, which scales the yield, is directly related to the scattering probability. RBS is more sensitive to the detection of heavy elements than light ones because of the Z^2 dependence in equation 2.3. It can also be seen that sensitivity is greatest at small scattering angles and is inversely proportional to the square of the energy.

As a particle penetrates a material, it loses kinetic energy to the electrons of the target via excitation and ionization. Assuming a scattering event occurs at a depth x, the scattered particle exits the target with an energy further reduced during its outward path. By measuring the total energy loss, the depth to which the particle had penetrated can be determined. The amount of energy lost per unit thickness dE/dx is referred to as the stopping power. For a target containing N atoms per unit volume, the stopping cross-section is defined as $\varepsilon = dE/Ndx$. For a compound target consisting of molecules A_mB_n or a mixture with an equivalent composition, the stopping cross-section of a molecule is given by the Bragg rule, $\varepsilon^{A_mB_n} = m\varepsilon^A + n\varepsilon^B$. The stopping cross section is a slowly varying function of the particle energy and for a thin target, the energy lost by a particle scattered at depth t is[39]

$$\Delta E = [S]t = \left(\frac{K}{\cos\theta_1}\left.\frac{dE}{dx}\right|_{\bar{E}_{in}} + \frac{1}{\cos\theta_2}\left.\frac{dE}{dx}\right|_{\bar{E}_{out}}\right)t \qquad (2.4)$$

where dE/dx is evaluated at the surface. θ_1 and θ_2 are the angles between the surface normal and the incident and scattered particle directions respectively, as shown in Fig. 2.3. S is called the backscattering energy loss factor.

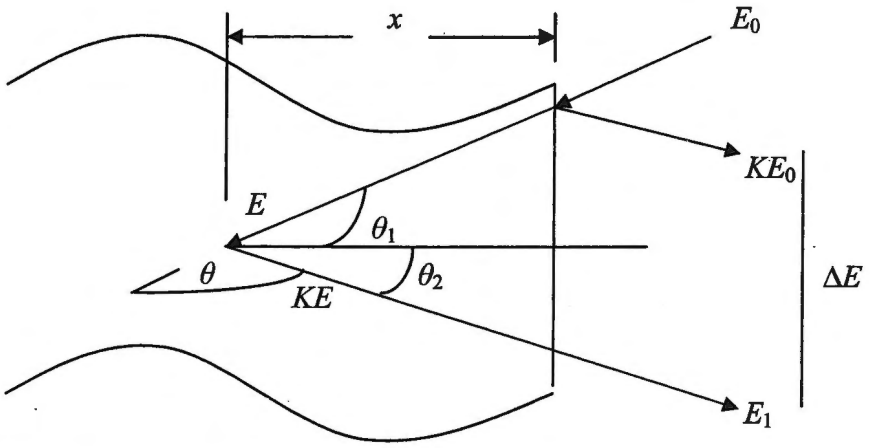

Figure 2.3: Depth illustration of a particle beam scattered through thickness x of a target sample.

The energy lost by a particle scattered from an element A at a depth t in a compound target of stoichiometry A_mB_n is

$$\Delta E_A = [S]_A^{A_mB_n} t = \left(\frac{K_A}{\cos\theta_1} \frac{dE}{dx}\bigg|_{E_0} + \frac{1}{\cos\theta_2} \frac{dE}{dx}\bigg|_{K_AE_0} \right) t \qquad (2.5)$$

Here the element A has a kinetic factor K_A. By the additive nature of stopping cross sections expressed in Bragg's law, the total energy loss will be

$$\Delta E = [S]^{A_mB_n} t = \frac{m}{m+n}[S]_A^{A_mB_n} t + \frac{n}{m+n}[S]_B^{A_mB_n} t \qquad (2.6)$$

The concentration of an element at a specific depth can be determined by the number of counts at the corresponding energy on an RBS spectrum. If Q is the number of particles incident on the sample, the number of counts originating from a layer of thickness τ_i at a depth x_i will be recorded in a channel i and is given by

$$H = Q\Omega N \frac{\tau_i}{\cos\theta_1} \frac{d\sigma}{d\Omega}\bigg|_{E_i} \qquad (2.7)$$

where N is the atomic density of the sample and $d\sigma/d\Omega$ is evaluated at energy E_i.

If δE is the energy width of a channel, then $\delta E = [S]\tau_i$ and the spectral counts can be written for element A in compound A_mB_n as

$$H_A = Q\Omega N_A \frac{\delta E}{[S]_A^{A_mB_n} \cos\theta_1} \left(\frac{d\sigma}{d\Omega}\right)_A \tag{2.8}$$

As an example relevant to this study, the relative atomic concentration of some metal M in the germanide M_mGe_n can be found from the peak height ratios

$$H_M = Q\Omega N_M \frac{\delta E}{[S]_M^{M_mGe_n} \cos\theta_1} \sigma_M \tag{2.9}$$

and

$$H_{G_e} = Q\Omega N_{G_e} \frac{\delta E}{[S]_{Ge}^{M_mGe_n} \cos\theta_1} \sigma_{Ge} \tag{2.10}$$

where $\sigma = (1/\Omega)\int (d\sigma/d\Omega)d\Omega$ is the average scattering cross section. Since m and n are proportional to N_m and N_{Ge} we get

$$\frac{n}{m} = \frac{\sigma_M}{\sigma_{Ge}} \frac{H_{Ge}}{H_M} \frac{[S]_M^{M_mGe_n}}{[S]_{Ge}^{M_mGe_n}} \tag{2.11}$$

A simulated backscattering spectrum for the Ir-Ge system is displayed in Fig. 2.4.

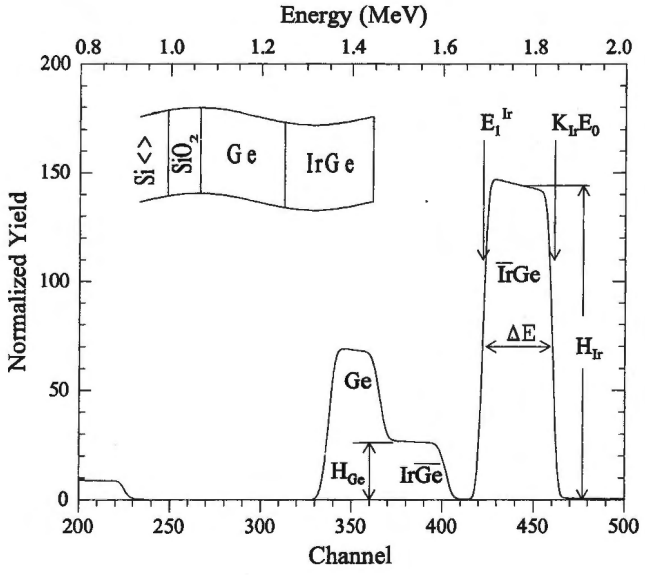

Figure 2.4: A simulated Backscttering spectrum for the Ir-Ge system.

Elemental and depth information is often convoluted in RBS spectra. RUMP is a popular computer package that was used to extract information from RBS spectra by simulating them from given target specifications. The details of this package are presented in Appendix B.

Although RBS has many attractive features, the main disadvantage of this technique with regard to this study is its inability to resolve elements whose mass differences is small as the peaks tend to overlap. Particle Induced X-ray Emission (PIXE) becomes more useful in such cases.

2.2.2 Particle Induced X-ray Emission (PIXE)

Particle Induced X-ray Emission or PIXE[41-45] is an analytical technique based upon X-ray spectrometry. Like RBS, it is non-destructive. A beam of particles is used to excite or eject inner-shell electrons of atoms in a specimen. The resulting vacancies may then be filled by outer-shell electrons emitting characteristic X-rays whose energies identify the particular atom. Auger electrons may also be emitted during de-excitation. The probability of the X-ray emission is known as the fluorescence yield ω_Z. The X-rays are classified according to the levels between which the transition occurs. Those resulting from transitions filling vacancies in the innermost shell are called K X-rays. Those from transitions filling the next shell are L X-rays, whose energies are much lower. We also get M X-rays and so on. Each set of X-rays is further classified according to the levels from which the transition occurs, for example K_α, K_β, K_γ, ...from the levels L,M,N, ... respectively, as shown in Fig. 2.5. In this study, elements of medium mass like Pd, Rh, Co and Ni contributed significant intensities of K X-rays while the heavier ones were studied via their L X-rays. 2 MeV alpha particles were used as a source of excitation, although proton beams are generally favored and PIXE would usually refer to Proton Induced X-ray Emission.

To determine the probability that an incident particle will effect inner shell ionization in a target atom, thereby leading to possible X-ray emission, an ionization cross-section can be calculated. Three fundamental models describing the ionization cross- section are:

1. the Semi-Classical Approximation (SCA);

2. the Binary Encounter (or Impulse) Approximation (BEA)
3. and the Plane Wave Born Approximation (PWBA)

When the beam particle energy is not much larger than the electron binding energy, the SCA model is used. This uses an impact-parameter formalism for the interaction between the target nucleus and the beam particle. The BEA model treats the system in a two body sense while the PWBA uses a Coulomb field based Born approximation. The PIXE software analysis packages use tabulated values of the ionization cross-section based on the Energy loss during collision, coulomb field deflection, perturbation of atomic stationary states and relativistic effects (ECPSSR) theory, which is a modification of the PWBA model.

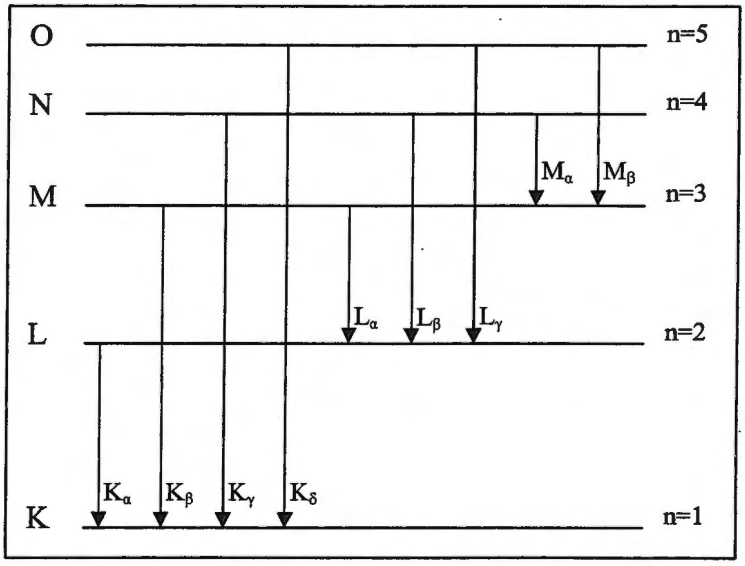

Figure 2.5: An atomic level diagram showing K, L and M X-ray transitions [41].

The yield of characteristic X-rays of any elements in a sample depends on its thickness. Thin samples hardly decrease the beam energy during transit and the yield can be determined by the ionization cross-section $\sigma_Z(E_0)$ at the incident particle energy. It should be mentioned that the transit energy loss mechanisms for a beam particle in PIXE are the same as in RBS, hence the stopping power will have the same expression as that for the inward path in RBS. The yield of characteristic X-rays due to passage of N_p beam

particles through area A of a sample of atomic number Z and atomic mass A_Z is given by[41]

$$Y_0 = \frac{N_p M}{A} \frac{\sigma_Z(E_0)\omega_Z b_Z \varepsilon_Z N_{av}}{A_Z} \tag{2.12}$$

where ω_Z is the K or L fluorescence yield, b_Z the branching ratio which is the fraction of K or L X-rays that appears in the K_α or L_α line, ε_z the detector efficiency and N_{av} Avogadro's number. The so-called thin target sensitivity is defined as

$$k(Z) = \frac{\sigma_Z(E_0)\omega_Z b_Z \varepsilon_Z N_{av}}{A_Z} \tag{2.13}$$

The yield ratio of say, a metallic element M to that of Ge would then be

$$\frac{Y(\mathrm{M})}{Y(\mathrm{Ge})} = \frac{M_{\mathrm{M}} k(\mathrm{M})}{M_{\mathrm{Ge}} k(\mathrm{Ge})} \tag{2.14}$$

Since the masses in this equation can be replaced by the corresponding concentrations, this gives us the stoichiometry.

A typical PIXE spectrum consists of characteristic X-ray peaks superimposed on a background due to various bremsstrahlung processes. Escape peaks and pile-up may also be observed. When an electric charge is accelerated (or decelerated), electromagnetic radiation known as bremsstrahlung is emitted. A beam of ions dissipates energy within the sample through inelastic encounters with bound electrons emitting bremsstrahlung photons. These will have energies distributed right up to the projectile kinetic energy. The cross-section for the beam ion bremsstrahlung is[41]

$$\frac{d\sigma}{d\Omega} = \frac{cA_p Z_p^2 Z^2}{E_p E_X} \left(\frac{Z_p}{A_p} - \frac{Z}{A} \right)^2 \tag{2.15}$$

where E_X is the radiated photon energy, Z_p, A_p and E_p refer to the projectile, while Z and A refer to the target, c is a constant and the other symbols have their usual meanings. We sometimes get secondary bremsstrahlung in which the incident particles not only cause excitation of the target atoms but eject electrons which in turn produce bremsstrahlung. Escape peaks result from photo-electric interactions close to the front

surface of the detector. The ratio of escape peak to parent peak intensities can be approximated theoretically with reasonable accuracy.[41]

When two photons enter a detector within sufficiently short time intervals, they may be recorded as a single event. This gives rise to pile-up peaks which, like escape peaks, can masquerade as other lines. This is normally taken care of by the electronics in the amplifier system.

As can be deduced from equation 2.14, the area of each peak is related directly to the concentration of the corresponding element in the sample. Due to the number of overlaps and the strongly energy-dependent background, a manual analysis of PIXE spectra is not feasible. Computer packages have been developed to deconvolute spectra and very accurately calculate peak areas using a data base of atomic physics information. The package used for this work was GeoPIXE II[44,45] which uses tabulated values for the ionization cross-section based on the ECPSSR theory mentioned earlier. This package uses what is referred to as the Dynamic Analysis method. The highly vectorized code works efficiently with the vector and matrix features of IDL (Interactive Data Language).[46] A new 'Line Traverse' feature made it possible to use PIXE for lateral diffusion as explained in the next section. Details of the GeoPIXE II package are given in Appendix C.

The huge advantage of PIXE over RBS is its ability to resolve trace elements of very close atomic mass. Regular PIXE cannot be used to obtain depth information and in this respect falls short of RBS. This makes the two techniques complementary and this was put to use in this study. Though PIXE is not a good analytical technique for extracting depth information, some depth information may be obtained by changing the beam energy, changing the sample angle or by using two detectors.

2.2.3 Nuclear Microprobe (NMP)

The more recent variants of RBS and PIXE, referred to as μRBS and μPIXE respectively, involve focusing of the beam to small areal dimensions, typically a few microns. It is then scanned across the surface of the sample, providing elemental distribution data as a function of lateral position. This is achieved using the Nuclear Microprobe (NMP). The

NMP used in this work lies at the end of the 0° beam line of a 6 MV van de Graaff accelerator. As seen in Fig. 2.6, the beam passes through an analyzing magnet that selects the energy. It is then coilimated to size before entering the actual microprobe via a manually opened beam stop, the beam line having been pumped down to a pressure of less than 10^{-6} torr. Initial focusing of the beam is done by a quadruple doublet before a triplet focuses it down to sizes of close to 1 μm at the target. The X-Y steering coils facilitate the positioning and scanning of the beam. This is automated with a PC interface as is the data acquisition system. The features in the NMP target chamber include: a filter aided X-ray detector for PIXE measurements at 135° to the incoming beam direction, an

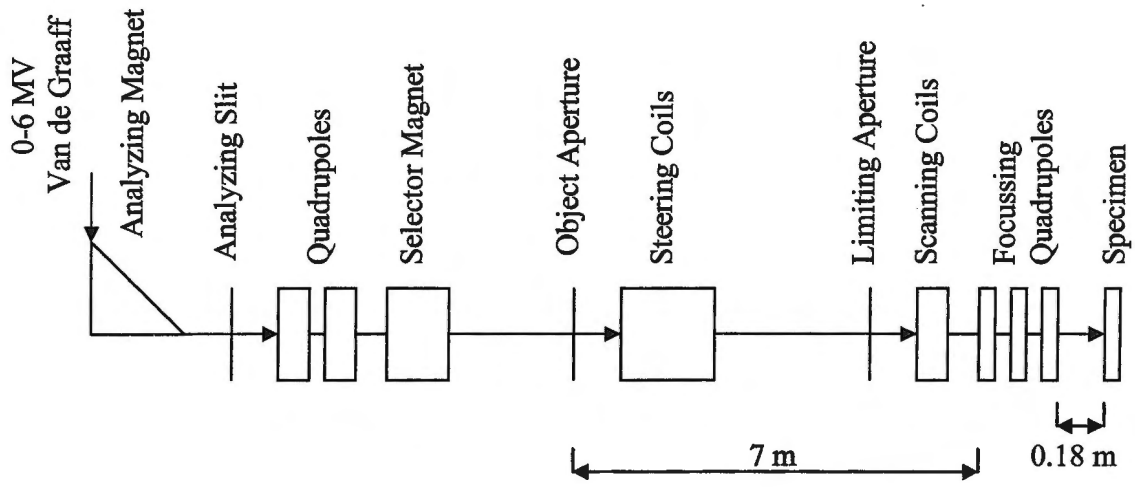

Figure 2.6: Nuclear microprobe layout, not drawn to scale.

annular silicon surface barrier (SSB) detector at 176° used for RBS measurements and another SSB detector positioned at 30° to the beam direction for elastic recoil detection analysis (ERDA) and scanning transmission ion microscopy (STIM) measurements. Other features are: a channeltron electron detector for secondary electron imaging and an optical microscope at 45° to the sample normal.

Whereas the mechanical automation was handled by LABVIEW[47] based software, the data acquisition was done with the general-purpose system XSYS.[48] In this study a rectangular area covering all regions of interest on the sample was scanned. Typically, 128 × 128 spectra were generated in each run and recorded along with position

information. The data were saved in event by event mode which could subsequently be played back by different software for analysis. For easy analysis, scanned areas were adjusted in such a way that the interfaces of the regions of interest lay horizontally in line with the original island edge. All spectra along the same horizontal line could then be added, resulting in a traverse of only 128 spectra for further analysis. This optimally exploits beam position while improving on statistics. From sets of spectra generated in this way, both RBS and PIXE results were produced as a function of the lateral diffusion distance.

Imaging with the NMP has its limitations. Firstly, resolution is limited by the diameter of the ion beam, hence smoothing out features of smaller dimensions. Secondly, the necessity for small beam sizes results in very low and sometimes unstable beam currents. This results in lengthy runs which could lead to unique concerns depending on the system. A gradual carbon build-up across the scanned area of the sample, believed to originate from diffusion pump oil vapor, was of concern in our system. Though this was controlled to avoid significant alteration of the sample structure it was used to our advantage during optical microscopy measurements, in the sense that exact scanned areas could be identified by the carbon darkening. The final disadvantage of the technique, which was a consequence of our method of analysis, was that features that varied along the vertical line through which spectra were added were not resolvable, resulting in rather misleading information, as explained in Chapter 5. This was resolved by complementing the technique with scanning electron microscopy (SEM).

2.2.4 Scanning Electron Microscopy (SEM)

Electron microscopy an electron beam is considered as a matter wave interacting with a sample. The microscopy is based on studying the scattered electrons. Transmission Electron Microscopy (TEM) gives the best resolution in electron diffraction imaging of very thin samples. For thicker samples or those deposited on substrates, Scanning Electron Microscopy (SEM)[49-51] provides an alternative. In SEM, images are formed by recording specific signals as a function of the scanning probe position. Surface structures are generally imaged from secondary electron signals. Secondary electrons are produced

during inelastic collisions which excite atomic electrons above the Fermi level making them energetic enough to leave the sample. Elastic scattering by the Coulomb potential of the positively charged atomic nucleus is most important for obtaining high-resolution structural information in TEM. Inelastic interactions with atomic electrons resulting in excitation or inner-shell ionization provide analytical information about the chemical composition of the sample.

To get an indication of the relative number of electrons inelastically scattered to those elastically scattered, the theoretical ratio of their respective total cross sections is

$$\frac{\sigma_{inel}}{\sigma_{el}} \cong \frac{26}{Z} \tag{2.16}$$

or experimentally,

$$\frac{\sigma_{inel}}{\sigma_{el}} \cong \frac{18}{Z} \tag{2.17}$$

showing that inelastic scattering is dominant in light atoms.

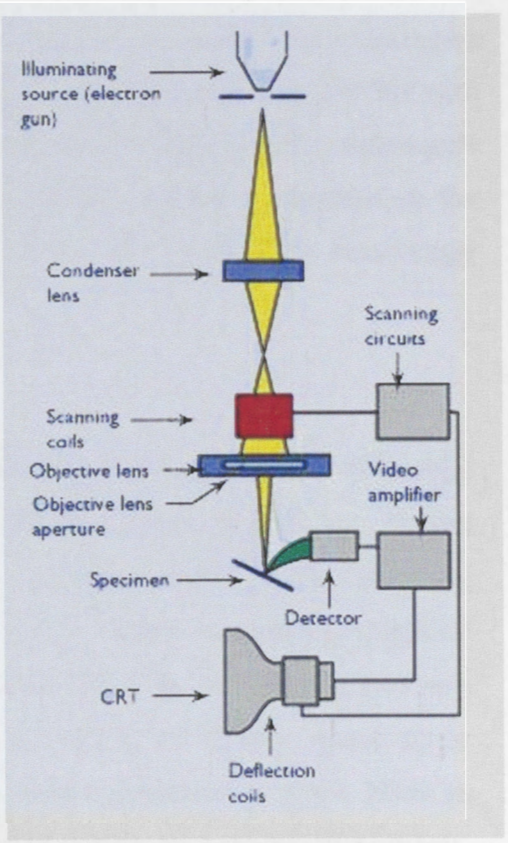

Figure 2.7: Diagram showing the main features and the electron beam path of a two lens SEM [49].

The SEM works as follows: Electrons from the electron gun are accelerated through a high voltage. They are caused to converge by the condenser lens and brought to a focal point at the specimen surface by another electro-magnetic lens (Fig. 2.7). The scanning coils scan the beam across the sample while the detector records the secondary electrons given off. The spot of a cathode ray tube (CRT), of brightness dependent on the amplified detector signal, is simultaneously scanned on a screen. The two scans are coupled so as to give a one to one position presentation. This in effect gives an image of the number of secondary electrons given off as a function of position. Electrons deposited onto the sample have to be conducted away to earth. Samples are normally vacuum coated with metal to render them conductive. The coating should be of uniform thickness and significantly thinner than the smallest topographic details of interest. A Pd-Au alloy was used in this case. Both, surface topographic and chemical compositional analysis was carried out.

One disadvantage of SEM is that it cannot be described as entirely non-destructive because of the required metal film coating, although this is generally a minor bother with materials science samples. The main short fall as regards this study was the technique's inability to present height information save for the contour implied by contrast on the images. Accurate height information was obtained by use of Atomic Force Microscopy (AFM).

2.2.5 Atomic Force Microscopy (AFM)

Atomic Force Microscopy (AFM)[52-54] is a non-diffractive technique. It is one of a series of Scanning Probe Microscopies (SPMs) based on different physical principles. Central to this family of techniques is the presence of a tip, typically less than 100 nm in radius, scanned over and in very close proximity to the sample surface. A particular physical property is measured and imaged over the scanned area. Scanning Tunneling Microscopy (STM) was the first of the SPM techniques to be developed. In STM, a biased tip is brought within around 10 Å of the sample surface using a piezoelectric drive. There is overlap of the tip and sample wavefunctions at the gap, resulting in a tunneling current. Electrons flow from the occupied states of the tip to the unoccupied states in the sample, or vice versa, depending on the polarity of the bias. The spatial distribution of electronic

states can then be scanned, imaged and interpreted in terms of surface topography with some knowledge of the electron density of states of both the sample and the tip. The major limitation of STM is its inability to analyze insulators. To overcome this, AFM, also known as Scanning Force Microscopy, SFM was developed. This technique is based on force rather than current as the imaging parameter. The tip in this case is a stylus on the end of a cantilever as shown, in Fig. 2.8. The cantilever is of spring constant k, which is lower than that typically between atoms. By Hooke's law, $F = -kx$, the tip is displaced by an amount x related to its force of interaction, F, with the sample. A spring deflection sensor converts this force into an electrical signal. A piezoelectric drive is used to move either the tip or the sample as shown in the diagram of Fig. 2.9. By means of a feedback loop connected to the z-piezo, and using the spring deflector sensor current as a control parameter, the tip-sample spacing is controlled very precisely. The z-piezo signal is displayed as a function of the x and y coordinates, giving a force map. This image gives direct topographic information of the sample surface.

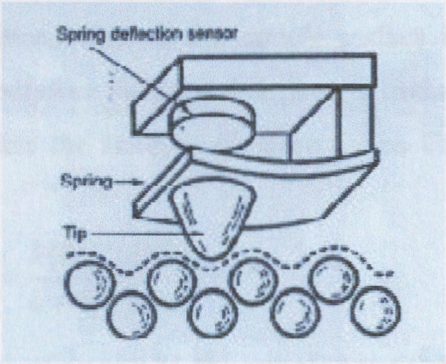

Figure 2.8: Schematic diagram of an AFM force tip showing a spring deflection sensor device [54].

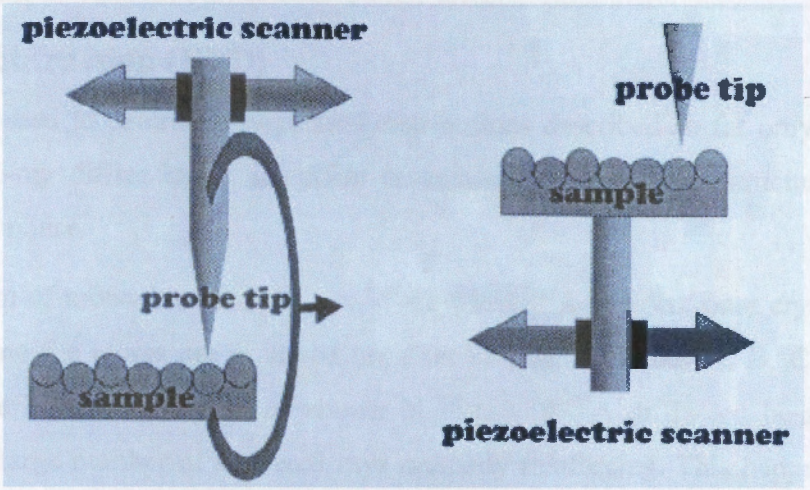

Figure 2.9: Schematic view of the sample-tip arrangement in an AFM show two different configuration of the piezoelectric drive [54].

Several forces act on the tip. Firstly, there is the spring force due to the cantilever. Secondly there are several interactions with the sample including attractive van der Waals forces, repulsive forces and chemical bonding interactions. Finally, AFM is ordinarily used under ambient conditions wherein the sample surface is covered with a layer of water. A meniscus forms between the tip and surface, introducing an attractive capillary force. As the tip approaches the sample, all these forces contribute to the total force gradient[54]

$$\frac{\partial F}{\partial D} = \frac{k(\partial^2 U/\partial D^2)}{k + \partial^2 U/\partial D^2} \tag{2.18}$$

where D is the sample separation and U the sample potential. $\partial^2 U/\partial D^2$ is negative for attraction. If this term becomes equal to k, the total force gradient becomes instantaneously infinite and the tip jumps towards the sample. One therefore needs to choose a stiff enough cantilever to make sure that k is greater than $\partial^2 U/\partial D^2$ for all relevant separations D. Depending on the choice of values of D, there are three variations of the technique; contact, non-contact and intermittent-contact AFM. Atomic resolution can be achieved by operation in ultrahigh vacuum.

2.2.6 X-ray diffraction (XRD)

All techniques used to determine elemental distributions described so far only give the composition. X-ray diffraction[55] identifies materials by their crystal structure, hence establishing the phase.

Consider a beam of monochromatic X-rays of wavelength λ incident on a crystal at an angle θ. Assume the atoms are arranged on a set of parallel planes A, B, C,..., with spacing d. The beam is scattered as shown in Fig. 2.10. A diffracted beam is one composed of a large number of scattered rays mutually reinforcing. This happens when the path difference $2d\sin\theta$ between adjacent scattered rays is equal to a whole number n of wavelengths, i.e.,

$$n\lambda = 2d\sin\theta \tag{2.19}$$

which is known as the Bragg law. The intensity I of a diffracted beam will depend on a number of factors, viz., the incident X-ray intensity, the structure factor F, the Lorentz-polarization factor and the multiplicity factor P, it is given by

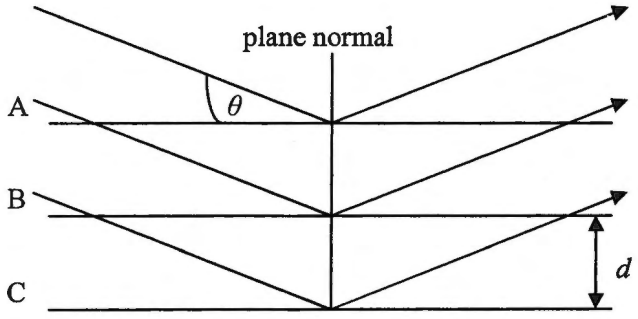

Figure 2.10: Ray diagram, showing the diffraction of X-rays by a crystal [55].

$$I = F^2 p\left[\frac{1+\cos^2 2\theta}{\sin^2\theta\cos\theta}\right] \tag{2.20}$$

A description of these quantities is given in any standard text. In practice the intensity also depends greatly on the amount of energy absorption within the sample and several instrumental factors.

Experimentally, structure analysis was done by using X-rays of known wavelength λ from a Cu tube T (Fig. 2.11). The rays are scattered from the sample C at O. A detector D

measures the intensity of the scattered beam while sweeping through an arc of varying values of 2θ. The range of 2θ swept was from 10° to 80° in steps of 0.2° and a dwell time of 10 seconds. For phase identification, powder diffraction data files were used.

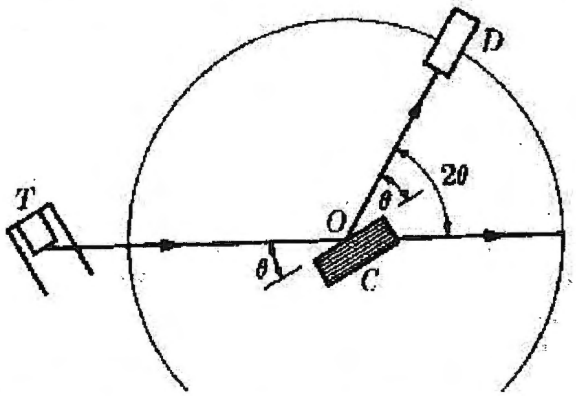

Figure 2.11: Diagrammatic view of an X-ray diffraction unit [55].

The obvious advantage of this technique is that one is able to carry out phase identification. The disadvantage for this study is that it can only be used for the characterization of conventional thin films. To use X-rays on lateral diffusion couples, an X-ray microscope would have to be used, which poses a great instrumentational challenge. Optical microscopy was however extensively used on lateral diffusion couples.

2.2.7 Optical Microscopy

Compared to other microscopic techniques, optical microscopy[56-57] give the quickest way to access the structure of materials. It is contact free and can resolve lateral structure down to a size of around 0.2μm. An objective lens provides a real magnified image of the object in the focal plane of an eyepiece, which is then focused on to the retina of the eye. This study made use of a NIKON LABOPHOT microscope. Both transmitted and reflected light modes were used. The variable objectives were marked with their magnification M_{obj} as was the eyepiece, which was marked with $M_{eyepiece}$.The total magnification M_{tatol} achievable is the product

$$M_{total} = M_{obj} M_{eyepiece} \tag{2.21}$$

which ranged from 50 to 1000. Apart from the limitation imposed by the maximum possible magnification, resolution of lateral structures is further limited by the diffraction

limit of resolution. If diffracted light enters a medium of refractive index n, the minimum resolvable separation $a_{\min}$ between two structures is given by $n\sin\alpha = \lambda/a_{\min}$. Applied to the object lens, α would be half the angle formed by the collected light cone whose vertex lies along the optical axis. $\lambda/a_{\min}$ is then described as the numerical aperture A_{obj} of the objective lens. An aperture of the illumination system A_{ill} can also be defined, in which case the smallest resolvable structure is given by

$$a_{\min} = \lambda/(A_{obj} + A_{ill}) \tag{2.22}$$

Violet light was used for illumination to optimize resolution. In this case, a numerical aperture of about 0.9 for the microscope gives a resolution limit around 0.2 μm. This was adequate for measuring the length of the growth regions in lateral diffusion couples, a task in which this technique was put to extensive use.

A color digital CCD (Charge Coupled Device) video camera was mounted onto the microscope. Images were projected onto a PC screen in real time. These images were saved in digital format using the miro VIDEO DC20 software system. They were subsequently read by specialized analysis software.

CHAPTER 3

THE IRIDIUM – GERMANIUM SYSTEM

3.1 Introduction

An extensive literature search showed that insufficient data have yet been accumulated to draw a comprehensive phase diagram for the germanium – iridium system. Analysis reported by Bhan and Schubert[58] indicated the formation in bulk diffusion couples of the phases IrGe (orthorhombic), Ir_4Ge_5 (tetragonal), Ir_3Ge_7 (body-centered cubic) and $IrGe_4$ (hexagonal), after heat treatment at temperatures between 520°C and 1000°C, using X-ray, powder and single crystal diffraction. In that work, the phases IrGe and Ir_4Ge_5 were observed to co-exist. Further work by Schubert and Pfisterer[59,60] indicated an apparent formation of the phase Ir_3Ge_4.

Because of the limited availability of data for the Ir-Ge system, the Miedema model is made use of in the present study. Table 3.1 shows heat of formation values for expected phases of the Ir–Ge system, as calculated on the basis of this model. The curve of predicted heat of formation values as a function of composition for this system was presented earlier in Fig. 1.2.

Ir-Ge Phase	Miedema heat of formation ΔH (kJ $mol^{-1}atm^{-1}$)
IrGe	-35.4
Ir_4Ge_5	-34.0
Ir_3Ge_7	-26.0
$IrGe_4$	-17.5

Table 3.1: Heat of formation values in the Ir–Ge system, obtained from the Miedema's semiempirical model.

3.2 Thin Film Couples

Knowledge of the phase formation sequence of a system is useful in determining optimum parameters for a particular investigation. It is for this reason that a study of the phase formation sequence was carried out prior to the lateral diffusion study. This study was carried out with conventional thin film couples using RBS and XRD for phase identification. A sample structure SiO_2/Ti (20Å)/Ge (5500Å)/Ir (900Å) was used. This configuration and thickness of Ge and Ir was found to be the best in maximizing the X-ray yields while avoiding excessive RBS peak overlap. The excess Ge also allowed for the more Ge rich phases to form. The thin layer of titanium (20 Å) was deposited onto the SiO_2 prior to the deposition of the Ge. This Ti layer reacted with SiO_2 forming a 'glue' without which the structure did not adhere, as seen in the optical micrograph of Fig. 3.1 where part of the sample had a Ti layer while the rest did not. It was only in this system that a Ti 'glue-layer' was found necessary.

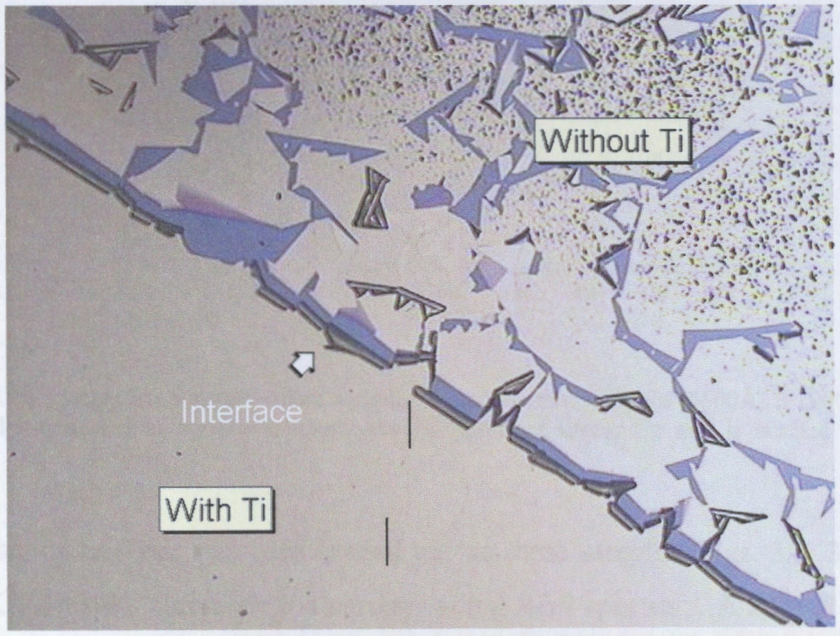

Figure 3.1: Optical micrograph of the interface between a SiO_2/Ge (5500Å)/Ir (900Å) structure with a 20 Å Ti layer between SiO_2 and Ge (bottom left) and the same structure but with out the Ti (top right).

3.2.1 Phase Formation Sequence Results

Fig. 3.2 shows RBS spectra from an unreacted sample and a series of samples that were annealed at temperatures between 370°C and 800°C for different times. The expected Ir height for the various phases is indicated on the right of the diagram.

It must be noted that the film thickness values indicated in figure captions (in Å) were those intended to be achieved during film depositing and were monitored using a vibrating crystal. Any values shown on the actual figures in units of areal density ($x10^{15}$ atoms.cm^{-2} which we will normally write as /cm^{-2}) work were determined using Rutherford Backscattering Spectrometry and are more accurate.

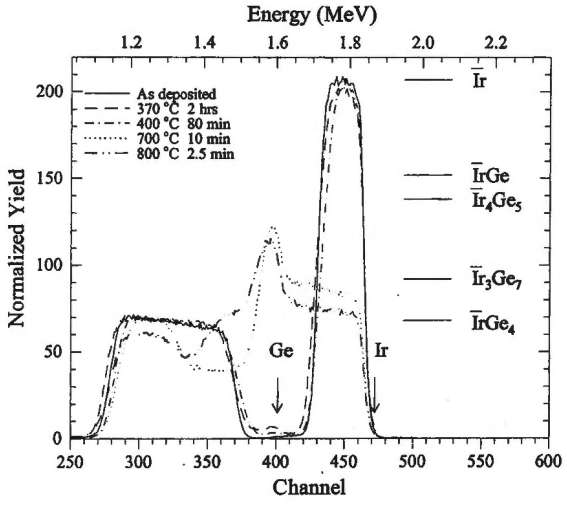

Figure 3.2: RBS spectra from an unreacted sample of composition SiO_2/Ge (5500Å)/Ir (900Å) and from similar samples annealed at various temperatures for different times. Ge and Ir surface positions are indicated.

X-ray diffraction analysis was also carried out on these samples. Figs. 3.3, 3.4, 3.5 and 3.6 show XRD results alongside the corresponding RBS spectrum. A RUMP simulation of the RBS spectrum is also shown.

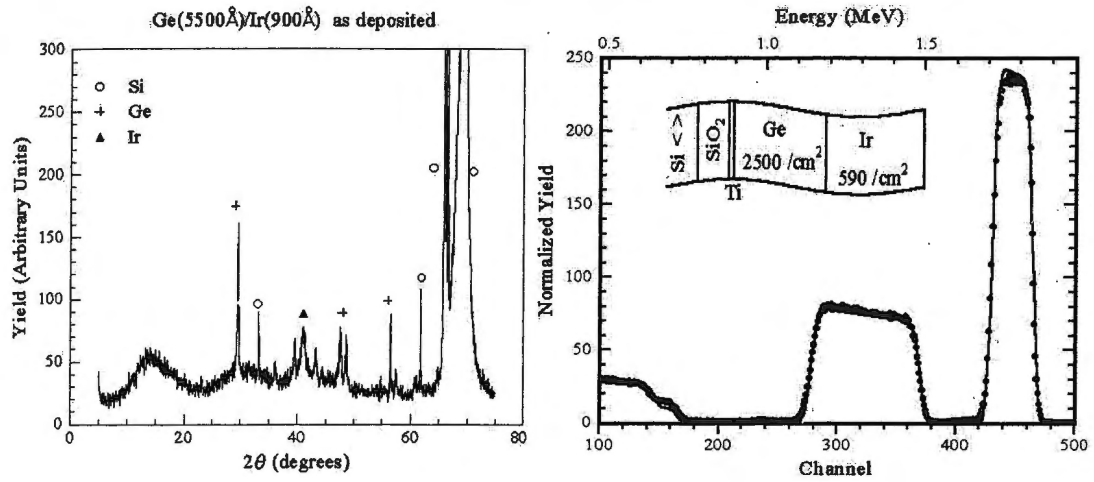

Figure 3.3: X-ray diffraction and corresponding RBS spectra, of a sample of composition SiO_2/Ge (5500Å)/Ir (900Å) before annealing.

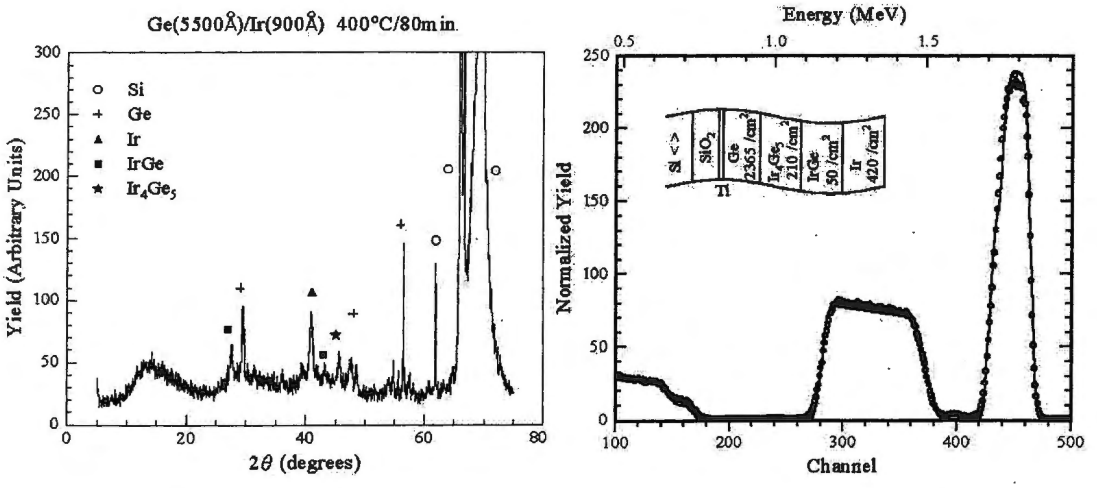

Figure 3.4: X-ray diffraction and corresponding RBS spectra, of a sample of composition SiO_2/Ge (5500Å)/Ir (900Å) after annealing at 400°C for 80 min. The phases IrGe and Ir_4Ge_5 are seen to coexist.

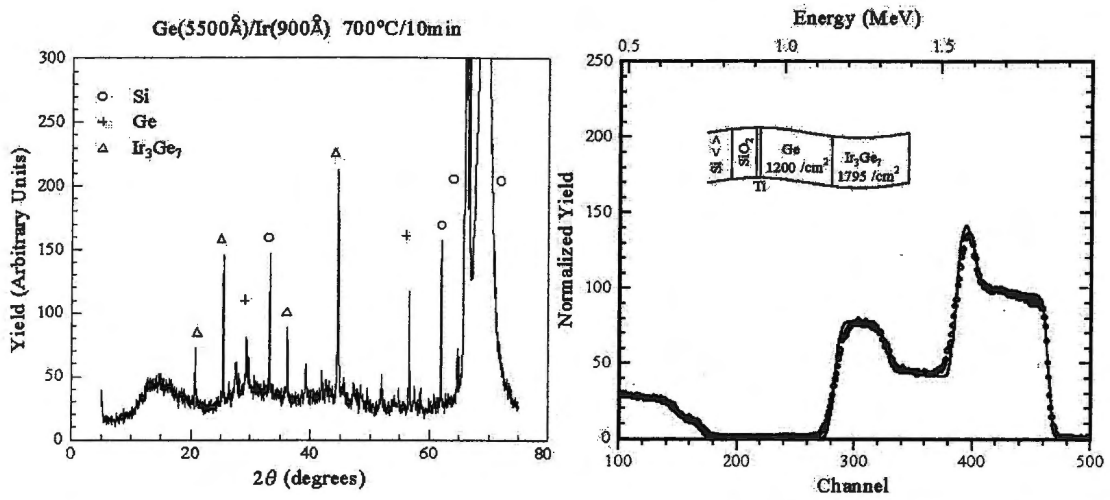

Figure 3.5: X-ray diffraction and corresponding RBS spectra, of a sample of composition SiO_2/Ge (5500Å)/Ir (900Å) after annealing at 700°C for 10 min.

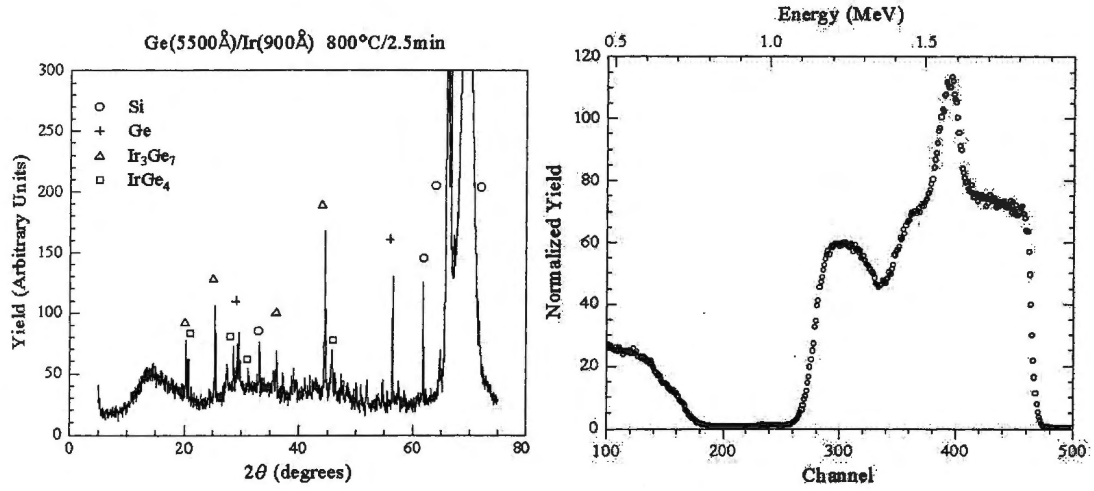

Figure 3.6: X-ray diffraction and corresponding RBS spectra, of a sample of composition SiO_2/Ge (5500Å)/Ir (900Å) after annealing at 800°C for 2.5 min. $IrGe_4$ only forms at and above 800°C.

In summary, these results show that the phases IrGe and Ir_4Ge_5 where the first to form and coexisted at annealing temperatures of around 350°C (Fig. 3.4 shows the case at 400 °C but other spectra not included show that the reaction began around 350 °C). After these two phases Ir_3Ge_7 formed (Fig. 3.5), from our data it was not possible to tell whether all the Ir was consumed before Ir_3Ge_7 appeared. The $IrGe_4$ phase only formed above 800°C (Fig. 3.6) while Ir_3Ge_4 was not observed in the present study. The range of temperatures between 400°C and 800°C was also studied.

3.2.2 Marker Results

The inert marker technique was used to monitor atomic mobility during phase formation. A thin Ti (12 Å) layer was used as a marker between Ir and Ge layers. According to Thomas et al.[61,62] Ti reacts with Ge at around 500°C, forming Ti_6Ge as the first phase. This investigation was therefore carried out at temperatures well below 500°C, where there is no reported Ti-Ge interaction. Since the RBS peak for Ti lies at lower energies than both the Ge and Ir peaks, two factors were considered in determining sample structure. Firstly, the Ge had to overlay the Ir, as the reverse configuration would push the Ge peak to lower channels, possibly obscuring the marker signal. Secondly, as a Ti (20Å) layer was also used as a 'glue', two Ti signals were expected, and the overlaying Ir layer therefore had to be thick enough to keep these two Ti signals well separated. An RBS spectrum and RUMP simulation of the structure using, SiO_2/Ti(9/cm^2)/Ir(280/cm^2)/Ti(7/cm^2)Ti(Ge(380/cm^2), is shown in Fig. 3.7. This structure was annealed at 400°C for different times and the relative shift of the marker Ti signal was monitored. Fig. 3.8 shows an RBS spectrum and RUMP simulation of the sample annealed at 400°C for 20 minutes. The resulting structure shows that Ge diffused across the marker to form IrGe and Ir_4Ge_5.

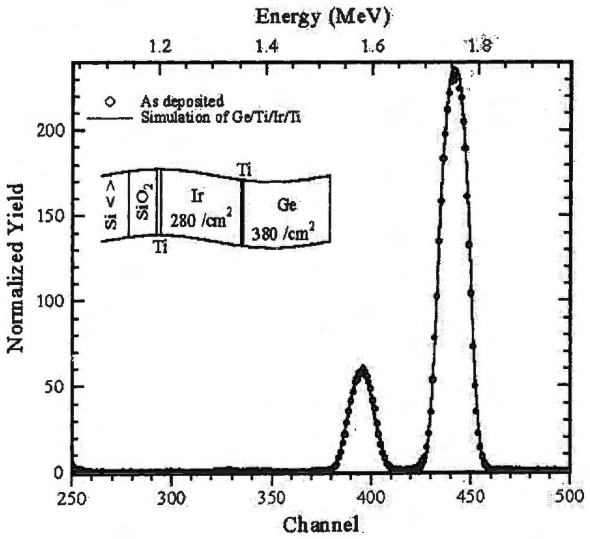

Figure 3.7: RBS spectrum and RUMP simulation of the virgin marker structure used in determining atomic mobility during phase formation.

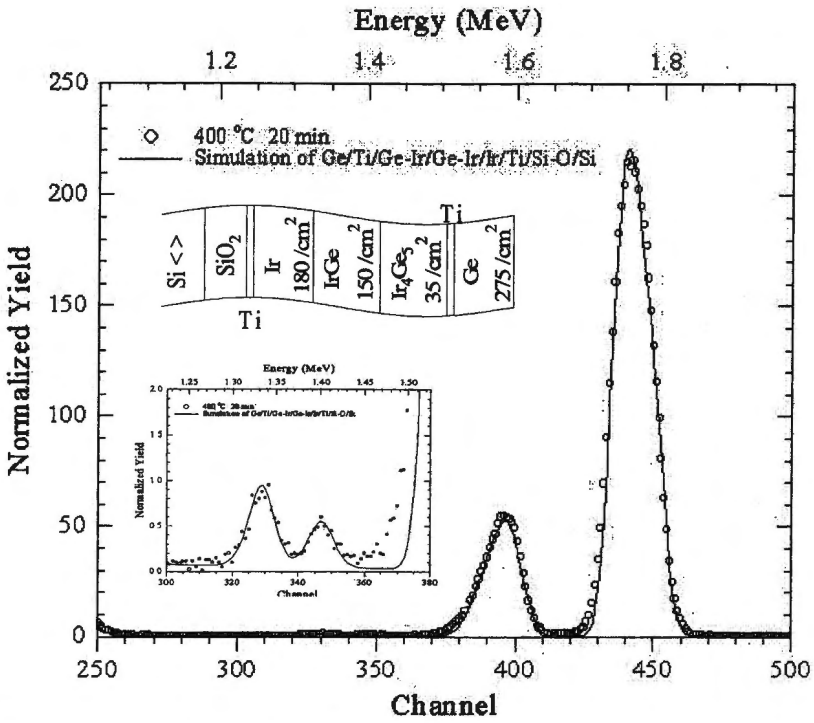

Figure 3.8: RBS spectrum and RUMP simulation of a marker structure annealed at 400°C for 20 minutes. The subplot is a blow up of the Ti marker region of the spectrum.

Fig. 3.9 shows a blow up of the Ti 'glue' and Ti marker signals with an overlaying RUMP simulation (left). Upon annealing at 400°C for 20 minutes, the Ti marker signal shifted by 5 channels to higher energies while the 'glue' Ti signal did not shift (as was to be expected). Clearly, Ge was the sole moving species during the initial stages of germanide formation.

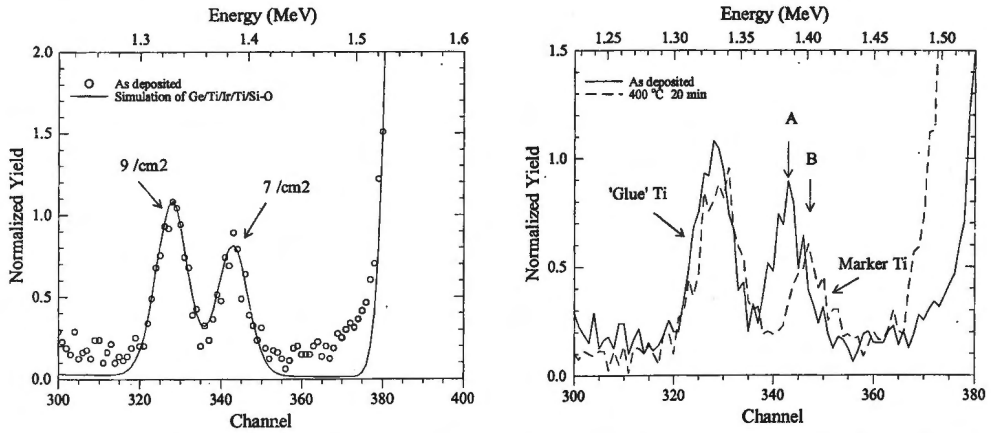

Figure 3.9: Blow up of the Ti 'glue' and Ti marker signals with an overlaying RUMP simulation (left). Upon annealing at 400°C for 20 minutes, the Ti marker signal shifts from channel 342 to channel 347 (right), while the Ti 'glue' signal does not shift.

3.3 Lateral Diffusion Couples

Samples for lateral diffusion study were prepared as described in Chapter 2. Both possible configurations were investigated, viz., thick Ir islands on thin Ge films, and thick Ge islands on thin Ir films. In the case of the latter, the thickness of the Ge island was chosen to result in atomic ratios of Ge to Ir far larger than that of the most Ge rich phase of the system, $IrGe_4$. This was in order that sufficient germanium remained after the initial reaction to diffuse laterally outwards into the surrounding Ir film. By the same token, the atomic ratio of Ir to Ge for Ir islands on Ge film samples was larger than the most Ir rich phase of the system, IrGe. The samples were annealed within a range of temperatures between 600 to 850°C for different lengths of time.

Fig. 3.10 shows an optical micrograph of an 'as deposited' sample of an Ir island (2000Å) on a Ge film (500Å). The island edges were sharp, showing no signs of Ir-Ge interaction.

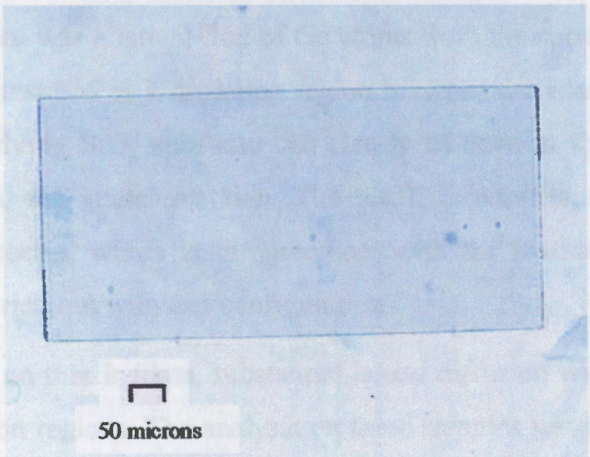

Figure 3.10: Optical micrograph of an 'as deposited' sample of a thick Ir island (2000Å) on a thin Ge film (500Å).

Fig. 3.11 is a micrograph of this sample after annealing at 800°C for 1 hour.

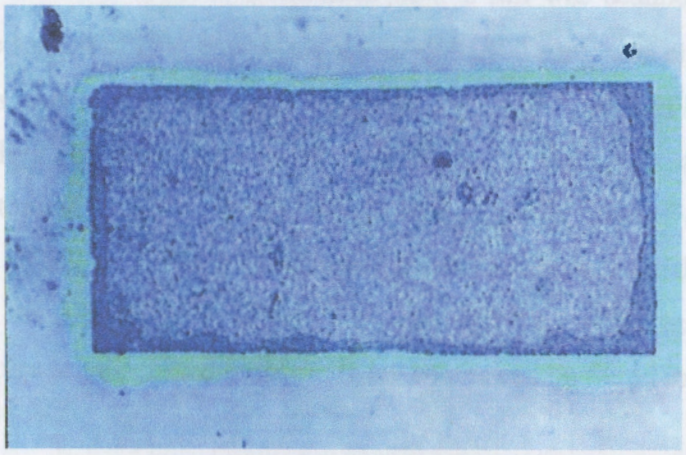

Figure 3.11: Optical micrograph of an Ir island (2000Å) on a Ge film (500Å) annealed at 800°C for 1 hour.

Marked blemishes were seen to form at this high temperature. Most prominent of the observed features was the Ge depletion region around the island and a reaction zone inside. From this, it can be inferred that after the underlying germanium was consumed in the island region, there was a lateral flux of Ge atoms from the surrounding film into the island region which resulted in a depletion region between the island boundary and the thin film. The underlying SiO_2 substrate can clearly be seen in the micrographs. This consequently stopped the lateral reaction. The result is consistent with Ge being the dominant moving species, which is in agreement with the marker results. No further investigation was carried out with this configuration.

For thick Ge islands on thin Ir films, substantial lateral diffusion was observed, resulting in a variety of reaction regions. The analysis on these samples was carried out in several stages. Firstly, for all samples, the various reaction zones were identified and their widths determined, using optical microscopy. Microprobe RBS and PIXE scanning of chosen regions was then carried out on selected samples. Finally, SEM and AFM were employed on the regions to obtain further information, the latter techniques being used as complementary rather than auxiliary.

A 2 MeV α-beam focused down to a diameter of ~ 2 μm was scanned across a well defined area of the samples. This area, typically of 400×400 μm^2, was chosen to include all reaction regions observed in the optical micrographs. Both RBS and PIXE data were recorded along with the position of the beam at that time. As explained in Chapter 2, this event by event system of data storage was placed in files (appropriately termed as event files) from which RBS and PIXE data were subsequently extracted and analyzed separately. Fifteen samples of the Ir-Ge system were analyzed on the microprobe. Two representative samples are discussed in this section; others can be found in Appendix A.

3.3.1 μRBS Results

The main advantage of μRBS is that it gives compositional information as a function of both lateral position and depth, thereby making it possible to generate three dimensional images of elemental concentration.

Fig. 3.12 is an optical micrograph of a sample with a Ge island (2500 Å) on an Ir film (250Å) annealed at 800°C for 30 minutes. The five different regions observed are labeled A to E. As explained in Chapter 2, a gradual carbon deposition of the scanned area was generally an undesirable characteristic of the NMP. As it turns out, this feature was useful in this work in that the scanned area was darkened by the carbon and hence easily identifiable in the optical micrographs as seen in Fig. 3.12. This sample was scanned twice; the two scanned areas are seen in this figure. Sample orientation was adjusted so that the microprobe beam scanned parallel to the original island interface. Once it had been established that no variation in composition was observed parallel to the interface, spectra were summed along this direction. This improved statistics and reduced the analysis to a one-dimensional scan perpendicular to the interface. The set of spectra generated in this way for the scanned area on the right, is shown in Fig. 3.13, as a function of lateral position.

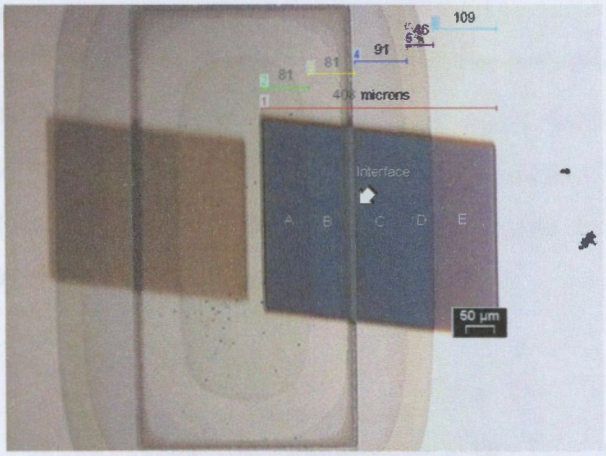

Figure 3.12: Optical micrograph of a Ge island (2500Å) on an Ir film (500Å) annealed at 800°C for 30 minutes.

The raw RBS data show good separation between the Ir and Ge peaks together with a small Ti 'glue' signal which was at a low enough energy as not to affect the analysis. The orientation of the figure is such that spectra from region A lie at the back while those derived from the unreacted Ir film are in front. From the varying heights of the Ge and Ir peaks, different regions are clearly evident. The substrate signal is also included.

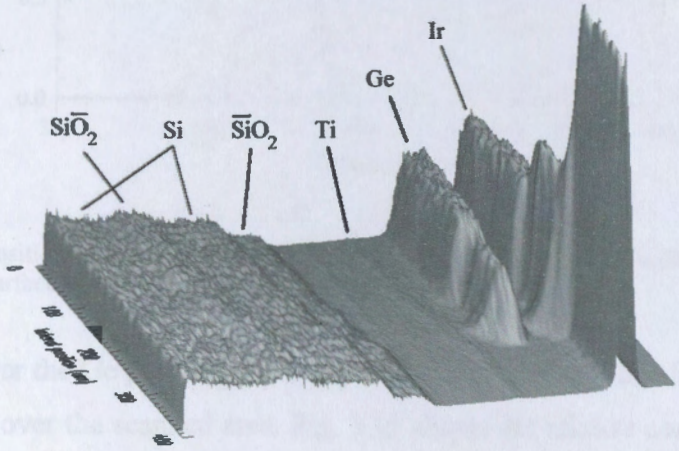

Figure 3.13: RBS spectra obtained from the scanned area as a function of lateral position.

A representative spectrum picked from the five regions labeled A to E is shown in Fig. 3.14. The spectrum from region E shows a peak of unreacted Ir and no Ge. Peak heights of the spectra taken from regions D, C and B show the phases Ir_4Ge_5, Ir_3Ge_7 and $IrGe_4$ respectively. The germanides in these three regions are seen at the surface position. On

the other hand, it can be seen from the solid line in the figure that the region A consisted of unreacted Ge and the phase $IrGe_4$. The Ir peak of the solid line lies below the surface position, indicating that there was no Ir at the surface. Region A therefore consisted of unreacted Ge overlaying the $IrGe_4$ phase.

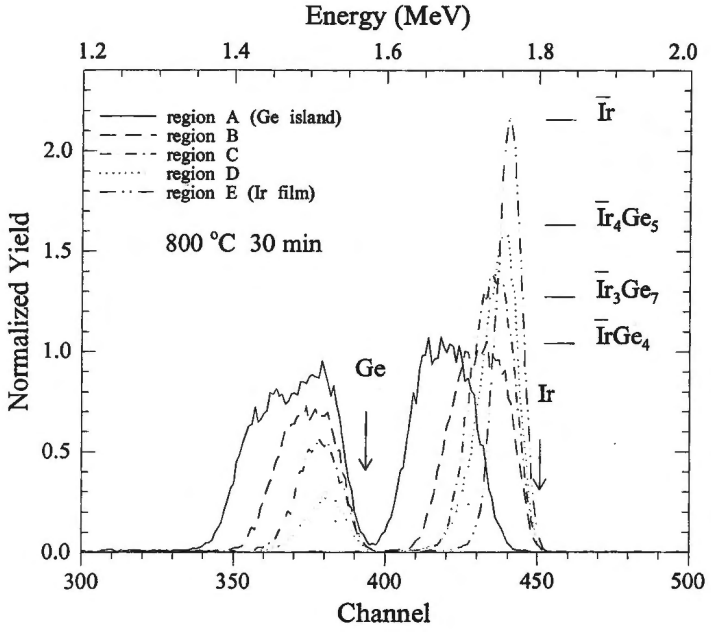

Figure 3.14: Superposition of selected RBS spectra from each of the five regions. Ir peak heights of the various phases and surface positions of Ge and Ir are indicated.

A gate was set over the Ge peak between channels 340 and 395 to obtain an RBS map of Ge concentration over the scanned area. Fig. 3.15 shows the relative concentration of Ge atoms in the five regions. The legend to the right shows the color code. The top of the figure was from inside the island which consisted of $IrGe_4$ together with overlaying Ge. This shows the highest Ge concentration. No Ge is seen at the bottom; this region corresponds to the unreacted Ir film. All other regions are distinct.

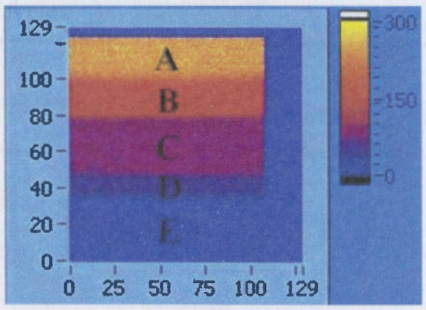

Figure 3.15: RBS map showing the relative concentration of Ge atoms in the five regions of the scanned area. The legend to the right give the color code.

When the gate was set between channels 440 to 450, a map of the Ir concentration at the surface of the sample was obtained; this is shown in Fig. 3.16. There is no surface Ir at the top of the figure. This corresponds to region A and shows that an unreacted Ge film overlays the compound phase in this region. The other regions are again distinct, with the highest concentration being that of the unreacted Ir film at the bottom.

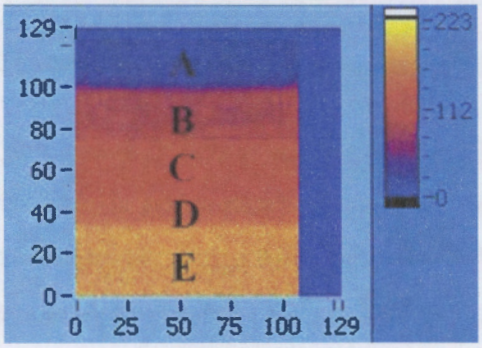

Figure 3.16: RBS map showing the relative concentration of surface Ir atoms in the five regions of the scanned area.

Since the yield or integrated count is directly related to concentration, Ir and Ge peaks were separately integrated at each beam position. The results are shown in Fig. 3.17.

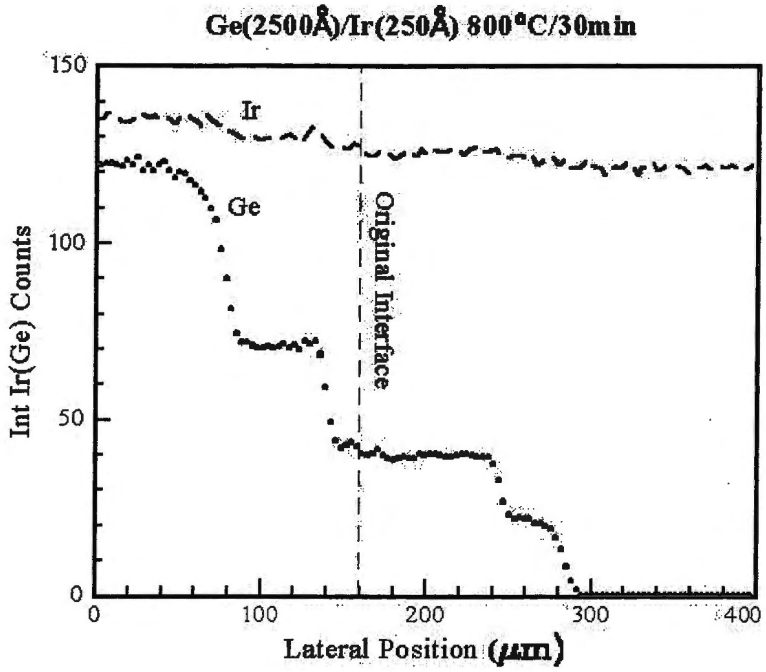

Figure 3.17: Integrated counts of the Ir and Ge peaks as a function of lateral position for a Ge island on an Ir film annealed at 800°C for 30 minutes. The data of Ir counts were offset above those of Ge for clarity.

There is a slight drop in integrated Ir counts as one moves outwards from the region where unreacted Ge exists. This is not a result of variation in Ir concentration, but a consequence of the inverse-square proportionality between differential scattering cross section and energy of backscattered particles $\left(d\sigma/d\Omega \propto 1/E^2\right)$. Due to energy loss along their incoming paths, alpha particles reaching Ir atoms underneath the Ge film in the center of the island will be less energetic than those scattered by the exposed Ir. The differential scattering cross section is therefore higher for Ir atoms in the middle of the island than outside the island, and hence the difference in yields.

The information in Fig. 3.17 was then converted to stoichiometric data and plotted, the result of which is shown in Fig. 3.18.

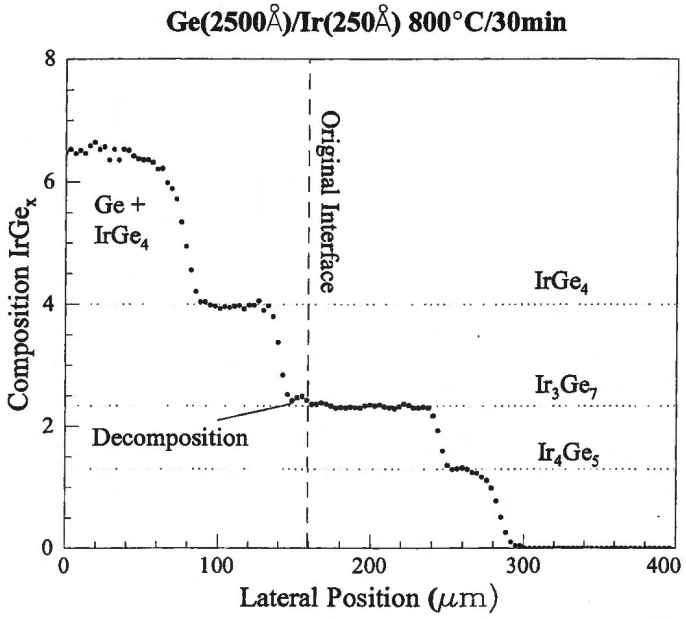

Figure 3.18: Stoichiometric information of a Ge island (2500Å) on an Ir film (500Å) annealed at 800°C for 30 minutes, derived from integrated counts of the Ir and Ge peaks as a function of position.

The lateral extent of the phases identified in Fig. 3.14 is now visible. An interesting feature is the presence of a small region of the phase Ir_3Ge_7 inside the original island region. The width of this region was observed to increase with annealing time, which can be seen in Appendix A. This suggests a gradual decomposition of the phase $IrGe_4$ into Ir_3Ge_7 by the reaction $3IrGe_4 \rightarrow Ir_3Ge_7 + 5Ge$. The Ge liberated in this reaction joins the flux of Ge atoms from the unreacted Ge source to facilitate reactions at the other interfaces further from the original island region.

Each RBS spectrum was then simulated by RUMP to obtain thickness information. This information is plotted in Fig. 3.19 as a function of lateral position. The figure shows relatively uniform thickness within each phase region (apart from the Ir_4Ge_5 region) and sharp steps between regions. A narrow step is seen in the Ir_4Ge_5 at the interface with Ir which may suggest the presence of the phase IrGe. This region was however too narrow to properly resolve and monitor.

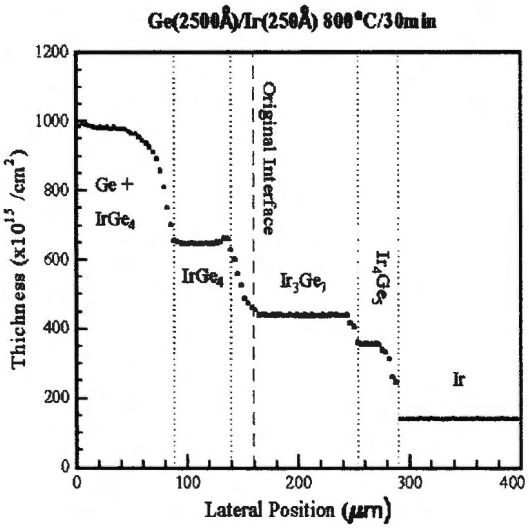

Figure 3.19: RUMP simulated thickness of the various phase regions as a function of lateral position.

As shown earlier, the phase $IrGe_4$ was only formed at temperatures of around 800°C and above. An optical micrograph of a Ge island (2500 Å) on an Ir film (250 Å) annealed at 750°C for 60 minutes (Fig. 3.20) demonstrates what happened at temperatures below 800°C. Indicated in the figure are different regions and areas scanned on the microprobe.

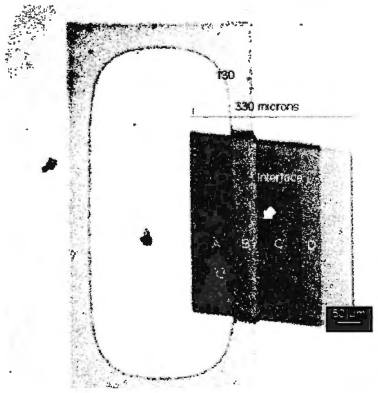

Figure 3.20: Optical micrograph of a Ge island (2500Å) on an Ir film (500Å) annealed at 750°C for 60 minutes.

The RBS data from the scanned area were analyzed and Fig. 3.21 shows the stoichiometric information derived from integrated counts of the Ir and Ge peaks as a function of lateral position. It can be seen that the Ir_3Ge_7 phase stretches through regions B and C right across the original island interface from the middle of the island where it is

overlaid with unreacted Ge. The only difference of this situation from that at 800°C, seen earlier, is the absence of the $IrGe_4$ phase; hence no region of decomposition is observed. This was as expected.

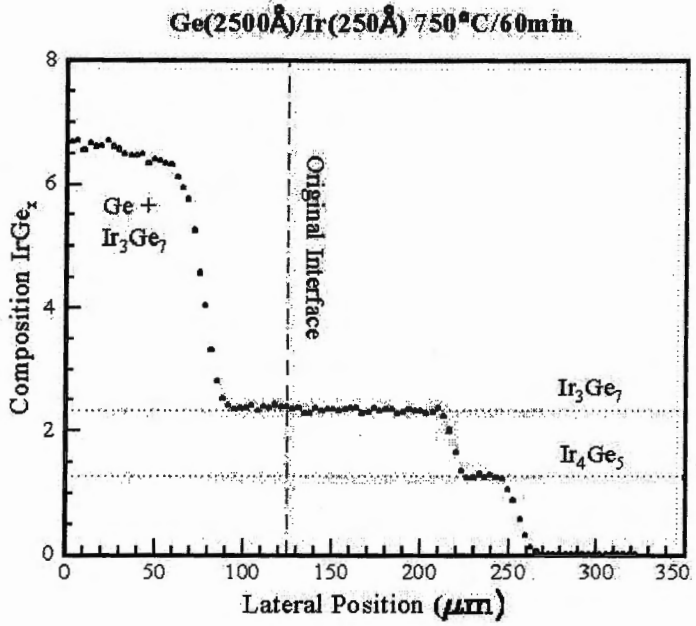

Figure 3.21: Stoichiometric information of a Ge island on an Ir film annealed at 750°C for 60 minutes.

3.3.2 μPIXE Results

No work has yet been reported of an application of PIXE in studying a lateral diffusion system. It was hoped that once PIXE had been established as an alternative to RBS, it could then be employed in studying lateral diffusion systems that exhibit excessive RBS peak overlap. RBS is hardly practical in studying such systems, as will be discussed in Chapter 6.

As described earlier, both RBS and PIXE data were recorded in all scans. Fig. 3.22 shows the combined PIXE spectrum from a uniform rectangular region chosen from the center of the island of the sample annealed at 800°C for 30 minutes.

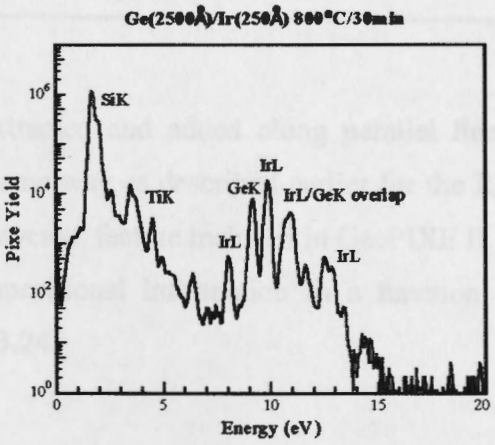

Figure 3.22: Average PIXE spectrum extracted from a region in the center of a Ge island on an Ir film annealed at 800°C for 30 minutes.

The Ge and Ir peaks used in the analysis are indicated in Fig. 3.22. The M lines were not used, as the K and L lines were more prominent and proved to be sufficient for the study.

Fig. 3.23 shows a PIXE map of relative Ge concentration over the scanned area. The color code is identical to that used in the RBS maps of the previous section. The five regions expected are clearly seen in this map. As explained in Chapter 2, obtaining depth information using PIXE was impossible with the present setup. It was therefore not possible to distinguish between the Ir at the surface and that below, and thus a map of surface Ir could not be obtained from the PIXE data.

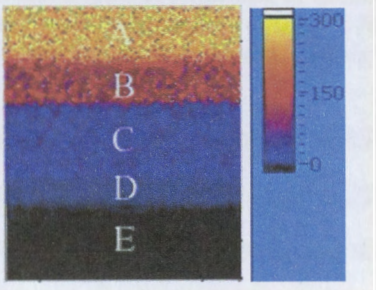

Figure 3.23: PIXE map showing the relative concentration of Ge atoms in the five regions of the scanned area. The color code being as that of the previous section.

The PIXE data were extracted and added along parallel lines aligned with regional interfaces, in much the same way as described earlier for the RBS data. This was made possible by a new 'line traverse' feature included in GeoPIXE II. These spectra were then analyzed to extract compositional information as a function of lateral position. The results are shown in Fig. 3.24.

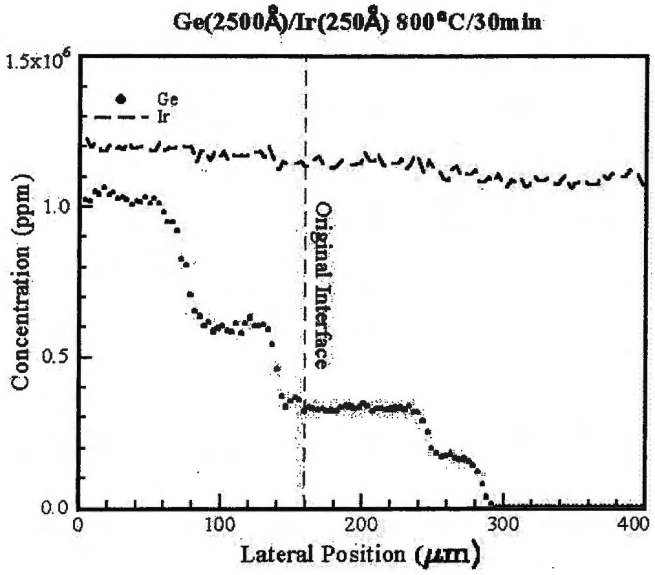

Figure 3.24: PIXE derived Ir and Ge concentration as a function of lateral position for a Ge island on an Ir film annealed at 800°C for 30 minutes. The Ir concentration data have been offset above those of Ge for clarity hence the actual concentration for this species in lower than that shown in ppm.

A comparison of the PIXE results to the corresponding RBS results in Fig. 3.17 shows excellent agreement between the two techniques. PIXE analysis was also carried out on the sample annealed at 750°C for 60 minutes; the results are shown in Fig. 3.25.

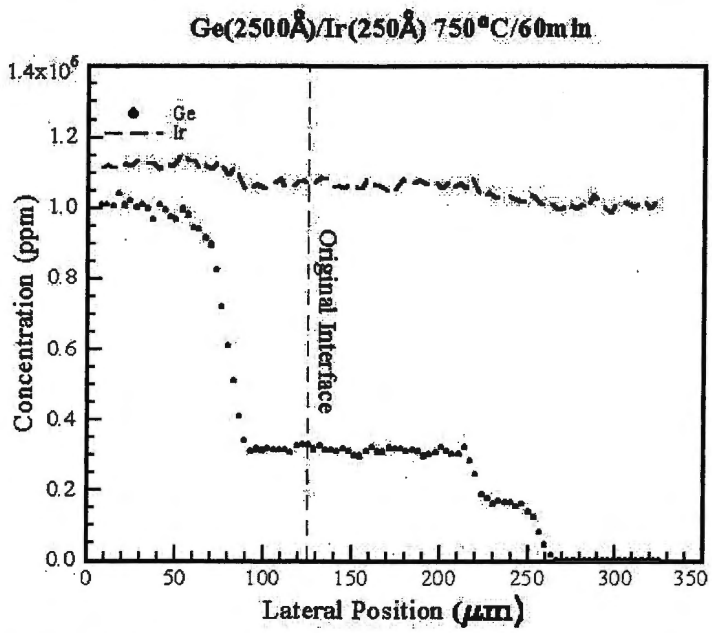

Figure 3.25: PIXE derived Ir and Ge concentration as a function of lateral position for a Ge island on a thin Ir film annealed at 750°C for 60 minutes. The Ir concentration data were raised above those of Ge for clarity hence the actual concentration for this species in lower than that shown in ppm.

The above results clearly demonstrate that μPIXE can indeed be used as an alternative or simply to complement μRBS in the study of lateral diffusion couples.

3.3.3 Scanning Electron Microscopy (SEM) Results

The two representative samples discussed in the previous sections were also analyzed using SEM. An SEM micrograph of the sample with a Ge island on an Ir film annealed at 800°C for 30 minutes is shown in Fig. 3.26. The micrograph was obtained from backscattered electrons. For improved clarity, a color negative of the actual micrograph has been used. The brightness of each region is a consequence of either thickness or composition of the compound or element therein; the different regions observed are labeled A to E. The lateral extent of these regions is in general agreement with that found by RBS and Optical Microscopy; values are presented in Table 3.2.

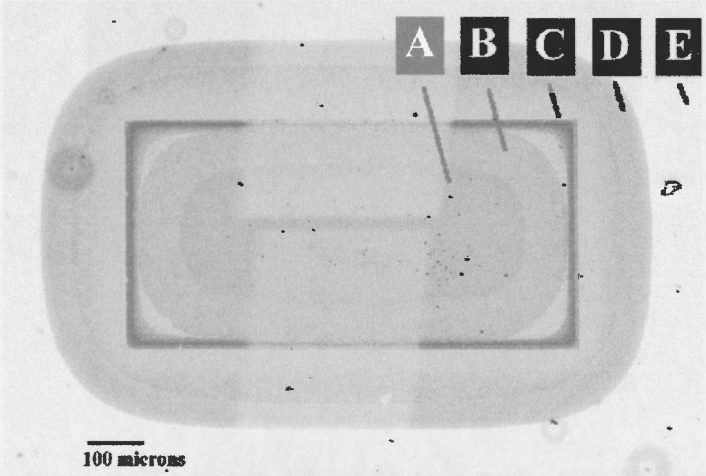

Figure 3.26: SEM micrograph of a Ge island (2500Å) on an Ir film (200Å) annealed at 800°C for 30 minutes showing the whole sample and different regions. A color negative of the micrograph was used for clarity.

Region	Width by RBS (μm)	Width by SEM(μm)	Width by Optical Microscopy (μm)
B	65	63	65
C	105	102	107
D	45	45	46

Table 3.2: Table showing that the number of regions and their lateral extent is in general agreement for the different techniques used.

Fig. 3.27 presents a scan of the regions A to D at higher magnification. The dark region on the far right is region E. We see a narrow band of lower brightness at the interface between regions D and E that supports our earlier observation that some IrGe may have formed in that region. Two other interesting features are observed in this micrograph. The region labeled 'Y' shows a unique texture which suggests a formation mechanism quite different from the ones at play in the regions B and C. The feature labeled 'X' is one of many grains that consistently formed in the middle of the island for all samples annealed at 800°C or above.

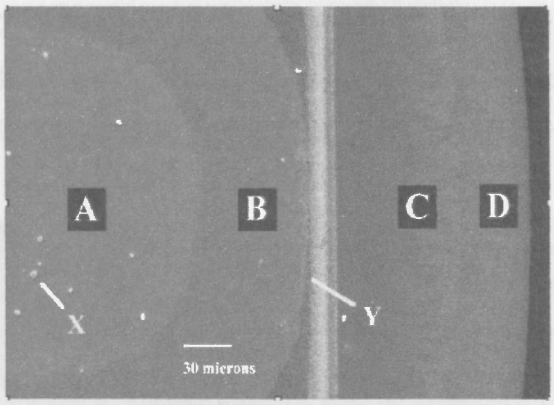

Figure 3.27: SEM micrograph of a Ge island (2500 Å) on an Ir film (500 Å) annealed at 800°C for 30 minutes, showing a close-up scan of the different regions and other features of interest.

The region labeled 'Y' was investigated further at higher magnification as presented in Fig. 3.28. In this figure, the position labeled 'W' was identified as the original island interface. Using results obtained from RBS and PIXE, the position labeled 'V' was identified as the reaction interface for the decomposition of the phase $IrGe_4$ into Ir_3Ge_7. A clear change in texture is seen at this interface. This is a result of both thickness and phase difference. The spots marked 'L' were the result of SEM 'line scans', which will be discussed later.

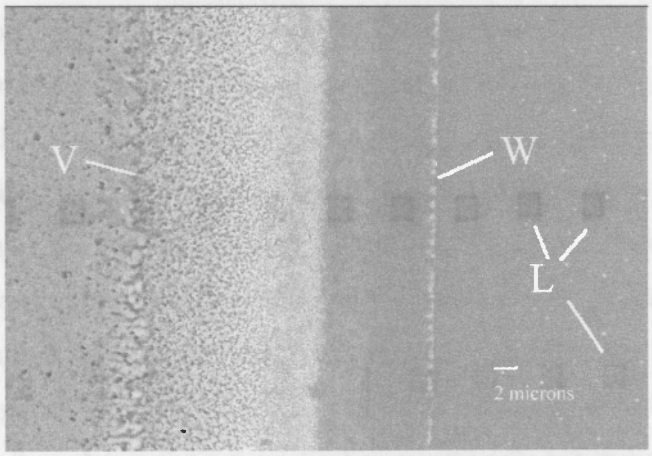

Figure 3.28: Magnified SEM scan of the region labeled 'Y' in Fig. 3.27, the original island interface (W) and a decomposition reaction interface (V).

The grains labeled 'X' in Fig. 3.27 were also viewed at higher magnification. These appeared to be crystals of Ge that formed on the surface of the unreacted Ge in the middle of the island. They are shown in Fig. 3.29.

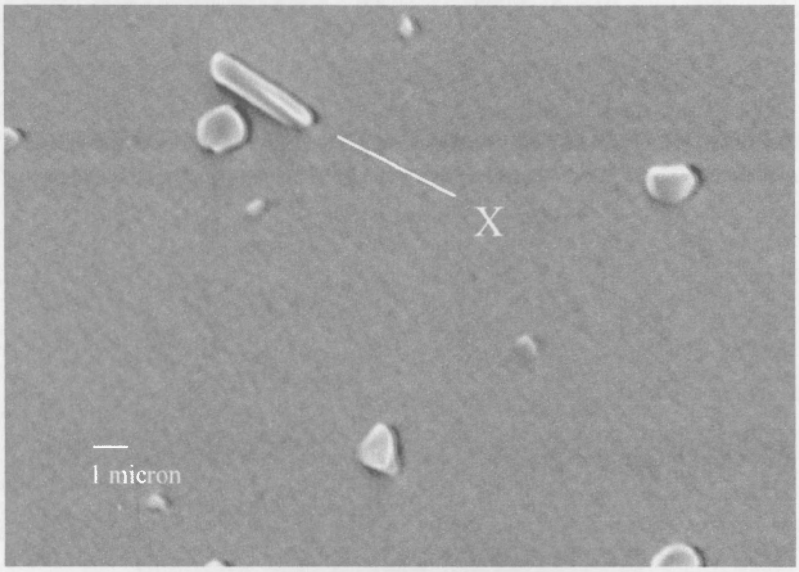

Figure 3.29: Magnified SEM scan of features labeled 'X' in Fig. 3.27. These turned out to be Ge crystals on the surface of unreacted Ge in the middle of the island.

A 'line scan' in SEM uses backscattered electrons to estimate the concentration of different atomic species within a sample as a function of position. The concentrations are estimated over squares of side 2 microns (marked 'L' in Fig. 3.28) and separated by about 5 microns. These spots lay along a straight line, hence the term 'line scan'. This was carried out over the observed region, results of which are given in Fig. 3.30. The line scan path is shown on the left. The top and bottom graphs on the right show the estimated Ge and Ir concentrations as a function of position, respectively. The line scan only gave **relative** concentrations of each element with position. To place the results on a more quantitative footing, points were picked within each region from B to E. The **percentage** concentration was then determined at each of them. Results are indicated in the figure. These percentages do not add up to 100 because the Si and O content was also included, overall.

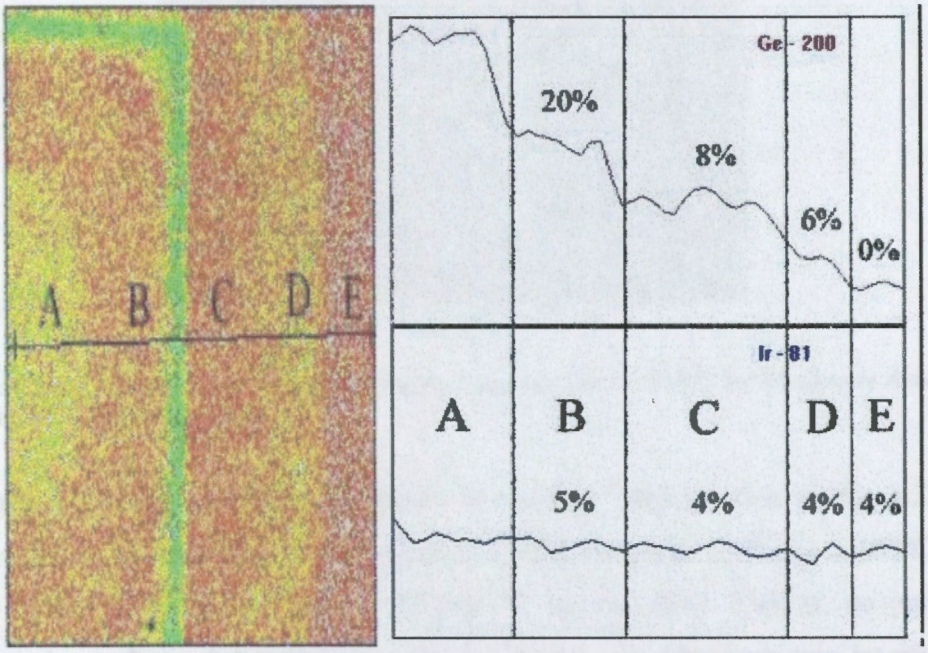

Figure 3.30: An SEM line scan giving an estimate of the concentration of different atomic species, as a function of position. The path of the line scan is show on the left. The top and bottom graphs, on the right show the estimated Ge and Ir concentrations as a function of position.

The ratios of these percentages give an estimate of the compound composition within each region. Close agreement with expected results is obtained, i.e., the regions B, C and D consisting of phases $IrGe_4$, Ir_3Ge_7 and Ir_4Ge_5 are expected to yield concentration ratios of Ir to Ge of 1:4, 1:2.3 and 1:1.25 respectively, while the ratios obtained were 1:4, 1:2 and 1:1.5 respectively.

The sample of a Ge island (2500Å) on an Ir film (250Å) annealed at 750°C for 60 minutes was also analyzed with SEM. Fig. 3.31 shows a micrograph of this sample.

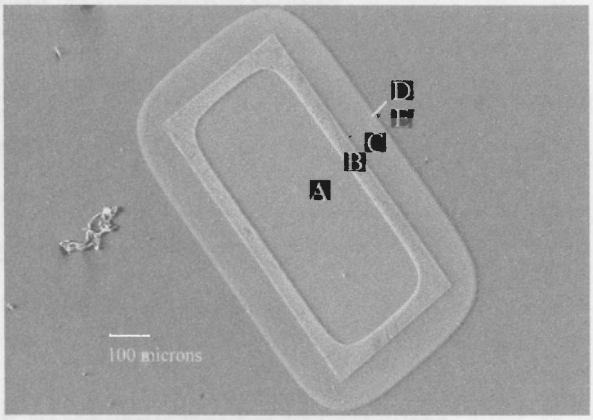

Figure 3.31: SEM micrograph of a Ge island on an Ir film annealed at 750°C for 60 minutes showing the whole sample and different regions.

Five regions are seen and these are shown at a higher magnification in Fig. 3.32. One sees that the main difference in the results at 750°C compared to those at 800°C is the absence of the two features marked 'X' and 'Y' in Fig. 3.27. That is, no grains are formed at the surface of the unreacted Ge and there is no decomposition interface just inside the original island interface. The number and lateral extent of the observed phase is in agreement with the results of the previous sections. The micrographs seem to show variation in height over the different regions, but one is unable to make any firm conclusion as it is difficult to distinguish between compositional difference and thickness variation. Further analysis by the use of AFM proved helpful in this regard.

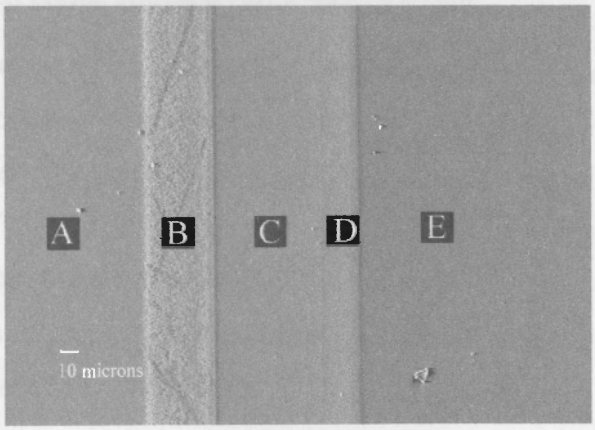

Figure 3.32: SEM micrograph of a thick Ge island on a thin Ir film annealed at 750°C for 30 minutes showing a close-up scan of different regions.

The regions B and C appear different but are known to consist of the same phase, Ir_3Ge_7, the difference between the two being that C originated from growth outside the original island region by outward diffusing Ge interacting with Ir_4Ge_5, while B was a result of exposure of the phase inside the island region following consumption of the overlaying Ge. This may explain the different appearance.

3.3.4 Atomic Force Microscopy (AFM) Results

Sample surfaces analyzed by RBS, SEM and Optical Microscopy were also scanned with an Atomic Force Microscope to obtain information of the relative surface heights as a function of lateral position. The maximum lateral distance that could be covered in a single scan was 100 μm and therefore to cover all reactions zones, various regions had to be scanned separately. The sample of the Ge island on an Ir film annealed at 800°C for 30 minutes was scanned over three different regions. Figs. 3.33 to 3.35 show the results of these scans. The top picture in Fig. 3.33 shows an SEM micrograph with lines indicating the location of the scans. The middle graph gives results of the AFM scan. The vertical axis gives relative surface height in nanometres, while the horizontal axis gives the corresponding lateral distance. It should be noted that the vertical scales and positions set as origins vary between figures. The table at the bottom of each figure gives the lateral distance between marked points and their difference in height.

The AFM results give us more detail than the corresponding RBS results shown in Fig. 3.19. Steps are observed from one region to another. We see in Fig 3.33 that as we move from the middle of the island (region A) to the region of the exposed $IrGe_4$ (region B), the overlaying thickness of unreacted Ge does not fall as sharply as suggested by the RBS results. This indicates that the central island of unreacted Ge is not only consumed from the edges but also from further inside. This was also observed from the RBS results in Fig.3.19, although in a less pronounced manner.

An approximately 40 nm high ridge is seen at the interface of regions B and C. This was probably the feature labeled 'V' in the SEM micrograph of Fig. 3.28. It lies at the reaction interface at which $IrGe_4$ decomposes into Ir_3Ge_7 and Ge, suggesting a slight

accumulation of material at this point. This feature could also be seen in the RBS results of Fig 3.19.

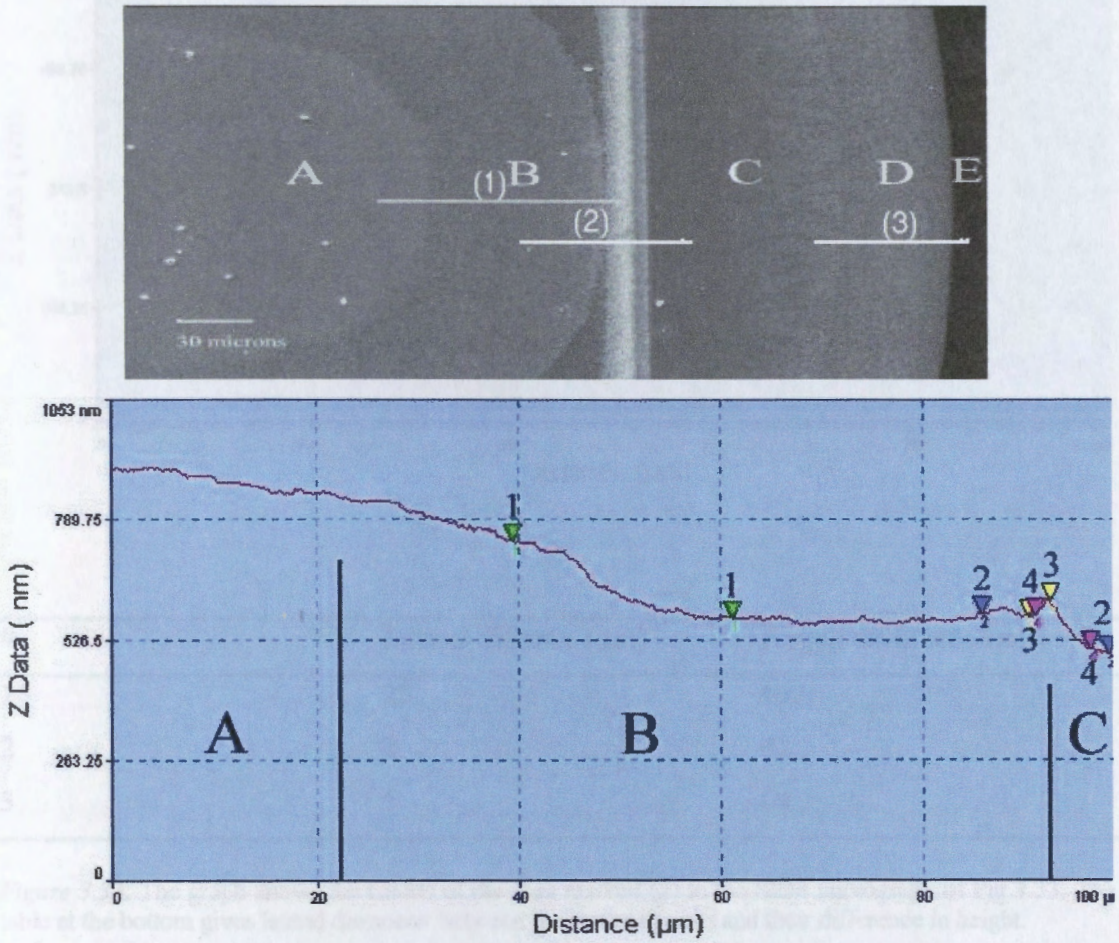

#	Lateral distance (µm)	Height difference (nm)
1	22	169
2	13	89
3	2	37
4	5	74

Figure 3.33: SEM micrograph with lines indicating the location of AFM scans. The middle graph gives results of the scan labeled (1). The table at the bottom gives lateral distances between the marked points and their difference in height.

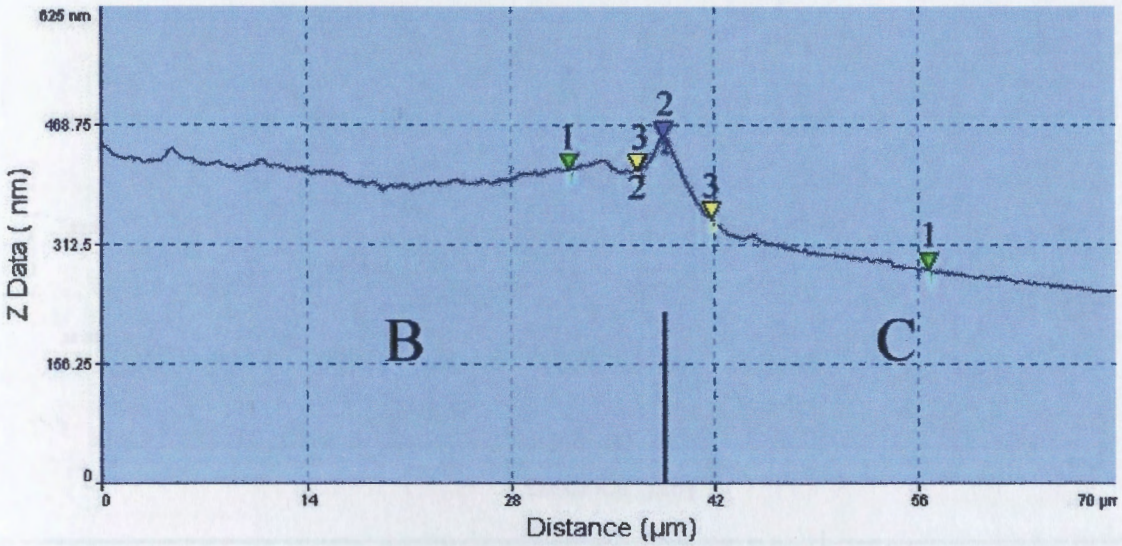

#	Lateral distance (µm)	Height difference (nm)
1	25	132
2	2	41
3	5	64

Figure 3.34: The graph shows the results of the scan marked (2) in the SEM micrograph of Fig.3.33. The table at the bottom gives lateral distances between the marked points and their difference in height.

Fig. 3.34 shows a graph of the results of the scan marked (2) in the SEM micrograph of Fig.3.33. The table at the bottom gives lateral distances between the marked points and the height differences. This scan was made to study the ridge marked with a 2 on the graph. Fig. 3.35 shows the results of the scan marked (3) in the SEM micrograph of Fig.3.33.

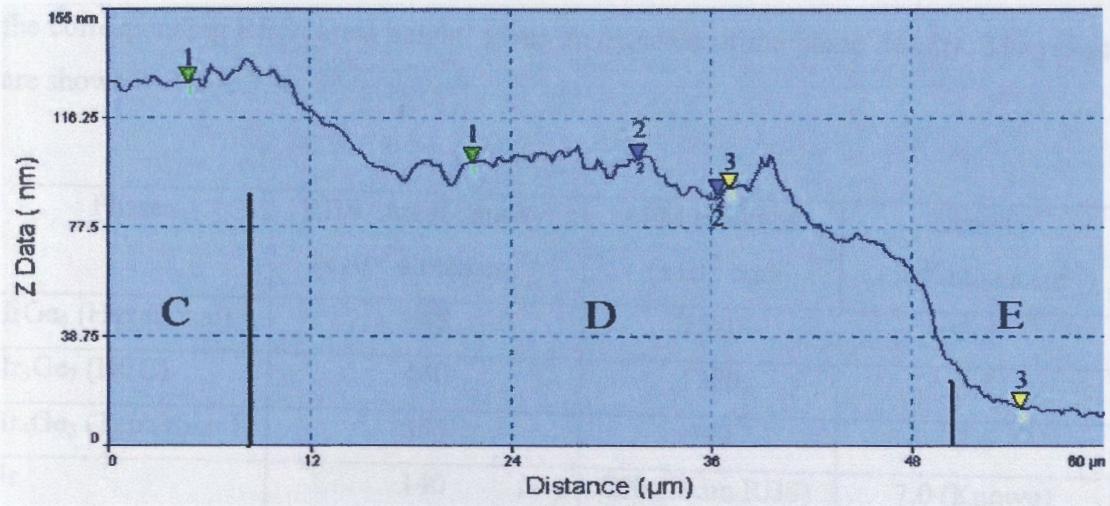

#	Lateral distance (µm)	Height difference (nm)
1	17	28
2	5	12
3	17	78

Figure 3.35: The graph shows the results of the scan marked (3) in the SEM micrograph of Fig.3.33. The table at the bottom gives lateral distances between the marked points and their difference in height.

A step is seen at the interface between regions D and E in Fig. 3.35. This supports the RBS and SEM observation of possible IrGe formation in this region. Comparing the part of the AFM scan that passes over region C in Fig. 3.34 and that in Fig. 3.35 for the same region, it may seem that the latter reveals more surface variation. This is however a result of the difference in scales of the vertical axis; the two figures actually show similar results for region C.

The average areal density of the unreacted Ir film, from the RBS results shown in Fig. 3.19, is found to be 140×10^{15} atms.cm^{-2}. The density of Ir is 7.0×10^{22} atms.cm^{-3}, which when divided into the areal density gives the thickness of unreacted Ir as 200×10^{-8} cm. By adding the appropriate step heights from AFM results in Figs. 3.33 - 3.35 to this base thickness, the thickness of each region was worked out. This thickness when divided into

the corresponding RBS 'areal height' gives an estimate of the phase density. The results are shown in Table 3.3.

Phase	RBS 'Areal density' ($x10^{15}$ atoms.cm^{-2})	AFM thickness ($x10^{-8}$ cm)	Density ($x10^{22}$ atoms.cm^{-3})
$IrGe_4$ (Hexagonal)	645	2580	2.5
Ir_3Ge_7 (BCC)	440	1260	3.5
Ir_4Ge_5 (Tetragonal)	355	980	3.6
Ir	140	200 (From RBS)	7.0 (Known)

Table 3.3: Approximate height of the steps between different phase regions as obtained from RBS and AFM. A density estimate is also given.

3.4 Analysis and Discussion

Our thin film measurements showed that the first two phases to form are IrGe and Ir_4Ge_5. These were found to co-exist, in agreement with the bulk diffusion couple results of Bhan and Schubert.[58] Observation of the separate formation of either compound as a first phase could not be achieved.

An EHF diagram of the system was drawn and is shown in Fig. 3.36. It is seen that the phases IrGe and Ir_4Ge_5 have higher EHF than the other two phases for an Ir concentration greater than 36%. In order for the EHF model to correctly predict Ir_4Ge_5 or IrGe as the first phase to form, the liquidus minimum would have to lie at an Ir concentration greater than 36%. Bhan and Schubert[58] observed a eutectic structure at 60% Ir, which they reported to be probably between Ir and IrGe. At 60% Ir the difference between the EHF values of IrGe and Ir_4Ge_5 is significant, therefore according to the EHF model we would not expect these phases to co-exist if the liquidus minimum were at this position but rather if it was around 48%. This EHF diagram was however drawn purely from theoretical calculations based on the Miedema semi-imperical model and could therefore be adjusted by incorporating experimental data.

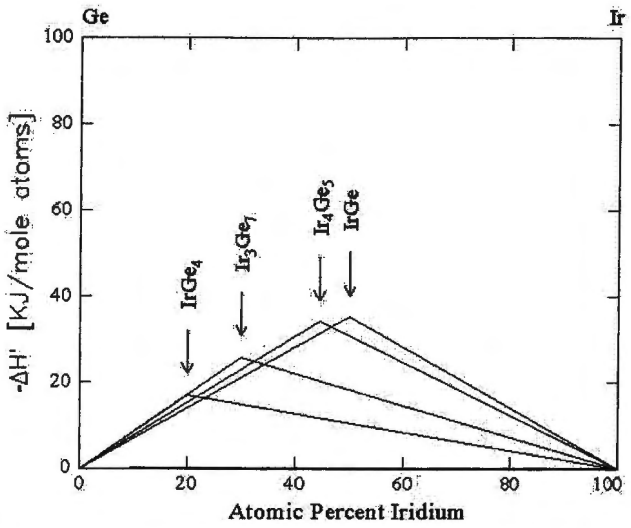

Figure 3.36: An EHF diagram, of the Ir – Ge system, drawn using the Miedema semi imperical model.

The phase Ir_3Ge_7 was observed to form after the first two phases. At 800°C the phase $IrGe_4$ was observed to nucleate. Bhan and Schubert reported that the phase Ir_3Ge_7 seemed to be in equilibrium with $IrGe_4$. From our results it was seen that these two phases were present but could hardly be said to be in equilibrium as the nucleation controlled reaction forming $IrGe_4$ took place very rapidly.

By observing the movement of a 12Å Ti marker, the direction of atomic mobility was monitored during the formation of the first two germanide phases of iridium. From the results of Fig. 3.9, which are depicted in Fig. 3.37, a conclusion can be drawn if certain assumptions are made. Firstly, if IrGe was the first phase to form, then Ge would be the sole moving species for both IrGe and Ir_4Ge_5 formation. This is so because had Ir been the moving species during either IrGe or Ir_4Ge_5 formation, it would have been observed to diffuse across the marker, which was not the case. Secondly, if Ir_4Ge_5 was the first phase to form, then all we can be sure of is that Ge was the sole moving species during Ir_4Ge_5 formation. During IrGe formation there would be no discernable indicator as to which species was moving, the marker being at the interface between Ir_4Ge_5 and Ge. The only firm conclusion we can draw from the marker results is that Ge was the sole diffusing species during Ir_4Ge_5 formation.

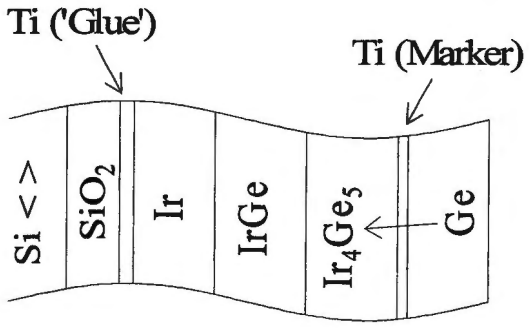

Figure 3.37: Depiction of marker results in the Ir-Ge system indicating the flow of Ge atoms as the sole moving species.

Lateral diffusion couples provide a pointer to the dominant diffusing species without the need to interpose a marker between coupling layers. Results of the samples with a thick Ir island on thin Ge films showed that the inward diffusion of Ge was much higher than any outward diffusion of Ir. This led to the formation of a Ge depletion layer around the edge of the island, which halted the reaction. In the reverse configuration with a thick Ge island on thin Ir films the reaction proceeded, therefore one can safely say that Ge was the diffusing species.

A schematic diagram of the different phase regions observed at 800°C with various parameters used to characterize growth kinetics is shown below. The subscripts α, β and γ refer to the phases $IrGe_4$, Ir_3Ge_7 and Ir_4Ge_5 respectively.

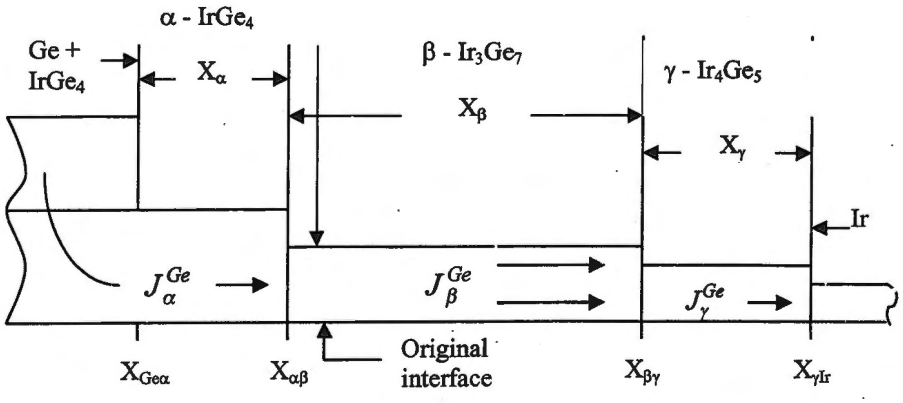

Figure 3.38: Diagram showing different phase regions and the various parameters used to characterize growth kinetic.

Widths of the respective phase regions will be represented by X_α, X_β and X_γ. Reaction interfaces between the different phases are $X_{\alpha\beta}$, $X_{\beta\gamma}$ and $X_{\gamma Ir}$ respectively, as shown in Fig. 3.38. Table 3.4 gives equations of the reactions that take place at each interface and the corresponding heats of reaction, calculated using the Miedema Approximation. Components of the calculations are shown beneath each equation. The heat of reaction of $IrGe_4$ decomposition into Ir_3Ge_7 and Ge is found to be approximately equal to zero. It is generally accepted that a nucleation controlled reaction is characterized by a heat of reaction close to zero. This suggests that $IrGe_4$, created by the reverse reaction, forms through a nucleation process and explains its sudden formation at high temperature.

Interface	Equation of Reaction	Heat of Reaction ΔH_R° (kJ $mol^{-1}atm^{-1}$)
$X_{\alpha\beta}$	$3IrGe_4 \rightarrow Ir_3Ge_7 + 5Ge$ $3x5(-17.2) \quad 10(-26.0) \quad 5(0)$	$\cong 0$
$X_{\beta\gamma}$	$13Ge + 3Ir_4Ge_5 \rightarrow 4Ir_3Ge_7$ $13(0) \quad 3x9(-34.3) \quad 4x10(-26.0)$	-2.9
$X_{\gamma Ir}$	$5Ge + 4Ir \rightarrow Ir_4Ge_5$ $5(0) \quad 4(0) \quad 9(-34.3)$	-34.3

Table 3.4: Equations of the reactions that take place at each interface and the corresponding heat of reaction, calculated using the Miedema Approximation. Components of the calculations are shown beneath each equation. The values in the table are per atom i.e. the total heats of formation for molecules are divided by the number of atoms in the molecule.

Atoms from the unreacted source of Ge in the middle of the island diffuse through the $IrGe_4$ with an atomic flux J_α^{Ge} towards the $X_{\alpha\beta}$ interface. Ge atoms from the decomposition reaction at this interface are added to this flux, resulting in J_β^{Ge} flowing through the phase Ir_3Ge_7. This flux 'feeds' the reaction at the $X_{\beta\gamma}$ interface were Ir_4Ge_5 is transformed into Ir_3Ge_7. As can be seen in Table 3.4, the reaction at $X_{\beta\gamma}$ consumes Ge thereby reducing the atomic flux from J_β^{Ge} to J_γ^{Ge}, which flows through the Ir_4Ge_5 phase. All of the latter atomic flux is consumed in extending the Ir_4Ge_5 phase at interface

$X_{\gamma Ir}$. The reaction at this interface has a highly negative heat of reaction as seen in Table 3.4.

The growth in this system was well defined with distinct interfaces between different phases. This allowed for accurate measurement of the growth widths. Optical microscopy and SEM were primarily used for this. The other techniques discussed were useful in the verification of results for selected samples. The growth of the phases Ir_3Ge_7 and Ir_4Ge_5 was monitored at the temperatures 700°C, 750°C and 800°C. Different annealing times were chosen to obtain a reasonable range of growth widths at each of the three temperatures. Results of the measurements are presented in Figs. 3.39, 3.40 and 3.41. The graph on the left of each figure is a plot of the reaction length with time of anneal, while that on the right is a similar plot with the reaction length squared. It must be emphasized that in Figs. 3.39 and 3.40 the growth curves for the regions labeled as Ir_3Ge_7 are a result of growth resulting from two different processes. The first is the Ir_3Ge_7 grown from Ir_4Ge_5 and the second is that exposed when Ge diffuses away from the island.

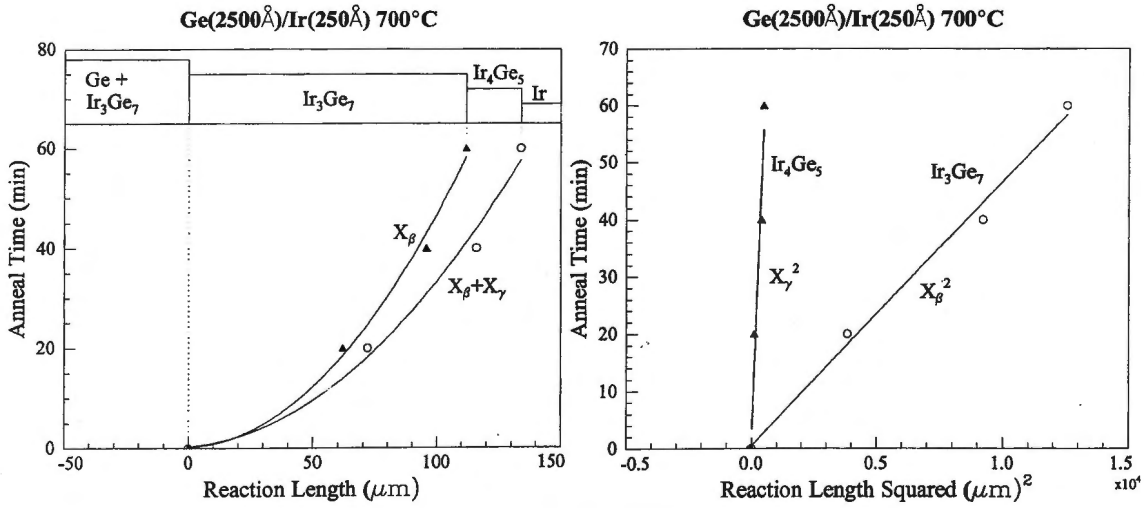

Figure 3.39: Plot of reaction length with time of anneal (left) and reaction length squared with time (right), for the phases Ir_3Ge_7 and Ir_4Ge_5.

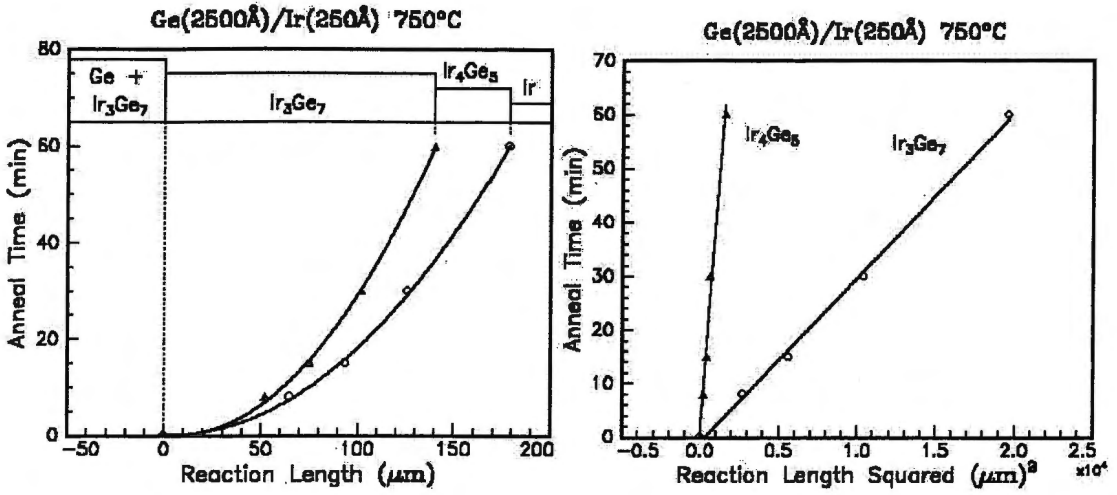

Figure 3.40: Plot of reaction length with time of anneal (left) and reaction length squared with time (right), for the phases Ir_3Ge_7 and Ir_4Ge_5.

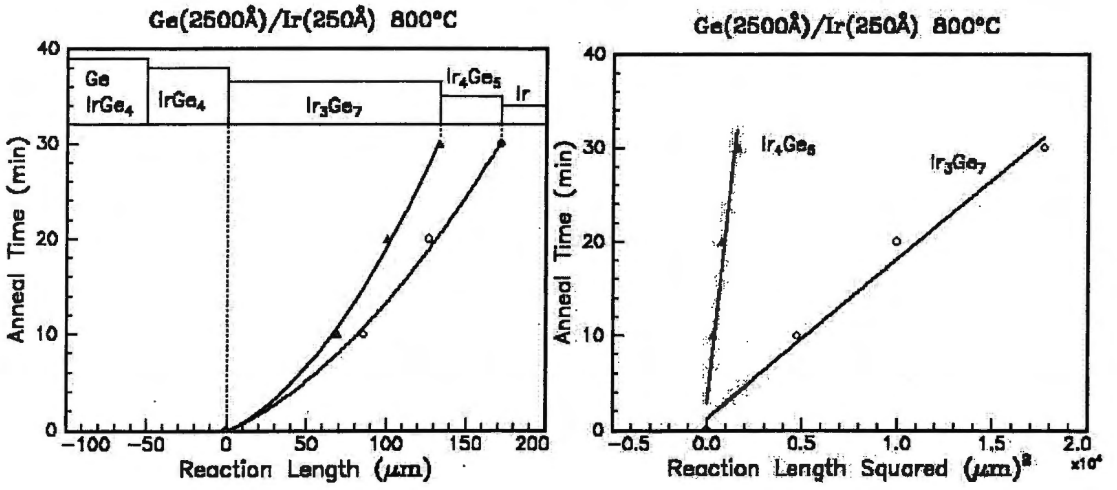

Figure 3.41: Plot of reaction length with time of anneal (left) and reaction length squared with time (right), for the phases Ir_3Ge_7 and Ir_4Ge_5.

The growth characteristics observed are parabolic with time. This is indicative of a diffusion controlled process which, as modeled by Kidson,[63] results in parabolic growth even in multi-phase systems. We do not observe the transition from interface reaction limited to the diffusion limited regime, as will be discussed further in Chapter 7.

The logarithm of the diffusional growth constant, $K_\beta = X_\beta^2 / t$ was plotted against the reciprocal of the product, k_bT of the Boltzmann constant and the absolute temperature, this Arrhenius plot for the phase Ir_4Ge_5 is shown in Fig 3.42.

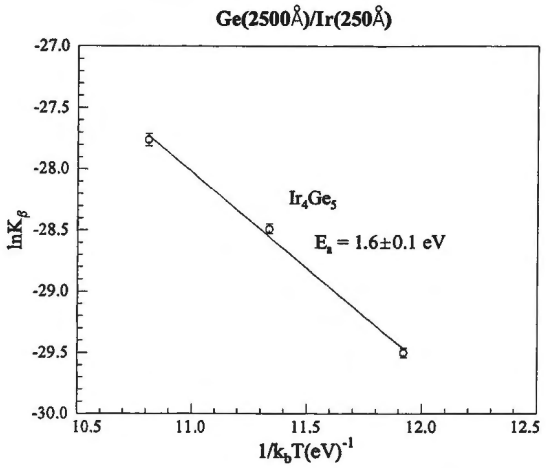

Figure 3.42: Arrhenius plot, lnK_β versus $1/k_bT$, showing temperature dependence of Ge diffusion rate through Ir_4Ge_5, yielding an average activation energy of 1.6 ± 0.1 eV. The diffusivities K_β are reciprocals of the slopes obtained from the plots in Figs. 3.39 to 3.41.

It must be mentioned that the right hand side plots in Figs. 3.39 to 3.41 (of reaction length squared with time) would normally be drawn with the time axis placed horizontally and the length axis vertically, in which case the diffusional growth constants, K_β, would be equal to the slopes. In our case the length is placed on the horizontal axis for easy comparison with the left hand side plots (of reaction length with time), hence the constants K_β are reciprocals of the slopes. The average activation energy determined for the diffusion process in the Ir_4Ge_5 phase was E_a = 1.6±0.1 eV. The magnitude of E_a suggests that the lateral diffusion reaction was not driven by surface diffusion of Ge atoms but rather the diffusion of Ge atoms through the interior of the lateral diffusion couple. Typical values for surface diffusion are around 0.6 eV. [64]

As seen earlier, the phase $IrGe_4$ only formed at and above 800°C. This phase was observed to decompose, forming Ir_3Ge_7. It is tempting to use the results of Fig. 3.41 together with those of Figs. 3.39 and 3.40 (the only two results obtained below 800°C for this particular group of samples) to obtain a value of the activation energy for the Ir_3Ge_7

phase. Unfortunately this could not be done because the mechanisms at play during Ir_3Ge_7 growth were not the same at 800°C as at temperatures below. At 800°C the Ir_3Ge_7 observed inside the island region was from the decomposition of $IrGe_4$ while that outside was formed by the interaction between Ir_4Ge_5 and the outward diffusing Ge atoms. Below 800°C the Ir_3Ge_7 outside was also formed by the interaction of Ge and Ir_4Ge_5 but that inside was observed as a result of exposure as Ge was consumed from the source region. On the other hand, Ir_4Ge_5 was formed by the interaction of Ge with the unreacted Ir film, both below and above 800°C and thus at all three temperatures.

Considering the growth depicted by Fig. 3.38, the system can be characterized by chemical inter-diffusion coefficients $\tilde{D}_\beta$ and $\tilde{D}_\gamma$ in the Ir_3Ge_7 and Ir_4Ge_5 regions respectively. The corresponding equilibrium values of the Ge concentration drop over the two regions are then represented by ΔC_β^{eq} and ΔC_γ^{eq} respectively. Since we have diffusion-controlled growth across both regions, if the theory of Gösele and Tu is assumed to hold, the ratio of the Ge atomic fluxes through the regions, $r = J_\beta^{Ge} / J_\gamma^{Ge}$ should be inversely proportional to the corresponding width ratio i.e., $r \propto X_\gamma / X_\beta$. This result follows from equation 1.40 of section 1.4.1, the growth should therefore be described by Fig. 1.9. Although equation 1.40 was derived for conventional thin film couples, a geometrical modification to correct for the additional weighted difference between the atomic fluxes in lateral diffusion couples only introduces a constant thickness ratio $r \propto z_\gamma / z_\beta$ into the expression and hence does not affect the inverse proportionality of the width ratio $r \propto x_\gamma / x_\beta$ to the flux ratio $r = J_\beta^{Ge} / J_\gamma^{Ge}$. Table 3.5 gives the values of the width ratios as a function of the annealing time at various temperatures.

TEMP [T (°C)]	TIME [t (min)]	WIDTH OF Ir_3Ge_7 [X_β (μm)]	WIDTH OF Ir_4Ge_5 [X_γ (μm)]	RATIO X_γ/X_β
700	20	62	10	0.16
	40	96	20	0.21
	60	112	22	0.20
750	8	52	13	0.25
	15	75	19	0.25
	30	102	24	0.24
	60	140	39	0.28
800	10	69	17	0.25
	20	100	27	0.27
	30	133	39	0.29

Table 3.5 Values of the width ratios for the phases Ir_3Ge_7 and Ir_4Ge_5 as a function of the annealing time at various temperatures.

The results show that the diffusion system acquired an approximately constant flux ratio indicating that the annealing periods were sufficiently long so that it became self-regulating. This constant flux ratio is labeled as r^{eq} in Fig. 1.9 of Chapter 1. Referring to that figure, it is clear that the growth in the present system lies in the region $r_1<r<r_2$ since neither the Ir_3Ge_7 nor the Ir_4Ge_5 phase is observed to shrinks during the diffusion process.

As explained in Chapter 1, in a multiphase system the geometrically modified equations of the Gösele and Tu model give the growth rate as a function of the weighted difference between the atomic fluxes in adjacent phases. The weighting consists of factors that contain compositional and geometric terms. In our case the growth is diffusion limited, interfacial reaction barriers appeared not to play a limiting role indicating that we have relatively fast reactions at the interfaces i.e., κ_β^{eff} and $\kappa_\gamma^{eff} \rightarrow \infty$. We can therefore eliminate the interfacial reaction contribution to the diffusion flux expression of equation 1.30. By fitting the experimental data to algebraic functions which were then substituted into the coupled differential equations 1.47 and 1.48, solutions were obtained for the products, $\Delta C_\beta^{eq} \tilde{D}_\beta$ of the chemical inter-diffusion coefficients and equilibrium values of the Ge concentration difference across the phases.

Neither RBS nor PIXE were found adequate for determining the concentration profiles of Ge atoms across each region to obtain accurate values of ΔC_β^{eq} and ΔC_γ^{eq}, this is

discussed further in Chapter 7. If we assume that ΔC_{β}^{eq} and ΔC_{γ}^{eq} are time-independent as assumed in equation 1.14, a plot of $\ln(\Delta C_{\beta}^{eq}\tilde{D}_{\beta})$ by $1/k_bT$ should yield the activation energy of the growth process since $\tilde{D}_{\beta}$ obeys an Arrhenius type relationship with the absolute temperature.

The growth depicted by Fig 3.38 can be treated as being that of a two phase growth regime. Table 3.6 gives the parameters that are relevant to the geometrically modified Gösele and Tu model that result from such a treatment.

A	$A_{\beta}B$	$A_{\gamma}B$	B
Ge	Ir_3Ge_7	Ir_4Ge_5	Ir
	β=7/3	γ=5/4	
	$z_{\beta}=4.39\times10^{17}$ atoms/cm^2	$z_{\gamma}=3.55\times10^{17}$ atoms/cm^2	

Table 3.6: Parameters that are relevant to the geometrically modified Gösele and Tu calculation for the phases Ir_3Ge_7 and Ir_4Ge_5.

The values of z_{β} and z_{γ} were obtained using RBS.

The quantities G_{β} and G_{γ}, which contain compositional and volumetric information are,

$$G_{\beta} = \Omega_0 \frac{(1+\beta)(1+\gamma)}{\beta-\gamma} = 6.92\Omega_0,$$

and (4.1)

$$G_{\gamma} = \Omega_0(1+\gamma)\left[\frac{1+Ir}{\gamma-Ir}+\frac{z_{\gamma}(1+\beta)}{z_{\beta}(\beta-Ir)}\right] = 4.39\Omega_0$$

The value used for the atomic volume Ω_0 was 16×10^{-24} cm^3/at.[32] Table 3.7 shows the values of $\Delta C_{\gamma}^{eq}\tilde{D}_{\gamma}$ obtained from the calculations at each temperature.

T (°C)	$\Delta C_\gamma^{eq}\tilde{D}_\gamma$ $(10^{15} m^{-1}s^{-1})$
700	18.4
750	36.6
800	70.4

Table 3.7: Values of $\Delta C_\gamma^{eq}\tilde{D}_\gamma$ obtained from the modified Gösele and Tu calculation at each annealing temperature.

Letting $\chi = \Delta C_\gamma^{eq}\tilde{D}_\gamma$, the logarithm of χ was plotted against the reciprocal of the product, k_bT of the Boltzmann constant and the absolute temperature, this Arrhenius plot for the phase Ir_4Ge_5 is shown in Fig. 3.43.

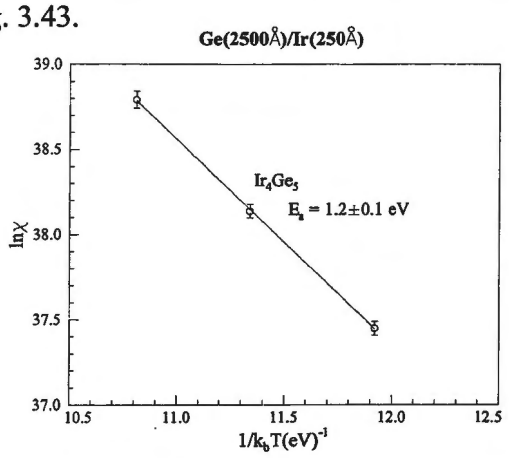

Figure 3.43: Arrhenius plot, $ln\chi$ versus $1/k_bT$, showing temperature dependence of Ge diffusion rate through Ir_4Ge_5, yielding an activation energy of 1.2 ± 0.1 eV. The quantity χ is the product, $\Delta C_\beta^{eq}\tilde{D}_\beta$ of the chemical inter-diffusion coefficients and equilibrium values of the Ge concentration difference across the phase.

The results of Fig. 3.43 from the modified Gösele and Tu calculations show tolerable agreement with the ones obtained from an Arrhenius plot of lnK_β versus $1/k_bT$ shown in Fig. 3.42. These results and the ones given in Table 3.5 showing the self-regulation of the diffusion system with regard to the flux ratio between phases verify that the Gösele and Tu model can be applied to our data.

The overall lateral diffusion results are largely summed up by considering the case of a Ge island on an Ir film annealed at 800°C. Upon annealing, interaction took place in the source region between Ge and Ir atoms in the underlying thin film, resulting in the formation of the most Ge rich phase, $IrGe_4$. This interaction continued until the underlying Ir atoms were consumed. Ge atoms were still in excess at this stage and started diffusing out of the island to form the phases Ir_3Ge_7 and Ir_4Ge_5.

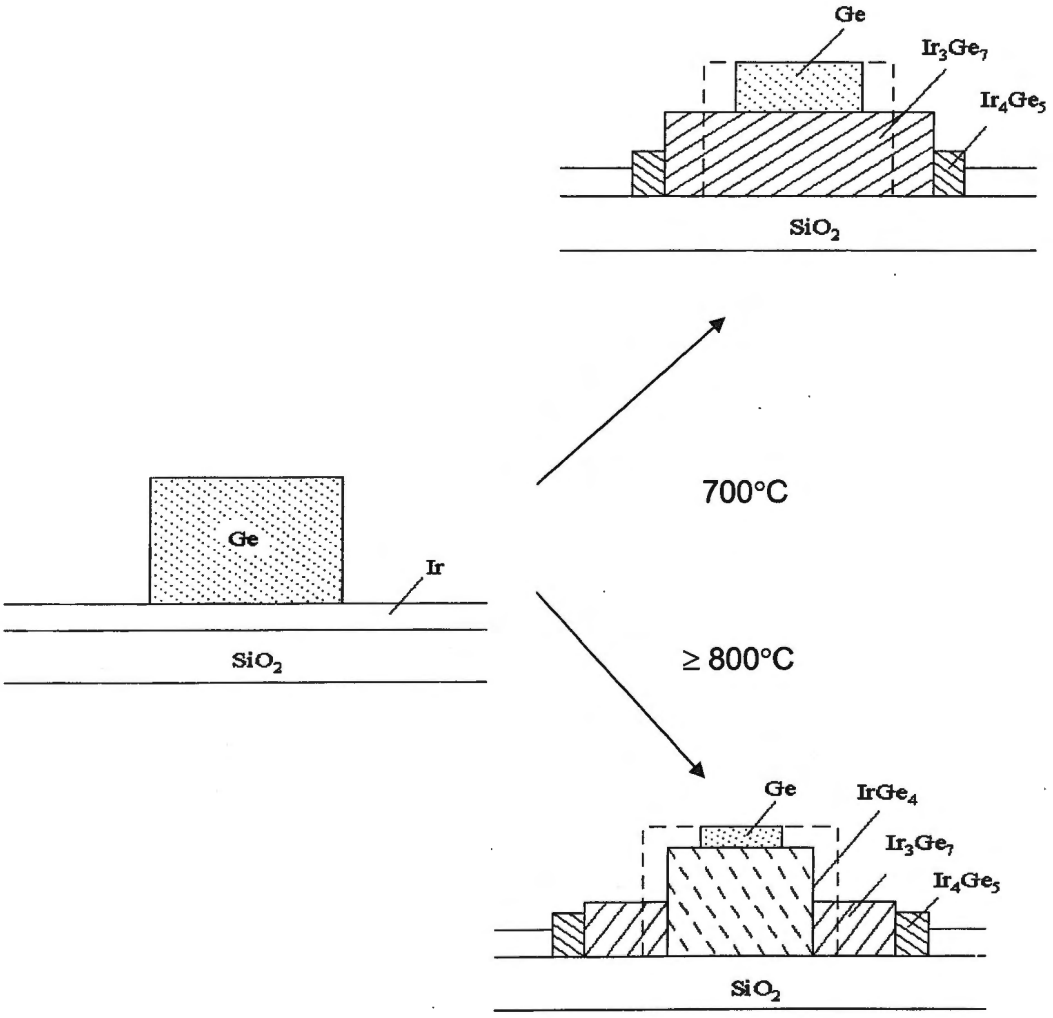

Figure 3.44: Schematic presentation Ir-Ge interaction in lateral diffusion couples. The situation below 800°C differs only by the absence of the $IrGe_4$ phase (layer thicknesses are not to scale).

There was evidence of a narrow region of IrGe from RBS, SEM and AFM results, as seen in the Figures: 3.19 3.27 and 3.35 respectively. This was at the periphery of the reaction region and was not easily resolvable in most cases as it seemed overwhelmed by the Ir_4Ge_5 formation.

The consumption of Ge atoms from the source region gradually exposed the $IrGe_4$. This phase started to decompose through the mechanism $3IrGe_4 \rightarrow Ir_3Ge_7 + 5Ge$. This then complemented the Ge supply to reaction interfaces farther out. The depletion of unreacted Ge atoms from the source region continued in parallel with the $IrGe_4$ decomposition. A gradual increase in the width of exposed $IrGe_4$ indicated that the latter process was slower. The width of the phase Ir_3Ge_7 was controlled by two processes: firstly, by the $IrGe_4$ decomposition at the interface with $IrGe_4$ and secondly, the mechanism $13Ge + 3Ir_4Ge_5 \rightarrow 4Ir_3Ge_7$ at the interface with Ir_4Ge_5. On the other hand, the phase Ir_4Ge_5 was effected by two competing processes. The first resulted in the consumption of Ir_4Ge_5 and the second was the mechanism $5Ge + 4Ir \rightarrow Ir_4Ge_5$ at its far interface. The latter was the faster of the two since it increased the width of the region while the former tended to decrease it and there was overall increase observed. The picture for samples annealed at temperatures below 800°C differed only by the absence of the $IrGe_4$, phase as shown in Fig. 3.44.

CHAPTER 4

THE PLATINUM – GERMANIUM SYSTEM

4.1 Introduction

The Pt – Ge system has 6 equilibrium phases, viz., Pt_3Ge, Pt_2Ge, Pt_3Ge_2, PtGe, Pt_2Ge_3 and $PtGe_2$. A phase diagram for the system is displayed in Fig. 4.1. While this system has been investigated before, reported results reveal existing uncertainty regarding phases observed and their formation temperatures.[30,65-68] Marshall et al.[65,66] reported observing Pt_2Ge at 250°C, followed by PtGe between 260-300°C. Pt_2Ge_3 was observed at 400°C and the last detected phase was $PtGe_2$ in the temperature range 500-600°C. In another experiment, Hsieh and Chen[67] detected Pt_2Ge, PtGe, Pt_2Ge_3 and $PtGe_2$ at temperatures of 160, 250, 350 and 400°C respectively. Grimaldi et al.[68] observed Pt_3Ge_2, PtGe, Pt_2Ge_3 and $PtGe_2$ at 250, 300, 350 and 450°C respectively. In later work, Nemutudi et al.[30] inferred from their results that this system had a tendency to skip its non-congruent phases Pt_3Ge_2 and Pt_2Ge_3 in thin films. Phases observed were Pt_2Ge, PtGe and $PtGe_2$, in that sequence. The initial reaction was detected at around 200°C. The latter researchers studied both the conventional thin film and lateral diffusion regimes of this system.

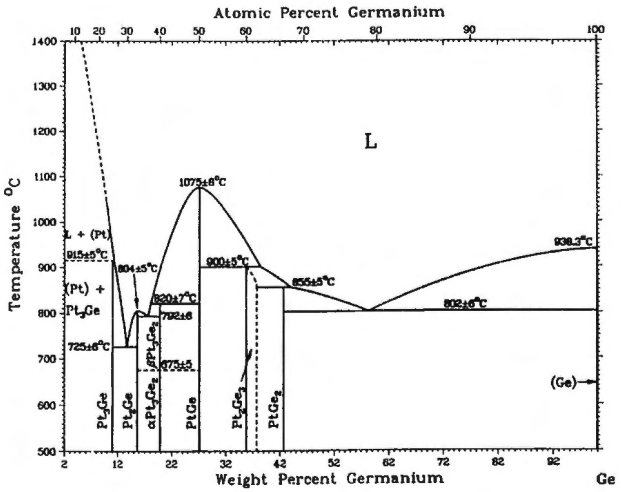

Figure 4.1: Phase diagram for the Pt – Ge system [69].

4.2 Thin Film Couples

As an attempt to clear the confusion surrounding the phase sequence and temperatures of formation, a study was carried out with conventional thin film couples of the Pt-Ge system. RBS and XRD were used for phase identification. A sample structure: SiO_2/Ge (5000Å)/Pt (1200Å) was used. This configuration and thickness of Ge and Pt was found to be the best in maximization of the X-ray yields while avoiding excessive RBS peak overlap.

4.2.1 Phase Formation Sequence Results

Displayed in Fig. 4.2 are RBS spectra from an unreacted sample and ones annealed at temperatures between 190 and 275°C. The expected Pt height for various phases is indicated.

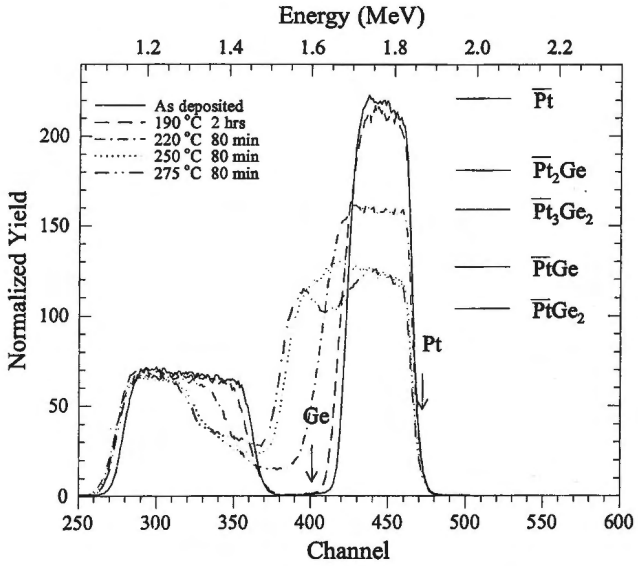

Figure 4.2: RBS spectra from an unreacted sample of composition SiO_2/Ge (5000Å)/Pt (120Å) and from similar samples annealed at various temperatures. Ge and Pt surface positions are indicated.

The samples for which RBS spectra are shown in Fig. 4.2 were also analyzed using X-ray diffraction. Fig. 4.3 and Fig. 4.4 show XRD results along side the corresponding RBS spectrum. RUMP simulations of the RBS spectra are included.

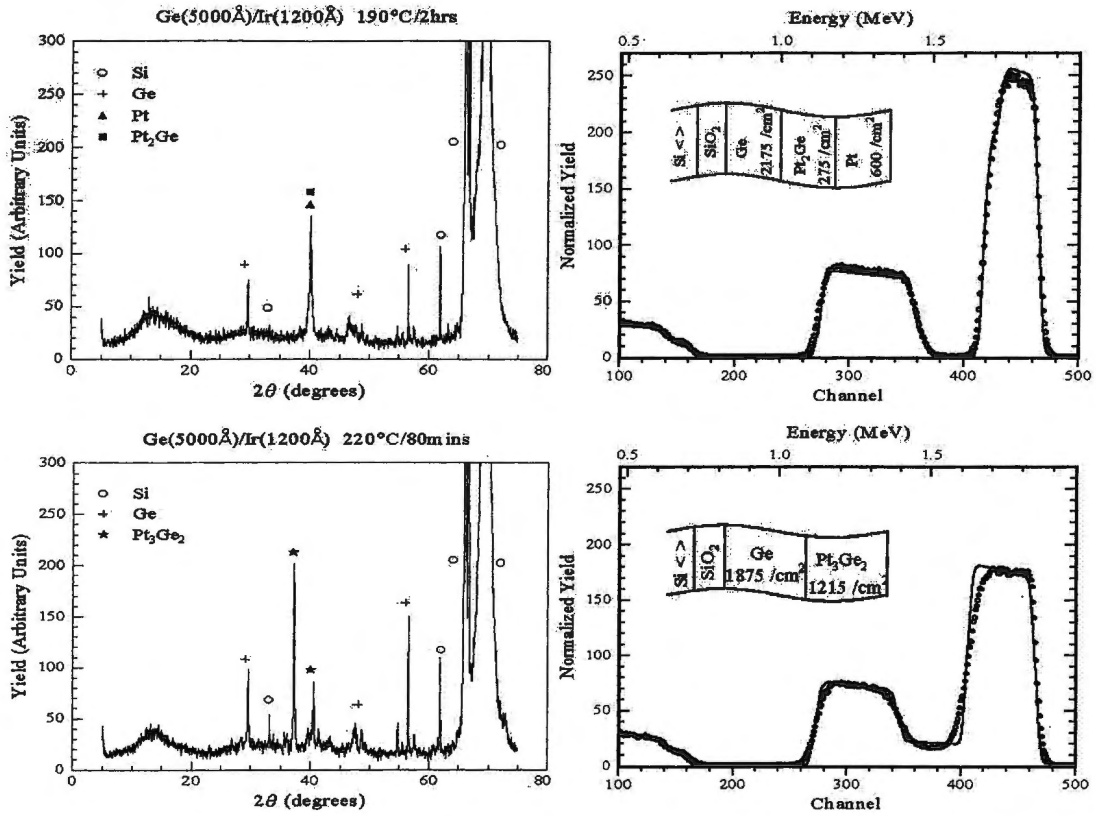

Figure 4.3: X-ray diffraction and corresponding RBS spectra of a sample of composition SiO_2/Ge (5000Å)/Pt (1200Å) after annealing at 190°C for 2 hours and at 220°C for 80 min respectively. The phase Pt_2Ge is observed to form first followed by the non-congruent phase Pt_3Ge_2.

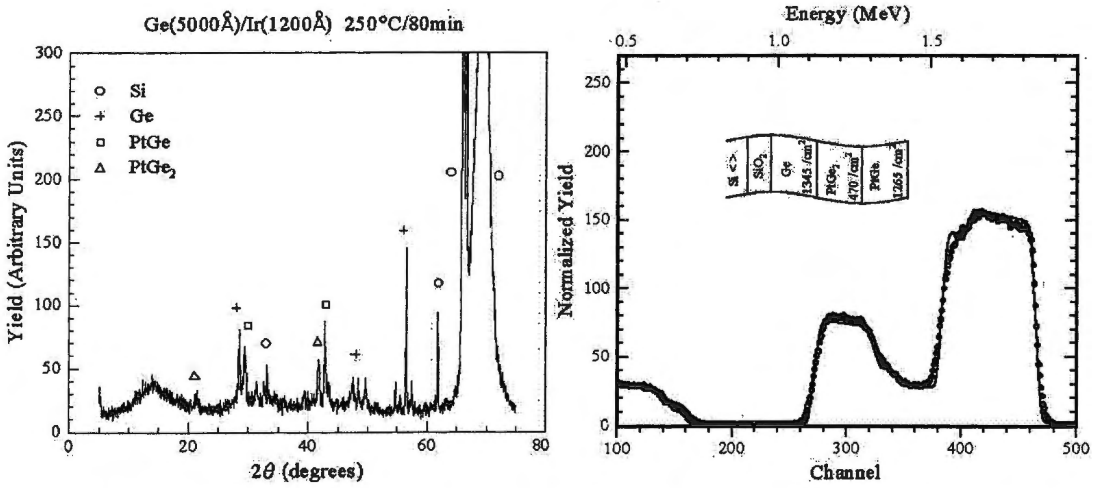

Figure 4.4: X-ray diffraction and corresponding RBS spectra of a sample of composition SiO_2/Ge (5000Å)/Pt (1200Å) after annealing at 250°C for 50 min. The phases PtGe and $PtGe_2$ are observed to form.

The results show Pt_2Ge as the first phase formed, which was at 190°C. In the upper XRD spectrum of Fig. 4.3, the Pt and Pt_2Ge peaks overlap. The Pt peak without Pt_2Ge overlap was seen to be much smaller in a spectrum (which is not included) from the unreacted

sample. The non-congruent phase Pt_3Ge_2 was observed at 220°C, contrary to the results of Nemutudi et al.[30] From our data it was not possible to tell whether all the Pt was consumed before Pt_3Ge_2 appeared. The next detected phase was PtGe at 250°C. The last phase observed was $PtGe_2$ which formed from the interaction of PtGe with unreacted Ge. The non-congruent phase Pt_2Ge_3 was clearly skipped between the last two phases, in agreement with the findings of Nemutudi et al. The phase Pt_3Ge was not observed in the present study as was the case in all previous studies.

4.2.2 Marker Results

To monitor atomic mobility during phase formation, the inert marker technique was used. A thin Ti (12Å) layer was used between Pt and Ge layers. Fig. 4.5 displays an RBS spectrum with a RUMP simulation from an as-deposited sample.

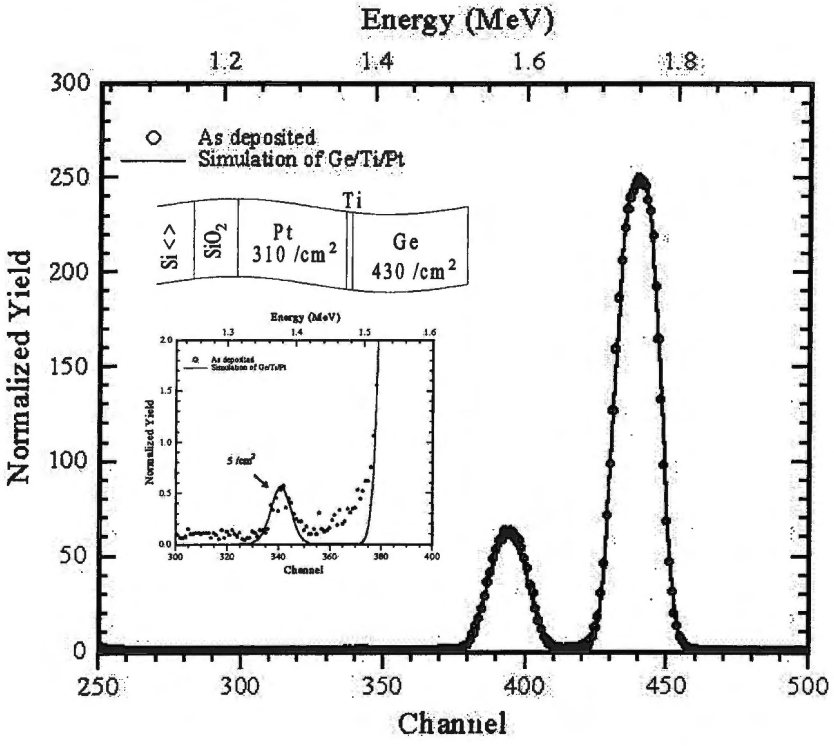

Figure 4.5: RBS spectrum and RUMP simulation of the virgin marker structure used in determining atomic mobility during phase formation.

The virgin structure used was SiO_2/Pt (310/cm^2)/Ti (5/cm^2)/Ge (430/cm^2). The sub-plot is a blow up of the Ti marker signal together with the RUMP simulation. A backscattering

spectrum from a sample annealed at 250°C for 20 min is shown in Fig. 4.6. In order to show relative shift, the Ti signal from this sample is displayed with that of the as-deposited sample in Fig. 4.7. It can be seen from the figure that the Ti signal had shifted to lower energy, from channel 342 to 335 (A to B). From the results it is clear that both Pt and Ge atoms were present on either side of the maker.

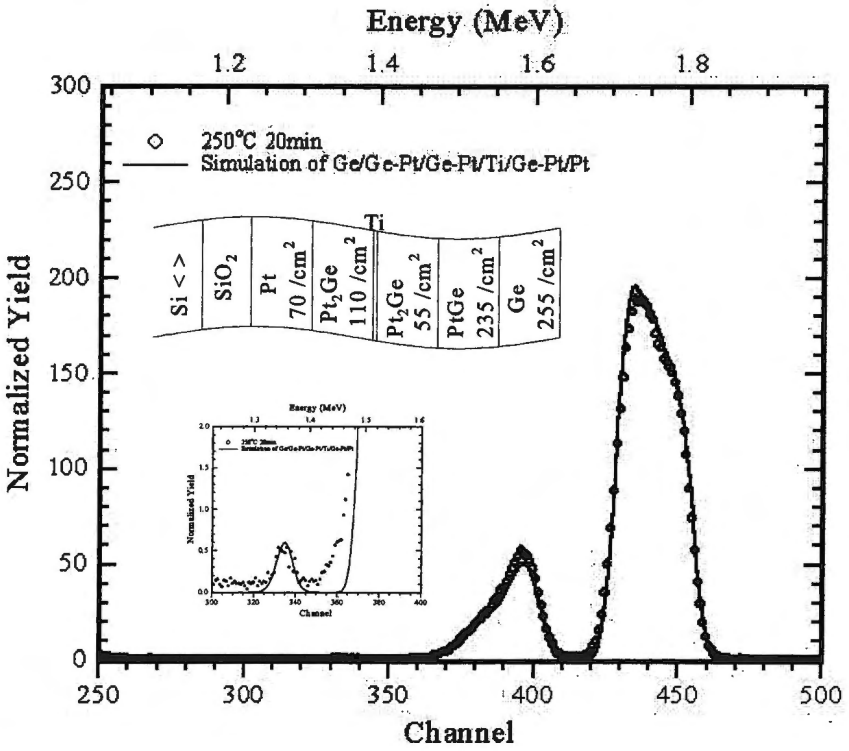

Figure 4.6: RBS spectrum and RUMP simulation of a marker structure annealed at 250°C for 20 minutes. The subplot is a blow up of the Ti marker region of the spectrum.

Both species migrated across the marker to interact, forming Pt_2Ge. The marker signal was observed to shift to lower energy and the simulation showed a significant amount (235 /cm^2) of PtGe above the marker, between Pt_2Ge and unreacted germanium. Two possible mechanisms by which PtGe could have been formed are $Pt_2Ge \rightarrow PtGe + Pt$ and $Pt_2Ge + Ge \rightarrow 2PtGe$. No PtGe was seen below the marker; therefore, the first of these two processes did not take place in that region as it would have left some PtGe there. It is therefore unlikely for the first process to have taken place above the marker. The second reaction is the one most likely to have taken place above the marker.

The amount of platinum above the marker in units of 10^{15} at / cm^2 is given by:

$$\#\,Pt = 2/3\ (55)\ (\text{from } Pt_2Ge) + ½\ (235)\ (\text{from PtGe}) = 154 \qquad (4.1)$$

The amount of germanium below the marker is given by:

$$\#\,Ge = 1/3\ (110)\ (\text{from } Pt_2Ge) = 37 \qquad (4.2)$$

The Pt:Ge ratio is about 4:1, therefore Pt was the dominant moving species during the growth of the phase Pt_2Ge. These results say nothing about the moving species during PtGe formation.

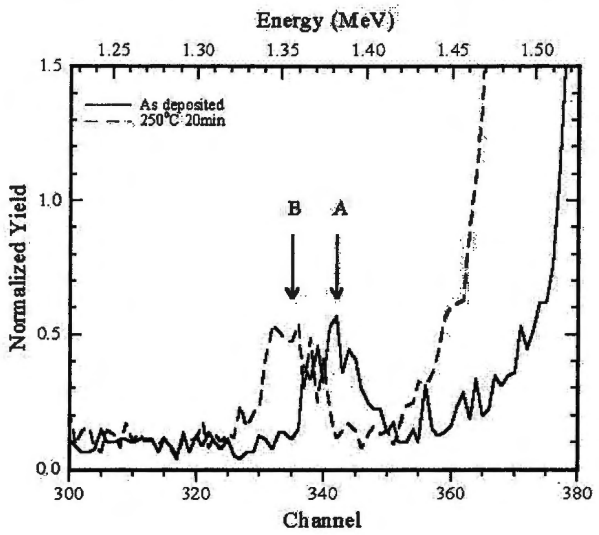

Figure 4.7: Upon annealing at 250°C for 20 minutes, the marker Ti signal shifts from channel 342 to channel 335 (A to B).

An attempt was made to observe marker mobility during the initial stages of Pt_2Ge growth, before the onset of any secondary phase formation. A result is displayed in Fig. 4.8, for a sample annealed at 200°C for 80 min. The Ti signal of this sample is displayed with that of the unreacted sample in Fig. 4.9. It is seen that the marker shifted to lower energy from channel 342 to 340 (A to B), confirming the earlier result.

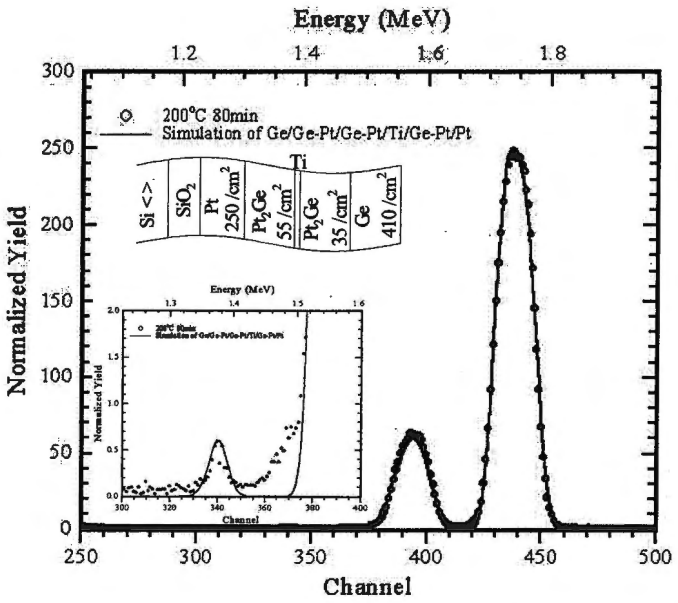

Figure 4.8: RBS spectrum and RUMP simulation of a marker structure annealed at 200°C for 80 minutes. The subplot is a blow up of the Ti marker region of the spectrum.

After examining the amounts of Pt and Ge above and below the marker respectively, as shown earlier, the results show that platinum atoms are the dominant diffusing species during Pt_2Ge formation. This is in agreement with the results of Marshall et al.[65,66] who used molybdenum as a marker and also with those of Nemutudi et al.[30]

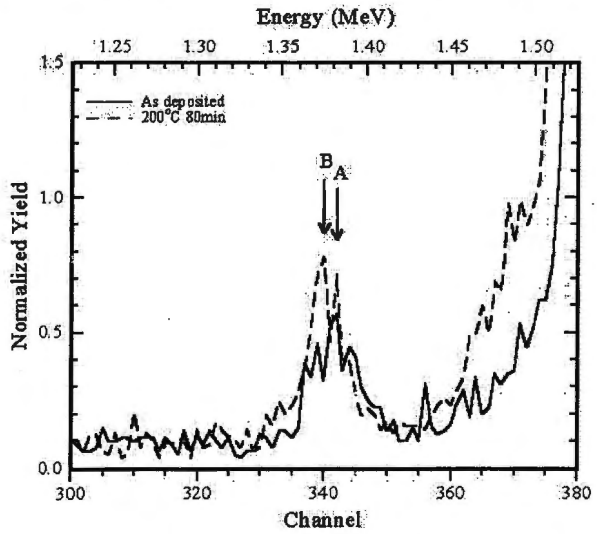

Figure 4.9: Graph showing the shift of the marker Ti signal from channel 342 to channel 340 (A to B) upon annealing at 200°C for 80 minutes.

The phase Pt_3Ge_2 was not observed to form in the presence of the Ti marker; PtGe was formed after Pt_2Ge skipping Pt_3Ge_2, which was observed in our thin film work on this system and also that of Grimaldi et al.[68]

4.3 Lateral Diffusion Couples

As mentioned in the previous chapter, the results of lateral diffusion studies on samples with Ir islands on Ge films showed that the inward diffusion of Ge was much higher than any outward diffusion of Ir. This led to the formation of a Ge depletion layer around the edge of the island, which halted the reaction. The reaction only proceeded in the reverse configuration with Ge islands on Ir films. Nemutudi et al.[30] observed similar behavior in the Pt-Ge system where the reaction only proceeded with Ge islands on Pt films. This was surprising since our work and that of Nemutudi et. al. showed that Pt was the dominant moving species in the early stages of reaction. On the basis of the above, we prepared the lateral diffusion samples used to study the Pt-Ge systems with the configuration of Ge islands evaporated onto Pt films.

Samples were prepared and annealed at various temperatures for different lengths of time. For all samples, the various reaction zones were identified and their widths determined using optical microscopy. Microprobe RBS and PIXE scanning of chosen regions on selected samples was then carried out. Finally, SEM was employed on the regions. Thirteen samples of the Pt-Ge system were analyzed on the microprobe . Only one representative sample is discussed in this section.

4.3.1 μRBS Results

Displayed in Fig. 4.10 is an optical micrograph of a sample with a Ge island (1450Å) on a Pt film (350Å) annealed at 450°C for 24 hours. The darkened area was scanned on the microprobe. Five different regions observed are labeled A to E. Sample orientation was adjusted so that the microprobe beam scanned parallel to the original island interface. The

set of spectra generated in this way for the scanned area is displayed in Fig. 4.11 as a function of lateral position. The figure is orientated such that spectra from the middle of the island lie at the back while those derived from the unreacted Pt film are in front, various phases can clearly be seen.

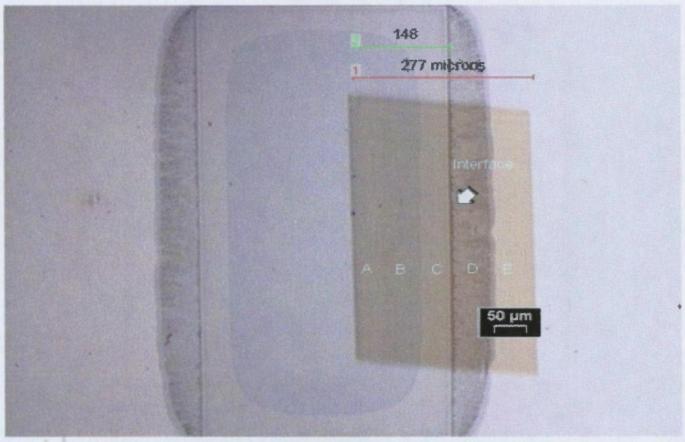

Figure 4.10: Optical micrograph of a Ge island (1450Å) on a Pt film (350Å) annealed at 450°C for 24 hours.

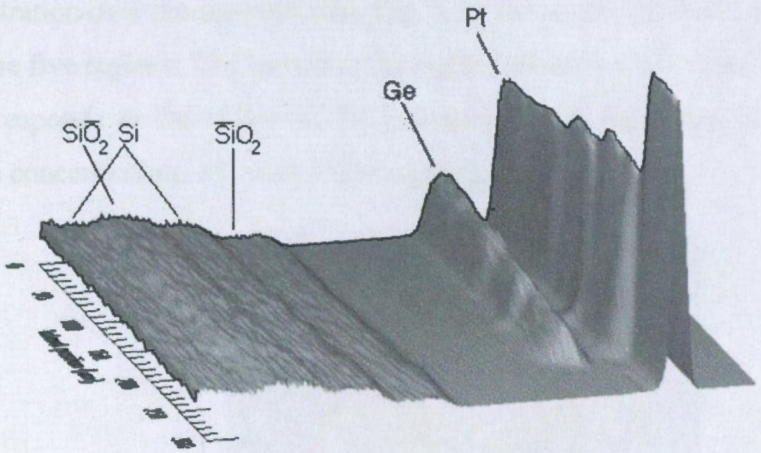

Figure 4.11: RBS spectra obtained from the scanned area as a function of lateral position.

A representative spectrum picked from each of the five regions labeled A to E is shown in Fig. 4.12. The spectrum from region E shows a peak of unreacted Pt and no Ge. Peak heights of the spectra taken from regions D, C and B show the phases PtGe, Pt_2Ge_3 and $PtGe_2$ respectively. The germanides in these three regions are seen at the surface position. It is seen from the solid line in the figure that the region A consisted of unreacted Ge and

the phase $PtGe_2$. The Pt peak of the solid line lies at the surface position. This shows that there was some Pt at the surface. The 'shoulder' marked in the figure however indicates that there is less Pt at the surface than deeper down. Region A therefore consisted of $PtGe_2$ at the bottom while at the top there was unreacted Ge together with the phase $PtGe_2$.

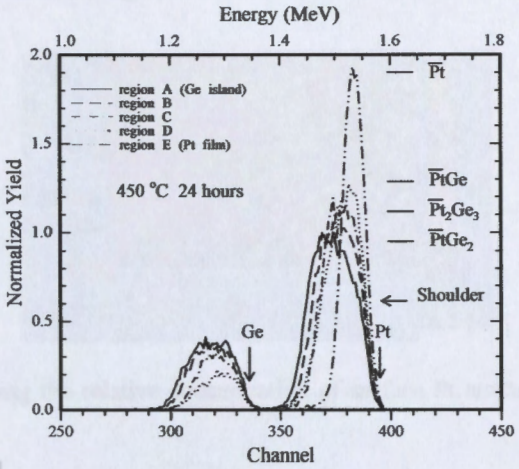

Figure 4.12: Superposition of selected RBS spectra from each of the five regions. Pt peak heights of the various phases and surface positions of Ge and Pt are indicated.

A gate was set over the Ge peak between channels 290 and 340 to obtain an RBS map of Ge concentration over the scanned area. Fig. 4.13 shows the relative concentrations of Ge atoms in the five regions. The legend to the right shows the color code. The bottom of the figure corresponds to the region of $PtGe_2$ together with unreacted Ge. This shows the highest Ge concentration. All other regions are distinct.

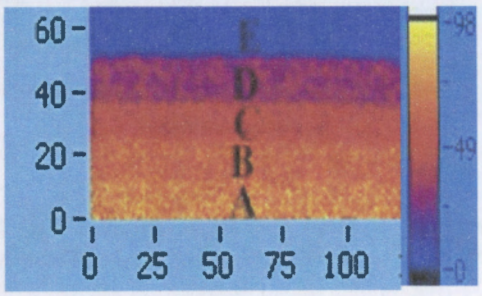

Figure 4.13: RBS map showing the relative concentration of Ge atoms in the five regions of the scanned area. The legend to the right gives the color code.

A gate was then set between channels 385 to 400 and a map of the Pt concentration at the surface of the sample was obtained. This is shown in Fig. 4.14. Some surface Pt is seen at the bottom of the figure. This corresponds to region A and shows that unreacted Ge at the surface is mixed with the compound phase in this region. The other regions are distinct, with the highest concentration being that of the unreacted Pt film at the top of the figure.

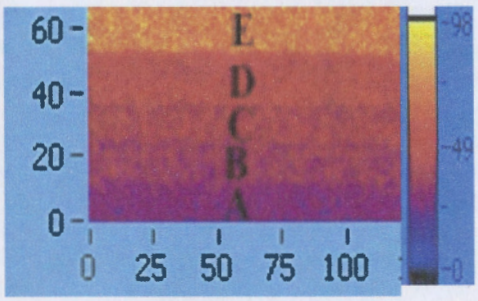

Figure 4.14: RBS map showing the relative concentration of surface Pt atoms in the five regions of the scanned area.

Pt and Ge peaks were separately integrated at each beam position. The results are shown in Fig. 4.15.

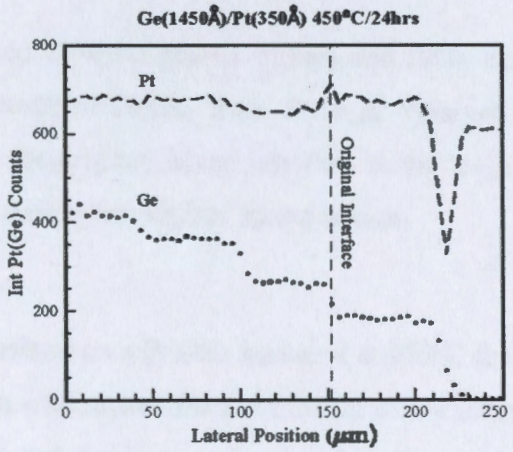

Figure 4.15: Integrated counts of the Pt and Ge peaks as a function of lateral position for a Ge island (1450Å) on a thin Pt film (350Å) annealed at 450°C for 24 hours. The data for Pt counts were raised above those for Ge for clarity.

A sharp Pt depletion is observed at the interface between regions D and E. The information in Fig. 4.15 was then converted to stoichiometric data and plotted, the result of which is shown in Fig. 4.16.

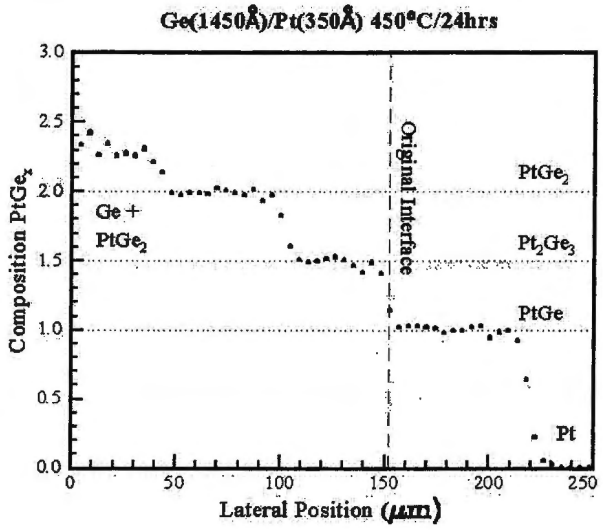

Figure 4.16: Stoichiometric information of a Ge island (1450Å) on a thin Pt film (350Å) annealed at 450°C for 24 hours, derived from integrated counts of the Pt and Ge peaks, as a function of lateral position.

It is seen that the interface between phases Pt_2Ge_3 and PtGe lies at the original island interface position, no growth of Pt_2Ge_3 from PtGe is observed (unlike the growth of Ir_3Ge_7 from Ir_4Ge_5 across the original island interface in the Ir-Ge system). The most Ge rich phase $PtGe_2$ lies well inside the original island region.

4.3.2 μPIXE Results

For the sample with a Ge island on a Pt film annealed at 450°C for 24 hours (Fig. 4.10), a uniform rectangular region was chosen from the center of the island. All PIXE spectra in this region were extracted and the average is plotted in Fig. 4.17. The Ge and Pt peaks used in the analysis are indicated in the figure. These were simulated using GeoPIXE II to extract compositional information. M lines were not used in the analysis. As can be seen in the figure, there was some overlap between Pt and Ge peaks but this was well dealt with by GeoPIXE II.

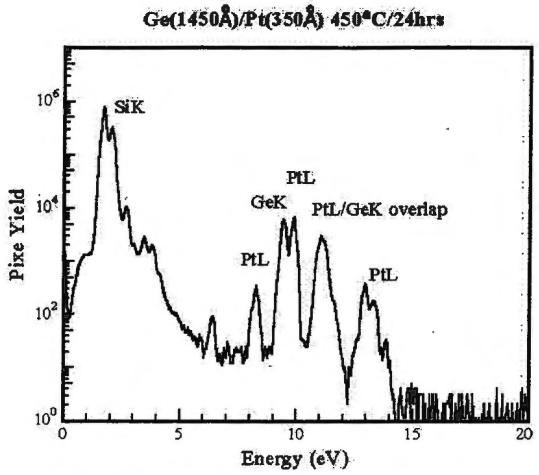

Figure 4.17: Average PIXE spectrum extracted from a region in the center of a thick Ge island (1450Å) on a thin Pt film (350Å) annealed at 450°C for 24 hours.

The PIXE data were extracted and added along parallel lines aligned with regional interfaces, in the same way as described earlier for the RBS data. These spectra were then analyzed to extract compositional information as a function of lateral position. The results are shown in Fig. 4.18. This figure shows results similar to those obtained from the RBS analysis (Fig. 4.15).

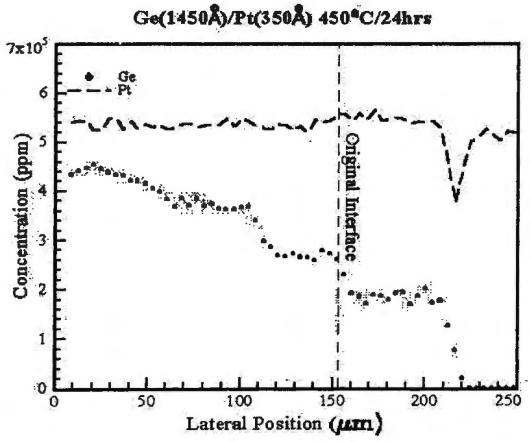

Figure 4.18: PIXE derived Pt and Ge concentration (in ppm) as a function of lateral position for a Ge island (1450Å) on a thin Pt film (350Å) annealed at 450°C for 24 hours. The Pt concentration data were raised above those of Ge for clarity.

4.3.3 Scanning Electron Microscopy (SEM) Results

The sample with a Ge island on a Pt film annealed at 450°C for 24 hours was analyzed using SEM. Fig. 4.19 is an SEM micrograph of the sample. The lateral extent of the regions is consistent with the results from other techniques, presented earlier.

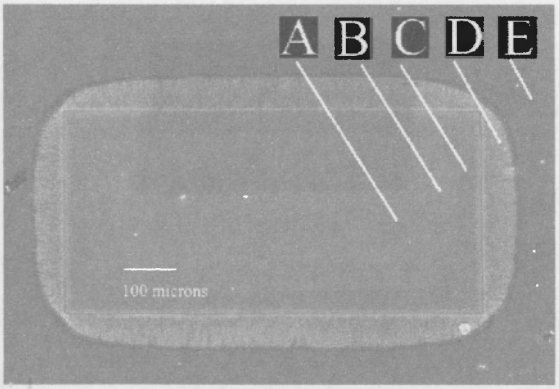

Figure 4.19: SEM micrograph of a Ge island (1450Å) on a thin Pt film (350Å) annealed at 450°C for 24 hours, showing the whole sample and different regions.

Displayed in Fig. 4.20 is a closer-up scan of the regions A to E. There is a dark region marked 'X', observed between regions D and E. This coincides with the region of Pt depletion observed using RBS and PIXE.

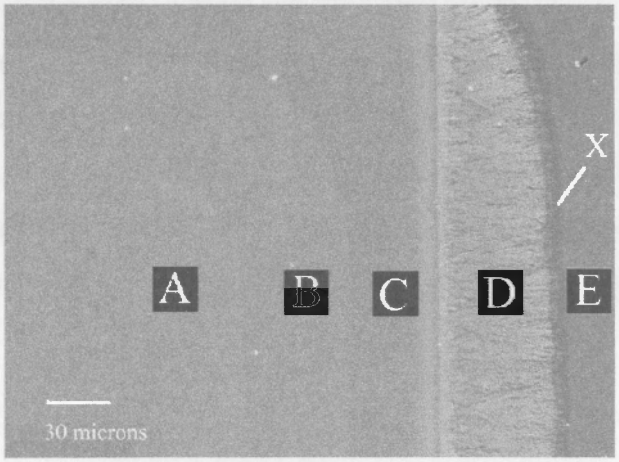

Figure 4.20: SEM micrograph a Ge island (1450Å) on a thin Pt film (350Å) annealed at 450°C for 24 hours, showing a close-up scan of the different regions.

The region around the original island interface was investigated further at higher magnification as presented in Fig. 4.21. This figure gives a closer look at features around the interface between regions C and D. Interesting features, one of which is labeled 'Y', are observed in region C. These features appear to be pores in the matrix of the phase Pt_2Ge_3.

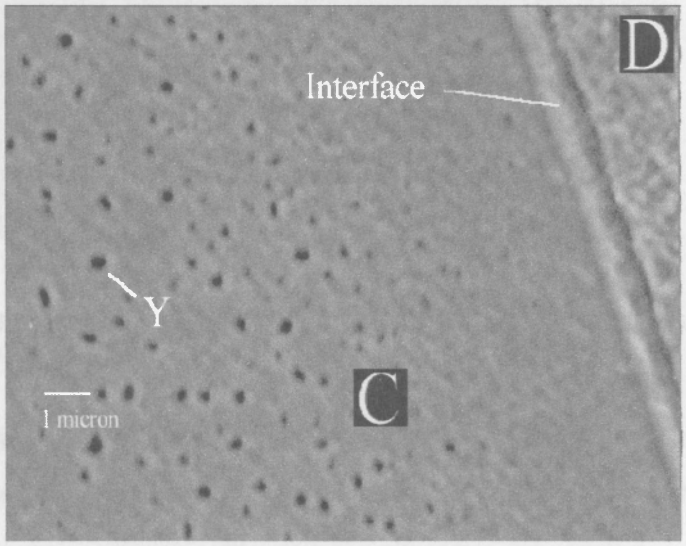

Figure 4.21: Magnified SEM scan of the region around the original interface, showing pores labeled 'Y'.

The interface between regions A and B was also studied at higher magnification, a micrograph of which is shown in Fig. 4.22. The voids labeled 'Y' are also seen in region B which consists of the exposed $PtGe_2$ phase. These features are not observed in region A. It may be recalled from section 4.3.1 that region A was observed to consist of $PtGe_2$ and unreacted Ge. It was noted in that section that some Pt was observed at the surface of

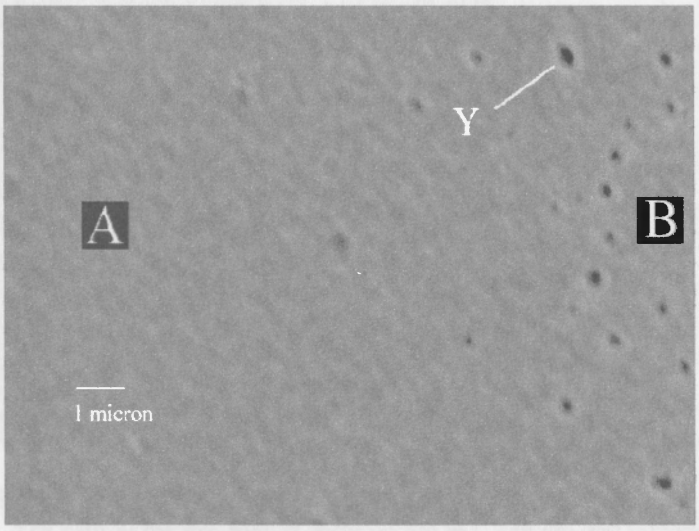

Figure 4.22: Magnified SEM scan of features around the interface between regions A and B. The pores 'Y' are seen in region B, in region A they seem filled with Ge.

this region. The voids seen in our SEM results now suggest an explanation as to why both unreacted Ge and some Pt were observed at the surface in the middle of the island, this is discussed later.

An SEM line scan was carried out over the observed region; results are given in Fig. 4.23. The path of the line scan is shown on the left. The top and bottom graphs, on the right, show the estimated relative concentrations of Ge and Pt as a function of position, respectively. Points were picked within each region from B to E. The percentage concentration was then determined at each. Results are indicated in the figure. As explained in the previous chapter, these percentages do not add up to 100 because Si and O content was also included.

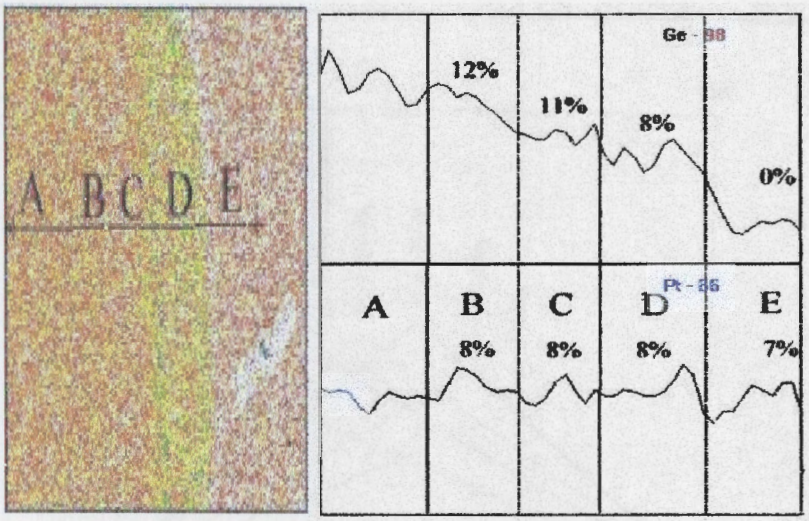

Figure 4.23: An SEM line scan giving an estimate of the concentration of different atomic species as a function of position. The path of the line scan is show on the left. The top and bottom graphs on the right show the estimated Ge and Pt concentrations as a function of position.

The regions B, C and D consist of phases $PtGe_2$, Pt_2Ge_3 and PtGe. These phases are expected to yield concentration ratios of Pt to Ge; 1:2, 1:1.5 and 1:1 respectively. The ratios obtained were 1:1.5, 1:1.4 and 1:1 respectively.

4.4 Analysis and discussion

The Pt_2Ge phase was observed as the first to be formed in the thin films, which was at 190°C. Formation of the non-congruent Pt_3Ge_2 phase was observed at 220°C. This was followed by PtGe at 250°C and the final phase $PtGe_2$ was then observed. The non-congruent Pt_2Ge_3 phase was skipped, in agreement with Nemutudi et al.[30] An EHF diagram, of the system is shown in Fig.4.24. The congruent phase Pt_2Ge has the most negative effective heat of formation at the liquidus minimum (70 atomic % Pt). It is therefore the phase predicted by the EHF model as the first to form, which is in agreement with our results.

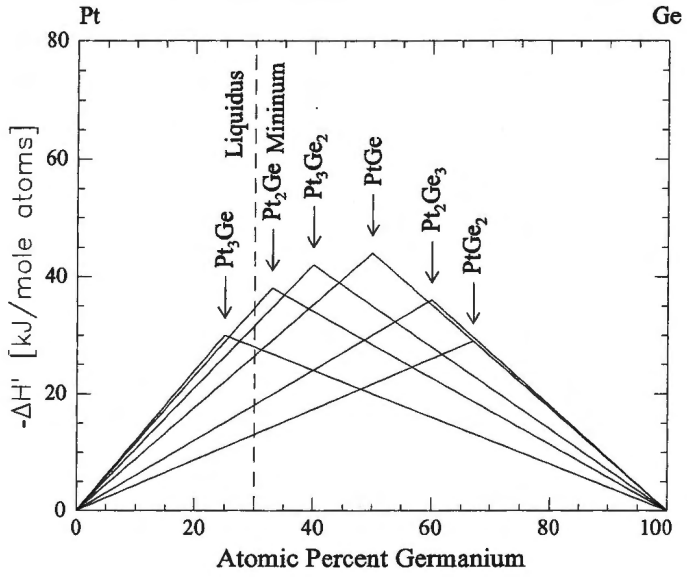

Figure 4.24: An EHF diagram, of the Pt– Ge system, drawn using the Miedema semi imperical model.

The direction of atomic mobility was monitored during the formation of Pt_2Ge, by observing the movement of a Ti (12Å) marker. The results showed that both Ge and Pt diffused across the marker but Pt atoms were the dominant diffusing species. This is in agreement with work reported in the literature.[30,65,66] The phase Pt_3Ge_2 was not observed to form in the presence of the Ti marker; PtGe was formed after Pt_2Ge skipping Pt_3Ge_2, which was observed in our thin film work on this system. The marker may have acted as a barrier for Pt atoms resulting in the formation of the less Pt rich phase PtGe rather than Pt_3Ge_2. Further, since Pt_3Ge_2 is reported as having been skipped in the thin film work of Hsieh and Chen, Marshall et al. and Nemutudi et al., it is evident that this phase does not form easily. The marker may have therefore introduced an impurity which inhibited the formation of the phase.

Regions observed in the lateral diffusion couples of the Pt-Ge system are schematically represented in Fig. 4.25. The different phases and position of the original interface are indicated. Knowledge of the position at which the original interface lay was vital in analysis of the reactions taking place between different phase regions. Depending on how the reaction interfaces shifted with respect to the original interface for different times of annealing, one is able to determine whether a phase transformation or decomposition

process occurred at that interface. If the interface between two phases did not move with respect to the original interface position then one concluded that there was no resultant growth interaction at that interface.

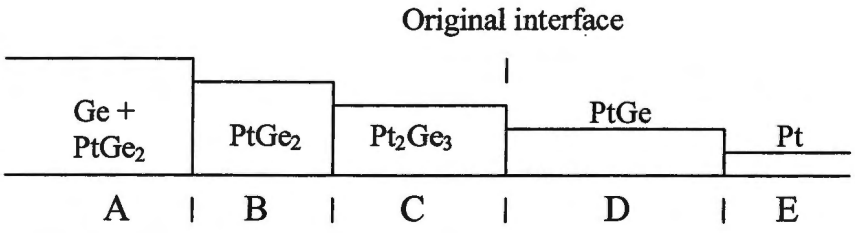

Figure 4.25: Diagram showing different phase regions observed in lateral diffusion couples of the Pt-Ge system.

Equations for the reactions that took place at each interface and the corresponding heats of reaction are given in Table 4.1. Components of the calculations are shown beneath each equation. The heat of formation values used here were as compiled by Pretorius et al.,[14] using criteria that incorporated both the Miedema Approximation[9] and carefully selected experimental data.

Interface	Equation of Reaction	Heat of Reaction ΔH_R° (kJmol^{-1}atm^{-1})
B-C	$2PtGe_2 \rightarrow Pt_2Ge_3 + Ge$ 2x3(-28.8) 5(-36.6) 1(0)	-1.7
C-D	No resultant reaction	
D-E	$Pt + Ge \rightarrow PtGe$ 1(0) 1(0) 2(-43.1)	-43.1

Table 4.1: Equations of the reactions that take place at each interface and the corresponding heat of reaction, calculated using the Miedema Approximation. Components of the calculations are shown beneath each equation. The values in the table are per atom i.e. the total heats of formation for molecules are divided by the number of atoms in the molecules.

Initially, the Ge in the thick island interacted with underlying Pt (presumably going through a sequence of phases including the phases Pt_2Ge and Pt_3Ge_2 which were observed as the first and second phases to form in the thin film study) until the most

germaniun rich $PtGe_2$ phase was formed. As the excess Ge atoms from the source diffused through the $PtGe_2$ to form PtGe outside the original island interface, the $PtGe_2$ was exposed and a decomposition reaction then took place that resulted in the formation of the Pt_2Ge_3 phase from $PtGe_2$. The Pt_2Ge_3 phase was formed inside the original island interface between the phases $PtGe_2$ and PtGe; the equation of the decomposition reaction by which this phase was formed is shown in the table. The decomposition of $PtGe_2$ resulted in the release of Ge atoms, as can be seen from the equation in Table 4.1; these are added to the flux of atoms from unreacted Ge in the middle of the island, flowing through the phase $PtGe_2$. The resultant Ge flux diffuses through Pt_2Ge_3, and PtGe facilitating the growth of the latter phase at the interface with unreacted Pt. The equation for this reaction is also given in the table, and shows a large negative value for the heat of formation. Ordinarily, the non-congruent phase Pt_2Ge_3 would not be expected to form since it was clearly skipped in the thin film study of this system. It was only observed in the lateral diffusion couples as a result of decomposition of $PtGe_2$ to supplement the flow of Ge atoms to the PtGe/Pt reaction interface. The interface between Pt_2Ge_3 and PtGe lay at the position of the original island interface and did not shift with increase in anneal time; suggesting that there was no resultant growth interaction at this interface.

The Pt peak of the solid line in Fig. 4.12 lies at the surface position. This shows that there was some Pt at the surface, unlike the case with Ir in the Ir-Ge system. As mentioned earlier, the 'shoulder' marked in that figure indicated that there was less Pt at the surface than deeper down. This region therefore consisted of $PtGe_2$ at the bottom while at the top there was unreacted Ge together with the phase $PtGe_2$. Our SEM results further revealed the formation of characteristic voids at the surface of the original island region. To explain these results it was deduced that the most germaniun rich $PtGe_2$ phase rose to the surface in patches during the initial stages of growth. The Ge between the $PtGe_2$ patches was later consumed resulting in the formation of voids.

A Pt depletion region was observed at the interface between PtGe and the unreacted Pt film. This region moved along with the PtGe/Pt interface as the PtGe region grew outwards which implied a movement of Pt atoms from the unreacted thin film into the outer reaction interface during the growth process. Pt was found to be the dominant moving species during the formation of the phase Pt_2Ge which was the first phase to form

in the thin film investigation. It could be that this phase was also the first to be formed at the outer reaction interface in lateral diffusion couples. The formation of this precursor phase could have caused the movement of Pt atoms into the interface thereby creating a Pt depletion region outside the interface. This depletion region then limited the supply of Pt into the reaction region hence inhibiting further growth of Pt_2Ge favoring the growth of the less Pt rich phase PtGe.

Optical microscopy and SEM were used for measurement of the growth widths. Different annealing times were carefully chosen to obtain a reasonable range of growth widths for the three observed phases at temperatures of 450, 500 and 550°C. The results are presented in Figs. 4.26, 4.27 and 4.28.

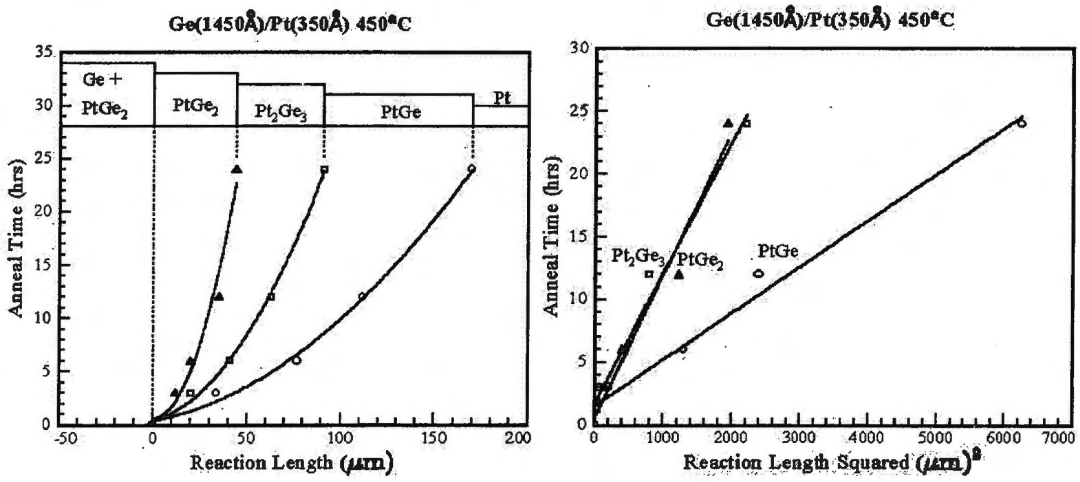

Figure 4.26: Plot of reaction length with time of anneal (left) and reaction length squared with time (right), for the phases $PtGe_2$, Pt_2Ge_3 and PtGe at annealing temperature of 450°C.

The figures on the left are plots of the reaction length with time of anneal, while those on the right are similar plots with the reaction length squared.

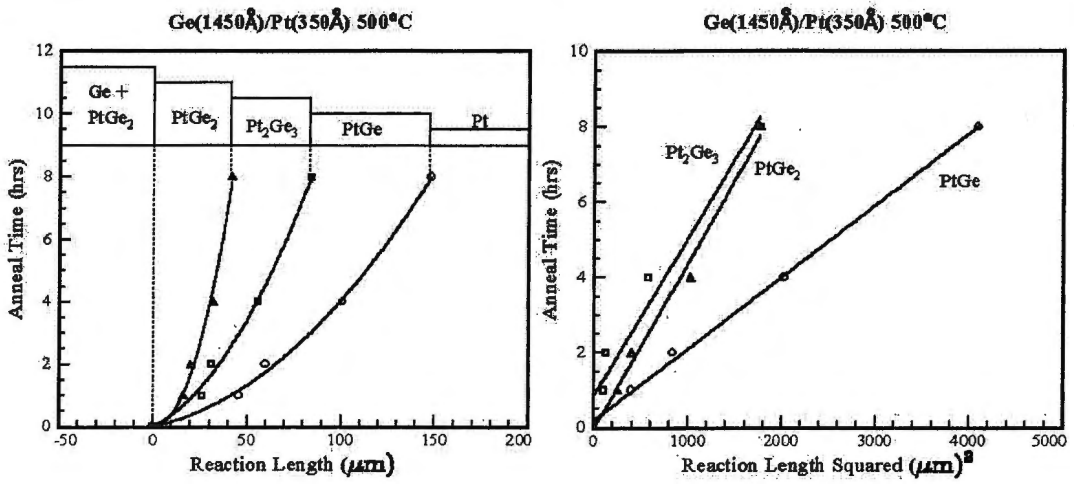

Figure 4.27: Plot of anneal time against reaction length and of anneal time versus reaction length squared with for the phases $PtGe_2$, Pt_2Ge_3 and PtGe at annealing temperature of 500°C.

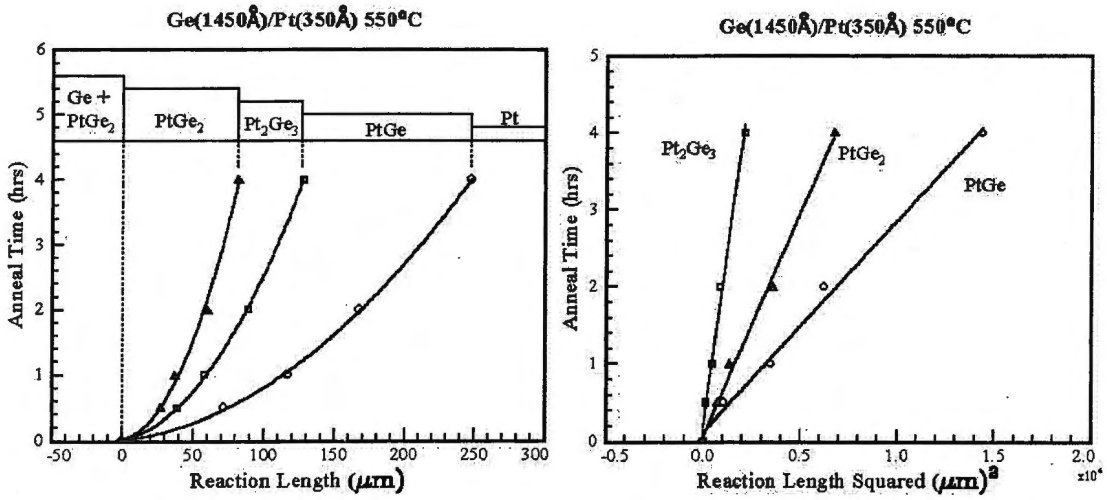

Figure 4.28: Plot of anneal time against reaction length and of anneal time versus reaction length squared with for the phases $PtGe_2$, Pt_2Ge_3 and PtGe at annealing temperature of 550°C.

From the results it is seen that the growth characteristics are parabolic with time, indicating diffusion controlled processes. We do not observe the transition from interface reaction limited to the diffusion limited regime.

Arrhenius plots (lnK_β versus $1/k_bT$), showing the temperature dependence of the diffusion rate of Ge atoms through the phases $PtGe_2$, Pt_2Ge_3 and PtGe, are shown in Fig. 4.29.

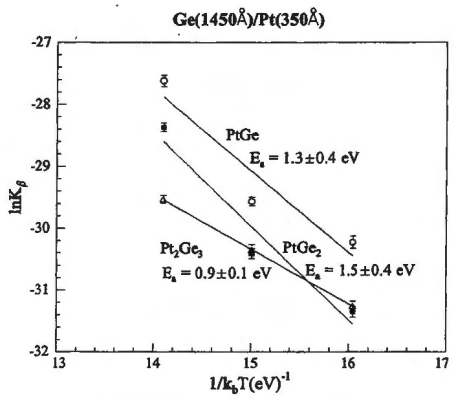

Figure 4.29: Arrhenius plots, lnK_β versus $1/k_bT$, showing temperature dependence of Ge diffusion rate through $PtGe_2$, Pt_2Ge_3 and PtGe yielding average activation energies of 1.5 ± 0.4 eV, 0.9 ± 0.1 eV and 1.3 ± 0.4 eV respectively.

The average activation energies determined from the growth rates of $PtGe_2$, Pt_2Ge_3 and PtGe were E_a = 1.5 ± 0.4 eV, 0.9 ± 0.1 eV and 1.3 ± 0.4 eV respectively.

Table 4.2 gives the values of the width ratios of the different phase regions as a function of the annealing time at various temperatures.

TEMP [T (°C)]	TIME [t (hrs)]	WIDTH OF $PtGe_2$ [x_α (μm)]	WIDTH OF Pt_2Ge_3 [x_β (μm)]	WIDTH OF PtGe [x_γ (μm)]	RATIO x_β/x_α	RATIO x_γ/x_β
450	3	12	8	14	0.7	1.8
	6	20	21	36	1.1	1.7
	12	35	28	49	0.8	1.8
	24	44	47	99	1.1	2.1
500	1	16	10	20	0.6	2.0
	2	20	11	29	0.6	2.6
	4	32	24	45	0.8	1.9
	8	42	42	64	1.0	1.5
550	0.5	27	12	33	0.4	2.8
	1	37	21	59	0.6	2.8
	2	60	29	79	0.5	2.7
	4	82	46	120	0.6	2.6

Table 4.2: Values of the width ratios for the phases $PtGe_2$, Pt_2Ge_3 and PtGe as a function of the annealing time at various temperatures.

Apart from those at 500°C, the values of the width ratios were fairly constant at each temperature which according to the theory of Gösele and Tu[24] implies that the annealing periods were sufficiently long so that the diffusion system became self-regulating.

The growth in this system can be treated as being that of a three phase growth regime. The table below gives the parameters in the geometrically modified Gösele and Tu[24] model that result from this treatment.

A	$A_\alpha B$	$A_\beta B$	$A_\gamma B$	B
Ge	$PtGe_2$	Pt_2Ge_3	PtGe	Pt
	α=2	β=3/2	γ=1	
	z_α=5.5×10^{17} atoms/cm^2	z_β=5.3×10^{17} atoms/cm^2	z_γ=4.9×10^{17} atoms/cm^2	

Table 4.3: Parameters that are relevant to the geometrically modified Gösele and Tu calculation for the phases $PtGe_2$, Pt_2Ge_3 and PtGe.

The quantities G_α, G_β, and G_γ have values:

$$G_\alpha = \Omega_0 \frac{(1+\alpha)(1+\beta)}{\alpha-\beta} = 15\Omega_0,$$

$$G_\beta = \Omega_0(1+\beta)\left[\frac{1+\gamma}{\beta-\gamma} + \frac{z_\beta(1+\alpha)}{z_\alpha(\alpha-\gamma)}\right] = 17.2\Omega_0 \qquad (4.3)$$

and

$$G_\gamma = \Omega_0(1+\gamma)\left[\frac{1+Pt}{\gamma-Pt} + \frac{z_\gamma(1+\beta)}{z_\beta(\beta-Pt)}\right] = 5.08\Omega_0.$$

As in the Chapter 3, the value used for the atomic volume Ω_0 was 16 × 10^{-24} cm^3/at.[32] Table 4.4 shows the values of $\Delta C_\gamma^{eq}\tilde{D}_\gamma$ obtained from the calculations at each temperature.

T (°C)	$\Delta C_{\alpha}^{eq}\tilde{D}_{\alpha}$ $(10^{15} m^{-1}s^{-1})$	$\Delta C_{\beta}^{eq}\tilde{D}_{\beta}$ $(10^{15} m^{-1}s^{-1})$	$\Delta C_{\gamma}^{eq}\tilde{D}_{\gamma}$ $(10^{15} m^{-1}s^{-1})$
450	0.284	0.280	1.93
500	0.728	0.704	4.16
550	5.21	2.70	28.2

Table 4.4: Values of $\Delta C_{\gamma}^{eq}\tilde{D}_{\gamma}$ obtained from the modified Gösele and Tu calculation at each annealing temperature.

The logarithm of χ was plotted against the reciprocal of the product, k_bT of theBoltzmann constant and the absolute temperature where $\chi = \Delta C_{\gamma}^{eq}\tilde{D}_{\gamma}$. This plot is shown in Fig. 4.30.

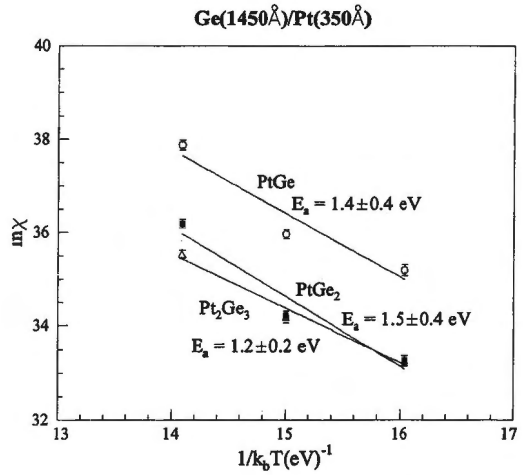

Figure 4.30: Arrhenius plot, $ln\chi$ versus $1/k_bT$, showing temperature dependence of Ge diffusion through $PtGe_2$, Pt_2Ge_3 and PtGe yielding activation energies of 1.5 ± 0.4 eV, 1.2 ± 0.2 eV and 1.4 ± 0.4 eV respectively. The quantity χ is the product, $\Delta C_{\beta}^{eq}\tilde{D}_{\beta}$ of the chemical inter-diffusion coefficients and equilibrium values of the Ge concentration difference across the phases.

The results of Fig. 4.30 from the modified Gösele and Tu calculations show reasonable agreement (except for the Pt_2Ge_3) with the ones obtained from the Arrhenius plots of lnK_{β} versus $1/k_bT$ shown in Fig. 4.29.

CHAPTER 5

THE PALLADIUM – GERMANIUM SYSTEM

5.1 Introduction

The Pd–Ge system has been well studied; its phase diagram is displayed in Fig. 5.1. This system has six equilibrium phases of which only two, Pd_2Ge and PdGe, are congruent. Pd_2Ge has consistently been reported as the first phase to form.[65,71-73] Hsieh et al.[72]

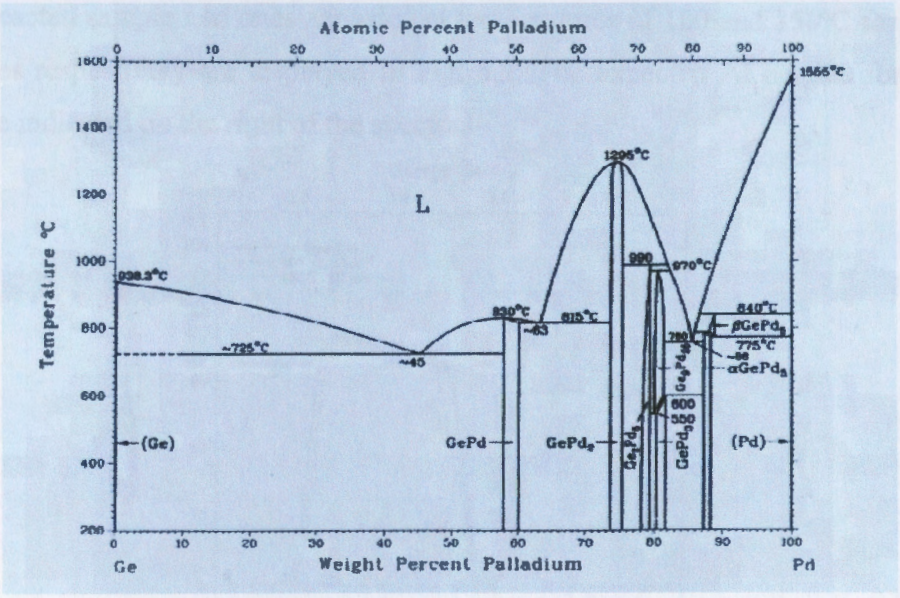

Figure 5.1: Phase diagram for the Pd-Ge system [69].

and a number of others[65,71,73] observed PdGe as the second phase in the formation sequence.

5.2 Thin Film Couples

Of major concern while determining the best thickness of our sample structure, was the likelihood of overlap between Pd and Ge RBS signals. This is by virtue of their having atomic numbers that lie relatively close to each other in the periodic table. At the same time, samples needed to comprise of elemental layers that were thick enough to yield an appreciable X–ray signal. The structure used was SiO_2/Ge (5000Å)/Pd (700Å). There was fairly good adhesion in the sample structure and a Ti glue layer was not required as for the Ir system.

5.2.1 Phase Formation Sequence Results

In this system, reaction was easily induced at relatively low temperatures. Spectral data of an unreacted sample and ones annealed at temperatures of 100 and 150°C for 120 and 80 minutes respectively are displayed in Fig. 5.2. The expected Pd heights for various phases are indicated on the right of the spectra.

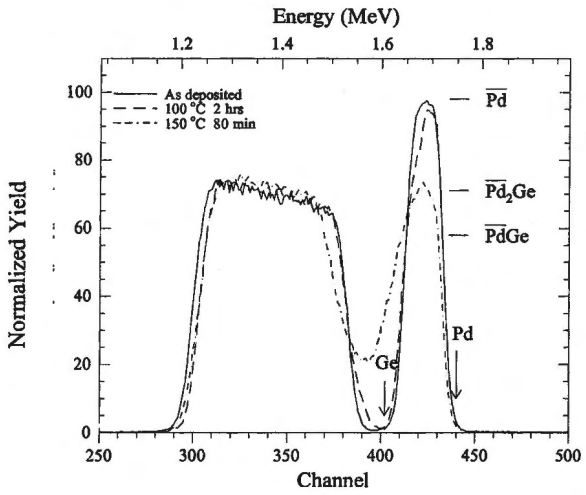

Figure 5.2: RBS spectra from an unreacted sample of composition SiO_2/Ge (5000Å)/Pd (700Å) and from similar samples annealed at 100 and 150°C for 120 and 80 minutes respectively. Ge and Pd surface positions are indicated.

Data from XRD analysis were also obtained to complement those shown above. These are displayed along side the corresponding RBS data in Figs 5.3 and 5.4. Layer thicknesses obtained by RUMP simulation (solid lines) are shown.

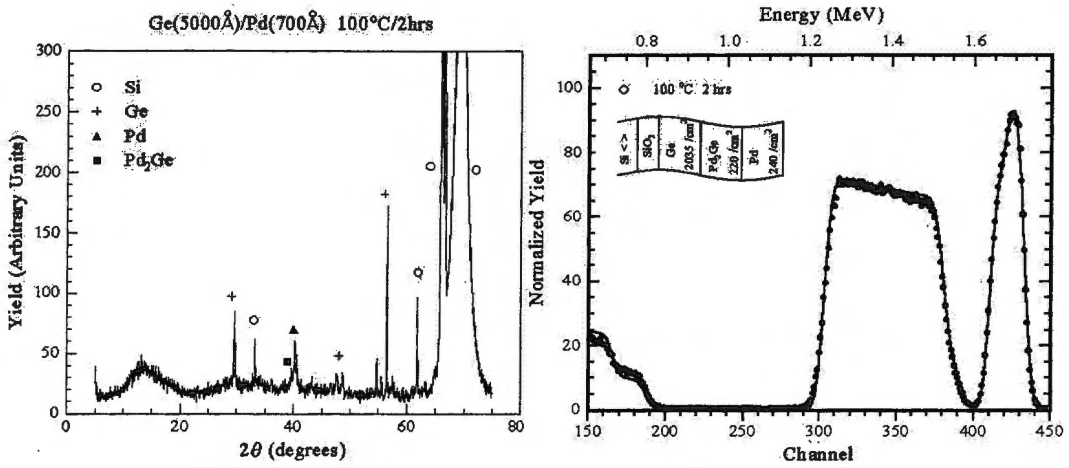

Figure 5.3: X-ray diffraction and corresponding RBS spectra, of a sample of composition SiO_2/Ge (5000Å)/Pd (700Å) after annealing at 100°c for 2 hrs. The phase Pd_2Ge is observed to form first.

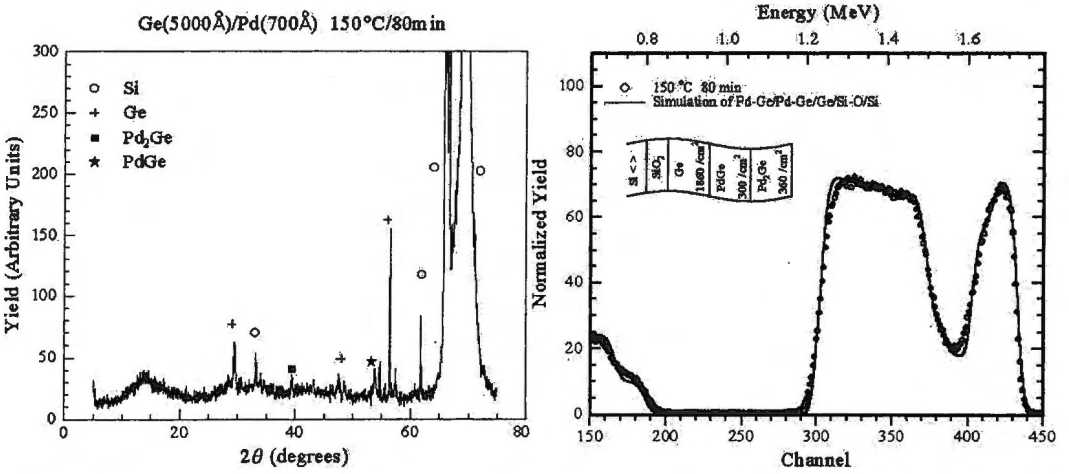

Figure 5.4: X-ray diffraction and corresponding RBS spectra of the sample of composition SiO_2/Ge (5000Å)/Pd (700Å) after annealing at 150°c for 80 min. The phase PdGe is observed to form after Pd_2Ge.

Rather straight forward behavior is observed in this system with the two congruent phases Pd_2Ge and PdGe being the only ones observed. Pd_2Ge was the first to form, which it did at around 100°C. The results are in agreement with those of similar studies on this system.[65,71-73]

5.3 Lateral Diffusion Couples

Samples for lateral diffusion study were prepared by deposition of thick Ge islands on thin Pd films. This configuration was chosen on the basis of the results observed in the Ir-Ge and Pt-Ge systems. Samples were annealed at various temperatures while time was monitored in the usual way. Relatively slow lateral diffusion was observed due to the low temperatures at which it was necessary to carry out this study, as will be discussed presently. The reaction zone was however clearly distinct and lateral data were obtained with relative ease. For all samples, the various reaction zones were identified and their widths determined using optical microscopy. Microprobe RBS and PIXE scanning of chosen regions on selected samples were then carried out. Finally, SEM and AFM were used.

5.3.1 μRBS Results

Eleven samples of the Pd-Ge system were analyzed on the microprobe. Three representative samples are discussed in this section. Fig. 5.5 is an optical micrograph of a sample with a Ge island (1000Å) on a Pd film (200Å) annealed at 325°C for 2 hours. The darkened area was scanned on the microprobe. The three different regions observed are labeled A to C. The absence of visible variation parallel to the interface, and knowledge of observed lateral behavior in similar systems, gave enough confidence to sum data along this direction, reducing the analysis to a one-dimensional scan perpendicular to the interface. As will be demonstrated later, this presented a unique problem in this particular system. Spectra generated as described above are displayed in Fig. 5.6 as a function of lateral position.

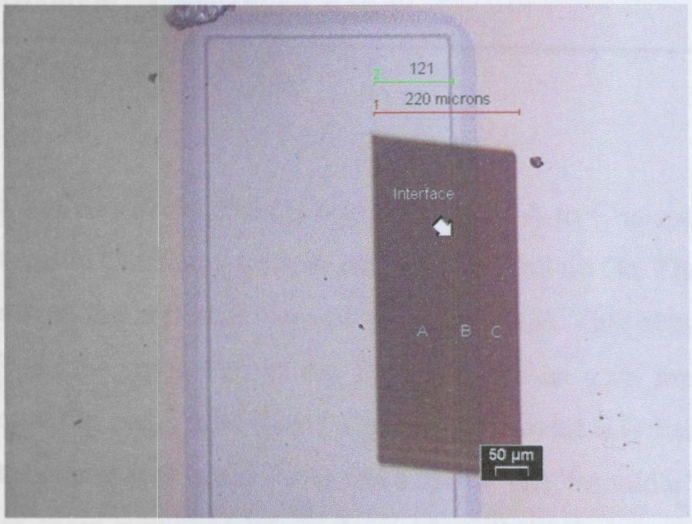

Figure 5.5: Optical micrograph of a Ge island (1000Å) on a Pd film (200Å) annealed at 325°C for 2 hours.

The data in Fig. 5.6 show that Pd and Ge peaks were relatively close but separated well enough for reasonable analysis. Orientation of the figure is such that spectra from region A lie at the back while those derived from the unreacted Pd film are in front. One is able to distinguish three regions immediately by looking at the Pd signal. It can also be seen that only a relatively small amount of Ge was able to diffuse from the source region.

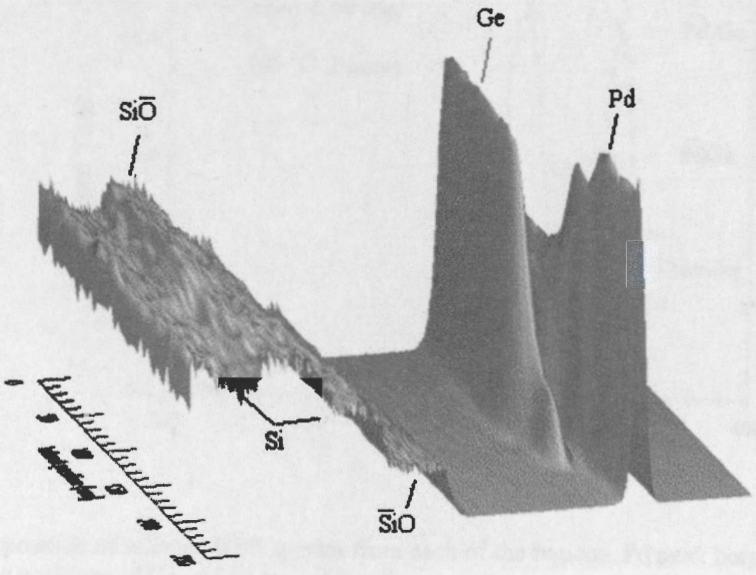

Figure 5.6: RBS spectra obtained from the scanned area as a function of lateral position.

A spectrum picked from each of the three regions labeled A to C is shown in Fig. 5.7. The spectrum from region C shows a peak of unreacted Pd and no Ge. The peak height of the spectrum taken from the region B shows the phase Pd_2Ge. This phase is seen at the surface position. From the solid line in the figure, it can be seen that the region A consisted of unreacted Ge and PdGe. The Pd peak of the solid line lies at the surface position, showing that there was some Pd at the surface. The 'shoulder' marked in the figure indicates that there was less Pd at the surface than deeper down. Region A therefore consisted of PdGe at the bottom while at the top there was unreacted Ge intermingled with PdGe. Pd and Ge peaks were separately integrated at each beam position; results are shown in Fig. 5.8.

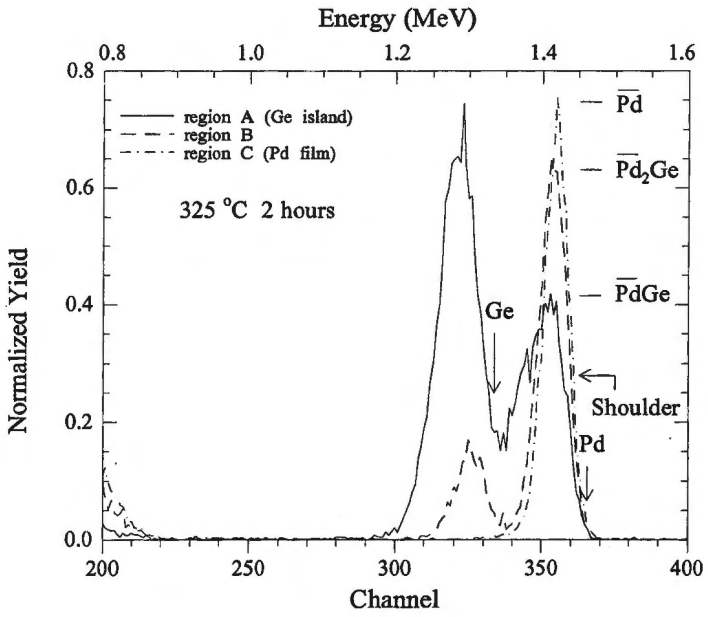

Figure 5.7: Superposition of selected RBS spectra from each of the regions. Pd peak heights of the various phases and surface positions of Ge and Pd are indicated.

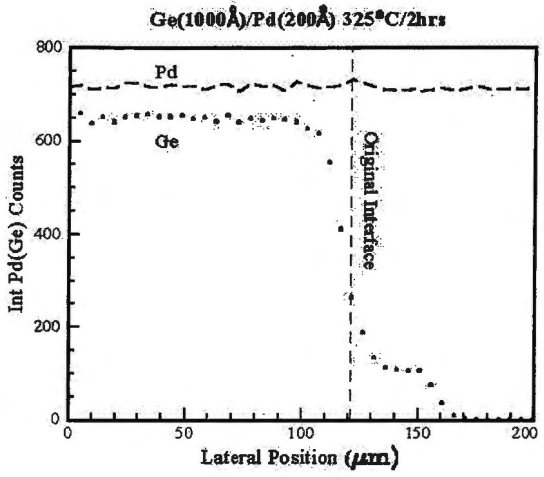

Figure 5.8: Integrated counts of the Pd and Ge peaks as a function of lateral position for the sample annealed at 325°C for 2 hours. The data of Pd counts were offset above those of Ge for clarity.

One feature that was consistently observed for all Pd–Ge lateral diffusion samples analyzed, and seen in Fig. 5.8, was the gradual drop in Ge concentration at the interface of region B with unreacted Pd. This was less abrupt in comparison with other systems that showed a relatively sharp drop in Ge signal at the edge of the outer-most interaction region.

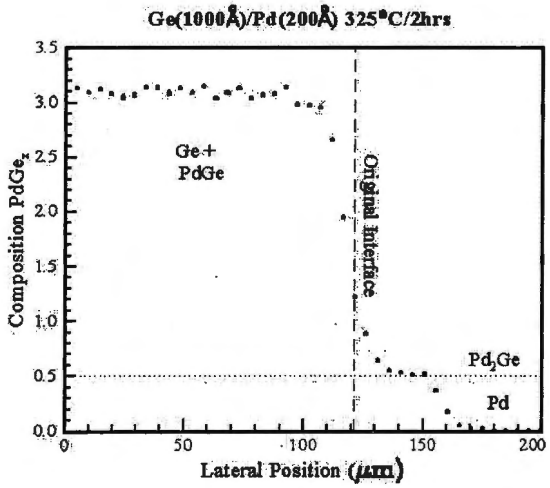

Figure 5.9: Stoichiometric information of the sample annealed at 325°C for 2 hours, derived from integrated counts of the Pd and Ge peaks, as a function of lateral position.

The phase Pd_2Ge is seen to grow outwards from the original island interface. Further out, the Ge component of the composition is seen to diminish somewhat gradually towards the unreacted Pd.

A sample annealed at 325°C for 1 hour was analyzed using AFM, as will be seen later. Variation in thickness between different regions of the sample was also determined using μRBS to compare with the AFM results. An optical micrograph of this sample is presented in Fig. 5.10, two areas scanned by the microprobe are seen in this picture. The following results refer to the area on the right, three different regions A to C are indicated within this scanned area.

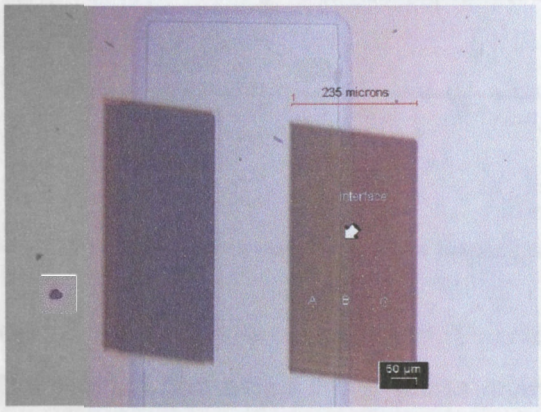

Figure 5.10: Optical micrograph of a sample annealed at 325°C for 1 hour.

Using RBS, it was found (results not shown) that the composition of the three regions was similar to that obtained for the sample annealed at 325°C for 2 hours. The RBS spectra were simulated by RUMP to obtain thickness information. This information is plotted in Fig. 5.11 as a function of lateral position. The thickness of the Pd_2Ge is seen to taper off at the interface with unreacted Pd.

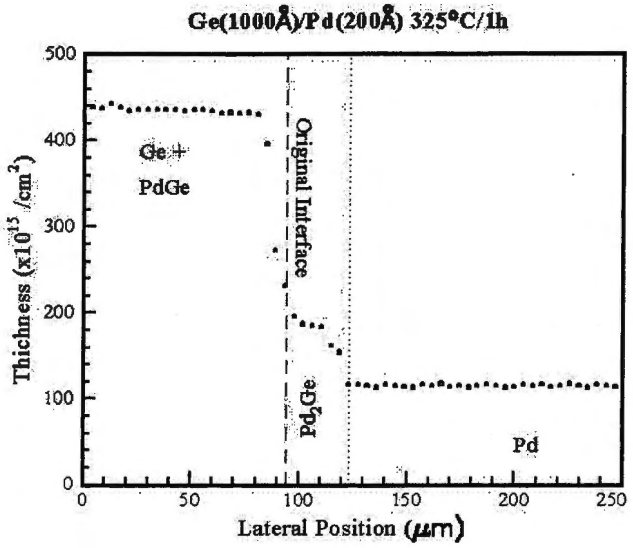

Figure 5.11: RUMP simulated thickness of the various phase regions as a function of lateral position.

The Pd–Ge system was studied at relatively low temperatures. The rate of lateral reaction was slow and in the samples studied, the whole PdGe phase region was overlaid by unreacted Ge. To get a better insight into the pattern of consumption of unreacted Ge, an attempt was then made to expose the Pd_2Ge by using a thicker Pd film which consumes more Ge and having longer anneal times. The stoichiometric result is shown in Fig. 5.12 for a sample of a Ge island (1150Å) on a Pd film (250Å) annealed at 275°C for 16 hours. The pattern of Ge consumption is seen to be much the same as that of other systems studied, with the most Ge-rich phase being gradually exposed towards the center of the island. It must be borne in mind that the virgin structure used for the last sample presented (275°C for 16 hours) was different from that for the two samples seen earlier; therefore this result can not be directly compared to the other two.

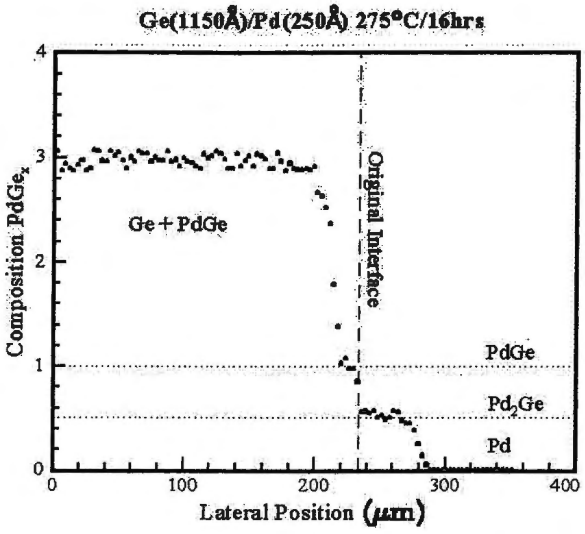

Figure 5.12: Stoichiometric information of a Ge island (1150Å) on a Pd film (200Å) annealed at 275°C for 16 hours.

5.3.2 μPIXE Results

As in all samples analyzed, both RBS and PIXE data were recorded in our scan on the sample shown in the optical micrograph of Fig. 5.5 which was annealed at 325°C for 2 hours. A uniform rectangular region was chosen from the center of the island. All PIXE spectra in this region were extracted; the combined spectrum is shown in Fig. 5.13.

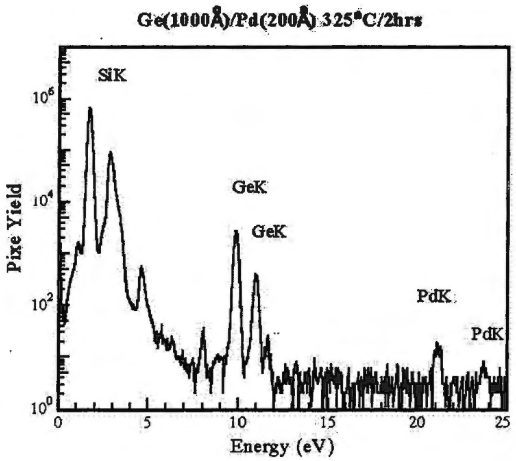

Figure 5.13: Average PIXE spectrum extracted from a region in the island center of the sample annealed at 325°C for 2 hours.

The Ge and Pd peaks used in analysis are indicated in the figure. M and L lines were not used as the K lines were sufficient for the study. The Ge and Pd peaks are well separated, allowing for easy analysis. As shown earlier, the Ge and Pd peaks in the RBS spectrum were not well separated, making PIXE a better technique for analyzing thicker samples of this system.

The spectra were then analyzed to extract compositional information as a function of lateral position; the results are shown in Fig. 5.14. This figure shows similar results to those obtained from the RBS analysis and presented in Fig. 5.8.

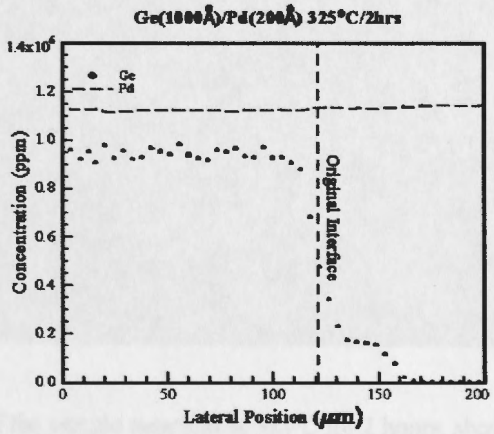

Figure 5.14: PIXE derived Pd and Ge concentration (in ppm) as a function of lateral position for the sample annealed at 325°C for 2 hours. The Pd concentration data were offset above those for Ge for clarity.

5.3.3 Scanning Electron Microscopy (SEM) Results

Displayed in Fig. 5.15 is an SEM micrograph of the sample annealed at 325°C for 2 hours.

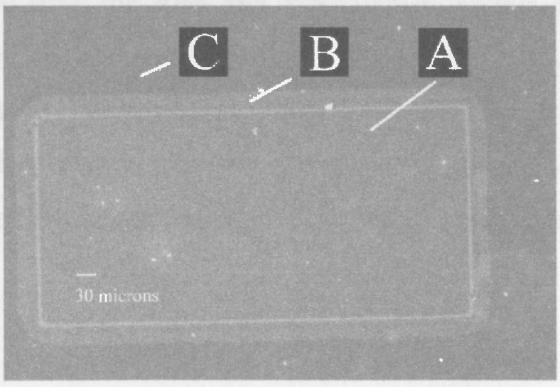

Figure 5.15: SEM micrograph of the sample annealed at 325°C for 2 hours showing the whole sample and different regions.

To observe more detail, Fig. 5.16 presents a scan of the regions A to C, at higher magnification. A number of interesting features are observed in this micrograph. Dark patches labeled 'X' are seen in the central region of the island. The region labeled 'Y' shows a unique texture in which are features that appear to be cracks. At the interface between regions B and C are areas labeled 'Z' that suggest irregular growth of the phase Pd_2Ge.

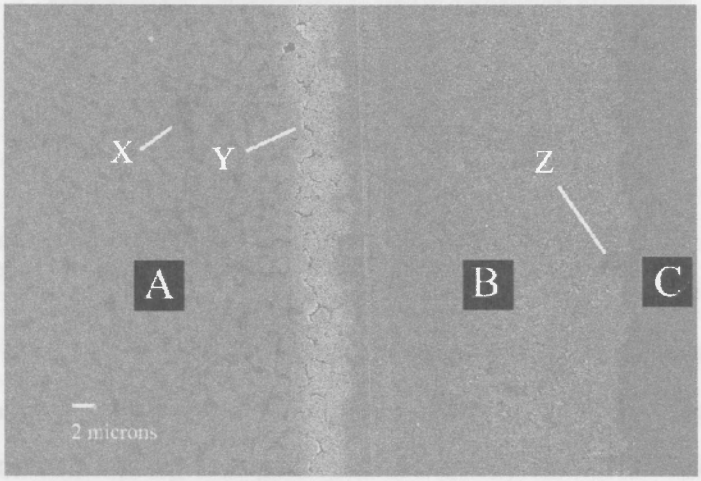

Figure 5.16: SEM micrograph of the sample annealed at 325°C for 2 hours, showing a close-up scan of the different regions and other features of interest.

A closer look at the feature labeled 'Z' is presented in Fig. 5.17. The phase Pd_2Ge has a fractal type of growth, with areas of unreacted Pd clearly visible within the growth region. This was not observed throughout region B but only in the section close to region C. It may be recalled from the RBS and PIXE results of this sample that this part of region B showed a gradual decrease in Ge concentration. It is now clear that this decrease was not as a result of a change in composition but rather the effect of summing data parallel to the interface across alternating areas of Pd_2Ge and unreacted Pd, thereby reducing the combined Ge concentration, the reduction being greater as one gets closer to region C.

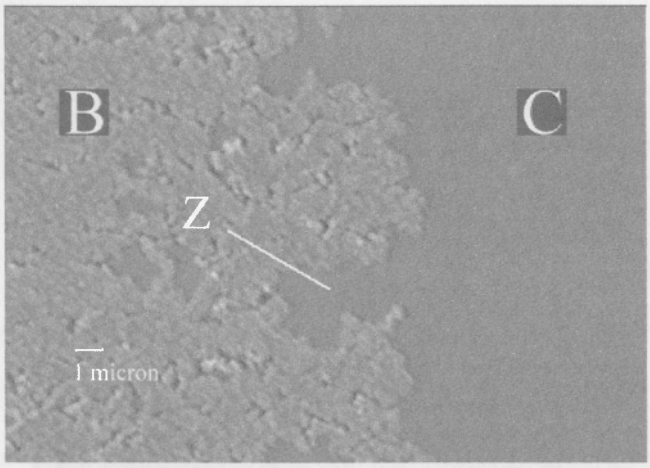

Figure 5.17: Magnified SEM scan of the area around the interface between regions B and C. The feature labeled 'Z' is unreacted Pd that gives a tentacle appearance to the Pd_2Ge growth.

Fig. 5.18 is a micrograph showing parts of regions A and B of a sample annealed at 325°C for 4 hours. It will be recalled that RBS results revealed the presence of Pd at the surface in region A. Looking at Figs. 5.16 and 5.18 it would seem that the phase PdGe was mixed with unreacted Ge at the surface, in a manner that produced the 'puffy' texture observed in region A. The features 'X' appear to be areas rich in unreacted Ge. As the Ge was consumed from these areas, the sample structure was weakened, resulting in cracks, this can clearly be seen in Fig. 5.18. These cracks introduced discontinuity in the matrix of the sample, thereby impeding Ge flow to the reaction interface. Consequently, further Pd_2Ge growth at the Pd interface was fractal due to insufficient and inhomogenous Ge supply.

The process described above made it difficult to observe PdGe in an exposed state. That was because PdGe exposure resulted in crack formation which inhibited and eventually stopped the reaction. It was only at a relatively low temperature and for long anneal times that exposure of a considerable amount of PdGe was achieved as presented in the RBS results of Fig. 5.12.

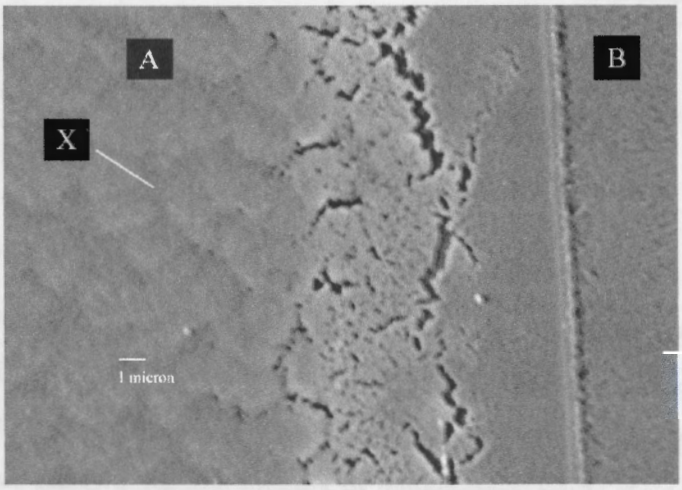

Figure 5.18: SEM micrograph a Ge island (1000Å) on a thin Pd film (200Å) annealed at 325°C for 4 hours, showing pronounced cracks in the area around the interface between regions A and B.

An SEM line scan is shown in Fig. 5.19. The path of the line scan is shown on the left. The top and bottom graphs, on the right, show the estimated relative Ge and Pd concentrations as a function of position, respectively. Percentage concentration was then determined in regions B and C; results are indicated in the figure.

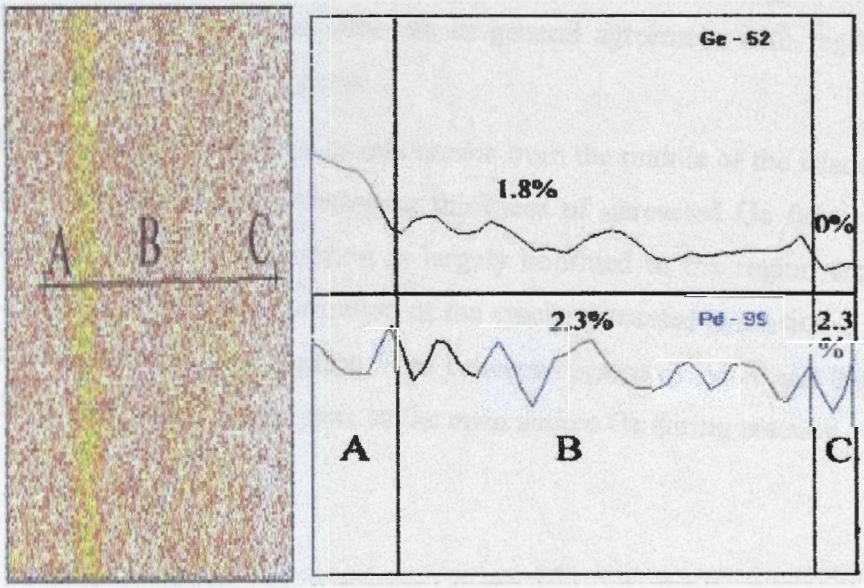

Figure 5.19: An SEM line scan giving an estimate of the concentration of different atomic species as a function of position. The path of the line scan is shown on the left. The top and bottom graphs on the right show the estimated Ge and Pd concentrations as a function of position.

Region B consisted of the phase Pd_2Ge which was expected to yield a concentration ratio of Pd to Ge of 1:0.5. The ratio obtained was 1:0.8.

5.3.4 Atomic Force Microscopy (AFM) Results

One of the samples scanned on the AFM was that annealed at 325°C for 1 hour; Fig. 5.20 shows the results. The top picture shows an optical micrograph on which is a line indicating the path of the scan. In the middle is a graph giving results of the AFM scan. The vertical axis gives relative surface heights in nanometres, while the horizontal axis gives the corresponding lateral distance in microns. At the bottom is a small table giving the lateral distance between the selected points and their difference in height.

Compared to the RBS results given in Fig. 5.11, AFM results show a quicker fall in thickness at the interface of region B with the unreacted Pd of region C. This gives further evidence that the gradual decrease observed in the RBS results was not as a result of a change in composition but rather the effect of summing data parallel to the interface across alternating areas of Pd_2Ge and unreacted Pd, thereby reducing the combined thickness. Results of the two techniques are in general agreement with regard to the observed steps between different regions.

From the AFM results, it is seen that as one moves from the middle of the island (region A) to the Pd_2Ge (region B), the overlaying thickness of unreacted Ge falls relatively quickly, indicating that Ge consumption is largely confined to the region around the island edges. This promotes early formation of the cracks discussed in section 5.2.3. The cracks are as a result of Ge consumption from between regions of PdGe and they occur around the island edge which is seen here as the main source Ge during reaction.

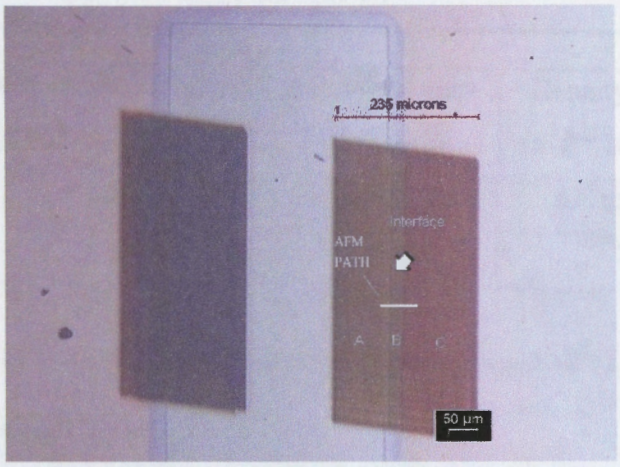

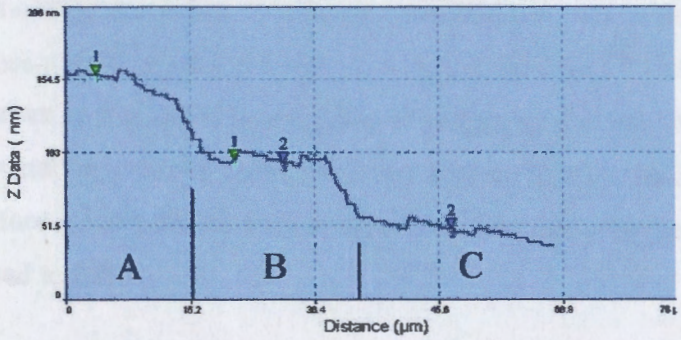

#	Lateral distance (µm)	Height difference (nm)
1	17	60
2	21	46

Figure 5.20: An optical micrograph with a line indicating the location of an AFM scan. The middle graph gives results of the scan. The table at the bottom gives lateral distances between the marked points and their difference in height.

By using the AFM and RBS results in Figs. 5.20 and 5.11 respectively, in a manner similar to that illustrated for the Ir-Ge system, a density estimate of Pd_2Ge was obtained and is given in Fig. 5.20.

Phase	RBS 'Areal Density' ($x10^{15}$ atoms.cm^{-2})	AFM thickness ($x10^{-8}$ cm)	Density Estimate ($x10^{22}$ atoms.cm^{-3})
Pd	115	170 (From RBS)	6.8 (Known)
Pd_2Ge	185	630	2.9

Table 5.1: The RBS and AFM results used in obtaining a value for the density of Pd_2Ge.

5.4 Analysis and discussion

As seen in the phase diagram of Fig. 5.1, this system has eutectics at 36 and 81 atm. % Pd; the liquidus minimum is generally accepted as that at 64% Ge.[69,70] An EHF diagram of the system is shown in Fig. 5.21. Since PdGe is congruent and has the most negative effective heat of formation, it is the phase predicted to form first by the EHF model. Our results do not therefore agree with the EHF model since the other congruent phase, Pd_2Ge was the first observed to form.

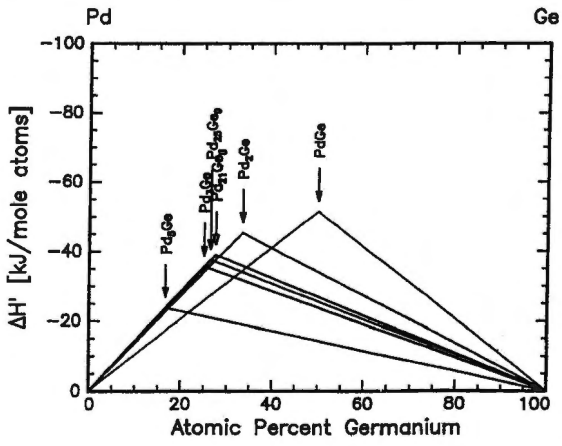

Figure 5.21: An EHF diagram of the Pd-Ge system.

It was found from thin film study of the Pd-Ge system that the congruent phase Pd_2Ge was the first to form. Reaction was observed to begin at around 100°C. The only other congruent phase of the system, PdGe, was seen to form second; no other phases were observed. These results are in agreement with those obtained by Hsieh et. el.[72] and others.[65,71,73]

Shown schematically in Fig. 5.22 are the three regions observed in the lateral diffusion couples of the Pd-Ge system. Phases and position of the original interface are indicated in the figure.

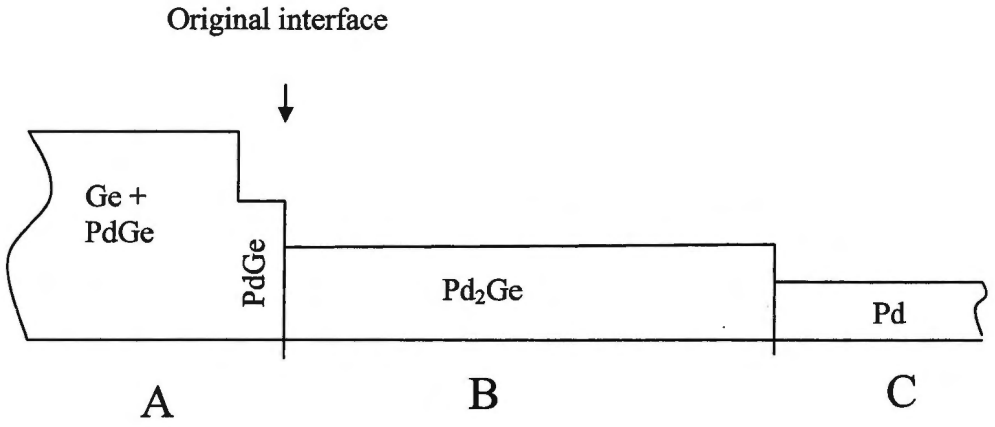

Figure 5.22: Diagram showing different phases observed in lateral diffusion couples of the Pd-Ge system.

The equations of reaction at each interface and corresponding heats of reaction are given in Table 5.2. Components of the calculations are shown beneath each equation. The heat of formation values used were as compiled by Pretorius et al.[14]

Interface	Equation of Reaction	Heat of Reaction ΔH_R° (kJ mol^{-1}atm^{-1})
A-B	No reaction	
B-C	2Pd + Ge → Pd_2Ge 2(0) 1(0) 3(-45.3)	-45.3

Table 5.2: The equation of reaction at the B-C interface and the corresponding heat of reaction. The values in the table are per atom i.e. the total heat of formation for the molecule is divided by the number of atoms in the molecule.

As mentioned earlier, the Pd peak of the solid line in Fig. 5.7 lies at the surface position, indicating that there was some Pd at the surface. As in the Pt-Ge case, the 'shoulder' marked in that figure indicated that there was less Pd at the surface than deeper down. This region consisted of PdGe at the bottom while at the top there was unreacted Ge intermingled with PdGe. Our SEM results further revealed the formation of cracks in the source region near the original island interface.

The process by which the Pd rose to the surface could be described in much the same way as for the Pt-Ge system. Ge in the island reacted with the underlying Pd eventually forming the most Ge rich phase PdGe which rose to the surface in columns hence giving the surface a 'puffy' appearance as observed in the SEM. Excess Ge then diffused from the source through the PdGe to form Pd_2Ge outside the original island interface. It is believed that as the Ge between the columns was consumed the structure was weakened, resulting in the cracks observed by our SEM. These cracks were clearly seen as forming between the 'puffs' and they introduced discontinuity in the matrix of the sample, thereby impeding Ge flow to the reaction interface where the phase Pd_2Ge was growing. Further Pd_2Ge growth at the Pd interface was then characteristically fractal due to insufficient and inhomogenious Ge supply. The equation of the reaction by which Pd_2Ge was formed is given in Table 5.2; this reaction is seen to have a highly negative heat of reaction. The interface between PdGe and Pd_2Ge lies at the position of the original island interface and does not shift with increase in anneal time, suggesting that there was no resultant growth interaction at this interface. The exposure rate of the phase PdGe could not be monitored for the reasons explained earlier.

Growth of the phase Pd_2Ge was monitored at the temperatures 275°C, 300°C and 325°C. The periods of annealing were chosen so as to obtain a reasonable range of growth widths at each of the three temperatures; results are presented in Fig. 5.23. Fig. 5.24 is a plot of the squares of the reaction lengths with time of annealing at the three temperatures.

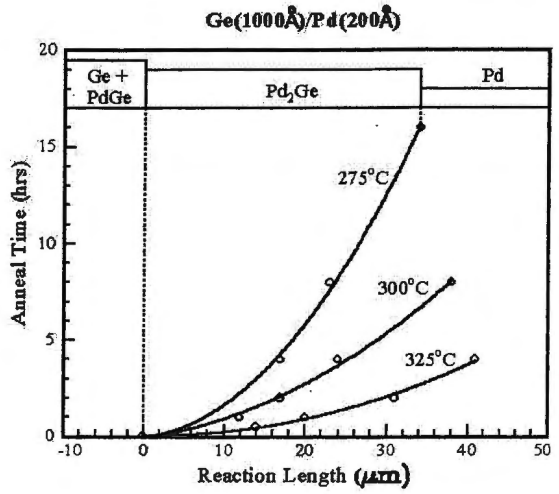

Figure 5.23: Plot of reaction length with time of annealing for the phase Pd_2Ge temperatures 275, 300 and 325°C.

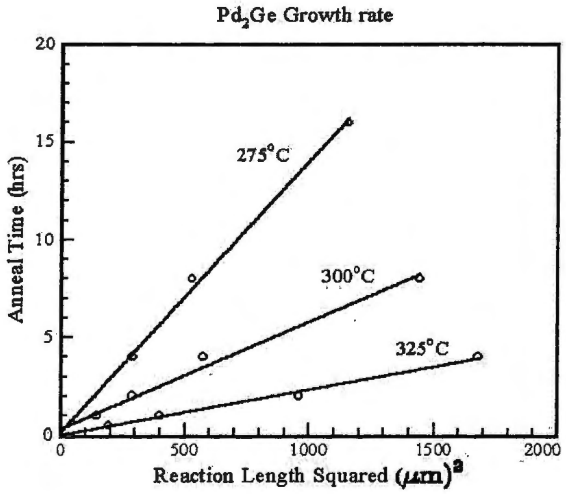

Figure 5.24: Plot of reaction length squared with time of annealing for the phase Pd_2Ge at temperatures 275, 300 and 325°C.

Like the growth process of phases in the Ir and Pt systems, the parabolic nature of the Pd_2Ge growth characteristics indicates relatively fast reactions at the interfaces. Interfacial reaction barriers do not play a limiting role in the growth, which is diffusion controlled.

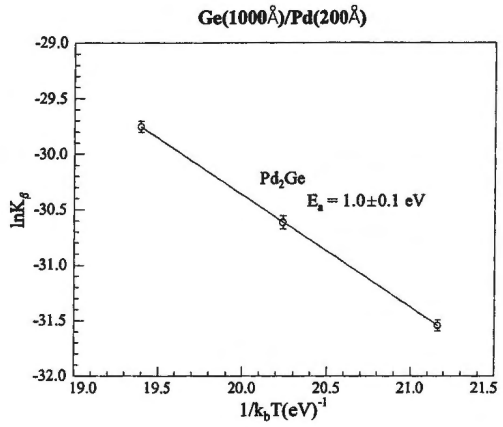

Figure 5.25: Arrhenius plots, lnK_β versus $1/k_bT$, showing temperature dependence of Ge diffusion rate through Pd_2Ge, yielding an average activation energy of 1.0 ± 0.1 eV.

Fig. 5.25 is an Arrhenius plot showing the temperature dependence of the Ge diffusion rate through Pd_2Ge. The activation energy determined from this plot, E_a = 1.0±0.1 eV, is high enough to characterize a non surface diffusion process.

Table 5.3 shows how this system can be treating as one of single phase growth in the kinetic barrier model of Gösele and Tu.[24]

A	$A_\gamma B$	B
Ge	Pd_2Ge	Pd
	γ=1/2	

Table 5.3: A table showing how the growth in the Pd-Ge lateral diffusion system can be treating as one of single phase growth in the kinetic barrier model of Gösele and Tu.

From equation 1.45,

$$G_\gamma = \Omega_0 \frac{(1+\gamma)(1+Pd)}{\gamma - Pd} = 3\Omega_0 \qquad (5.1)$$

As in the previous two chapters, the value used for the atomic volume Ω_0 was 16×10^{-24} $cm^3/at.$[32] Table 5.4 shows the values of $\Delta C_\gamma^{eq} \tilde{D}_\gamma$ obtained from the calculations at each temperature.

T (°C)	$\Delta C_\gamma^{eq} \tilde{D}_\gamma$ $(10^{15} m^{-1} s^{-1})$
275	0.209
300	0.528
325	1.25

Table 5.4: Values of $\Delta C_\gamma^{eq} \tilde{D}_\gamma$ obtained from the modified Gösele and Tu calculation at each annealing temperature.

A plot of the logarithm of χ against the reciprocal of the product, k_bT of the Boltzmann constant and the absolute temperature is shown in Fig. 5.26, where $\chi = \Delta C_\gamma^{eq} \tilde{D}_\gamma$.

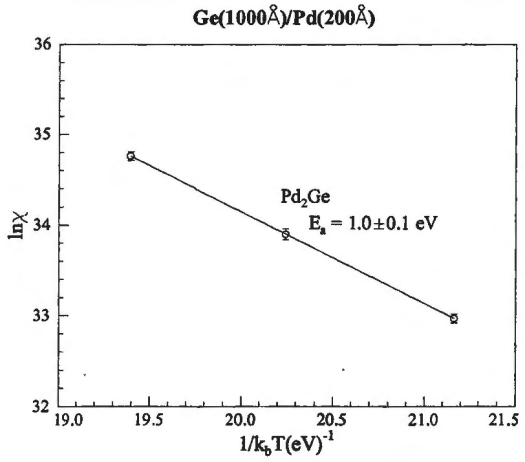

Figure 5.26: Arrhenius plot, $ln\chi$ versus $1/k_bT$, showing temperature dependence of Ge diffusion rate through Pd_2Ge, yielding an activation energy of 1.0 ± 0.1 eV. The quantity χ is the product, $\Delta C_\beta^{eq} \tilde{D}_\beta$ of the chemical inter-diffusion coefficients and equilibrium values of the Ge concentration difference across the phase.

The result of Fig. 5.26 from the modified Gösele and Tu calculation shows excellent agreement with the one obtained from the Arrhenius plot of lnK_β versus $1/k_bT$ shown in Fig. 5.25.

CHAPTER 6

THE RHODIUM – GERMANIUM SYSTEM

6.1 Introduction

Only 4 equilibrium phases exist for the Rh – Ge system viz., Rh_2Ge, Rh_5Ge_3, GeRh and $Rh_{17}Ge_{22}$, as can be seen from the phase diagram in Fig. 6.1. Wittmer et al.[71] observed RhGe as the first phase to form and $Rh_{17}Ge_{22}$ as the second. No other phases were observed in that work. There is no evidence of any other lateral diffusion work reported on this system.

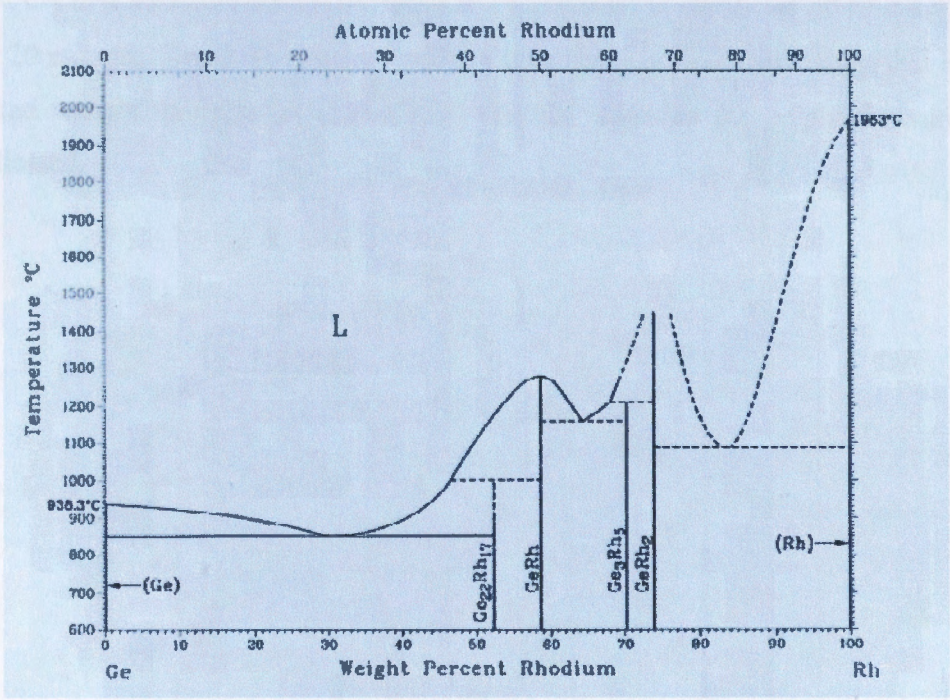

Figure 6.1: Phase diagram for the Rh – Ge system [69].

6.2 Thin Film Couples

The chance of getting excessive overlap of RBS peaks was greater in this system than in any other yet reported on in the present study, great care was taken to abate this. Two different sample structures were used in this study. The first structure was designed to observe initial stages of reaction and possible formation of any Rh rich germanides. For this, the structure SiO_2/Ge (170 /cm^2)/Rh (340 /cm^2) was used. These samples turned out to be too thin for X–ray analysis. The second structure was SiO_2/Ge (5000Å)/Rh (600Å), which was used to observe all other possible reactions. The matrix was enhanced to induce a good X–ray yield.

6.2.1 Phase Formation Sequence Results

Samples of the first structure described above were annealed at 300°C for 30 minutes and 350°C for 20 minutes. The RBS spectra obtained from these samples, including that from an unreacted sample, are shown in Fig. 6.2, with the expected Rh height for various phases indicated.

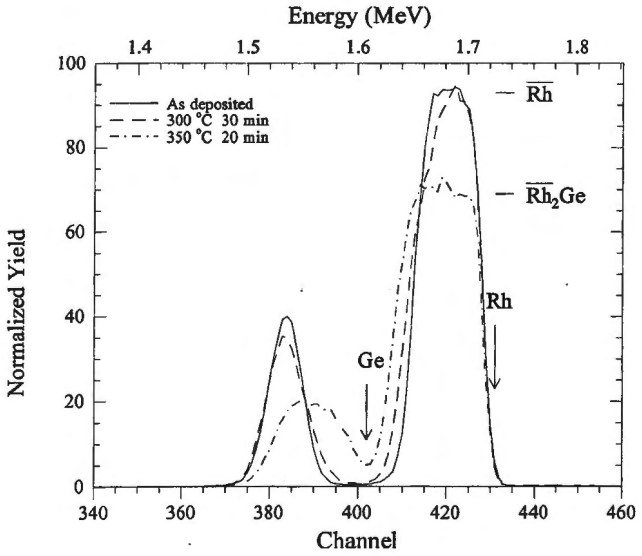

Figure 6.2: RBS spectra from an unreacted sample of composition SiO_2/Ge (170 /cm^2)/Rh (340 /cm^2) and from similar samples annealed at 300°C for 30 minutes and 350°C for 20 minutes. Ge and Rh surface positions are indicated.

RUMP simulations of the above spectra are shown in Fig. 6.3. Thickness and compositional information obtained is indicated in the inserts.

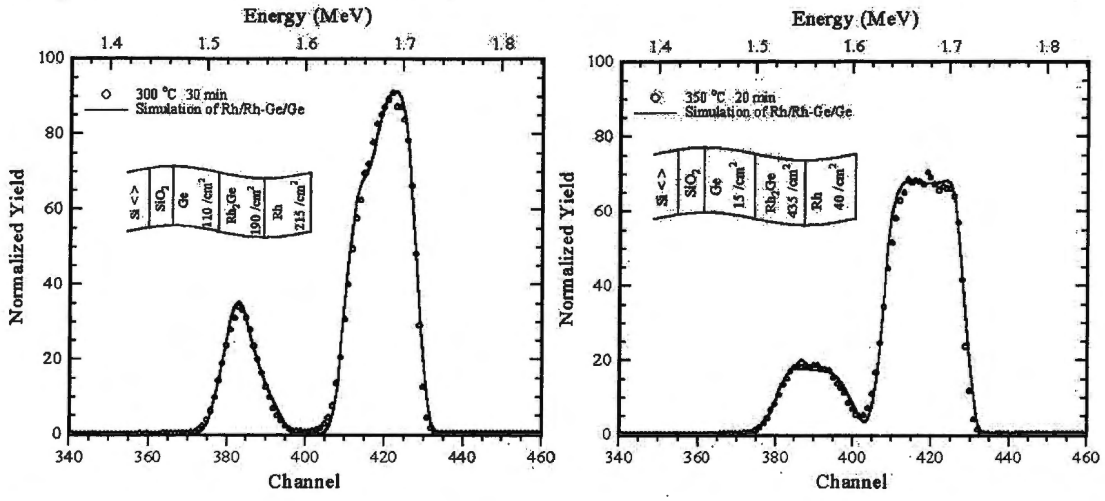

Figure 6.3: RBS spectra of samples SiO_2/Ge (170 /cm^2)/Rh (340 /cm^2) after annealing at 300°C for 30 minutes (left) and 350°C for 20 minutes (right). Only the phase Rh_2Ge is observed to form.

The only phase to form was Rh_2Ge. Where-as the limited amount of Ge atoms may have prevented more Ge rich phases from forming in the later part of the reaction, Rh_2Ge was the favored phase with some amount of unreacted Ge still present.

To observe further possible reaction in this system, the more Ge rich structure SiO_2/Ge (5000Å)/Rh (600Å) was annealed between 320 and 400°C, for times that were longer than those of the previous investigation. The RBS results are displayed in Fig. 6.4.

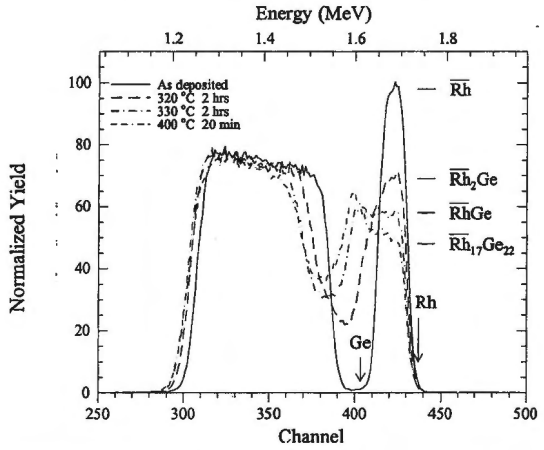

Figure 6.4: RBS spectra from an unreacted sample of composition SiO_2/Ge (5000Å)/Rh (600Å) and from similar samples annealed at various temperatures. Ge and Rh surface positions are indicated.

X-ray diffraction analysis was carried out on these samples. Fig. 6.5 and Fig. 6.6 show XRD results along side RBS spectra with simulations.

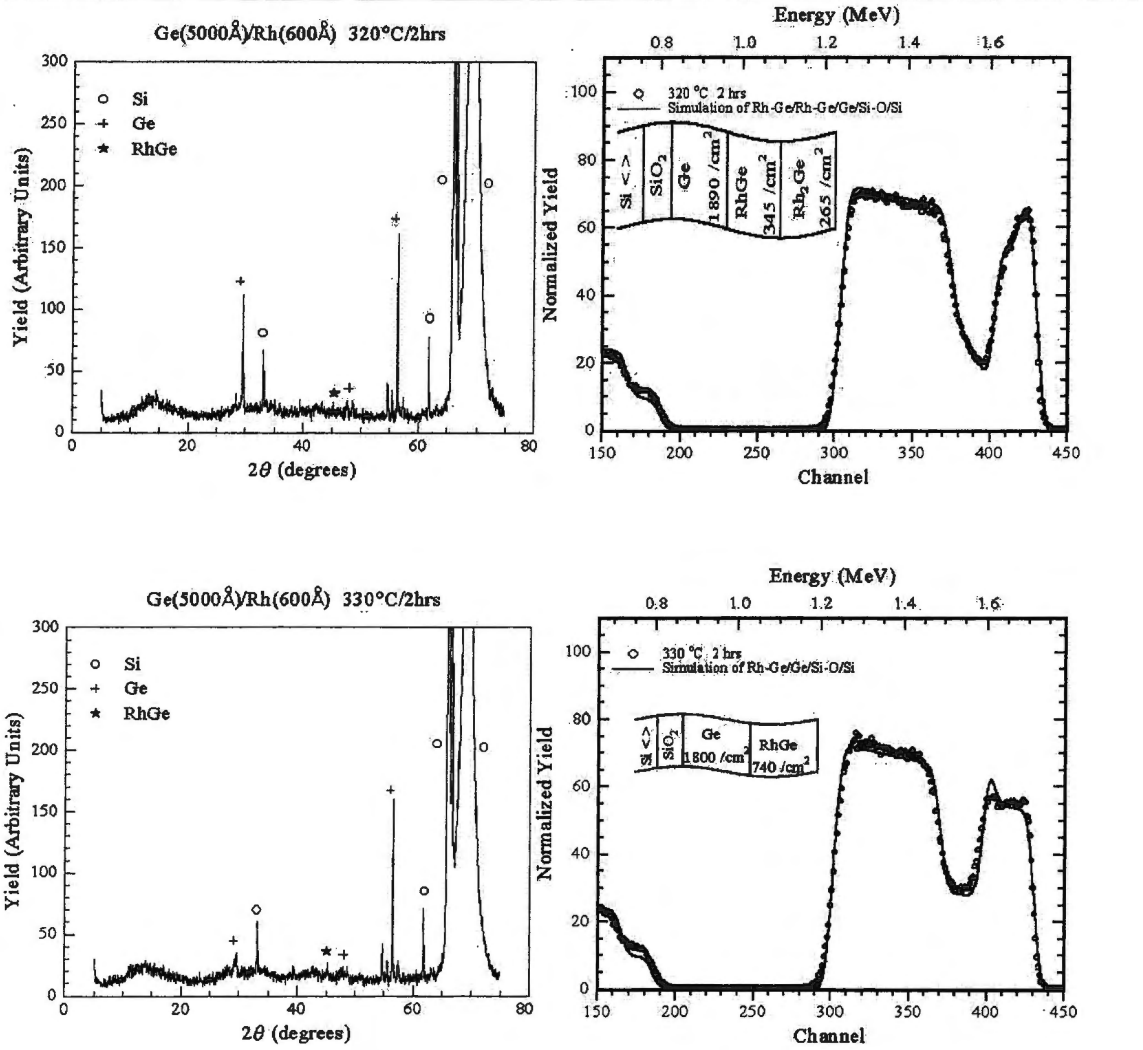

Figure 6.5: X-ray diffraction and corresponding RBS spectra of a sample of composition SiO_2/Ge (5000Å)/Rh (600Å) after annealing at 320°C and 330°C for 2 hours each. From RBS data the non-congruent phase Rh_2Ge is observed to convert to RhGe, Rh_2Ge X-ray peaks could not be observed.

Our RBS data strongly suggests the formation of the non-congruent phase Rh_2Ge as the first phase but there is no firm evidence of this from the X-ray data. Rh_2Ge appears to give way to RhGe and from Fig. 6.6 we see that $Rh_{17}Ge_{22}$ is formed after the latter phase. Only RhGe and $Rh_{17}Ge_{22}$ peaks were observed from the X-ray results, probably because the Rh_2Ge layer was too thin to induce a good X–ray yield. This result is in disagreement with Wittmer et al.[71], who did not observe Rh_2Ge formation but rather found RhGe as the first phase to form, followed by $Rh_{17}Ge_{22}$.

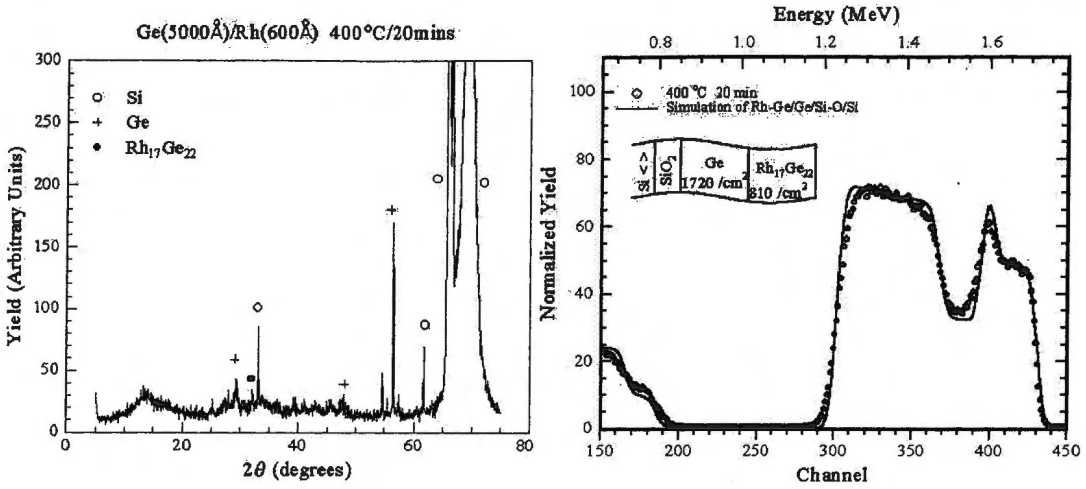

Figure 6.6: X-ray diffraction and corresponding RBS spectra of a sample of composition SiO_2/Ge (5000Å)/Rh (600Å) after annealing at 400°C for 20 min. The phases $Rh_{17}Ge_{22}$ is observed.

6.3 Lateral Diffusion Couples

Samples of Ge islands on thin Rh films were prepared and annealed at various temperatures for different lengths of time. Marked lateral diffusion was observed. For all samples, the various reaction zones were identified and their widths determined using optical microscopy. Microprobe RBS and PIXE scanning of chosen regions on selected samples was then carried out. SEM was also used. Eleven samples of the Rh-Ge system were analyzed on the microprobe of which two representative samples are discussed in this section (some others are presented in Appendix A).

6.3.1 μRBS Results

Shown in Fig. 6.7 is an optical micrograph of a sample with a Ge island (1000Å) on an Rh film (200Å) annealed at 600°C for 15 minutes. The darkened area was scanned on the microprobe. Four different regions observed are labeled A to D. The set of spectra generated for the scanned area is displayed in Fig. 6.8 as a function of lateral position. The figure is orientated such that spectra from the middle of the island lie at the back while those derived from the unreacted Rh film are in front.

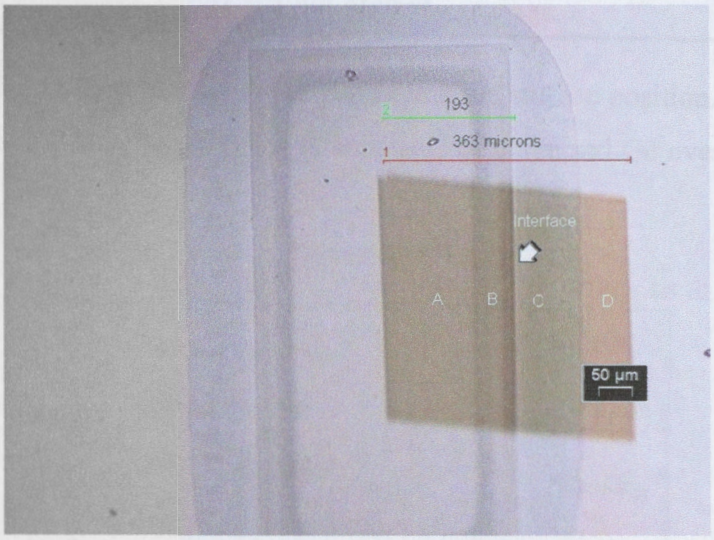

Figure 6.7: Optical micrograph of a Ge island (1000Å) on an Rh film (200Å) annealed at 600°C for 15 minutes.

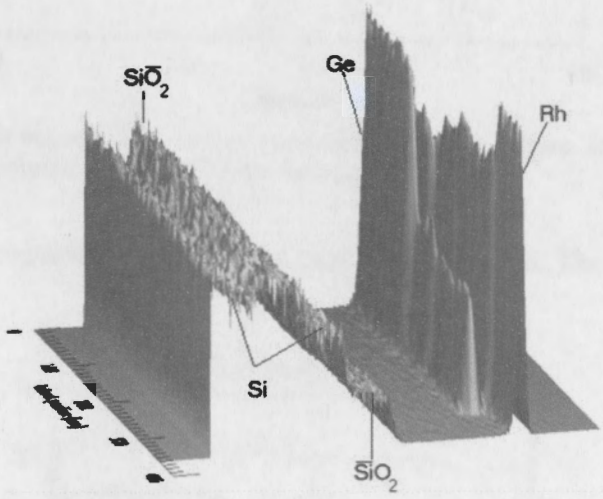

Figure 6.8: RBS spectra obtained from the scanned area as a function of lateral position.

A spectrum picked from each of the four regions labeled A to D is shown in Fig. 6.9. The spectrum from region D shows a peak of unreacted Rh and no Ge. Peak heights of the spectra taken from regions C and B show the phases RhGe and $Rh_{17}Ge_{22}$ respectively. The germanides in these two regions are seen at the surface position. It can be seen from the solid line in the figure that the region A consisted of unreacted Ge and the phase

$Rh_{17}Ge_{22}$. The Rh peak of the solid line lies below the surface position. This shows that there was no Rh at the surface. Region A consisted of unreacted Ge overlaying the phase $Rh_{17}Ge_{22}$.

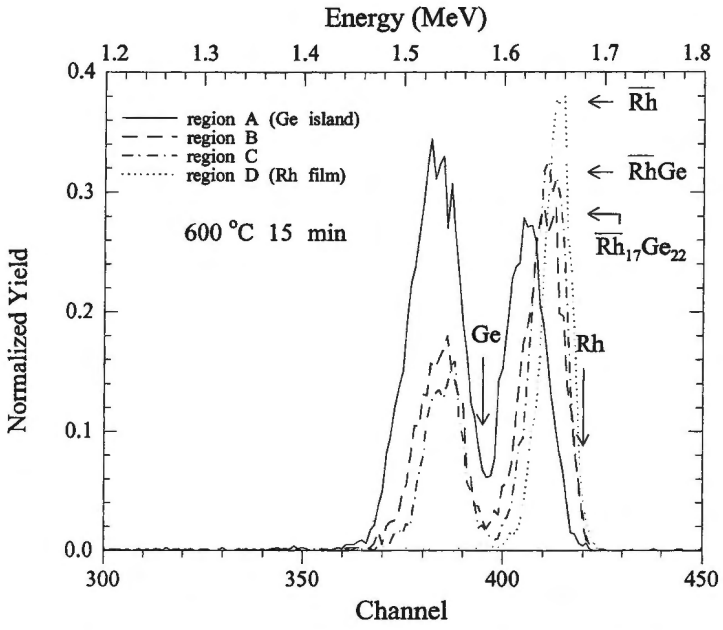

Figure 6.9: Superposition of selected RBS spectra from each of the five regions. Rh peak heights of the various phases and surface positions of Ge and Rh are indicated.

Rh and Ge peaks were separately integrated at each beam position. The results are shown in Fig. 6.10.

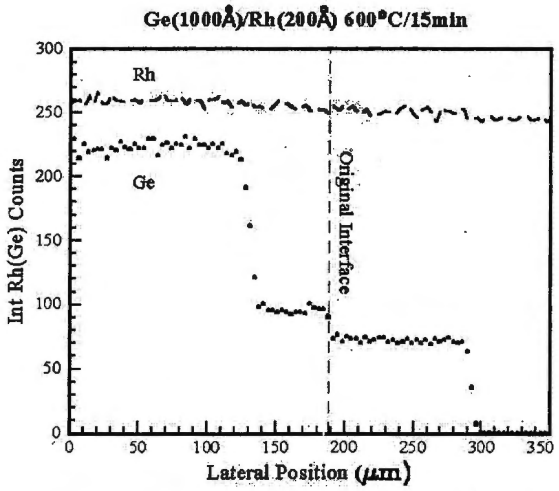

Figure 6.10: Integrated counts of the Rh and Ge peaks as a function of lateral position for a Ge island (1000Å) on an Rh film (200Å) annealed at 600°C for 15 minutes. The data of Rh counts were raised above those for Ge for clarity.

A sharp drop in the Ge signal is observed between different regions and at the edge of the outermost reaction region unlike the case in the Pd-Ge system.

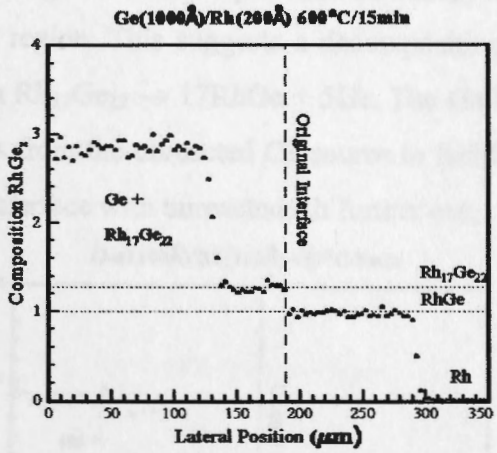

Figure 6.11: Stoichiometric information of a Ge island (1000Å) on an Rh film (200Å) annealed at 600°C for 15 minutes, derived from integrated counts of the Rh and Ge peaks, as a function of lateral position.

Fig. 6.11 shows the stoichiometric information, the interface between the phases $Rh_{17}Ge_{22}$ and RhGe lies at the original island interface position. Sharp compositional change is seen between the regions.

To demonstrate what was observed at temperatures above 600°C, an optical micrograph of a Ge island (1000Å) on an Rh film (200Å) annealed at 650°C for 5 minutes is presented in Fig. 6.12. Indicated are different regions and areas scanned on the microprobe.

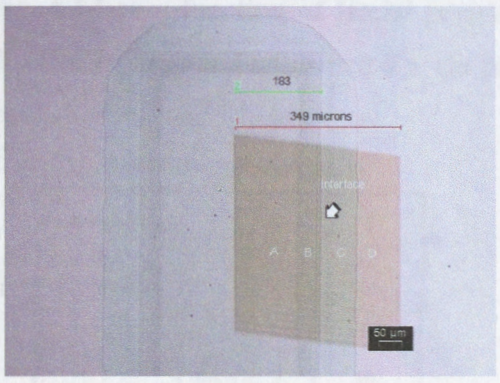

Figure 6.12: Optical micrograph of a Ge island (1000Å) on an Rh film (200Å) annealed at 650°C for 5 minutes.

The RBS data from the scanned area was analyzed and Fig. 6.13 shows the stoichiometric information derived from integrated counts of the Rh and Ge peaks as a function of

lateral position. An interesting feature is the presence of a small region of the phase RhGe inside the original island region. This suggests a decomposition of the phase $Rh_{17}Ge_{22}$ into RhGe by the reaction $Rh_{17}Ge_{22} \rightarrow 17RhGe + 5Ge$. The Ge liberated in this reaction joins the flux of Ge atoms from the unreacted Ge source to facilitate the growth reaction $Rh + Ge \rightarrow RhGe$ at the interface with unreacted Rh further out.

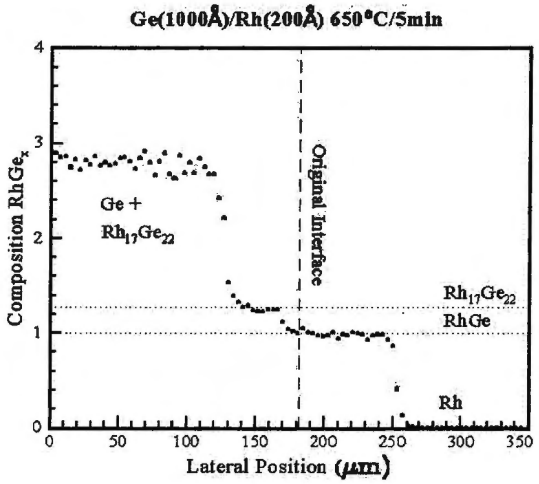

Figure 6.13: Stoichiometric information of a Ge island (1000Å) on an Rh film (200Å) annealed at 650°C for 5 minutes.

Each RBS spectrum was then simulated by RUMP to obtain thickness information. This information is plotted in Fig. 6.14 as a function of lateral position. A sharp change in thickness is seen between the RhGe phase and unreacted Rh. On the other hand, we see a fairly gradual change between $Rh_{17}Ge_{22}$ and RhGe.

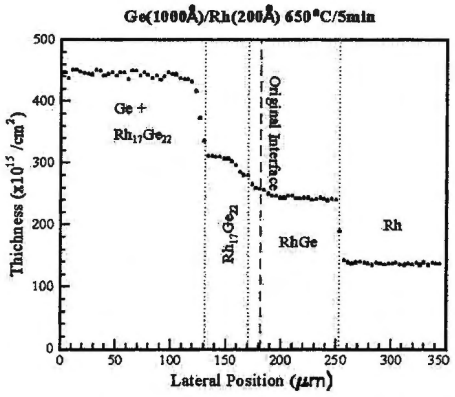

Figure 6.14: RUMP simulated thickness of the various phase regions as a function of lateral position.

6.3.2 μPIXE Results

A uniform rectangular region was selected from the center of the island for the sample with a Ge island (1000Å) on an Rh film (200Å) annealed at 600°C for 15 minutes (Fig. 6.7). All PIXE spectra in this region were extracted and the average is displayed in Fig. 6.15.

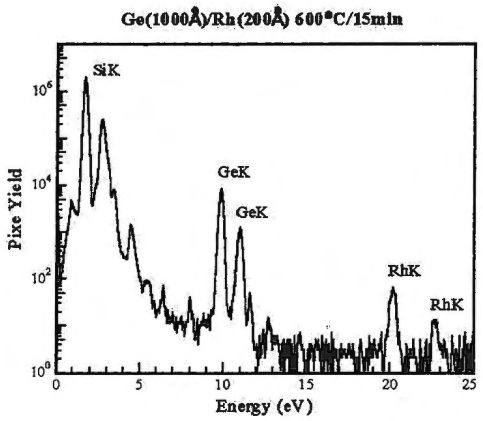

Figure 6.15: Average PIXE spectrum extracted from a region in the center of a Ge island (1000Å) on an Rh film (200Å) annealed at 600°C for 15 minutes.

The Ge and Rh peaks used in PIXE analysis using GeoPIXE II simulation are indicated in the figure. The K lines were prominent and proved to be sufficient for the study. As shown earlier, the Ge and Rh peaks in the RBS spectrum were not well separated. In the PIXE spectra these are well separated, making this a more convenient technique for use on relatively thick samples.

PIXE data were extracted and added along parallel lines aligned with regional interfaces. These spectra were then analyzed to extract compositional information as a function of lateral position; results are shown in Fig. 6.16. This figure shows similar results to those obtained from the RBS analysis and presented in Fig. 6.10.

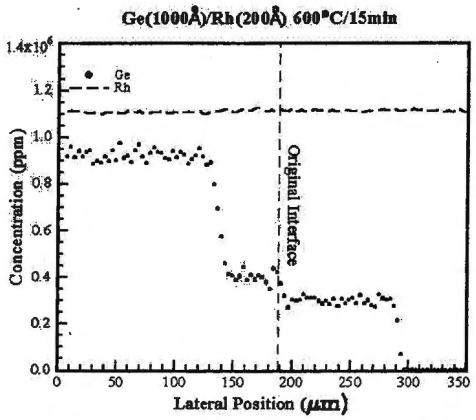

Figure 6.16: PIXE derived Rh and Ge concentration (in ppm) as a function of lateral position for a Ge island (1000Å) on an Rh film (200Å) annealed at 600°C for 15 minutes. The Rh concentration data were raised above those for Ge for clarity.

PIXE analysis was also carried out on the sample of a Ge island (1000Å) on an Rh film (200Å) annealed at 650°C for 5 minutes, shown in the optical micrograph of Fig. 6.12. The results are shown in Fig. 6.17 and are also in agreement with RBS results.

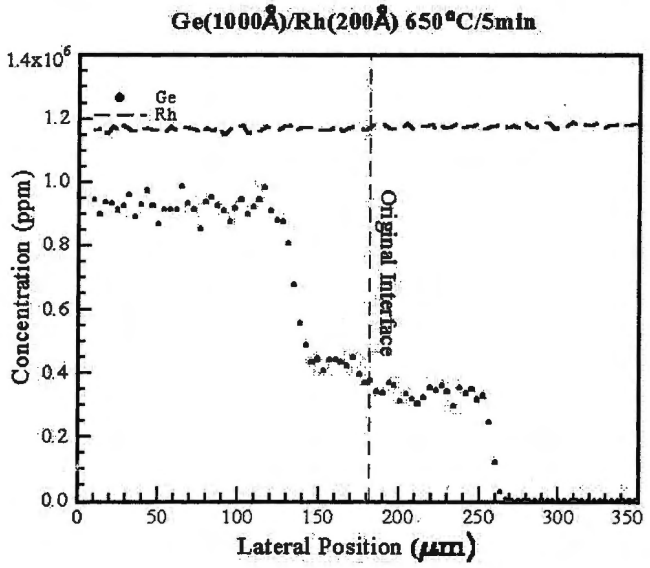

Figure 6.17: PIXE derived Rh and Ge concentration (in ppm) as a function of lateral position for a Ge island (1000Å) on an Rh film (200Å) annealed at 650°C for 5 minutes. The Rh concentration data were raised above those of Ge for clarity.

6.3.3 Scanning Electron Microscopy (SEM) Results

The first sample discussed in the previous sections, i.e., with a Ge island (1000Å) on an Rh film (200Å) annealed at 600°C for 15 minutes, was analyzed using SEM. The

micrograph is shown in Fig. 6.18. The lateral extent of observed regions is in agreement with the results of previous sections.

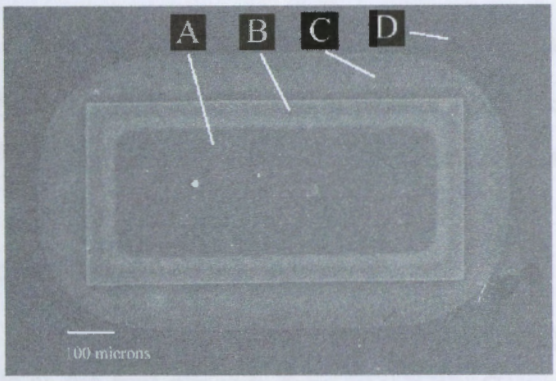

Figure 6.18: SEM micrograph of a Ge island (1000Å) on an Rh film (200Å) annealed at 600°C for 15 minutes showing the whole sample and different regions.

Structurally, this system exhibits a very 'well behaved' form of growth without any unique features of particular interest.

A line scan to estimate the concentration of different atomic species within the sample was carried out; the results are presented in Fig. 6.19. On the left of this figure is the scan path while the top and bottom graphs on the right show the estimated relative Ge and Rh concentrations as a function of position, respectively. Percentage concentrations were determined for each region; results are indicated in the figure.

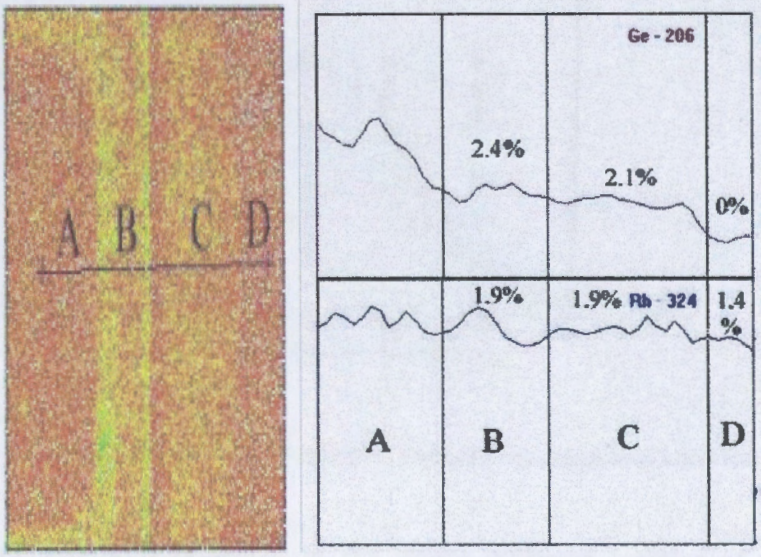

Figure 6.19: An SEM line scan giving an estimate of the concentration of different atomic species as a function of position. The path of the line scan is shown on the left. The top and bottom graph, on the right show the estimated Ge and Rh concentrations as a function of position.

Regions B and C are composed of the phases $Rh_{17}Ge_{22}$ and RhGe which are expected to give concentration ratios of Rh to Ge, 1:1.3, and 1:1 respectively. The ratios obtained were in perfect agreement with expected results, also being 1:1.3 and 1:1.1 respectively.

6.4 Analysis and discussion

Our RBS data from the thin film study of this system strongly suggested the non-congruent phase Rh_2Ge as the first phase to form in the Rh–Ge system (there was no firm evidence of this from the X-ray data). This is in disagreement with Wittmer et al.[71] who observed RhGe as the first phase to be formed, followed by $Rh_{17}Ge_{22}$. Our results show Rh_2Ge giving way to RhGe, and $Rh_{17}Ge_{22}$ was formed after that.

The EHF diagram of the Rh-Ge system is shown in Fig. 6.20. Clearly our results do not agree with that EHF model since Rh_2Ge is not the phase with the most negative effective heat of formation at the liquidus minimum.

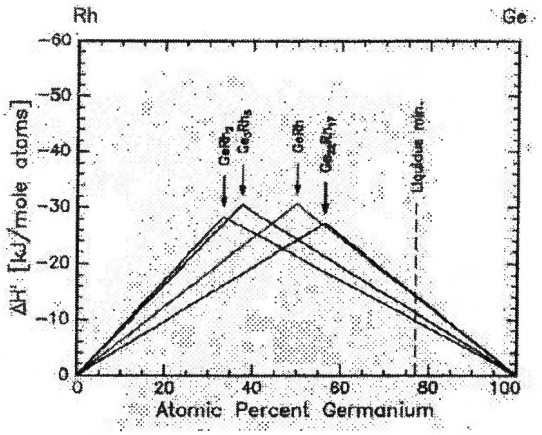

Figure 6.20: An EHF diagram, of the Rh–Ge system drawn using the Miedema semi imperical model.

There were 4 distinct regions observed in the lateral diffusion couples of the Rh-Ge system; these are represented schematically in Fig. 6.21. The relative position of the original interface and different phases are shown. As mentioned earlier, knowledge of the position at which the original interface lay was vital in analysis of the reactions taking place between different phase regions. This was particularly so in this system with wide

reaction regions and a slight shift of the reaction interface between regions B and C with respect to the original interface for different times of annealing. The situation is similar to that observed in the Ir system.

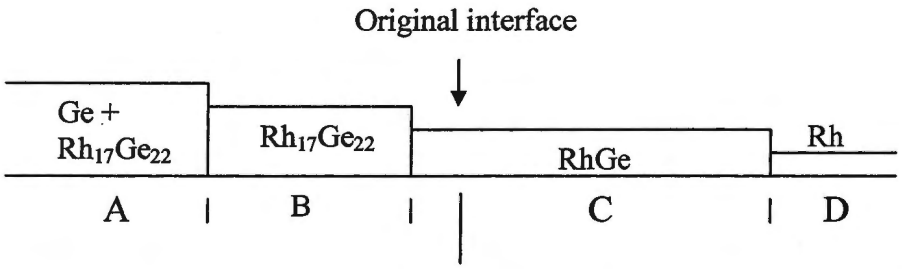

Figure 6.21: Diagram showing different phase regions observed in lateral diffusion couples of the Rh-Ge system.

Reactions at different interfaces and corresponding heats of reaction are given in Table 6.1. Components of the calculations are shown beneath each equation. Heat of formation values used are as compiled by Pretorius et al.[14]

Interface	Equation of Reaction	Heat of Reaction ΔH_R° (kJ mol^{-1}atm^{-1})
B-C	$Rh_{17}Ge_{22} \rightarrow 17RhGe + 5Ge$ 39(-27.2) 2x17(-30.6) 5(0)	≅ 0
C-D	Ge + Rh → RhGe 1(0) 1(0) 2(-30.6)	-30.6

Table 6.1: Reactions at different interfaces and corresponding heats of reaction. Components of the calculations are shown beneath each equation. The values in the table are per atom i.e. the total heats of formation for molecules are divided by the number of atoms in the molecules.

The reaction process in this system was that Ge in the thick island interacted with the underlying Rh film resulting in $Rh_{17}Ge_{22}$. Atoms of Ge from the unreacted source diffused through the $Rh_{17}Ge_{22}$ to form RhGe outside the original island interface. As the overlying Ge was consumed, $Rh_{17}Ge_{22}$ was exposed and a slow decomposition reaction took place that resulted in the formation of the phase RhGe from $Rh_{17}Ge_{22}$, inside the

original island interface. As seen in Table 6.1, the heat of reaction of the decomposition is close to zero. It is surprising that this phase was not formed by a nucleation process as was $IrGe_4$ which was also formed by a process with a heat of reaction which was close to zero. It may be worth mentioning that the Rh-Si system has a nucleation controlled phase, Rh_4Si_5.[74] The decomposition of $Rh_{17}Ge_{22}$ gave out Ge atoms, which were added to the flux from the unreacted Ge source and diffused to the interaction interface with unreacted Rh forming RhGe. The heat of formation for the latter reaction has a relatively large negative value, as seen in Table 6.1.

The growths of $Rh_{17}Ge_{22}$ and RhGe were monitored by optical microscopy and SEM at the temperatures 450, 500 and 600°C. Results for carefully chosen annealing times are presented in Figs. 6.22, 6.23 and 6.24. The temperature range and annealing times were chosen in such a way that the decomposition of $Rh_{17}Ge_{22}$ into RhGe was not significant.

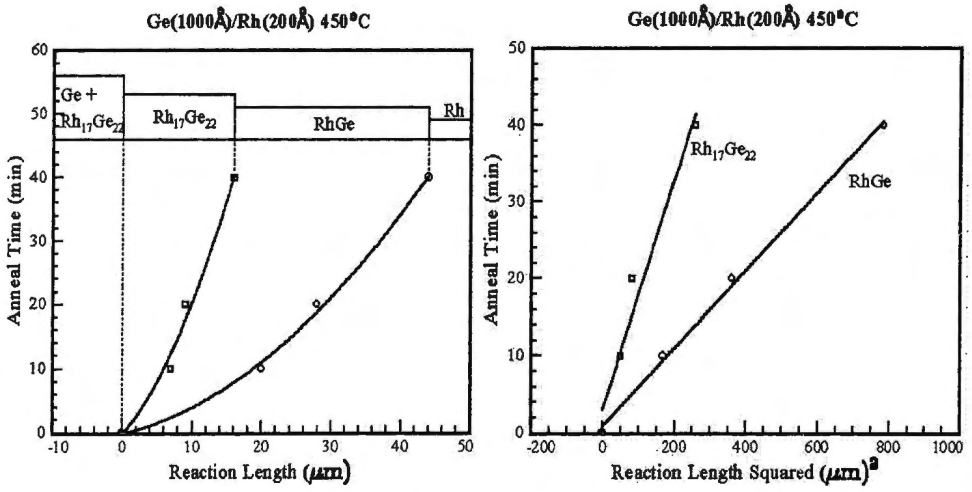

Figure 6.22: Plots of anneal time against reaction length and of anneal time against reaction length squared for the phases $Rh_{17}Ge_{22}$ and RhGe at 450°C.

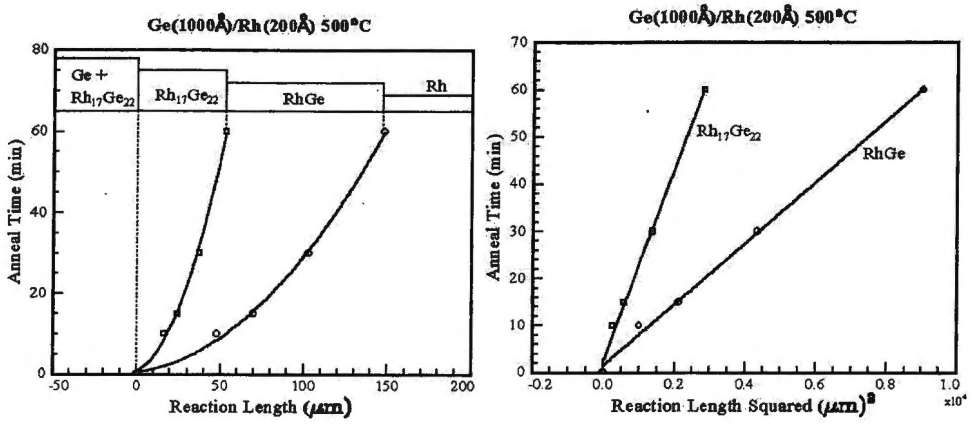

Figure 6.23: Plots of anneal time against reaction length and of anneal time against reaction length squared for the phases $Rh_{17}Ge_{22}$ and RhGe at 500°C.

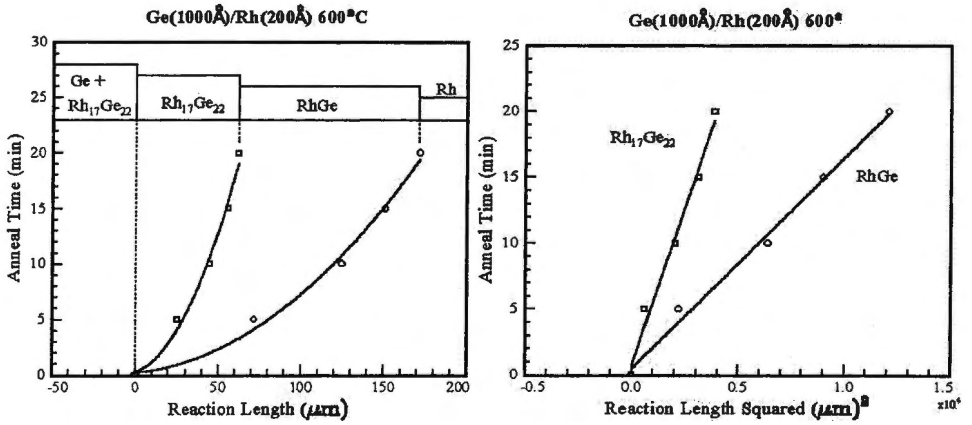

Figure 6.24: Plots of anneal time against reaction length and of anneal time against reaction length squared for the phases $Rh_{17}Ge_{22}$ and RhGe at 600°C.

Parabolic growth characteristics which indicate diffusion controlled growth are observed. Neither a transition from reaction to diffusion limited growth nor a critical length of one phase before another started to grow were observed. Arrhenius plots for the phases $Rh_{17}Ge_{22}$ and RhGe are shown in Fig. 6.25.

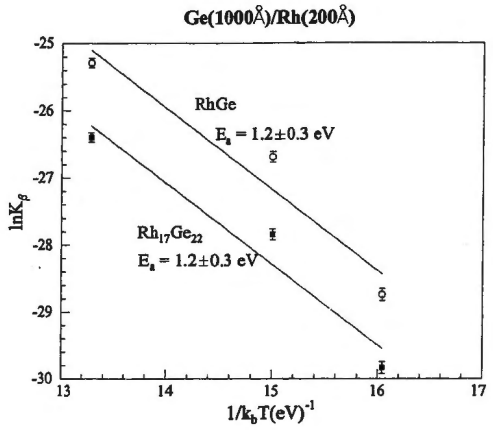

Figure 6.25: Arrhenius plots, lnK_β versus $1/k_bT$, showing temperature dependence of Ge diffusion rate through $Rh_{17}Ge_{22}$ and RhGe, yielding an average activation energy of 1.2 ± 0.3 eV for both phases.

The Arrhenius plots yield an average activation energy E_a = 1.2±0.3 eV for both $Rh_{17}Ge_{22}$ and RhGe.

Table 6.2 gives the values of the width ratios of the different phase regions as a function of the annealing time at the temperatures 450, 500 and 600°C.

TEMP [T (°C)]	TIME [t (min)]	WIDTH OF $Rh_{17}Ge_{22}$ [x_β (μm)]	WIDTH OF RhGe [x_γ (μm)]	RATIO x_γ/x_β
450	10	7	6	0.9
	20	9	10	1.1
	40	16	12	0.8
500	10	16	32	2.0
	15	24	46	1.9
	30	37	65	1.8
	60	53	95	1.8
600	5	25	47	1.9
	10	45	80	1.8
	15	56	95	1.7
	20	62	110	1.8

Table 6.2: Values of the width ratios for the phases $Rh_{17}Ge_{22}$ and RhGe as a function of the annealing time at various temperatures.

The width ratios are reasonably consistent at each temperature, which implies that the diffusion system acquired constant flux ratios as explained in section 1.4.1.

This system can be modeled as one with a two phase regime of growth. Table 6.3 shows the parameters used in this modeling within the framework of the geometrically modified kinetic barrier model of Gösele and Tu.[24]

A	$A_\beta B$	$A_\gamma B$	B
Ge	$Rh_{17}Ge_{22}$	RhGe	Rh
	β=22/17	γ=1	
	z_β=3.1×10^{17} atoms/cm^2	z_γ=2.4×10^{17} atoms/cm^2	

Table 6.3: Parameters that are relevant to the geometrically modified Gösele and Tu calculation for the phases $Rh_{17}Ge_{22}$ and RhGe.

The values of the coefficients G_β and G_γ are;

$$G_\beta = \Omega_0 \frac{(1+\beta)(1+\gamma)}{\beta-\gamma} = 15.6\Omega_0 \qquad (6.1)$$

and

$$G_\gamma = \Omega_0 (1+\gamma)\left[\frac{1+Rh}{\gamma-Rh} + \frac{z_\gamma(1+\beta)}{z_\beta(\beta-Rh)}\right] = 4.75\Omega_0 .$$

As in the previous chapters, the value used for the atomic volume Ω_0 was 16 × 10^{-24} cm^3/at.[32] Table 6.4 shows the values of $\Delta C_\gamma^{eq}\tilde{D}_\gamma$ obtained from the calculations at each temperature.

T (°C)	$\Delta C_{\beta}^{eq}\tilde{D}_{\beta}$ $(10^{15} m^{-1}s^{-1})$	$\Delta C_{\gamma}^{eq}\tilde{D}_{\gamma}$ $(10^{15} m^{-1}s^{-1})$
450	0.830	1.35
500	6.29	10.7
600	26.1	42.9

Table 6.4: Values of $\Delta C_{\gamma}^{eq}\tilde{D}_{\gamma}$ obtained from the modified Gösele and Tu calculation at each annealing temperature.

A plot showing the logarithm of χ against the reciprocal of the product, k_bT of the Boltzmann constant and the absolute temperature is presented in Fig. 6.26, where $\chi = \Delta C_{\gamma}^{eq}\tilde{D}_{\gamma}$.

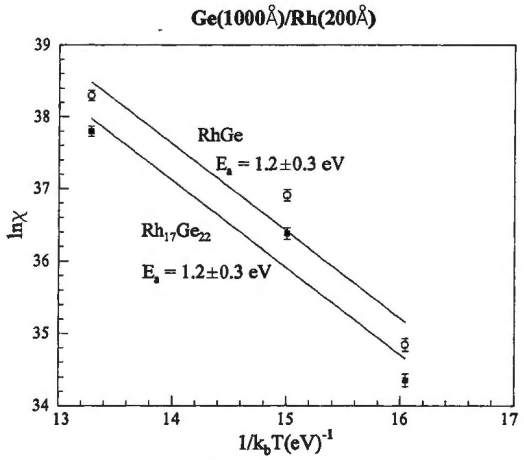

Figure 6.26: Arrhenius plot, $ln\chi$ versus $1/k_bT$, showing temperature dependence of Ge diffusion rate through $Rh_{17}Ge_{22}$ and RhGe, yielding an activation energy of 1.2 ± 0.3 eV for both phases. The quantity χ is the product, $\Delta C_{\gamma}^{eq}\tilde{D}_{\gamma}$ of the chemical inter-diffusion coefficients and equilibrium values of the Ge concentration difference across the phase.

The results of Fig. 6.26 from the modified Gösele and Tu calculations show excellent agreement with the ones obtained from the Arrhenius plots of lnK_{β} versus $1/k_bT$ shown in Fig. 6.25.

6.5 Use of PIXE in the study of Ni-Ge and Co-Ge lateral diffusion couples

As mentioned in Chapter 1, an important objective of this study was to see if PIXE could be used to study lateral diffusion systems that can not be studied using RBS due to excessive peak overlap. Representative lateral diffusion couples of the systems Co-Ge and Ni-Ge were studied and a brief demonstration of how this was done is given here. The two systems were chosen because of their position on the periodic table which is close (in terms of atomic number) to Ge and also because of the research interest that they have generated in recent years.

The phase diagram of the Ni-Ge system is shown in Fig. 6.27.

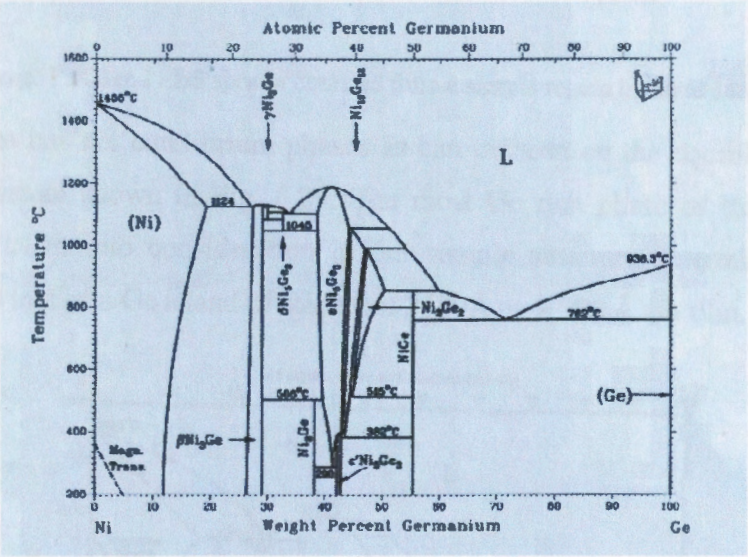

Figure 6.27: Phase diagram of the Ni-Ge system [69].

The system has five equilibrium phases with NiGe being the most Ge rich. Using this information, a structure with a Ge island of thickness 2500Å deposited on an Ni film of thickness 350 Å was found suitable for studying lateral diffusion in this system. Microprobe RBS and microprobe PIXE measurements were carried out on such samples. Fig. 6.28 shows the average PIXE and RBS spectra obtained from the same sample region in the middle of an island. It is clearly seen in this figure that the use of μRBS is not practical due to the excessive peak overlap. No amount of adjustment to the sample

structure could eliminate the overlap to a workable extent and still achieve the desired lateral diffusion. The PIXE spectrum on the other hand showed considerable spacing between the Ni and Ge peaks making it ideal for GeoPIXE II analysis.

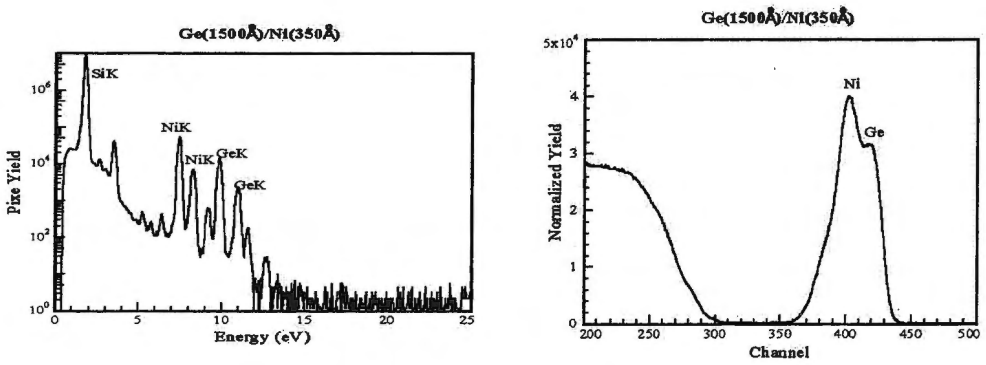

Figure 6.28: The average PIXE and RBS spectra obtained from a sample region in the middle of an island.

The Co-Ge system has six equilibrium phases as can be seen on the equilibrium phase diagram of the system shown in Fig. 6.29. The most Ge rich phase of this system is $CoGe_2$, this was taken into consideration in our sample structure determination. The structure used was that of a Ge island of thickness 2500Å on a 300 Å Co film.

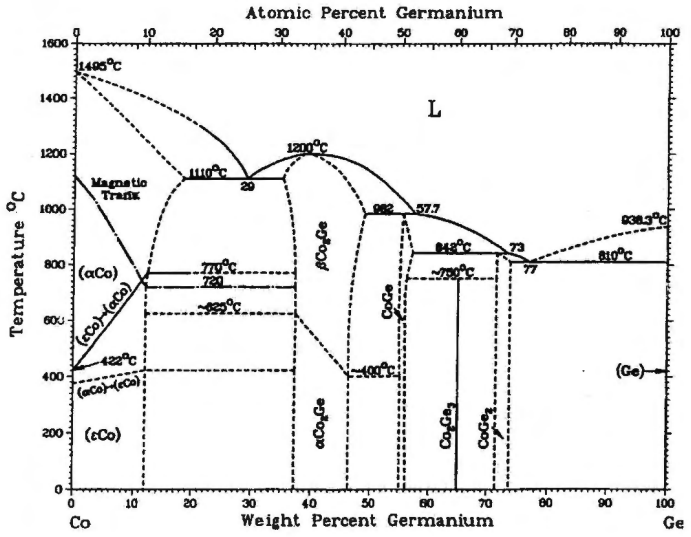

Figure 6.29: Phase and EHF diagrams of the Co-Ge systems [69].

As with the Ni, both RBS and PIXE data were collected from the same region of this system and Fig. 6.30 is the Co equivalent of the Fig. 6.28 for Ni.

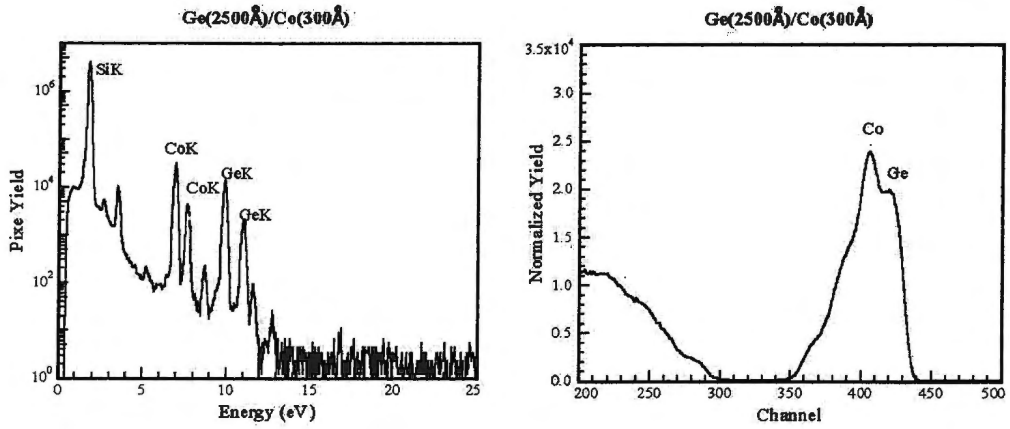

Figure 6.30: The average PIXE and RBS spectra obtained from a sample region in the middle of an island.

It can clearly be seen that for studying lateral diffusion couples of both the Ni-Ge and Co-Ge systems, μRBS is not practical whereas μPIXE is a suitable technique. A detailed report on this work may be presented within the scope of a future study.

CHAPTER 7

SUMMARY AND CONCLUSION

In this work we used conventional thin film couples to study the sequence of phase formation in germanide systems of the four Platinum Group Metals, Ir, Pt, Pd and Rh.

IrGe and Ir_4Ge_5 where the first phases to form in the Ir-Ge system and co-existed at annealing temperatures of around 350°C. These two phases were also found to co-existed in bulk diffusion couples.[58] Ir_3Ge_7 formed after these two phases while the $IrGe_4$ phase only appeared above 800°C. Ir_3Ge_4 which was reported to form in the work of Schubert and Pfisterer[59] was not observed in the present study.

In the Pt-Ge system, Pt_2Ge was the first phase formed, in agreement with the literature.[30,65-67] The second phase observed in the present work was Pt_3Ge_2. There is some disagreement in the literature about this phase, it was observed by some workers[68] while others[30,65-67] reported it as having been skipped. The next phase detected was PtGe and the last was $PtGe_2$. In the present work the non-congruent phase Pt_2Ge_3 was skipped between the last two phases in agreement with some workers[30] but not others.[65-68]

The only phases observed in the Pd-Ge system were the two congruent phases Pd_2Ge and PdGe. Pd_2Ge which has consistently been reported as the first phase to form in similar studies on this system,[65, 71-73] formed at around 100°C followed by PdGe, in agreement with Hsieh et al.[72] and a number of others.[65,71,73]

Our RBS data strongly suggested the formation of Rh_2Ge as the first phase in the Rh-Ge system but there was no firm evidence of this from the X-ray data because the samples were too thin to give a good X-ray yield. This phase appeared to give way to RhGe while $Rh_{17}Ge_{22}$ was formed as the last phase. Our results are in disagreement with Wittmer et al.[71] who found RhGe as the first phase to form using X-ray diffraction.

The results of our thin film study are summarized in Table 7.1. Temperatures at which the first reactions were observed to begin are indicated.

SYSTEM	PHASE FORMATION SEQUENCE	TEMPERATURE AT WHICH FIRST REACTION BEGINS
Ir-Ge	1st IrGe and Ir_4Ge_5 (Co-existing) 2nd Ir_3Ge_7 3rd $IrGe_4$	350°C
Pt-Ge	1st Pt_2Ge 2nd Pt_3Ge_2 3rd PtGe 4th $PtGe_2$	190°C
Pd-Ge	1st Pd_2Ge 2nd PdGe	100°C
Rh-Ge	1st Rh_2Ge 2nd RhGe 3rd $Rh_{17}Ge_{22}$	280°C

Table 7.1: Summary of the phase formation sequence results for the four systems studied. The temperatures at which the first reactions were observed to start are indicated.

By interposing a thin layer of Ti (12Å) to act as an inert marker between the coupling layers in the Ir-Ge system, the direction of atomic mobility was successfully monitored during the initial stages of the reaction. In the marker samples, IrGe and Ir_4Ge_5 were again found to coexist from the first stages of reaction. The movement of the marker indicated that Ge was the sole moving species during Ir_4Ge_5 formation. It was not certain whether Ge was also the sole moving species during IrGe formation, as explained in Chapter 3. It is interesting to note that in similar work on the Ir-Si system,[75,76] Si was found as the dominant diffusing species in the growth of the first two phases to form, which were IrSi and $IrSi_{1.75}$. The marker technique was also applied to the Pt-Ge system. Pt was found to be the dominant diffusing species during Pt_2Ge formation although some

Ge diffusion also occurred. This was in agreement with the results of a number of other workers.[30,65,66]

We have observed and analyzed some interesting aspects of lateral diffusion reactions. Lateral diffusion couples were found to give a useful insight into three important aspects of binary interactions:

1. They can be used as a qualitative means of determining the dominant diffusing species without the need of interposing an inert marker between the two coupling layers. An example of this was that when Ir islands were placed on Ge thin films, the lateral extent of the diffusion zone upon annealing was limited. It was observed that the Ge had a higher inward mobility than the outward diffusing Ir, leading to a thin diffusion zone on the periphery of the source region and inside the island region. Further annealing eventually lead to crack formation between the island interface and the surrounding thin film, consequently halting the lateral reaction. The opposite configuration with a Ge island on an Ir film resulted in marked lateral diffusion upon annealing. This showed that Ge was the dominant moving species during the formation of the outermost phase (at the Ir interface).

2. They provide a way of studying the transition from thin film to bulk diffusion. The determination of a critical thickness that a phase grows before another begins to form is a good example of this. More details on this in terms of the present work are given later.

3. By observing the pattern by which the unreacted island material is consumed, one can get information about the diffusion mechanism. When the unreacted island material shrinks laterally inwards during phase formation we conclude that the diffusing material is sourced to the reaction region from the edge of the island. On the other hand situations have been found where the edge of the unreacted island material does not move as growth in the surrounding film progresses, implying that the diffusing material is not only sourced from the edge but throughout the island as a whole. An example of such a case is the lateral diffusion work by de Waal[31] using Al islands in the Pt-Al and Ru-Al systems. Consumption of unreacted material from throughout the island region is generally associated with

the mechanism of grain boundary diffusion. (Al is well known to diffuse quickly along grain boundaries in noble metal-aluminide systems.[77,78]) Consumption from around the island edges is mainly associated with lattice diffusion processes (rotational, interstitial, crowdian, vacancy mechanisms, etc.). The diffusion rate due to the latter mechanisms is not fast enough to supply material to the reaction region from anywhere in the island without limiting the growth. Our RBS and SEM results in the Ir-Ge, Pt-Ge and Rh-Ge systems indicated that the Ge was consumed predominantly from around the island edges which suggested the dominance of lattice diffusion processes. However, a more detailed examination by AFM revealed that some material from further inside the island was also consumed, thereby indicating that some grain boundary diffusion could have also played a part.

The lateral diffusion samples used in this study were prepared with the configuration of Ge islands evaporated onto metal films. In all systems, the germanide phases were seen to spread out from the source region in their decreasing order of germanium content. Table 7.2 gives a summary of the various phases observed in each system and the corresponding activation energies obtained.

SYSTEM	PHASES OBSERVED DURING LATERAL DIFFUSION AND ACTIVATION ENERGIES OBTAINED		
Ir-Ge	$IrGe_4$	Ir_3Ge_7	Ir_4Ge_5 $E_a = 1.6\pm0.1$eV
Pt-Ge	$PtGe_2$ $E_a = 1.5\pm0.4$ eV	Pt_2Ge_3 $E_a = 0.9\pm0.1$ eV	PtGe $E_a = 1.3\pm0.2$ eV
Pd-Ge	PdGe	Pd_2Ge $E_a = 1.0\pm0.1$ eV	
Rh-Ge	$Rh_{17}Ge_{22}$ $E_a = 1.2\pm0.3$ eV	RhGe $E_a = 1.2\pm0.3$ eV	

Table 7.2: Summary of the germanide phases seen to spread out from the source region in their decreasing order of germanium content during lateral diffusion. Corresponding activation energies obtained are included.

The activation energy results in Table 7.2 were derived from Arrhenius plots of lnK_β versus $1/k_bT$, the symbols having been explained in previous chapters. Activation energies were also obtained using the modified Gösele and Tu model[32] and the results were in reasonable agreement with those in Table 7.2. The magnitudes of E_a suggest that the lateral diffusion reactions in all four systems were not driven by surface diffusion but rather diffusion through the interior of the lateral diffusion couple; typical values for surface diffusion being around 0.6 eV. [64]

The values of the width ratios for the different phase regions were found to be fairly constant as a function of the annealing time at various temperatures. According to the Gösele and Tu model, this showed that the annealing periods were sufficiently long so that the diffusion systems became self-regulating hence acquiring the constant flux ratio labeled as r^{eq} in Fig. 1.11 of Chapter 1. Referring to that figure, it was observed that the growth in all four systems lay in the region $r_1<r<r_2$.

A notable aspect of the four lateral diffusion systems studied was that each system exhibited some interesting, unique and reproducible features. Some of these features will now be summarized, after which comparisons will be made between the behavior of the different systems.

The phases observed to form in lateral diffusion couples of the Ir-Ge system were the same as those observed in the thin film study on this system with the possible exception of IrGe (i.e. $IrGe_4$, Ir_3Ge_7, and Ir_4Ge_5). Assuming that the results of lateral diffusion couple studies by Liu and Mayer,[37] Zheng et al.[26] and Blanpain et al.[32] reflect a typical range of values for the critical growth length of one phase before the next begins to form (in those studies the range of critical length values in the temperature range between 300°C and 600°C was from 3.9 μm to 25 μm), the range of widths of the phase Ir_4Ge_5 studied in the present work, which was up to around 25 μm, may have been below the critical length for the phase IrGe to start growing. Within the resolution limit of our experimental setup, the two phases Ir_3Ge_7 and Ir_4Ge_5 appeared to grow simultaneously from the beginning. This implied that the magnitudes of their interfacial reaction barriers were close and it was therefore not possible to determine the critical growth width of one

phase before the other started to grow. The phase Ir_3Ge_7 was seen to stretch across the original island interface at all temperatures. As in the results of the thin film couples, the phase $IrGe_4$ was only observed to nucleate at temperatures above 800°C.

Three phases were observed in the Pt-Ge system; $PtGe_2$ and Pt_2Ge_3 inside the original island region and PtGe outside. The Pt_2Ge and Pt_3Ge_2 phases observed in the thin film study of the system were absent in the lateral diffusion couples. Our SEM results revealed the formation of characteristic voids at the surface in the original island region. A characteristic Pt depletion region was also observed at the interface between PtGe and the unreacted Pt film. Because of the part that this Pt depletion layer plays in the growth process, it is probably not possible to study the critical length phenomenon in lateral diffusion couples of this system.

The only two phases PdGe and Pd_2Ge which were observed to form in the thin film study of the Pd-Ge system were also the two observed in the lateral diffusion couples. The middle of the island consisted of unreacted Ge overlaying the phase PdGe while the growth region outside the original island interface consisted of the phase Pd_2Ge. Our SEM results showed the formation of cracks inside the source region near the original island interface. The cracks don't appear to be related to Pd diffusion into the island as the region surrounding the growth interface does not become depleted in Pd. Pd_2Ge growth at the Pd interface was characteristically fractal. This system exhibited low temperature reaction but the extent of growth was limited because the cracks in the matrix eventually halted the reaction. At high temperatures the reaction was rapid but quickly ceased.

The phase $Rh_{17}Ge_{22}$ was observed inside the original island region in the Rh-Ge system while RhGe grew outside in most cases. Under certain conditions, the latter phase was observed to slowly stretch across the original interface into the island region. This suggested a slow decomposition of $Rh_{17}Ge_{22}$ into RhGe. As mentioned earlier, our RBS data from the thin film study of this system strongly suggested the formation of the non-congruent phase Rh_2Ge but this phase was not observed in the lateral diffusion couples. On the basis of comparison with some other work reported on the critical length phenomenon,[26,32,37] it seems unlikely that the range of widths of the phase RhGe in our

study (which went up to over 150 μm) could have not reached the critical length for the phase Rh_2Ge to start growing. Wittmer et al.[71] did not observe the phase Rh_2Ge in their thin film work, which could indicate that this phase does not form easily, hence its absence in the lateral diffusion couples.

From the above, a wide range of different behaviours were observed in the four systems. Given that Ir and Pt are neighbours in the same row of the periodic table, similarities would be expected between the Ir-Ge and Pt-Ge systems. (A similar argument could be advanced for the Rh-Ge and Pd-Ge systems.) Among the similarities observed are that both the Ir-Ge and Pt-Ge systems exhibited phases that were formed from the decomposition of more germanium rich phases; the Ir_3Ge_7 which formed inside the original island region was from the decomposition of $IrGe_4$ and Pt_2Ge_3 was all formed from $PtGe_2$ decomposition. The two systems were also phase rich, in both of them, four phases were observed in the thin film work and three in the lateral diffusion couples.

Perhaps surprisingly, there are a significant number of differences between the two systems which we shall now discuss and in some cases suggest plausible explanations for their different behaviour.

The Ir-Ge system had a nucleation controlled phase, $IrGe_4$. No nucleation controlled phase was observed in the Pt-Ge system, nor in any of the other two systems studied. A comparison of the heats of reaction for the various reaction processes presented in this thesis shows that of $IrGe_4$ formation as having one of the closest values to zero. (It is generally accepted that nucleation controlled reactions are usually characterized by a heat of reaction close to zero.) It may be worth mentioning that the Ir-Si system also has a nucleation controlled phase, $IrSi_3$,[79,80] while there is no nucleation controlled phase in the Pt-Si system. Interestingly, $IrSi_3$ is the most Si-rich of all transition metal silicides[81] while $IrGe_4$ is probably the most Ge-rich of all transition metal germanides. Another feature unique to the Ir-Ge system was the formation of Ge crystals on the surface of the unreacted Ge at temperatures greater than 800°C.

Another difference is that the Ir-Ge system has a phase (Ir_3Ge_7) that extended across the interface while in the Pt-Ge system the original interface formed the boundary between the Pt_2Ge_3 and the PtGe phase. It is believed that this difference was a consequence of the

decomposition process. In the Ir-Ge system, after the formation of $IrGe_4$ within the island, excess Ge atoms diffused laterally outwards forming the phases Ir_3Ge_7 and Ir_4Ge_5 (these three phases were also present in thin films). Once the supply of Ge dropped, $IrGe_4$ started to decompose into Ir_3Ge_7 thereby supplying more Ge atoms. This resulted in a Ir_3Ge_7 region stretching from inside the original island region to the outside across the original island interface; that outside having been formed by the interaction between Ir_4Ge_5 and the outward diffusing Ge atoms, while that observed inside from the decomposition of $IrGe_4$. In the Pt-Ge system, after the formation of $PtGe_2$, Ge atoms diffused laterally forming the phase PtGe outside the island region, this phase was also one of those observed in thin films. Like the $IrGe_4$, $PtGe_2$ also decomposed but in this case to Pt_2Ge_3, supplementing the flow of Ge atoms to the reaction interface. The difference lies in the fact that unlike Ir_3Ge_7, the non-congruent phase Pt_2Ge_3 would not ordinarily appear since it was clearly skipped in the thin film study of this system. For this reason Pt_2Ge_3 did not grow outside and hence did not stretch over the original island interface.

A further difference was that the Pt-Ge system showed a Pt depletion layer at the growth interface while the Ir-Ge and other systems studied did not show any metal depletion layer. The presence of the depletion region indicated that Pt had diffused laterally during the reaction otherwise its lateral concentration would have remained constant. From our marker results we observed that Pt was the dominant moving species during the formation of the first phase Pt_2Ge, it could be that Ge atoms diffused from the island source to the reaction interface while Pt also diffused from the unreacted Pt film to this interface creating a depletion region in the film. The two atomic species could then have interacted forming Pt_2Ge. The depletion region then limited the supply of Pt hence inhibiting further growth of Pt_2Ge favoring the growth of the less Pt rich phase PtGe. An Ir depletion region was not seen in the Ir-Ge system because, as seen in our marker results, Ge was the sole moving species during the formation of Ir_4Ge_5. Ge was therefore the only moving species to the outer reaction interface which was between Ir_4Ge_5 and Ir.

One final difference is that the exposed layer of $PtGe_2$ appeared to have a sponge-like form while $IrGe_4$ did not. This was due to the nature of the original island growth where Pt reacted all the way up to the surface while Ir was buried below a layer of Ge. The

sponge-like form appeared after unreacted Ge diffused away from the island exposing $PtGe_2$, as explained in Chapter 4.

Similarities between the Pd-Ge and the Rh-Ge systems are that in both systems only two phases were observed in the lateral diffusion couples and the activation energies obtained from the Pd_2Ge and RhGe growth kinetics were similar in magnitude.

A significant difference in behaviour between the above two systems was that the Rh-Ge system was very well behaved while fractal formation and cracking occurred in the Pd-Ge system. As mentioned earlier, the cracks did not appear to be related to Pd diffusion but rather the columnar nature of the original island growth. The fractal growth was probably due to insufficient and inhomogenious Ge supply to the growth interface which was related to the crack formation as explained in Chapter 5.

Since Pt and Pd are in the same column of the periodic table, some similarities might also be expected between the Pt-Ge and Pd-Ge systems. The two systems had the common feature of having metal atoms of the underlying film rising to the surface in the early stages of the reaction. It appears that the difference in growth between these two systems was that in the Pd-Ge case the germanide (PdGe) grew as islands in a matrix of unreacted germanium while in the Pt-Ge it was the germanide ($PtGe_2$) that formed a matrix around germanium islands, i.e. in the Pt-Ge system the unreacted Ge was more localized resulting in the formation of voids rather than cracks after the Ge was consumed.

Ir and Rh are also in the same column of the periodic table therefore we would expect some similarities in the Ir-Ge and Rh-Ge systems. Aside from having a well behaved layer by layer rather than a columnar growth in the early stages of the reaction, the Ir-Ge and Rh-Ge systems had the common feature of a relatively high temperature at which the first reaction began. Further, both systems had a phase that stretched across the island interface; Ir_3Ge_7 and RhGe respectively.

From a theoretical stand point, within the framework of the kinetic model of Gösele and Tu,[24] the compound phase with the lowest effective interfacial reaction barrier will form first and initially grow linearly with time (interface limited growth) and then with a parabolic growth law (diffusion limited). After the thickness of the first compound phase

exceeds a critical value x_β^{crit}, the second compound phase will start to form. In all four systems studied, we did not observe the transition from interface reaction limited to the diffusion limited regime. This was a result of the following factors,

(a) the phases studied had relatively low interfacial reaction barriers, and

(b) due to the geometry of the lateral diffusion couples, the experimental resolution was limited by the size of the beam.

For a detailed study of the interfacial reaction region, the experimental set-up used by Schröder and Samwer[82] could be more appropriate, where an in-situ resistivity experiment is performed in a deposition chamber with the substrate at the reaction temperature, thus minimizing the effect of the heat-up period.

As mentioned in Chapter 1, the primary objective of this investigation was to develop an understanding of the interactions between germanium and the Platinum Group Metals in lateral diffusion couples. This has been achieved using the established techniques RBS, PIXE, SEM, AFM and Optical Microscopy. While the research reported on in this thesis has led to better understanding it has at the same time raised a wide range of new questions suggesting possible areas for future work.

In the thin film study of the Ir-Ge system, the phases IrGe and Ir_4Ge_5 appeared to coexist right from the onset of the reaction. An investigation could be carried out to establish which of the two is the actual phase to form first. In the lateral diffusion study of the same system, the two phases Ir_3Ge_7 and Ir_4Ge_5 appeared to grow simultaneously from the beginning as observed within the resolution limit of our experimental setup. A critical growth width of one phase before the other starts to grow could perhaps be determined using other techniques like TEM which was used successfully by Blanpain et al.[32] for similar work. Our SEM results showed a hint of some slowly growing region at the interface between Ir_4Ge_5 and the unreacted Ir film but the width of this region was too narrow for conclusive RBS analysis in order to determine the composition. It was suggested that this could have been a region of the phase IrGe, confirmation of this could be an area of further investigation. It would generally be nice to see more work done on the Ir-Ge system since there has been so little documented in the literature and an

apparent lack of interest in this system is evident by the non-availability of an equilibrium phase diagram.

In the Pt-Ge system, a Pt deletion region at the interface between PtGe and the surrounding Pt film suggested that Pt atoms diffused towards the reaction zone. It is not clear whether this resulted during the formation of PtGe or some precursor phases that were not detectable by the present set up, this requires further investigation. Since SEM is generally restricted to surface topography, Transmission Electron microscopy (TEM) could give more detail of the subsurface structure. It was hoped that PIXE would offer a direct way of obtaining percentage concentrations of the diffusing species as a function of lateral position, which could then be used to estimate the concentration profile across a phase region $\Delta C_{\beta}^{eq} = C_{\beta\alpha}^{eq} - C_{\beta\gamma}^{eq}$, described earlier in the framework of the kinetic model of Gösele and Tu.[24] It was found that μPIXE was not well suited for achieving this to a workable resolution. A more appropriate technique for this is Scanning Transmission Electron Microscopy (STEM) as used for the above purpose in the work of Blanpain.[32-34] In that work the concentration profile of a diffusing element was determined using the STEM mode of a JEOL 200CX microscope equipped with a standard energy dispersive detector system.

An important achievement in this work was the successful use of Particle Induced X-ray Emission (PIXE) on the Nuclear Microprobe in the μPIXE scanning mode to study lateral diffusion couples. To our knowledge, this is the first time PIXE has been used in this regard. This extends the range of possible systems that can now be studied on the microprobe since the use of μRBS is limited to couples of elements that are not close in atomic number. As demonstrated in Chapter 6, μPIXE can readily be used to study systems like the Ni-Ge and Co-Ge where μRBS cannot be used due to excessive peak overlap. The study of such systems is an obvious area for future research.

On the whole, this investigation was important because it deepened the understanding of the systems studied. One of the strengths of this work is that it gives a good demonstration of the power of using a combination of techniques in obtaining compositional as well as depth information which is necessary in making detailed

comparisons between the behaviour of different diffusion systems. A few examples of how the combination of techniques was useful in this regard are presented below.

From our RBS and PIXE results of the Pd-Ge samples, the region at the outer reaction interface showed a gradual decrease in Ge concentration. By using SEM it became clear that this decrease was not as a result of a gradual change in composition but rather the effect of summing data parallel to the interface across alternating areas of Pd_2Ge and unreacted Pd in a region of fractal growth, thereby reducing the combined Ge concentration.

Another example is that our RBS and SEM results in the Ir-Ge, Pt-Ge and Rh-Ge systems indicated that Ge was consumed predominantly from around the island edges. However, a more detailed examination by AFM revealed that some material from further inside the island was also consumed. AFM was also used in conjuction with RBS to estimate the densities of the phases formed.

The origin of the voids and cracks observed in our SEM results of the Pt-Ge and Pd-Ge systems respectively was only explained after analysis of the RBS results, which revealed that some metal atoms rose to the surface during the early stages of the reactions. Finally the depleting region in the Pt-Ge system was clearly visible in the SEM results but only identified as a Pt depletion region using PIXE and RBS.

While lateral diffusion couples were first studied in the early 1980's,[25-28] newly adopted techniques and apparatus have been used to study them. This work has shown that these techniques provide valuable insight, especially when used in conjunction with each other.

Appendix A

Additional Representative Spectra

A.1 RBS

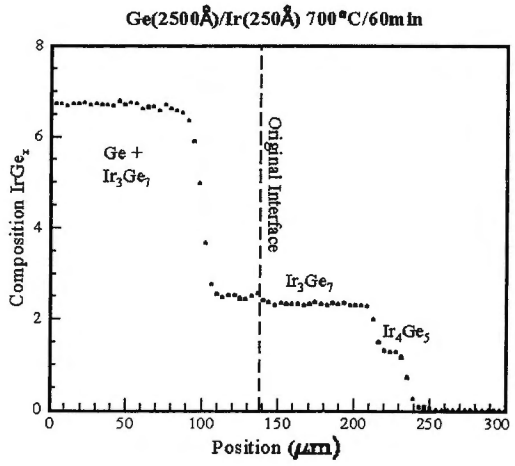

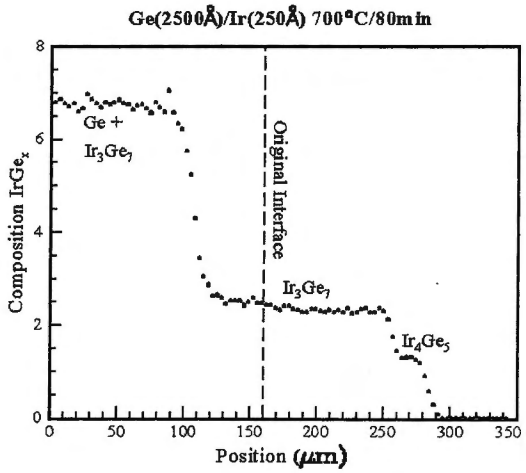

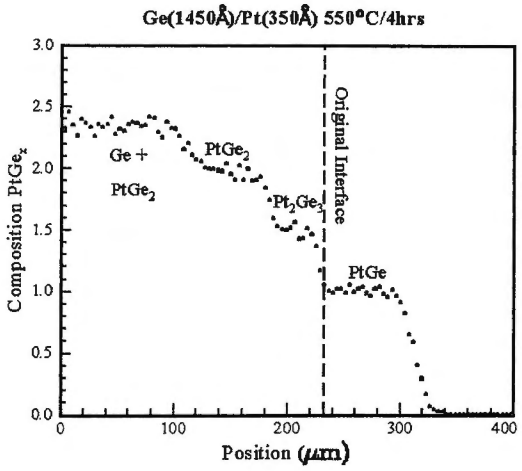

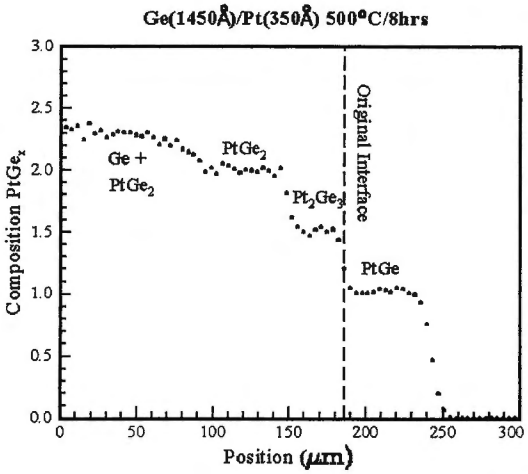

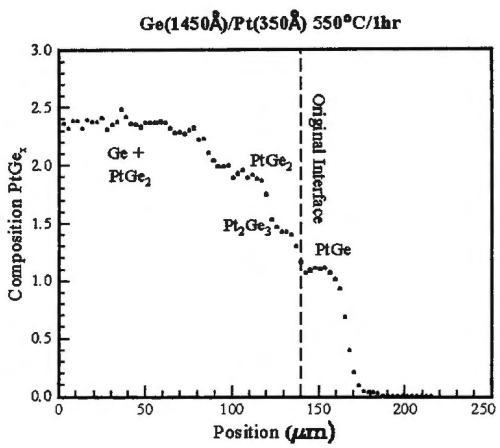
Ge(1450Å)/Pt(350Å) 550°C/1hr
Composition PtGe$_x$
Position (μm)
Original Interface
Ge + PtGe$_2$
PtGe$_2$
Pt$_2$Ge$_3$
PtGe

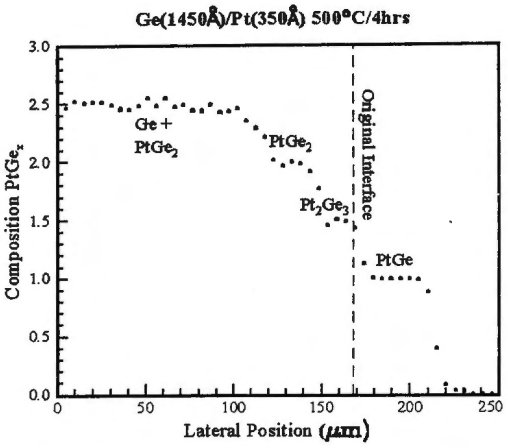
Ge(1450Å)/Pt(350Å) 500°C/4hrs
Composition PtGe$_x$
Lateral Position (μm)
Original Interface
Ge + PtGe$_2$
PtGe$_2$
Pt$_2$Ge$_3$
PtGe

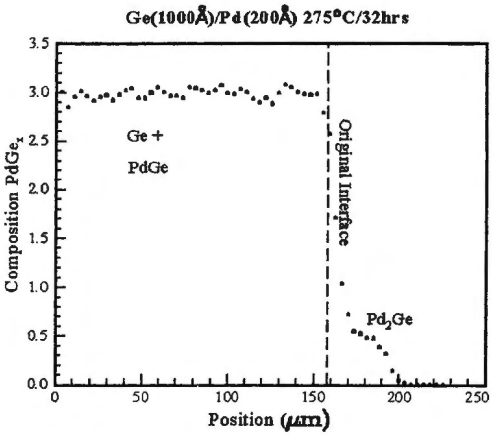
Ge(1000Å)/Pd(200Å) 275°C/32hrs
Composition PdGe$_x$
Position (μm)
Original Interface
Ge + PdGe
Pd$_2$Ge

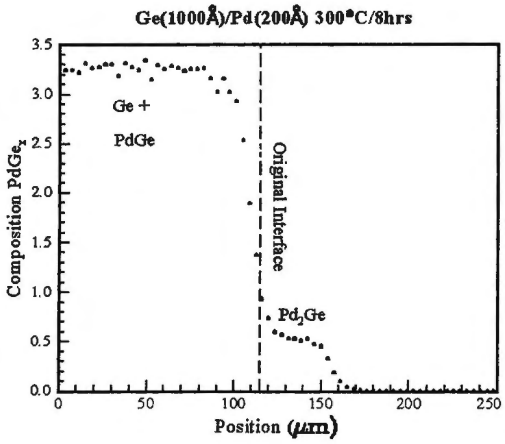
Ge(1000Å)/Pd(200Å) 300°C/8hrs
Composition PdGe$_x$
Position (μm)
Original Interface
Ge + PdGe
Pd$_2$Ge

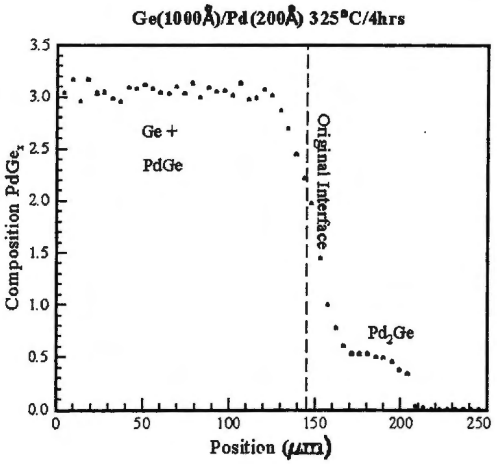
Ge(1000Å)/Pd(200Å) 325°C/4hrs
Composition PdGe$_x$
Position (μm)
Original Interface
Ge + PdGe
Pd$_2$Ge

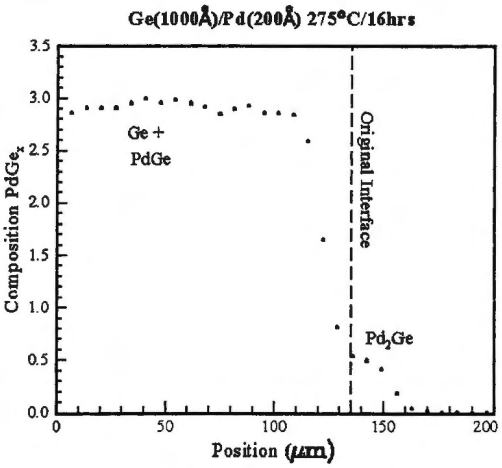
Ge(1000Å)/Pd(200Å) 275°C/16hrs
Composition PdGe$_x$
Position (μm)
Original Interface
Ge + PdGe
Pd$_2$Ge

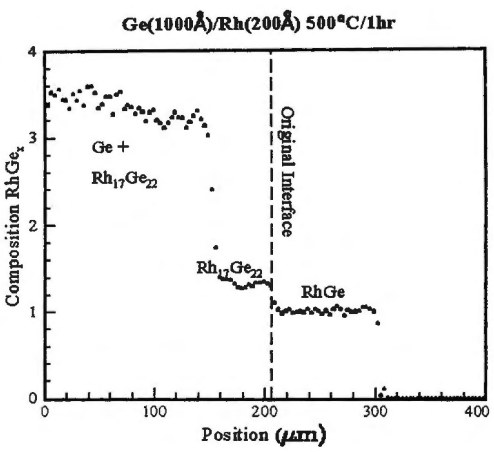
Ge(1000Å)/Rh(200Å) 500°C/1hr
Composition RhGe$_x$
Position (μm)
Original Interface
Ge +
Rh$_{17}$Ge$_{22}$
Rh$_{17}$Ge$_{22}$
RhGe

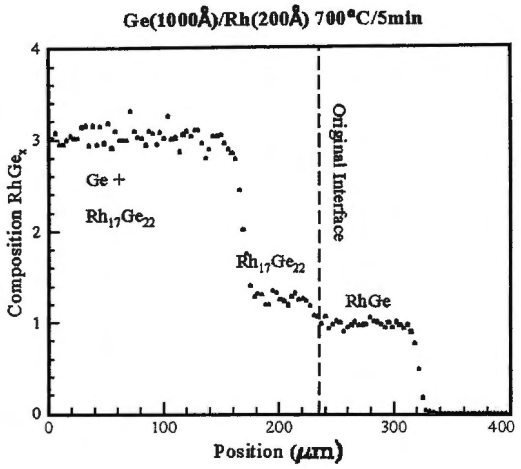
Ge(1000Å)/Rh(200Å) 700°C/5min
Composition RhGe$_x$
Position (μm)
Original Interface
Ge +
Rh$_{17}$Ge$_{22}$
Rh$_{17}$Ge$_{22}$
RhGe

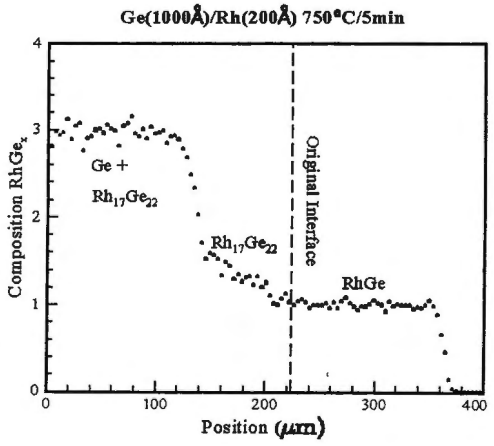
Ge(1000Å)/Rh(200Å) 750°C/5min
Composition RhGe$_x$
Position (μm)
Original Interface
Ge +
Rh$_{17}$Ge$_{22}$
Rh$_{17}$Ge$_{22}$
RhGe

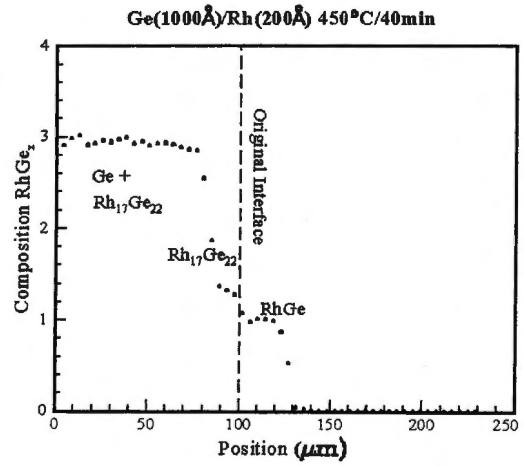
Ge(1000Å)/Rh(200Å) 450°C/40min
Composition RhGe$_x$
Position (μm)
Original Interface
Ge +
Rh$_{17}$Ge$_{22}$
Rh$_{17}$Ge$_{22}$
RhGe

A.2 PIXE

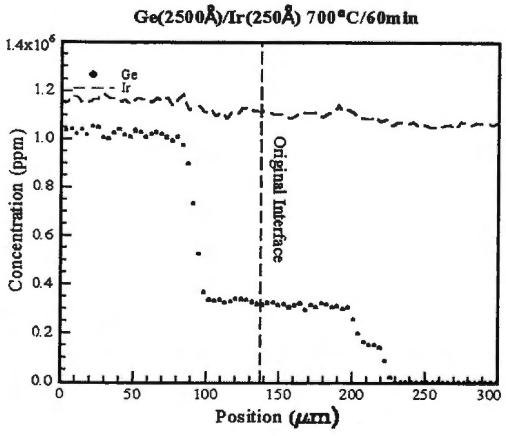
Ge(2500Å)/Ir(250Å) 700°C/60min
Concentration (ppm)
Position (μm)
Original Interface
Ge
Ir

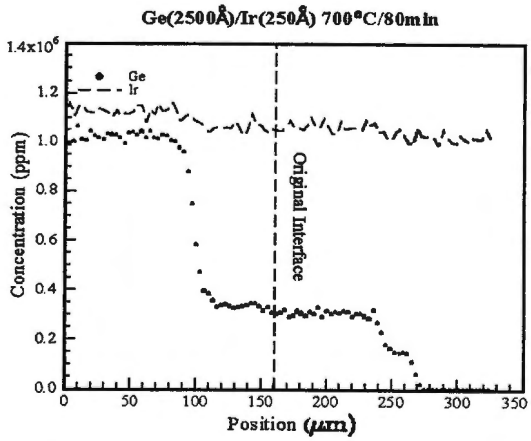
Ge(2500Å)/Ir(250Å) 700°C/80min
Concentration (ppm)
Position (μm)
Original Interface
Ge
Ir

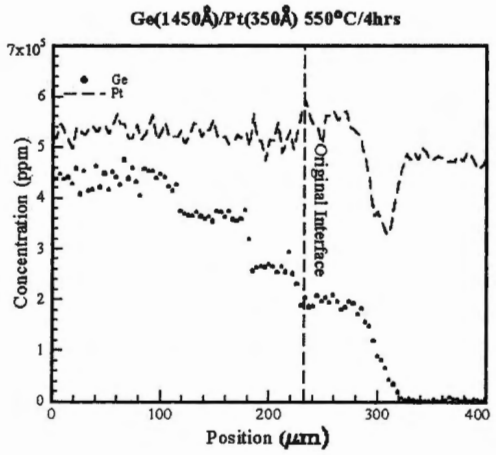
Ge(1450Å)/Pt(350Å) 550°C/4hrs
7x10^5
Ge
Pt
Original Interface
Concentration (ppm)
Position (μm)

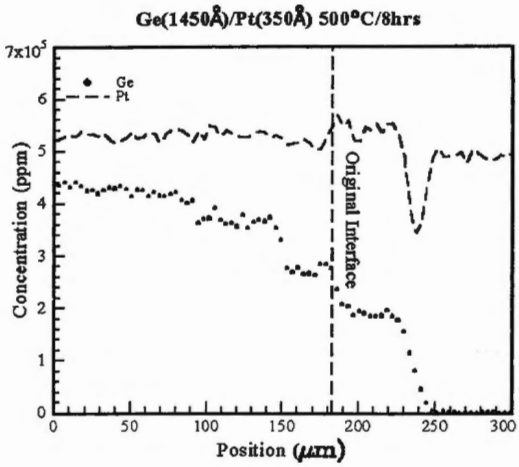
Ge(1450Å)/Pt(350Å) 500°C/8hrs
7x10^5
Ge
Pt
Original Interface
Concentration (ppm)
Position (μm)

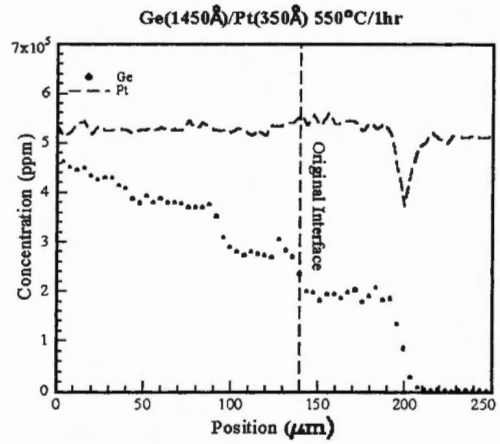
Ge(1450Å)/Pt(350Å) 550°C/1hr
7x10^5
Ge
Pt
Original Interface
Concentration (ppm)
Position (μm)

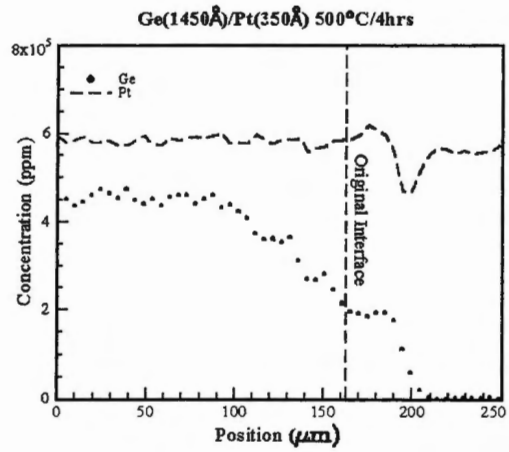
Ge(1450Å)/Pt(350Å) 500°C/4hrs
8x10^5
Ge
Pt
Original Interface
Concentration (ppm)
Position (μm)

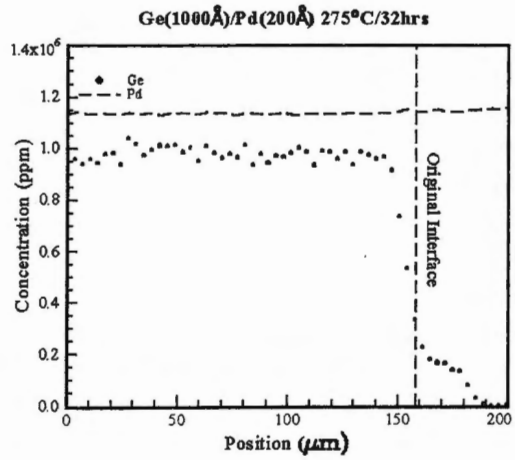
Ge(1000Å)/Pd(200Å) 275°C/32hrs
1.4x10^6
Ge
Pd
Original Interface
Concentration (ppm)
Position (μm)

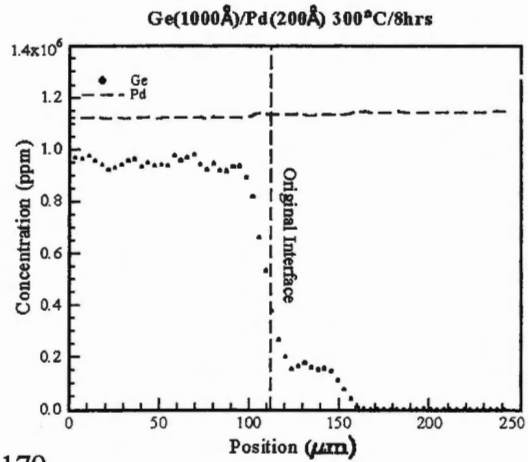
Ge(1000Å)/Pd(200Å) 300°C/8hrs
1.4x10^6
Ge
Pd
Original Interface
Concentration (ppm)
Position (μm)

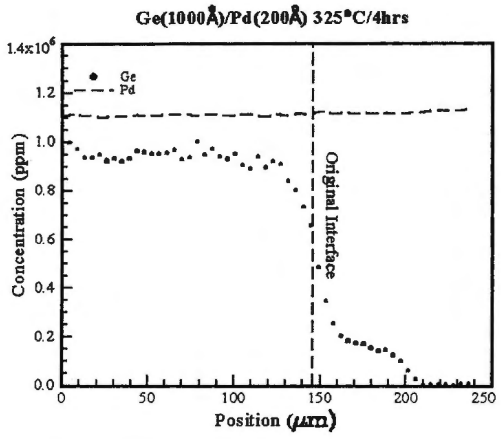
Ge(1000Å)/Pd(200Å) 325°C/4hrs
Ge
Pd
Original Interface
Concentration (ppm)
Position (μm)

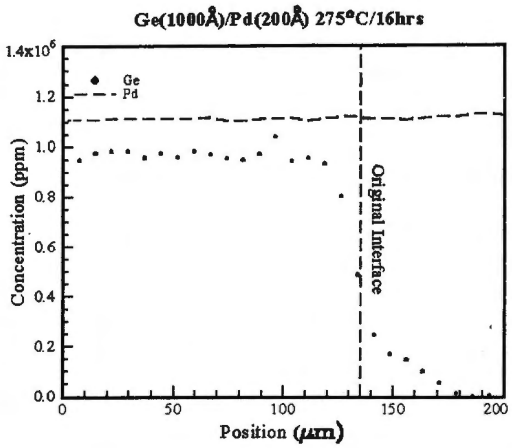
Ge(1000Å)/Pd(200Å) 275°C/16hrs
Ge
Pd
Original Interface
Concentration (ppm)
Position (μm)

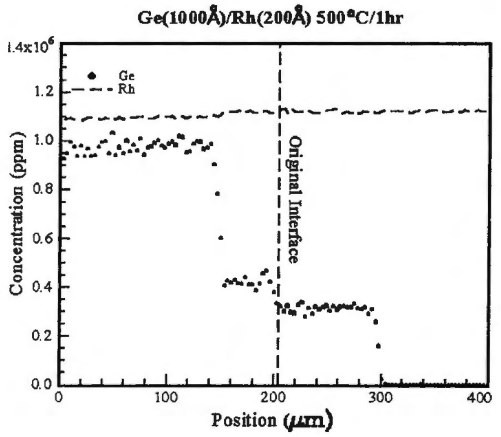
Ge(1000Å)/Rh(200Å) 500°C/1hr
Ge
Rh
Original Interface
Concentration (ppm)
Position (μm)

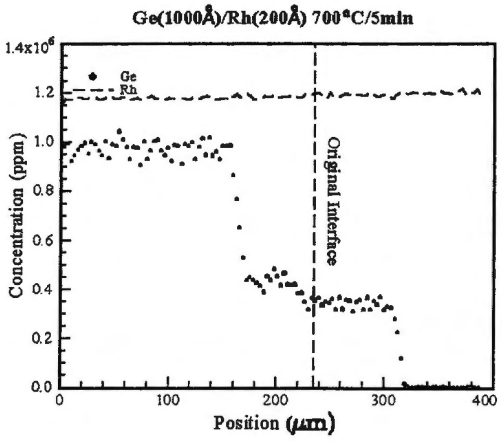
Ge(1000Å)/Rh(200Å) 700°C/5min
Ge
Rh
Original Interface
Concentration (ppm)
Position (μm)

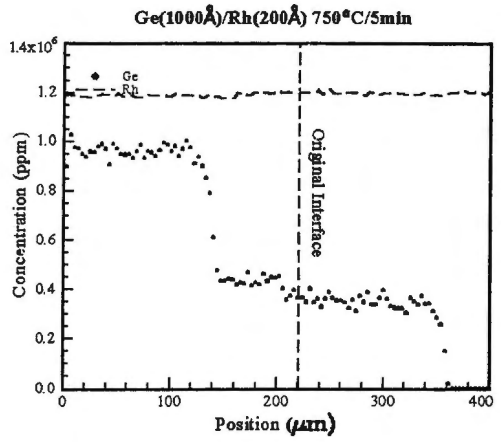
Ge(1000Å)/Rh(200Å) 750°C/5min
Ge
Rh
Original Interface
Concentration (ppm)
Position (μm)

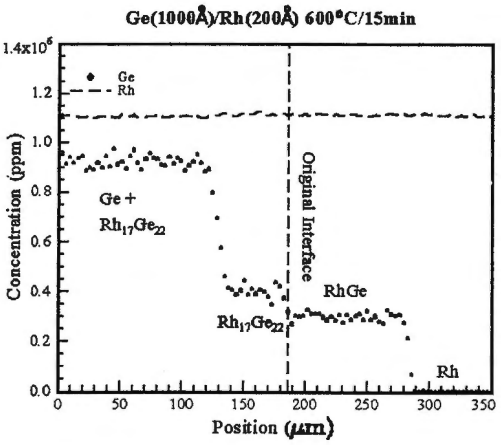
Ge(1000Å)/Rh(200Å) 600°C/15min
Ge
Rh
Ge +
Rh17Ge22
Original Interface
RhGe
Rh17Ge22
Rh
Concentration (ppm)
Position (μm)

Appendix B

RUMP Simulation of RBS Spectra

B.1 Algorithm

RUMP is a Rutherford Backscattering data analysis, plotting and simulation package. Theron[83] summarised the essential features of the Rump simulation algorithm. In a RUMP simulation[84-86] an ideal sample is assumed to consist of a finite number of layers of uniform composition with sharp interfaces. Layers are assumed to have arbitrary thickness but if a layer exceeds a certain maximum thickness it is subdivided into sublayers. The spectral contribution from every isotope of every sublayer in the simulation is referred to as a brick. To work out the energy location of a brick, the energy lost by the beam along its inward and outward paths should be evaluated according to the equation

$$\frac{dE}{da} = -\varepsilon(E),$$

where $\varepsilon(E)$ is the energy dependent stopping cross section and a is the path length into the sample in areal density units. The algorithm[84] uses a fifth order polynomial least squares fit to Ziegler's data.[87] Using Bragg's rule for the linear additivity of stopping cross sections in non-elemental materials, the coefficients defining stopping cross sections for every sublayer are computed. Assuming an initial beam energy $E(0)$ the problem is to evaluate the energy $E(Nt\sec\theta)$ of the beam after passing through a thickness Nt at an angle θ to the normal. To do this a Taylor expansion of $E(a-0)$ around $E(0)$ is used,

$$E(a) = E(0) + a\left.\frac{dE}{da}\right|_0 + \frac{1}{2}a^2\left.\frac{d^2E}{da^2}\right|_0 + \frac{1}{6}a^3\left.\frac{d^3E}{da^3}\right|_0 + ...$$

If ε, ε' and ε'' are evaluated at $a=0$ and $E=E(0)$, neglecting terms beyond the third order the above above expansion reduces to

$$E(a) = E_0 - a\varepsilon + \frac{1}{2}a^2\varepsilon\varepsilon' - \frac{1}{6}a^3(\varepsilon''\varepsilon^2 + \varepsilon'^2\varepsilon).$$

The energy position of the brick is then determined by the energy loss along the inward and outward paths of the beam through the overlying sublayers and that of the scattering events from the front and back of the brick. These events are assumed to be simple elastic.

The yield of a nuclide A at interface i is:

$$y^A = \frac{x_A\sigma(E_i)}{[\varepsilon(E_i)]_A \cos\theta} \prod_{layers} \frac{\varepsilon(E_{in})}{\varepsilon(E_{out})},$$

where x_A is the atomic fraction of nuclide A in the sublayer, E_i is the energy of the beam when it strikes the interface and $[\varepsilon(E_i)]_A$ is the stopping cross section factor for component A given by:

$$[\varepsilon(E)]_A = K_A\,\varepsilon(E) + \varepsilon(K_A E),$$

K_A being the appropriate kinematic factor. The product term in the expression for y^A is that of the ratios of entry and exiting stopping powers over all overlying sublayers.[84] The brick is assumed to be quadratic in shape and the extra degree of freedom is thereafter linked to an independent computation of the area,

$$area = \int_0^{Nt\sec\theta} \sigma(E(a))da\,.$$

RUMP uses strictly Rutherford cross sections and does not attempt to correct for core electron screening which reduces the cross section from the Rutherford value at low energies. A virtual multi-channel analyzer is used to complete the simulation by integration over the energy ranges corresponding to a channel, thereby evaluating the quadratic expression for each brick.

B.2 Semi-automatic minimization code

Simulation of RBS spectra is based on overlaying a theoretical spectrum onto an experimental one and iteratively modifying the parameters until an adequate fit is achieved. Once a qualitative description of the sample has been established, the algorithm[85] searches for the 'best fit' values from a set of parameters. The statistical uncertainty of each parameter is then quantitatively determined.

To evaluate the 'distance' between a simulated and an experimental spectrum, the Poisson maximum likelihood function χ^2 is used,

$$\chi^2 = -2\sum(n_i(1-\ln(n_i/t_i))-t_i),$$

where t_i is the simulated number of counts in channel i and n_i is the experimental number of counts in that channel. If x represents the vector of parameters used to describe the sample,[85] an approximate expression for χ^2 near its minimum is determined by the minimization algorithm in the form

$$\chi^2(\mathrm{x}) \approx \chi_0^2 + \frac{1}{2}(\mathrm{x}-\mathrm{x}_0)^T H(\mathrm{x}-\mathrm{x}_0),$$

where x_0 represents the vector of 'best fit' values, χ_0^2 is the minimum χ^2 value obtained, which can be used as a guide to the 'goodness of fit'. H is the positive definite Hessian matrix which provides uncertainty information:

$$H_{ij}^{-1} = \sigma_{x_i x_j},$$

where the ij element of H^{-1} is the covariance of the ith and jth parameter.

Appendix C

GeoPIXE II Imaging and Analysis of PIXE Spectra

C.1 GeoPIXE II

GeoPIXE II[45] is a new PC based version of the GeoPIXE software package.[44] It is written in IDL (Interactive Data Language)[46] to facilitate platform independence and uses the established methods of GeoPIXE for spectrum fitting and yield calculation for multi-layered samples.[92-96] Like GeoPIXE it calculates the yields of all X-ray lines separately and fits the spectra with relative line intensities that accurately reflect the integral over the entire layered structure. To this it incorporates the generation of a Dynamic Analysis (DA) matrix[89] for projecting quantitative PIXE trace element images and extracting concentrations down to ~0.2 ppm. A 'line traverse' feature allows for the projection of the extracted concentration data onto a selected line across a sample thereby creating a line profile of element concentration against distance.

C.2 Dynamic Analysis

The principles of Dynamic Analysis (DA)[88-91] provide a matrix method of decomposing PIXE spectra into there elemental components. A spectrum vector $\boldsymbol{S}$ is transformed to a concentration vector $\boldsymbol{C}$ by the matrix transformation

$$\boldsymbol{C} = Q^{-1}\Gamma\boldsymbol{S},$$

Q being the integrated charge and Γ the DA transformation matrix.[89] During the on-line formation of 'event by event (EVT)' files on the Nuclear Microprobe or a later off-line playback of these files, each triplet (e,x,y) of energy e at position x,y contributes to the images M_k for elements k, each contribution can be represented as

$$\delta M_k(x,y) = \Gamma_{ke}$$

The images M_k are directly related to concentration by reference to the live-charge distribution $Q(x,y)$. The elemental distributions generated by the above equation exhibit three important properties: (a) The background is subtracted and element overlap is resolved. (b) Aside from some minor yield corrections discussed in the next

section, the images are quantitative in that the value in each pixel represents integrated charge times the concentration. (c) Images can be formed as an EVT file is being produced on-line, this helps in easy adjustment of the target area being scanned.

In any region of the image the average concentrations $<C_k>$ are given by

$$< C_k >= \frac{\Sigma_{region} M_k(x,y)}{\Sigma_{region} Q(x,y)}$$

C.3 Correction for spatial variation of sample composition

Due to spatial variation of sample composition at the pixel level, there could be regions with compositions that differ significantly from the ones assumed in determining the values Y_k of the thick target PIXE X-ray yields (counts per ppm), used to build the DA transformation matrix Γ. This in turn leads to errors in concentration determination. The concentration C_k of an element k in a pixel will generally contain contributions from all phases j that contain that element k:

$$C_k = \Sigma_j r_j P_{jk}$$

where P_{jk} is the concentration of element k in the phase j and r_j is the fraction of phase j at the pixel. The fractions of phases at each pixel (x,y) are therefore given by the matrix equation:

$$\boldsymbol{r} = \boldsymbol{C}\,\boldsymbol{P}^{-1}.$$

provided an inverse exists for $\boldsymbol{P}$.

To combine the thick target PIXE X-ray yields of components in estimating the yields from a mixture, we can weight the inverse yields by the mass fraction of each component. This gives the corrected yield for a pixel $Y_k^{correct}$ as

$$(Y_k^{correct})^{-1} = \Sigma_j r_j (Y_{jk}^{phase})^{-1}$$

where Y_{jk}^{phase} are the yields calculated for each separate phase j. A pixel in each image is then corrected by the factors $Y_k / Y_k^{correct}$ for that pixel, where the values of Y_k are the ones originally used to build the DA transformation matrix Γ. The corrected yields now lead to improved estimates of the concentration.

Bibliography

[1] F. J. J. van Loo and G. D. Rieck, *Acta Met.*, **21** (1973) 61.

[2] E. Philofsky, *Sol. State Electr.*, **13** (1970) 1391.

[3] L. S. Castleman and L. L. Siegle, *J. Met.*, **9** (1957) 1173.

[4] M. Epple and H.K. Cammenga, *Ber. bunsenges. Phys. Chem.*, **96** (1992) 1774.

[5] S.-L. Zhang and F. M. d'Heurle, *Thin Solid Films,* **256** (1995) 155.

[6] E. G. Colgan and F. M. d'Heurle, *J. Appl. Phys.*, **79** (1996) 4087.

[7] K. F. Dreyer, W. K. Neils, R. R. Chromik, D. Grosman, and E. J. Cotts, *Appl. Phys. Lett.*, **67** (1995) 2795.

[8] P. Knauth, A. Charaï, C. Bergman, and P. Gas, *J. Appl. Phys.* **76** (1994) 5195.

[9] A.R. Miedema, P.F. de Châtel and F.R. de Boer, *Physica,* **100B** (1980) 1.

[10] S. V. Meschel and O. J. Kleppa, *J. Alloys and Comp.*, **321**(2001)183.

[11] R.M. Walser and R.W. Bené, *Appl. Phys. Lett.*, **28** (1976) 624.

[12] B.Y. Tsaur, S.S. Lau, J.W. Mayer and M.A. Nicolet, *Appl. Phys. Lett.*, **38** (1981) 922.

[13] R. Pretorius, "Prediction of silicide first phase and phase sequence from heats of formation", *Mat. Res. Soc. Symp. Proc., Elsevier Science, New York,* **25** (1984) 15.

[14] R. Pretorius, T.K. Marais, and C.C. Theron, *Mater. Sci. Eng.*, **R10** (1993) 1.

[15] K.N. Tu, W.K. Chu and J.M. Mayer, *Thin Solid Films*, **25** (1975) 403.

[16] J. Olowolafe, M.A. Nicolet and J.W. Mayer, *Thin Solid Films*, **38** (1976) 143.

[17] D.M. Scott and M.A. Nicolet, *Nucl. Instr. and Meth.*, **182** (1981) 655.

[18] D.J. Coe and E.H. Rhoderick, *J. Phys. D: Appl. Phys.*, *9* (1976) 965.

[19] W.K. Chu, H. Kraütle, J.W. Mayer, H. Muller, M.A. Nicolet and K.N. Tu, *Appl.*

Phys. Lett., **25** (1974) 454.

[20] R. Pretorius, C.L. Ramiller, S.S. Lau and M.A. Nicolet, *Appl. Phys. Lett.*, **30** (1977) 501.

[21] G. Majni, C. Nobili, G. Ottaviani, M. Costato and E. Galli, *J. Appl. Phys.*, **52** (1981) 4047.

[22] S. U. Campisano. G. Foti, E. Rimini, S.S. Lau and J.W. Mayer, *Phil. Mag.*, **31** (1975) 903.

[23] G. Majni, G. Ottaviani and E. Galli, *J. Crystal Growth,* **47** (1979) 583.

[24] U. Gösele and K.N. Tu, *J. Appl. Phys.*, **53** (1982) 3252.

[25] L. R. Zheng and L. S. Hung and J. W. Mayer and G. Majni and G. Ottaviani, *Appl. Phys. Lett.*, **41** (1982) 646.

[26] L. R. Zheng and L. S. Hung and J. W. Mayer, *J. Vac. Sci. Technol.*, **A1** (1983) 758.

[27] L.R. Zheng, L.S. Hung and J.W. Mayer, *Thin Solid Films*, **104** (1983) 207.

[28] S. H. Chen and L. R. Zheng and J. C. Barbour and E. C. Zingu and L. S. Hung and C. B. Carter and J. W. Mayer, *Materials Letters,* **2** (1984) 469.

[29] P. J. Ding, R. Talevi, W. A. Lanford, S. Hymes and S. P. Murarka, *Nucl. Instr. Meth.*, **B85** (1994) 17.

[30] R.S. Nemutudi, C.M. Comrie and C.L. Churms, *Thin Solid Films*, **358** (2000) 270.

[31] H.S. de Waal, "The effect of diffusion barriers, stress and lateral diffusion on thin-film phase formation", (PhD thesis, University of Stellenbosch, South Africa, 1999).

[32] B. Blanpain and J. W. Mayer and J. C. Liu and K. N. Tu, *J. Appl. Phys.*, **68** (1990) 3259.

[33] B. Blanpain and J. W. Mayer and J. C. Liu and K. N. Tu, *Phy. Rev. Lett.*, **64** (1990) 2671.

[34] B. Blanpain, *Crucial Issues in Semiconductor Materials and Processing Technologies, Kluwer academic publishers,* **222** (1992) 421.

[35] Joyce C. Liu and J. W. Mayer and J. C. Barbour, *J. Appl. Phys.*, **64** (1988) 651.

[36] Joyce C. Liu and J. W. Mayer and J. C. Barbour, *J. Appl. Phys.*, **64** (1988) 656.

[37] J. C. Liu and J. W. Mayer, *J. Mater. Res.*, **5** (1990) 334.

[38] B. Tuck, "Introduction to diffusion in semiconductors", (Peter Peregrinus, UK., 1974).

[39] Wei-Kan Chu, James W. Mayer, Marc-A. Nicolet, "Backscattering Spectrometry", (Academic Press, New York, 1978).

[40] Appleton, B.R., and Foti, G., "Ion Beam Handbook for Material Analysis", (J. W. Mayer and E. Rimini, eds., Academic Press, New York 1977).

[41] Johansson, S.A.E and Campbell, J.L.," PIXE: A Novel Technique for Elemental Analysis", (Wiley, 1988).

[42] Johansson, S.A.E., Campbell, J.L. and Malmqvist, K.G.," Particle Induced X-ray Emission Spectrometry", (Wiley, 1995).

[43] Knoll, G.F., "Radiation detection and measurement", (Wiley, New York, 1979).

[44] Ryan, C.G. and Cousens, D.R., "GeoPIXE: PIXE Microanalysis Software System", (Users' Guide, 1992).

[45] Ryan C.G., "GeoPIXE II: Quantitative PIXE Trace Element Imaging and Analysis", (Users' Guide, 2001).

[46] "IDL. Interactive Data Language", (Users' Manual, Research Systems Inc. Boulder, 1993).

[47] Churms C., Pilcher J.V., Springhorn K. and Tapper U.A.S. (1993). *Nucl. Instr. Meth.*, **B 77** (1993) 56.

[48] "XSYS: A General Purpose Data Acquisition System", (Indiana University Report, Indiana,1985).

[49] Reimer L., "Scanning Electron Microscopy", (Springer, Berlin,1998).

[50] Zach J., *Optik*, **83** (1989)30.

[51] Boyde A., *Scanning Electron Microsc.*, **105** (1970)112.

[52] Wiesendanger R. "Scanning Probe Microscopy and Spectroscopy", (Cambridge

University Press, Cambridge, 1994).

[53] Wiesendanger R. and Güntherodt H. "Scanning Tunnelling Microscopy, vols I-III", (Springer, Berlin, 1995).

[54] Hansma P.K., Elings V.B., Marti O. and Bracker C.E., *Appl. Phys. Lett.*, **55** (1994) 1738.

[55] B.D. Cullity, "Elements of X-ray Diffraction", (Addison-Wesley, 1978).

[56] Amelinck S., van Dyck D., van Landuyt J. and van Trendelo G., "Handbook of Microscopy, Application in Materials Science, Solid State Physics an Chemistry", (VCH., Weinheim, 1996).

[57] Brabury S. and Everett B., "Contrast Techniques in Light Microscopy", (Microscopy Handbook, BIOS Scientific Publishers, Oxford, 1996).

[58] S. Bhan and K. Schubert, *Z. Metallkunde.*, **51** (1960) 327.

[59] K. Schubert and H. Pfisterer, *Z. Metallkunde*, **41** (1950) 433.

[60] H. Pfisterer and K. Schubert, *Z. Metallkunde*, **41** (1950) 358.

[61] O. Thomas, S. Delange, F.M. d'Heurle and G. Scilla, *Appl. Phys. Lett.* **54** (1989) 228.

[62] O. Thomas, F.M. d'Heurle and S. Delange, *J. Mater. Res.*, **5** (1990) 1453.

[63] G.V. Kidson, *J. Nucl. Mater.*, **3** (1961) 21.

[64] L. Eckertova, "Physics of thin films, 2nd Edition ", (Plenum, New York, 1989).

[65] E.D. Marshall, C.S. Wu, C.S. Pai, D.M. Scott and S.S. Lau, *MRS Symp. Proc.*, **47** (1985) 161.

[66] E.D. Marshall, B. Zhang, L.C. Wang, P.F. Jiao, W.X. Chen, T. Sawada and S. Laul, *J. Appl. Phys.*, **62** (1987) 942.

[67] Y.F. Hsieh and L.J. Chen, *J. Appl. Phys.*, **63** (1988) 1177.

[68] M.G. Grimaldi, L. Wielunski and M.A. Nicolet, *Thin Solid Films*, **81** (1981) 207.

[69] W.G. Moffat, "The Handbook of Binary Phase Diagrams", (Genium Publishing

Corporation, New York, 1984).

[70] T.B. Massalski, "Binary Alloy Phase Diagrams", (American Society for Metals, Metal Park, OH, 1986).

[71] M. Wittmer, M.A. Nicolet and J.W. Mayer, *Thin Solid Films*, **42** (1977) 51.

[72] Y.F. Hsieh and L.J. Chen, *Thin Solid Films*, **162** (1988) 295.

[73] G. Ottaviani, C. Canali, G. Ferrari, R. Ferrari, G. Majni, M. Prudenziati and S.S. Lau, *Thin Solid Films,* **47** (1977) 187.

[74] S. Petersson, R. Anderson, J. Bablin, J. Dempsey, W. Hammer, F. d'Heurle and S. LaPlaca, *J. Appl. Phys.*, **51** (1980) 373.

[75] R.S. Nemutudi, "Investigation of Iridium Silicide formation", (Honours degree project report, University of Cape Town, South Africa, 1994).

[76] S. Petersson, J. Baglin, W. Hammer, F. d'Heurle, T.S. Kuan, I. Ohdomari, J. de Sousa Pires and P. Tove, *J. Appl. Phys.*, **50** (1979) 3357.

[77] E.G. Colgan, *Materials Science Reports*, **5** (1990) 1.

[78] H.S. de Waal, R. Pretorius, V.M. Prozesky and C.L. Churms, *Nucl. Instr. And Meth.*, **B130** (1997) 722.

[79] F.M. d'Heurle, *J. Mater. Res.*, **3** (1988) 167.

[80] R. Anderson, J. Baglin, J. Dempsey, W. Hammer, F. d'Heurle and S. Petersson, *Appl. Phys. Lett.*, **35** (1979) 285.

[81] Marc A. Nicolet and S.S. Lau, "Formation and Characterization of Transition-Metal Silicides" in "VLSI Electronics: Microstructure Science, volume 6" (Academic Press, 1983).

[82] H. Schröder and K. Samwer, *J. Mater. Res.,* **3** (1988) 461.

[83] C. C. Theron, "In situ real time characterization of solid state reaction in thin films", (PhD thesis, University of Stellenbosch, South Africa,1997).

[84] L.R Doolittle, *Nucl. Instr. Meth.*, **B9** (1985) 344.

[85] L.R. Doolittle, *Nucl. Instr. Meth.*, **B15** (1986) 227.

[86] W.K. Chu, J.W. Mayer, and M.A. Nicolet, "Backscattering Spectrometry", (Academic Press, New York,1978).

[87] J.F. Ziegler, "Helium: Stopping powers and ranges in all elemental matter" in "The Stopping and Ranges of Ions in Matter, volume 4", (Pergamon Press, Oxford, 1977).

[88] C.G. Ryan, I*nternational Journal of Imaging Systems and Technology (Special issue on Quantitative Imaging)* **11** (2000) 219.

[89] C.G. Ryan, *Nucl. Instr. Meth.*, **B** (2001) 1.

[90] C.G. Ryan and D.N. Jamieson, *Nucl. Instr. Meth.*, **B77** (1993) 203.

[91] C.G. Ryan, D.N. Jamieson, C.L. Churms and J.V. Pilcher, *Nucl. Instr. Meth.*, **B104** (1995) 157.

[92] C.G. Ryan, D.R. Cousens, S.H. Sie, W.L. Griffin, G.F. Suter and E. Clayton, *Nucl. Instr. Meth.*, **B47** (1990) 55.

[93] C.G. Ryan, E. Clayton, W.L. Griffin, S.H. Sie and D.R. Cousens, *Nucl. Instr. Meth.*, **B34** (1988) 396.

[94] C.G. Ryan, D.R. Cousens, C.A. Heinrich, W.L. Griffin, S.H. Sie and T.P. Mernagh, *Nucl. Instr. and Meth.*, **B54** (1991) 292.

[95] C.G. Ryan, C.A. Heinrich and T.P. Mernagh, *Nucl. Meth.*, **B77** (1993) 463.

[96] C.G. Ryan, C.A. Heinrich, E. van Achterbergh, C. Ballhaus and T.P. Mernagh, *Nucl. Inst., Meth.*, **B104** (1995) 182.

[97] S. H. Chen and L. R. Zheng and C. B. Carter and J. W. Mayer, *J. Appl. Phys.*, **57** (1985) 258.

[98] Y. Hasumi, Lateral diffusion of In and formation of $AuIn_2$ in Au-In thin films, *J. Appl. Phys.*, **58** (1985) 3081.

[99] P. Reves and J. Gyimesi and L. Pogany and G. Peto, *J. Appl. Phys.*, **54** (1983) 2114.

[100] A. Singh and W. S. Khokle and M. Prudenziati and G. Majni and B. Morten, *J.*

Appl. Phys., **66** (1989) 1190.

[101] J. C. Barbour and P. E. Batson and J. W. Mayer, *MRS Proc.*, **54** (1986) 29.

[102] S. H. Chen and J. C. Barbour and L. R. Zheng and C. B. Carter and J. W. Mayer, *MRS Proc.*, **37** (1985) 635.

[103] R. W. Bene, *Appl. Phys. Lett.*, **41** (1982) 529.

[104] O. L. Sologub, P. S. Salamakha and C. Godart, *J. Alloys and Comp.*, **307** (2000) 31.

[105] L.S. Castleman and L.L. Siegle, *J. Met.*, **9** (1957) 1173.

[106] F.J.J. van Loo and G.D. Rieck, *Acta Met.*, **21** (1973) 61.

[107] M. Atzmon, J.D. Verhoeven, E.D. Gibson and W.L. Johnson, *Appl. Phys. Lett.*, **45** (1984) 1052.

[108] R.K. Ball and A.G. Todd, *Thin Sol. Films*, **149** (1989) 269.

[109] D.J. Coe and E.H. Rhoderick, *J. Phys.*, **D9** (1976) 965.

[110] E.L. Hall, N. Lewis, B.D. Hunt and L.J. Schowalter, *Norelco Reporter*, **33** (1986) 1.

[111] W.L. Johnson, *Progress in Material Science*, **30** (1986) 81.

[112] W.J. Meng, C.W. Nieh and W.L. Johnson, *Appl. Phys. Lett.*, **51** (1987) 1693.

[113] G.A. Smith et al, J. *Vac. Sci. Technol*, **A7** (1989) 3.

[114] Sorab K. Ghandi, "VLSI FABRICATION PRINCIPLES, Silicon and Gallium Arsenide", (John Wiley and sons, New York, 1982).

[115] Otto F. Sankey, Roland E. Allen and John D. Dow, *J. Vac. Sci. Technol.*, **B2** (1984) 491.

[116] H.K. Liou, X. Wu and U. Gennser, *Appl. Phys. Lett.*, **60** (1992) 577.

[117] K. Ismail, M. Arafa, K.L. Saenger, J.O. Chu and B.S. Meyerson, *Appl. Phys. Lett.*, **66** (1995) 1077.

[118] T. Koester, J. Gondermann, B. Hadam, B. Spangenberg, M. Schütze, H.G. Roskos, H. Kurz, J. Brunner and G. Abstreiter, *J. Vac, Sci. Technol.*, **B 14** (1996) 698.

[119] R. People, J.C. Bean, D.V. Lang, A.M. Sergent, H.L. Stormer, K.W. Wecht, R.T. Lynch, and K. Baldwin, *Appl. Phys. Lett.*, **45** (1984) 1231.

[120] Capasso and Alfred Y. Cho, "Surface Science, the first thirty years", (Edited by Charles Duke, North Holland,1994).

[121] M. Genut and M. Eizenburg, *Appl. Phys. Lett.*, **53** (1988) 672.

[122] J.C. Bean, *Proceedings of the First International Symposium on Si Molecular Beam Epitaxy,* (1985) 337.

[123] Peixin Zhong and Youndou Zheng *Appl. Phys. Lett.*, **62** (1993) 3258, 21 June 1993.

[124] Q.Z. Hong, J.G. Zhu C.B. Carter and J.W. Mayer, *J. Appl. Phys. Lett.*, **58** (1991) 905.

[125] E. Philofsky, *Sol. State. Electr.*, **13** (1970) 1391.

[126] King-King Tu, James W. Mayer and Leonard C. Feldman, "Electronic Thin Film Science for Electrical Engineers and Scientists", (Macmillan, New York, 1992).

[127] J.B. Rubin and R.B. Schwarz, *Appl. Phys. Lett.*, **55** (1989) 36.

[128] P.J. Ding, R. Talevi, W.A. Lanford, S. Hymes and S.P. Murarka, *Nucl. Instr. and Meth. in Phys. Res.*, **B85** (1994) 121.

[129] R. Pretorius, A.M. Fredenberg, F.W. Saris and R. de Reus, *J. Appl. Phys.*, **70** (1991) 1.

[130] C.M. Comrie and J.M. Egan, *J. Appl. Phys.*, **64** (1988) 1173.

[131] Leornard C. Feldman and James W. Mayer, "Fundamentals of Thin Films and Analysis", (North-Holland, 1986).

[132] E.O. Kirkendal, *Trans. AIME.*, **147** (1942) 104.

[133] C.M. Comrie, J.C. Liu, L.S. Hung and J.W. Mayer, *J. Appl. Phy.*, **63** (1988) 2402.

[134] J.M. Poate and T.C. Tisone, *Appl. Phys. Lett.*, **24** (1974) 391.

[135] Pluta M., "Advanced Light Microscopy, volume 1: Principles and Basic Properties",(Elsevier, Amsterdam, 1988).

[136] Pluta M., "Advanced Light Microscopy, volume 2: Advanced Methods", (Elsevier,

Amsterdam, 1989).

[137] W. Hume-Rothery and G.V. Raynor, "The Structure of Metals and Alloys", (Institute of Metals, London, 1956).

[138] W.O. Alexander, G.L. Davies, K.A. Reynold, and E.J. Bradbury, "Essential Metallurgy for Enginneers", (Van Nostrand Reinhold, UK.,1985).

[139] A.R. West, "Solid State Chemistry and its applications", (J. Wiley and Sons, 1984).

[140] Johansson T.B., Akselsson R. and Johansson S.A.E., *Nucl. Instr. Meth.*, **84** (1970) 141.

[141] Campbell J.L., Millman B.M., Maxwell J.A.., Perujo A. and Teesdale W.J., *Nucl. Instr. Meth.*, **B 9** (1985) 71.

[142 J.J. Chu and L.J. Chen, *J. Appl. Phys.*, **63** (1988) 1163.

[143] T. L. Lin, C.W. Nieh, S. Hashimoto and Q.F. Xiao, *Thin Solid Films*, **184** (1990) 343.

[144] Davis A. Lange, Gary A. Gibson and Charles M. Falco, *J. Appl. Phys.*, **75** (1994) 2917.

[145] D.M. Hoffman, J.T. McGinn, H. Gilmartin, L.R. Hewitt, A.M. Lanzillotto, D.J. Szostak, F.J. Tams III and J.H. Thomas III, *J. Vac. Sci. Technol.*, **A9** (1991) 456.

[146] H. Von Känel, J. Henz, M. Ospelt, J. Hugi, E. Müller and N. Onda, *Thin Solid Films*, **184** (1990) 295.